Study of the dimer Hubbard Model within Dynamical Mean Field Theory and its application to VO

Oscar Nájera Ocampo

université PARIS-SACLAY

NNT: 2017SACLS462

Thèse de doctorat

UNIVERSITÉ PARIS SUD

Comprendre le monde, construire l'avenir

Study of the dimer Hubbard Model within Dynamical Mean Field Theory and its application to VO_2

Thèse de doctorat de l'Université Paris-Saclay

préparée à Université Paris-Sud

Ecole doctorale n°564 Physique en Île-de-France

Spécialité de doctorat: Physique

Thèse présentée et soutenue à Orsay, le 5 Decembre 2017, par

Óscar Nájera

Composition du Jury:

M. Alexander Lichtenstein Universität Hambourg	(Rapporteur)
M. Massimo Capone Scuola Internazionale Superiore di Studi Avanzati	(Rapporteur)
M. Marino Marsi Université Paris-Sud	(Président)
Mme. Silke Biermann École Polytechnique	(Examinateur)
M. Sébastien Burdin Université de Bordeaux	(Examinateur)
M. Indranil Paul Université Paris Diderot-Paris 7	(Examinateur)
M. Marcelo Rozenberg Université Paris-Sud	(Directeur de thèse)
M. Marcello Civelli Université Paris-Sud	(Invité)

Title : Study of the dimer Hubbard Model within Dynamical Mean Field Theory and its application to VO_2

Keywords : DMFT, dimer Hubbard Model, Mott insulator, Peierls insulator, VO_2

We study in detail the solution of a basic strongly correlated model, namely, the dimer Hubbard model. This model is the simplest realization of a cluster DMFT problem.

We provide a detailed description of the solutions in the "coexistent region" where two (meta)stable states of the DMFT equations are found, one a metal and the other an insulator. Moreover, we describe in detail how these states break down at their respective critical lines. We clarify the key role played by the intra-dimer correlation, which here acts in addition to the onsite Coulomb correlations.

We review the important issue of the Mott-Peierls insulator crossover where we characterize a variety of physical regimes. In a subtle change in the electronic structure the Hubbard bands evolve from purely incoherent (Mott) to purely coherent (Peierls) through a state with unexpected mixed character. We find a singlet pairing temperature T^* below which the localized electrons at each atomic site can bind into a singlet and quench their entropy, this uncovers a new paradigm of a para-magnetic Mott insulator.

Finally, we discuss the relevance of our results for the interpretation of the recently discovered metastable phases of VO_2 in various experimental studies. We present a variety of arguments that allow us to advance the conclusion that the long-lived (metastable) metallic phase, induced in pump-probe experiments, and the thermally activated M_1 meta-stable metallic state in nano-domains are the same. In fact, they may all be qualitatively described by the dimerized correlated metal state of our model.

Titre : Étude du modèle de Hubbard dimérisé avec la théorie du champ moyen dynamique et ses applications à VO_2

Mots clefs : DMFT, Model Hubbard dimérisé, isolant Mott, isolant Peierls, VO_2

J'étudie en détail la solution d'un modèle simplifié d'électrons fortement corrélés, à savoir le modèle de Hubbard dimérisé. Ce modèle est la réalisation la plus simple d'un problème de cluster DMFT.

Je fournis une description détaillée des solutions dans une région de coexistence où l'on trouve deux états (méta) stables des équations DMFT, l'un métallique et l'autre isolant. De plus, je décris en détail comment ces états disparaissent à leurs lignes critiques respectives. Je clarifie le rôle clé joué par la corrélation intra-dimère, qui agit ici en complément des corrélations de Coulomb.

Je passe en revue la question importante du passage continue entre un isolant Mott et un isolant Peierls où je caractérise une variété de régimes physiques. Dans un subtil changement de la structure électronique, les bandes de Hubbard évoluent des bandes purement incohérentes (Mott) à des bandes purement cohérentes (Peierls) à travers un état inattendu au caractère mixte. Je trouve une température d'appariement singulet T^* en-dessous de laquelle les électrons localisés à chaque site atomique peuvent se lier dans un singulet et minimiser leur entropie. Ceci constitue un nouveau paradigme d'un isolant de Mott paramagnétique.

Enfin, je discute la pertinence de mes résultats pour l'interprétation de de phases metastables du VO_2 decouvertes recentement en différentes études expérimentales. Je présente plusieurs arguments qui me permettent d'avancer la conclusion que la phase métallique, à vie longue (métastable) induite dans les expériences pompe-sonde, et l'état métallique métastable M_1, thermiquement activé dans des nano-domaines, sont identiques. De plus, ils peuvent tous être qualitativement décrits, dans le cadre de notre modèle, par un métal corrélé dimérisé.

Acknowledgments

This thesis contains a sample of my work done at LPS. Lucky for you my reader this work only contains the results I mostly understood without all the confusing thought process to get to them. Otherwise this thesis would have been maybe 3 times longer, full of dead ends and 10 harder to understand. That is what the experience of research is about, figuring things out when the path is not clear.

This was not a solitary work, despite how quiet and introvert I am. I would really like to thank all the people who where by my side during all my research stay at LPS. I would like to thank my closest friend and my office colleague Sergueï Tchoumakov, with whom I started this research experience almost 4 years ago during our Masters internship in this very same laboratory. Together we shared more than a workspace, but many discussions about our work, and life here is Paris.

Yunlong, my fellow foreigner friend only you understood how hard it is to live in a foreing country, with family far away in a country we don't fully understand and nor are we understood back. Thank you for sharing your time with me, your advice, your knowledge and your patience.

Marcello, my unofficial but most present supervisor. How can I thank you for all the time you dedicated to me? You where around since the beginning, when I first tried to find a Masters internship. Counseling me regarding my PhD applications, mentoring me during my PhD time in this lab. I want to thank you for all the time and effort you dedicated to me and for the necessary "push" you gave me to complete all of this.

Marcelo, the true master mind behind all of this, with you I learned about autonomy since you where always moving around. Finding you in you office was rarely a possibility, and everything passed through emails. But there hasn't ever been a meeting between us two where discussion weren't overloaded of ideas, and many new things to try out. I deeply admire your passion and physical intuition. I also thank you for the confidence you always placed in me.

The *Laboratoire de Physique des Solides* is a great laboratory, but it is located on the top of a hill and every morning you have to climb this steep hill to get to your work. The only reason to do it is because the stimulating and friendly environment it host to do physics. I thank all the members of the *Groupe Théo*

for welcoming me and involving me in the group's life during all these years. I very much appreciated the lunch breaks where we would all discuss about life, entertain ourselves with the many jokes from Mark Goerbig. And because discussion are the big source of inspiration all the team would meet for the *Pause Café* occurring many times during the day, and where the friendly *Tea team* would be in serenity without having to worry about the broken coffee machine.

This work would have been impossible without the support of my family. I have been so lucky to have a loving and supporting family that was always by my side despite the long physical distances separating us. Having your support meant so much to me, and I'm extremely thankful.

Résumé

Les matériaux corrélés, pour lesquels la théorie des bandes standard des solides se décompose, présentent souvent une phase isolante, l'isolant de Mott, même si les bandes électroniques ne sont pas remplies. Dans ces systèmes, les effets quantiques à N-corps corrélés, qui sont négligés par la construction dans la théorie des bandes, jouent un rôle majeur et peuvent radicalement changer la nature de l'état fondamental en un nouvel état quantique. Outre les isolateurs Mott, des exemples frappants comprennent des phases présentant des propriétés magnétiques exotiques, comme la magnétorésistance colossale, les ondes de densité de charge et de spin, les mauvais métaux et la supraconductivité à haute température Imada et al. [1998]. Notre objectif principal a été de comprendre comment les électrons de ces matériaux interagissent les uns avec les autres pour donner lieu à de tels phénomènes quantiques inhabituels. Les équations physiques régissant ces systèmes sont bien connues, mais elles s'avèrent beaucoup trop complexes pour être résolues. En plus de cette complexité, une petite variation des paramètres tels que la température, la pression, la composition peut conduire à de grands changements dans les propriétés des matériaux. La possibilité de basculer entre plusieurs phases quantiques en ajustant un paramètre de contrôle externe ouvre de nouvelles voies de recherche vers des dispositifs quantiques multifonctionnels, qui pourraient constituer les éléments constitutifs des futures technologies de l'électronique atomique et de l'informatique quantique Ahn et al. [2006].

Dans ce scénario et avec des solutions exactes hors de portée, un traitement théorique convaincant des corrélations électroniques est le plus demandé. Au cours des dernières décennies, de grand progrès a été accomplis grâce au développement de la théorie du champ moyen dynamique (DMFT) Georges et al. [1996]. Cette méthode a pu prendre en compte la disparition des bandes électroniques entraînées par corrélation et résoudre le difficile problème de la transition Metal-Isolant Mott (MIT) dans le modèle de Hubbard. Cette solution, bien que exacte seulement dans la limite de dimension infinie, est une approximation réussie en beaucoup des matériaux réels, comme dans V_2O_3 et les sels organiques Powell and McKenzie [2006], et représente le paradigme universellement accepté de la transition de Mott Kotliar and Vollhardt [2004].

Il y a cependant des situations où une telle vision du DMFT a été remise en question. Emblématique est le cas du VO_2, qui est stoechiométriquement très proche du V_2O_3. En VO_2, le MIT entraîné par la température s'accompagne d'une transition structurelle d'une phase monoclinique à une phase rutile. Un mécanisme de Peierls au lieu d'un mécanisme électronique corrélé a ensuite été

préconisé comme la route vers le MIT. La relation ou la concurrence entre une dimérisation Peierls et la corrélation électronique, dans le VO_2 monoclinique, est resté une question débattue depuis longtemps Goodenough [1960], Pouget et al. [1974], Wentzcovitch et al. [1994], Biermann et al. [2005], Eyert [2011], Brito et al. [2016], Huffman et al. [2017]

VO_2 présente une transition métal-isolant au-dessus de la température ambiante Morin [1959], ce qui a facilité les recherches expérimentales et a inspiré la recherche de dispositifs électroniques à application industrielle. Malgré cet intérêt, nous manquons encore d'une compréhension complète de sa transition. À basse température, le système est toujours isolant et, dans le cas de la phase M_1, il n'y a pas de l'ordre magnétique. Si nous regardons alors la transition en fonction de la température, nous observons que le comportement est opposé à V_2O_3 avec la ligne de transition de pente opposée. Nous pouvons en effet induire à partir d'un isolant un état métallique en augmentant la température.

Les calculs modernes de la structure électronique soutenaient que seule la structure dimérisée pouvait ouvrir un gap semi-conducteur, mais ils n'ont pas réussi à reproduire le grand écart observé dans les expériences Wentzcovitch et al. [1994], Eyert [2002]. Le développement de méthodes pour incorporer des effets de corrélation fortes dans les calculs de réseaux réalistes a fourni une nouvelle lumière. Biermann et al. [2005], en utilisant la théorie du champ moyen dynamique (CDMFT) avec DFT, a montré que de fortes corrélations dues à la répulsion locale de Coulomb peuvent conduire à l'ouverture d'un gap. Par conséquent, l'état fondamental était considéré comme un "isolant de Peierls avec des corrélations dynamiques". Ce problème théorique a continué d'attirer l'attention au fur et à mesure que les techniques numériques ont été améliorées. L'image de bande a amélioré sa précision avec l'apparition des nouvelles fonctionnelles hybrides Eyert [2011] reliant la transition électronique uniquement au changement de la structure du réseau. Weber et al. [2012] a soutenu que le mécanisme à l'origine de l'état d'isolateur était mieux caractérisé comme une «transition Mott sélective orbitale assistée par Peierls». Ils ont observé que l'orbitale a_{1g} entraîne principalement l'ouverture du gap. D'autres développements conduisent à une étude plus récente où les atomes d'oxygène ont été explicitement inclus Brito et al. [2016], ce qui a permis de rendre compte plus en détail des différentes phases observées dans VO_2. Cependant, l'étude a également conduit à la réinterprétation de la transition comme une «transition de Mott en présence d'un échange intersite fort».

Alors que les améliorations techniques des méthodes de calcul des matériaux corrélés réalistes basés sur DFT + CDMFT représentent des avancées remarquables dans la description de leurs propriétés électroniques, la complexité technique de ces méthodes rend parfois difficile l'interprétation des mécanismes physiques

sous-jacents. Les transitions structurelles et électroniques semblent impossibles à démêler, car les méthodes théoriques actuelles de structure électronique ne peuvent caractériser que les phases connues stables, mais ne sont pas capables d'étudier la compétition entre elles, ce qui peut conduire au MIT thermique de premier ordre. Les études de températures finies sont en effet au-delà de l'applicabilité des méthodes DFT.

Notre affirmation est que la physique de VO_2 est radicalement différente de celle du site unique DMFT, et que l'on doit considérer le dimère comme la structure unitaire du treillis. Afin de comprendre les mécanismes physiques clés, nous introduisons un modèle de Hubbard dimérisé (DHM) et partons de la logique d'un réseau où la dimérisation structurelle est toujours présente, considérons donc le problème dans l'ordre inverse. Nous étudions la transition métal-isolant dans le réseau dimérisé et voyons si ses propriétés peuvent expliquer l'observation expérimentale dans les cas où la relaxation du réseau n'a pas eu lieu. Ceci est indépendant de l'instabilité structurelle de Peierls. Le point de départ remonte aux études de Pouget et al. [1974] sur un modèle de Hubbard à deux atomes portant la représentation minimale des chaînes linéaires d'atomes V en VO_2. Cette même unité de dimère reste au cœur des problèmes d'impureté dans les calculs CDMFT actuels Biermann et al. [2005], Brito et al. [2016]. Pour cette raison, une classification systématique des phénomènes physiques contenus dans ce modèle étudié dans le cadre du DMFT est la plus recommandée. Le modèle de Hubbard dimérisé, une extension naturelle du modèle de Hubbard, contient comme unité de base une paire d'atomes dans sa cellule unitaire. Le DMFT fournit un cadre raisonnable pour étudier la physique présente dans ce modèle, permettant l'étude méthodique de tout l'espace des paramètres et présentant la connexion et la compétition des mécanismes physiques en action. La simplification introduite par DMFT peut isoler les principales caractéristiques de ce modèle à partir de nombreuses autres caractéristiques secondaires qui entrent en jeu dans les matériaux réels, comme la structure de réseau explicite et les orbitales multiples. La compréhension acquise à partir du contexte simple de ce modèle peut ensuite être retransférée vers des études DFT + CDMFT plus avancées qui peuvent viser une comparaison plus réaliste avec des matériaux réels.

L'objectif principal de cette thèse est de montrer que le modèle de Hubbard dimère a les bons ingrédients pour représenter le MIT VO_2. Nous allons caractériser le MIT et montrer qu'il est différent du cas communément connu à une bande unique en DMFT. Cette étude montre que pour comprendre le MIT dans les matériaux corrélés, il est parfois nécessaire de dépasser le cas paradigmatique du site unique DMFT, et qu'une grande partie de la physique de VO_2 peut être expliquée avec ce modèle purement électronique.

D'un point de vue plus large, notre étude systématique de l'espace des paramètres du modèle de Hubbard devrait éclairer la classification d'une grande variété de systèmes d'oxydes de métaux de transition monocliniques avec la formule MO_2 Hiroi [2015] et plus généralement des structures avec une liaison dominante entre une paire d'ions métalliques corrélés. Les cas importants sont, bien sûr, VO_2, que nous considérons en détail dans la présente thèse, et aussi NbO_2, ce qui est également d'un grand intérêt car il a un IMT similaire à une température significativement plus élevée.

Ce modèle est également intéressant en lui-même car c'est sans doute la réalisation la plus simple d'un problème de cluster DMFT. Il est assez surprenant que, après presque 20 ans de sa formulation d'origine, Moeller et al. [1999] ce modèle de base est resté mal compris. Le comprendre s'avère être un défi et le comportement physique émergent que nous trouvons est riche, subtil et expérimentalement pertinent.

Nous fournissons une description détaillée des solutions dans la "région coexistante" où l'on trouve deux états (méta) stables des équations DMFT, l'un métallique et l'autre isolant. De plus, nous décrivons en détail comment ces états se décomposent à leurs lignes critiques respectives. Nous clarifions le rôle clé joué par la corrélation intra-dimère, qui agit ici en plus des corrélations de Coulomb sur site (Mott-Hubbard) déjà présentes dans le cas d'une bande. Leur interaction (c'est-à-dire le criblage de Kondo par rapport à RKKY) détermine la physique de la ligne de transition métal-isolant où les bandes de basse énergie renormalisées qui composent les bandes liantes anti-liantes se séparent. Cette transition a une ressemblance avec une transition de bande, mais ici on parle de bandes de quasi-particules fortement renormalisées. Le point de transition est déterminé par la corrélation intra-dimère renormalisant le saut intra-dimère $t_\perp$, plutôt que par la corrélation locale habituelle produisant un résidu quasiparticule Z, qui ne s'annule pas au point de transition. Ceci est rendu explicite au moyen de notre paramétrisation du modèle R2B, qui est toujours applicable du côté métallique sur le diagramme de phase $t_\perp - U$ à des fréquences assez basses.

La simplicité de la DHM fournit un aperçu physique nouveau et détaillé et nous permet de clarifier le problème important du croisement isolant Mott-Peierls. Nous trouvons une évolution étonnamment subtile de la structure électronique avec le changement systématique des paramètres du modèle. En fait, le passage de la limite de Mott à la limite de Peierls n'est pas trivial et nous avons caractérisé une variété de régimes physiques. Fait intéressant, nous avons constaté que les bandes de Hubbard évoluent de purement incohérent (Mott) à purement cohérent (Peierls) à travers un état avec un caractère mixte inattendu. Cette caractéristique peut être comprise comme suit: dans la limite de Mott, au faible

saut intra-dimère $t_\perp$, on a des degrés de liberté magnétiques émergents qui restent librement fluctuants au-dessus d'une (basse) température d'appariement singulet de spin T^*. L'augmentation du saut intra-dimère lie ces moments libres dans un état singulet de spin et ils acquièrent une cohérence (c'est-à-dire un état quantique bien défini) dans le dimère. Cependant, les excitations d'énergie supérieure d'un tel état manquent encore de cohérence à travers le réseau et donnent origine aux bandes d'Hubbard. Nous pouvons penser à cet état d'isolateur comme des singulet-dimères localisés dans Mott. Lors d'une augmentation supplémentaire du saut intra-dimère, l'orbitale de liaison devient complètement occupée, car on peut considérer la dimérisation de $t_\perp$ comme un champ cristallin efficace. Par conséquent, le système devient polarisé orbitalement en la base de liant/anti-liant, ce qui rend la structure électronique cohérente lorsque les fluctuations quantiques sont gelées. Néanmoins, même dans cette grande limite $t_\perp$, l'écart reste contrôlé par l'interaction U. Par conséquent, le système reste un isolant de Mott à une valeur suffisamment élevée U, bien qu'il soit dans un état orbitalement polarisé, en la base liant/anti-liant.

L'étude des températures finies de ce modèle nous permet de trouver une température d'appariement de singulet T^* en dessous de laquelle les électrons localisés de chaque site atomique peuvent se lier à un singulet et éteindre leur entropie, ceci découvre un nouveau paradigme de isolant Mott paramagnétique. Nous étudions également l'évolution des caractéristiques de la fonction spectrale de l'isolant en fonction de la température. En particulier, nous étudions en détail la question de la fermeture du gap et comment l'isolant se transforme en un mauvais métal à température finie. Nous montrons également comment la forme de la région de coexistence dépend du paramètre de dimérisation $t_\perp$, ce qui pourrait transformer la transition thermique métal-isolant bien connue du modèle de Hubbard à bande unique ($t_\perp = 0$) en un isolant à métal comme dans VO_2.

Le modèle de Hubbard dimérise sous DMFT présente le problème d'impureté plus simple (absence de multi orbites et de champs cristallins) mais présente néanmoins une forme analogue (dimère corrélé dans un milieu) à celle des approches techniquement complexes LDA + DMFT utilisées pour le caractérisation théorique de VO_2. Nous pensons que la présente solution du DHM peut apporter une compréhension physique équivalente pour VO_2, car les études DMFT du modèle Hubbard à une bande traitant la transition de Mott ont fourni celle de V_2O_3 paramagnétique dopé au Cr, qui est l'une des réalisations significatives de la référence DMFT Georges et al. [1996], Kotliar and Vollhardt [2004]. Plus précisément, notre travail contribue à faire la lumière sur la question de longue date de la force motrice derrière la transition Mott de VO_2.

Dans ce but, nous discutons la pertinence de nos résultats pour l'interprétation

de diverses études expérimentales en VO_2. Plusieurs mécanismes physiques ont clairement émergé de notre étude: le premier est un isolant de Mott où l'entropie magnétique des moments localisés est éteinte par un super-échange boosté, qui peut fournir une énergie de liaison supplémentaire pour stabiliser la déformation du réseau. La seconde est un métal corrélé avec deux bandes de quasi-particules lourdes qui sont séparées par le saut intra-dimère, ce qui donne une caractéristique particulière à la conductivité optique de l'état métallique corrélé observé dans la transition de phase activée thermiquement. Troisièmement, la fonction spectrale de l'isolateur n'est pas composé des bandes rigides, la température peut induire des changements drastiques dans la réponse optique du matériau permettant une caractérisation plus détaillée du matériau à la transition, comme le montre la microscopie optique en champ proche. Quatrièmement, le fait que les nano-régions métalliques qui se forment à proximité de la transition ne percolent pas montre l'enthalpie nette de formation entre ces phases mais aussi le caractère de coexistence entre les deux. Cinquièmement, la coexistence de ces phases peut s'étendre jusqu'à la température zéro comme trouvé par Cocker et al. [2012], avec un seuil de transition indépendant de la température, prouvant de plus amples informations sur la nature du caractère coexistant de ces deux phases. Nous présentons une variété d'arguments qui nous permettent d'avancer la conclusion que la phase métallique de longue vie (métastable) induite dans les expériences pompe-sonde et l'état métallique métastable M_1 thermiquement activé dans les nano-domaines accédés optiquement sont les mêmes, et qu'ils peuvent tous être qualitativement décrits par l'état de métal corrélé dimérisé de notre modèle.

Notre travail apporte quelques réponses mais ouvre également de nouvelles questions intéressantes, qui méritent d'être envisagées dans le futur. Par exemple, en ce qui concerne la transition dans VO_2, nous avons fourni une rationalisation de la transition isolant-métal induite thermiquement par chauffage. Nous avons discuté de l'instabilité entraînée par l'électronique du réseau dimérisé. Une fois que la transition vers l'état métallique monoclinique à température plus élevée a lieu, le réseau n'a clairement aucun avantage à conserver la distorsion. Ainsi, cela favorise la transition structurelle dans la phase rutile moins déformée, ce qui devrait améliorer l'énergie cinétique. Cette interprétation est très cohérente avec les données expérimentales pompe-sonde. Cependant, cela ouvre également la question de savoir s'il existe des caractéristiques précurseurs d'une transition métal-isolant lors du refroidissement. Une asymétrie éventuelle observée dans la dynamique de la croissance d'une phase dans l'autre par refroidissement par rapport au chauffage peut fournir des informations intéressantes à cet égard. Des études de ce genre ont déjà été faites dans le système V_2O_3 McLeod et al. [2016].

Une autre direction importante pour les travaux futurs c'est l'étude de l'effet du

dopage. Expérimentalement, c'est assez difficile de doper VO_2. Par conséquent, des études du DHM dopé peuvent fournir des informations très utiles. Nos études préliminaires font allusion à divers comportements inattendus, qui nécessitent certainement une étude plus approfondie et une vérification. Par exemple, de même que nous avons vu comment de petites variations de température peuvent faire fondre les quasiparticules étroites aux bords de la bande de Hubbard, nous avons observé que de petites variations du potentiel chimique peuvent aussi avoir un effet important. Puisque nous avons caractérisé le gap provenant de la dimérisation corrélée et la production de singulets locaux, nous pouvons supposer que le dopage peut présenter certaines similitudes avec la physique des supraconducteurs cuprates. C'est certainement une direction passionnante que mérite d'être poursuivie.

Contents

This thesis can be found at https://gitlab.com/Titan-C/dissertation for its latest errata.

Chapter 1

Introduction

Correlated materials, for which the standard band theory of solids breaks down, often display an insulating phase, the Mott insulator, even if the electronic bands are not filled. In these systems correlated quantum many-body effects, which are neglected by construction in band theory, play a major role and can radically change the nature of the ground-state into a novel quantum state. Besides Mott insulators, striking examples include phases displaying exotic magnetic properties, like e.g. colossal magneto-resistance, charge and spin density waves, the bad metals and high temperature superconductivity Imada et al. [1998]. Our main focus has been to understand how electrons in such materials interact among each other to give rise to such unusual quantum phenomena. The physical equations governing these systems are well known, but they turn out much too complex to be solved. On top of that complexity, small variation of parameters like temperature, pressure, composition may lead to large changes in the properties of the materials. The possibility to switch between multiple quantum phases by tuning an external control parameter opens new research paths towards multi-functional quantum devices, which could be the building blocks of future atomic-size electronics and quantum computing technologies Ahn et al. [2006].

Within this scenario and with exact solutions out of reach a compelling theoretical treatment of electronic correlations is most urged. In the last decades great advancement has been achieved thanks to the development of the Dynamical Mean Field Theory (DMFT)Georges et al. [1996]. This method has been able to take into account the break down of the electronic bands driven by correlation and to solve the difficult problem of the Mott Metal-Insulator Transition (MIT) in the the Hubbard Model. This solution, though exact only in the infinite dimensional limit, is a successful approximation of many real materials, like e.g. in V_2O_3 and organic salts Powell and McKenzie [2006], and represents the universally accepted paradigm of the Mott transition Kotliar and Vollhardt [2004].

There are however situations where such a DMFT vision has been questioned. Emblematic is the case of VO_2, which is stoichiometrically very close to V_2O_3. In VO_2 the temperature-driven MIT is accompanied by a structural transition from a monoclinic to a rutile phase. A Peierls mechanism instead of an electronic correlated one has then been advocated as the route to the MIT. The relation or competition between a Peierls dimerization and electronic

correlation, within monoclinic VO_2, has remained a long-time debated issue Goodenough [1960], Pouget et al. [1974], Wentzcovitch et al. [1994], Biermann et al. [2005], Eyert [2011], Brito et al. [2016], Huffman et al. [2017]

1.1 Canonical Mott metal-insulator transition: The vanadates

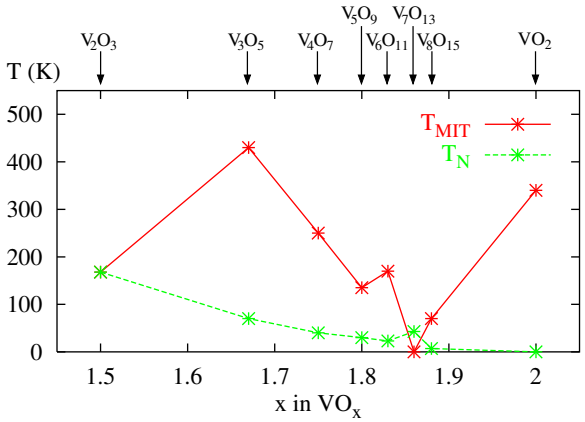

Figure 1.1: Comparison of the MIT temperatures and magnetic ordering temperatures of the Vanadium Magnéli compounds from Schwingenschlögl and Eyert [2004].

Let's first discuss the vanadates, binary compounds of Vanadium and Oxygen atoms, which are an illustrative example of the rich variety of the MIT in correlated materials. Vanadates are fascinating materials that provide a fertile playground to study non trivial phase transitions driven by the electronic correlation. Their structures follow the Magnéli series V_nO_{2n-1}. It is observed, in figure 1.1, that through the series, upon cooling, all these oxides undergo a first order metal-to-insulator transition at T_{MIT} which involves a structural change. Independently, magnetic ordering then sets in at a lower T_N. At the two extremes of the series we find V_2O_3, $(n = 2)$, where both transition temperatures coincide $T_{MIT} = T_N$, and VO_2 $(n = \infty)$ where the structural change takes place but there is no magnetic ordering at any temperature. Moreover, T_{MIT} has a temperature range of 100K to 400K without any systematic trend, while T_N decreases systematically with n. The sole exception is $n = 7$.

V_2O_3 is the prime example of a correlated-electron transition which can be well understood within DMFT Georges et al. [1996]. The relevant toy model used in early studies is the single band Hubbard model (cf. section 2.1) embedded in a Bethe lattice, which does not directly describe the real material's lattice, cf. inset in Fig. 1.2. Here vanadium atoms pair along the c axis at distances of 2.7 Å and each vanadium atom is surrounded by 3 equidistant neighbors in the orthogonal plane at a distance of 2.87 Å. The situation is then of a lattice with a rather high coordination, which is the case where the lattice-simplification adopted by DMFT is most applicable. The success of the DMFT approach in this case

proves that the key ruling correlated mechanism is independent of the lattice structure. In fact the single band Hubbard model solved with DMFT is able to capture the non-trivial features of the V_2O_3 phase diagram. In particular the fact that by starting from rather low temperatures in a Cr-doped metallic phase, the system can be tuned into an insulating high temperature phase. This feature is most uncommon as a standard metal does not usually become insulating upon heating. However, it is well portrayed by the DMFT Phase diagram shown on the right panel of Fig. 1.2. Where this phenomenon is well evidenced by the green arrow. Despite the well suited description discussed in the early DMFT literature, further advances in theoretical techniques do suggest a more involved situation when describing the real material at a multiorbital level cf. Poteryaev et al. [2007], Hansmann et al. [2013].

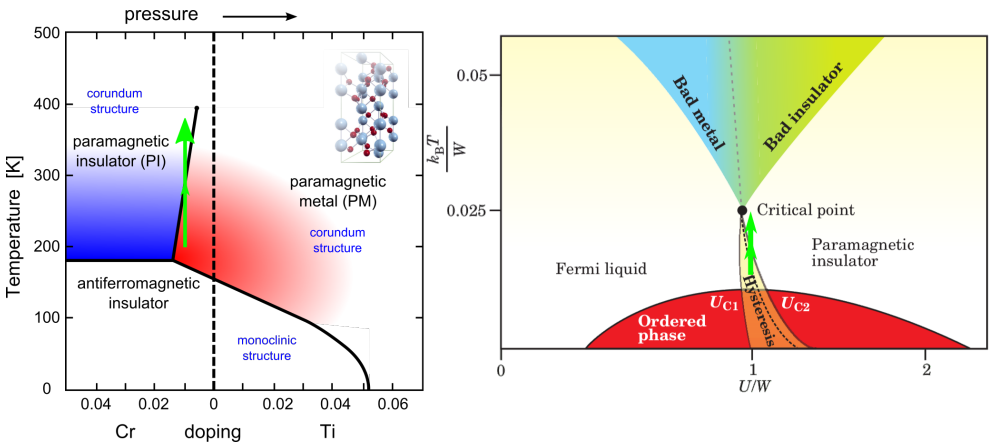

Figure 1.2: (left) V_2O_3 Temperature-doping phase diagram adapted from Hansmann et al. [2013]. (right) Half-filled single band Hubbard Model solved by DMFT from Kotliar and Vollhardt [2004]

In order to join the V_2O_3 compound on one end of the Magnéli series to VO_2 which is on the opposite side Schwingenschlögl and Eyert [2004] propose a nice and simple systematic way to trace the structural evolution in the intermediate compounds. The oxide structures can be thought of as interconnected 1D chains of V atoms of length n. The chains have $n-2$ "internal" atoms and 2 atoms at the ends. In this representation V_2O_3 is made of connected end-atoms alone and VO_2 has no end-atoms conforming an infinite chain of V atoms. The number of nearest-neighbors of each vanadium atom in the plane perpendicular to the chain also decreases as one advances in the series, dropping from 3 in-plane nearest neighbors per vanadium atom in V_2O_3 to none in VO_2. This rather different structure and at the same time also different metal insulator transition has inspired a long standing debate about the physical mechanism in action.

VO_2 presents a metal-insulator transition above room temperature Morin [1959], which has facilitated experimental investigation and inspired research for electronic devices with industrial application. Despite this interest we still lack a complete understanding of its transition. The VO_2 temperature driven MIT in the phase diagram of Fig. 1.3 appears sharply different to the previous V_2O_3 case. Focusing on the M_1 phase, at low temperatures

the system is always insulating, and in the case of the M_1 phase there is no magnetic order setting up. If we then look at the transition as a function of temperature, we observe the behavior is opposite to V_2O_3 with the transition line having opposite slope. We can in fact induce from an insulator a metallic state by increasing temperature.

In an influential early paper Goodenough [1960] focused on the 1D like chains of V atoms that form the structure of VO_2. In his vision, the closeness between the V metal cations allows for a direct conduction channel and at the same time it is prone to Peierls dimerization as the metal ions pair to build a covalent bond, at low temperatures. Hence a gap opens at a metal semiconductor transition. However, posterior identification of other stable insulating phases of VO_2, where the lattice does not dimerize along every of V chains, challenged this view Pouget et al. [1974]. The fact that in these different lattice structures the electronic transition remained unperturbed at the same temperature indicated that electrons localize within the V atoms and that the energy gap in the insulating phases is rather correlation-driven like in a Mott-Hubbard type transition. This competing scenarios have lead to an intense debate up to the present date.

1.2 The case of VO_2: Mott or Peierls

Modern electronic-structure calculations sustained that only the dimerized structure could open a semi-conducting gap, nevertheless they failed to reproduce the large gap seen in experiments Wentzcovitch et al. [1994], Eyert [2002]. The development of methods to incorporate strong correlation effects in realistic lattice calculations provided new light. Biermann et al. [2005] by using Cluster Dynamical Mean Field Theory (CDMFT) with DFT, showed that strong correlations due to local Coulomb repulsion may lead to the opening of a gap. Hence, the ground state was considered a "Peierls insulator with dynamical correlations". Further studies within this framework highlighted the relevance of the intersite self-energy leading to the claim that "the local interactions amplify Goodenough's scenario" giving a "many-body Peierls" insulator Tomczak and Biermann [2007], Tomczak et al. [2008]. This theoretical problem continued to attract attention as the numerical techniques were further improved. The band picture improved its accuracy with the appearance of new hybrid functionals Eyert [2011] linking back the electronic transition uniquely to the change in lattice structure. Weber et al. [2012] argued that the mechanism driving the insulator state was better characterized as a "Peierls assisted orbitally selective Mott transition". They observed that mainly the a_{1g} orbital drives the opening of the gap. Further developments lead to a more recent study where the oxygen atoms were explicitly included Brito et al. [2016], which enabled a more comprehensive account of the various phases observed in VO_2. However, the study also led to the reinterpretation of the transition as a "Mott transition in the presence of strong intersite exchange".

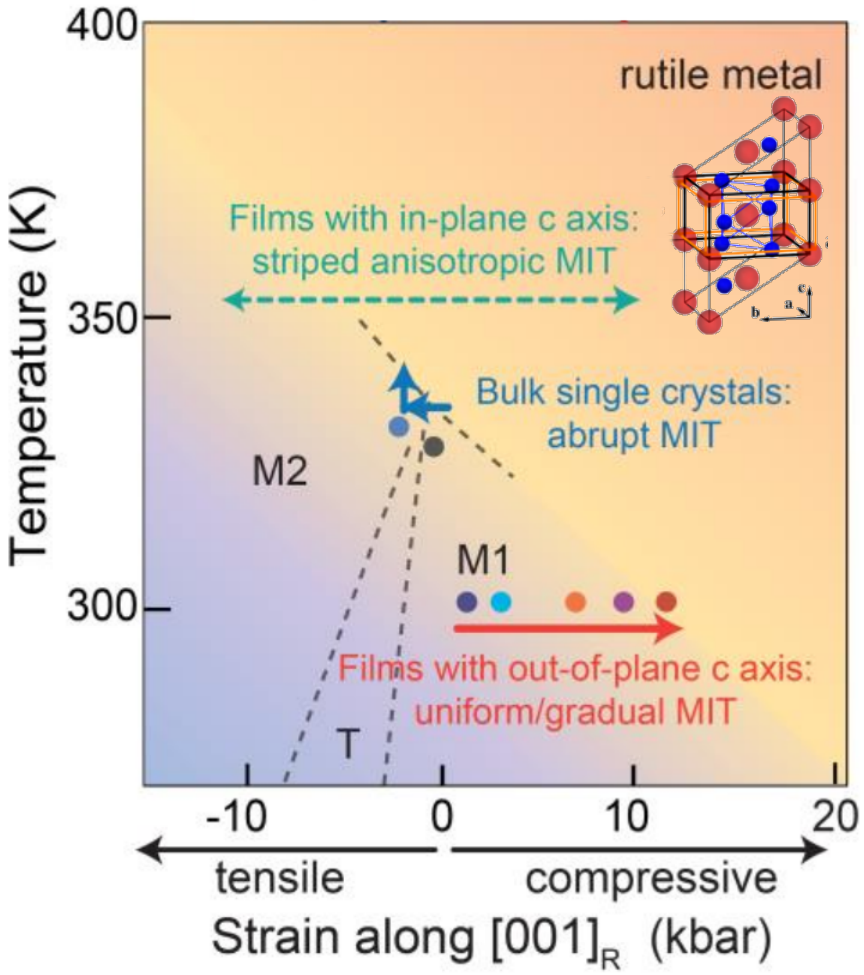

Figure 1.3: VO_2 Temperature-strain phase diagram Liu et al. [2015]. Inset shows the VO_2 crystal structure where V atoms(red spheres) align in 1D chains along the **c** axis(There is no meaning to the color background in the phasediagram).

While the technical improvements of the computational methods of realistic correlated materials based on DFT+CDMFT represent remarkable steps forward in describing their electronic properties, the technical complexity of this methods makes sometimes hard to interpret the underlying physical mechanisms. The structural and electronic transitions seem impossible to disentangle, as current theoretical electronic-structure methods can only characterize the stable known phases, but are not able to study the competition between them, which can lead to the first order thermal MIT. Finite temperature studies are in fact beyond the applicability of DFT methods.

Our claim is that, on the other side of the Magnéli series where we find VO_2, the physics is radically different from the single site DMFT one, and that one must consider the dimer as the unit structure of the lattice. In order to understand the key physical mechanisms we introduce a dimer Hubbard model Moeller et al. [1999], Tomczak and Biermann [2007], Tomczak et al. [2008] (cf. section 2.3) and start from the logic of a lattice where the structural dimerization is always present, consequently consider the problem in reverse order. We study the insulator to metal transition in the dimerized lattice and see if its properties can explain the experimental observation in cases where the lattice relaxation has not taken place. This is independent of Peierls structural instability. The starting point dates back to the studies of Pouget et al. [1974] on a two atom Hubbard model carrying the minimal representation of the occurring linear chains of V atoms in VO_2. This same dimer-unit remains at the heart of the impurity problems in current CDMFT calculations Biermann et al. [2005], Brito et al. [2016]. For such reason a systematic classification of the physical phenomena contained in this model studied under the framework of DMFT is most urged. The Dimer Hubbard model, a natural extension of the Hubbard model, contains as its basic unit a pair of atoms within its unit cell. DMFT provides a sensible framework to study the physics present within this model, enabling the methodical investigation of the whole parameter space and presenting the connection and competition between the physical mechanisms in action. The simplification introduced by DMFT can single out key features in this model from many other secondary features that come into play in the real materials, like for example explicit lattice structure and multiple orbitals. The understanding gained from the simple context of this model can be then transferred back to more advanced DFT+CDMFT studies that can aim to a more realistic comparison with real materials.

The main goal of this thesis is to show that the dimer Hubbard model has the right ingredients to portray the VO_2 MIT. We shall characterize the MIT and show it is the different from the commonly known case from the single band DMFT. This study shows that in order to understand the MIT in correlated materials it is sometimes necessary to go beyond the paradigmatic single site DMFT case, and that a great part of the physics of VO_2 can be explained with this purely electronic model.

Chapter 2

Theoretical Framework

All models are wrong but some are useful

G.E.P. Box (1979). *Robustness in the strategy of scientific model building.* Robustness in Statistics, 201–236.

In this chapter we shall introduce the theoretical tools used to extend our understanding about the Mott transition in the Dimer Hubbard Model, specifically the Dynamical Mean Field Theory. The key idea of this theory consists to replace the quantum many-body problem of the Hubbard model by an quantum impurity problem in an effective medium. Its detailed formulation, the numerical methods to solve the quantum impurity problem and solution for the single band Hubbard model are presented in the next sections. Subsequently, I'll extend the Hubbard model to the Dimer Hubbard Model and reformulate DMFT to be applicable in this particular case.

2.1 The Hubbard Model

The Hubbard model represents the minimal model that incorporates the competition between the delocalization of electrons driven by the kinetic energy and the localization of electrons due to their mutual repulsive Coulomb interaction. The one-band Hubbard Hamiltonian Hubbard [1963], Gutzwiller [1963] can be written in the language of second quantization as:

$$\mathcal{H} = -\sum_{\langle i,j\rangle,\sigma} (t_{ij} c^{\dagger}_{i\sigma} c_{j\sigma} + H.c.) + U \sum_{i} n_{i\uparrow} n_{i\downarrow} \tag{2.1}$$

where $c^{\dagger}_{i\sigma}$ ($c_{i\sigma}$) are the creation (annihilation) operators of the electronic wave-function at site i and with spin σ, $t > 0$ is the tunneling amplitude between the nearest neighboring sites denoted by $\langle i, j\rangle$, $U > 0$ is the on-site Hubbard repulsion, and for simplicity $n_{i\sigma} = c^{\dagger}_{i\sigma} c_{i\sigma}$ is the number operator of the particle on site i and spin σ.

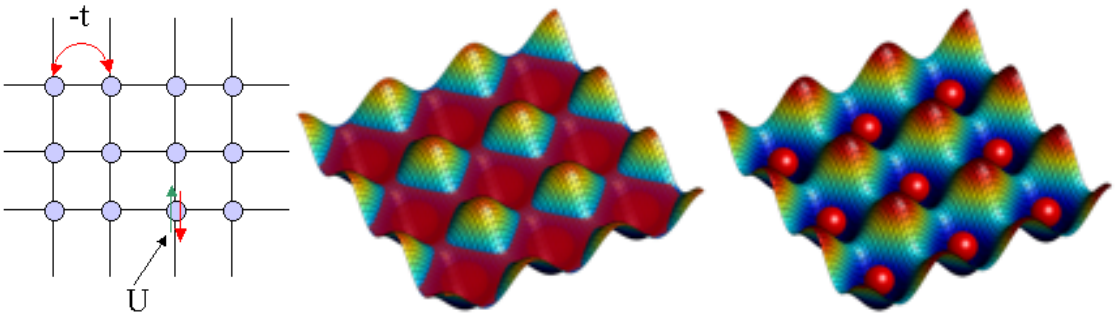

Figure 2.1: a) Lattice illustration of the Hubbard model b) Delocalized electrons forming a metal c) Localized electrons forming a Mott insulator

A pictorial representation of this model can be seen in figure 2.1. The first term of the Hamiltonian (2.1) is the Tight-Binding term, it enables electrons to hop between lattice sites gaining kinetic energy. This promotes their delocalization in the periodic potential of the lattice and gives the metallic behavior. The results is a delocalized electron sea, called Fermi sea, as illustrated in figure 2.1b. On the other hand, if the double occupation of a lattice site is severely penalized by the local Coulomb repulsion(U), the second term in the Hamiltonian (2.1), electrons prefer to localize and singly occupy each lattice site. This is the behavior depicted in figure 2.1c, the Mott insulator. The difficulty in solving this model essentially comes from the non-commutativity between the first term, the hopping which is diagonal in momentum space, and the local interaction term which is diagonal in real space, hindering us from simultaneously diagonalizing them.

2.2 Dynamical Mean Field theory

Great theoretical progress has been achieved in our understanding of the Hubbard Model thanks to Dynamical Mean Field theory Georges and Kotliar [1992], Georges et al. [1996] where one takes advantage that the diagrams of the lattice model become momentum independent in the limit of infinite dimensions (or infinite coordination)Metzner and Vollhardt [1989], Müller-Hartmann [1989b]. The many-body problem of the Hubbard Hamiltonian is transformed into a single quantum impurity problem supplemented by a self-consistency condition. In this way the lattice degrees of freedom are represented in mean field by the electronic bath of the impurity problem. The hybridization with the bath of non-interacting electrons allows the impurity to change its configuration as depicted in figure 2.2. The insight of neglecting the spatial dependence of the self-energy, which is true in the infinite coordination limit, allows the DMFT mapping of the lattice model into the impurity model to give a full local picture of the solid in terms of the impurity model at the expense of

neglecting spatial fluctuations.

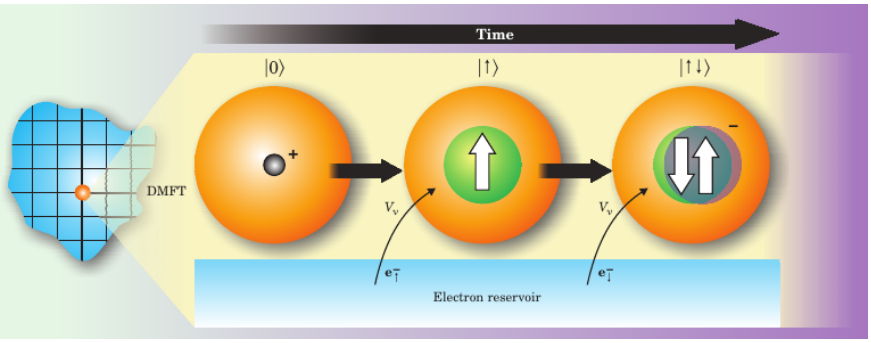

Figure 2.2: DMFT pictorial representation from Kotliar and Vollhardt [2004]

The partition function Z of the Hubbard Hamiltonian is evaluated under the path integral formalism Negele and Orland [1988], using the Grassmann variables $c_{i\sigma}(\tau)$, $c^{\dagger}_{i\sigma}(\tau)$:

$$Z = \int \prod_{i\sigma} \mathcal{D}c^{\dagger}_{i\sigma} \mathcal{D}c_{i\sigma} e^{-S} \tag{2.2}$$

and the action S:

$$\int_0^{\beta} d\tau \left[\sum_{i\sigma} c^{\dagger}_{i\sigma}(\tau)(\partial_\tau - \mu) c_{i\sigma}(\tau) + \mathcal{H}(c^{\dagger}_{i\sigma}(\tau), c_{i\sigma}(\tau)) \right] \tag{2.3}$$

To obtain the effective action of an arbitrary site, take $i = 0$, one has to integrate out the fermionic degrees of freedom from all other lattice sites but the selected before. This idea is expressed by:

$$\frac{1}{Z_{eff}} e^{-S_{eff}(c^{\dagger}_{0\sigma}, c_{0\sigma})} = \frac{1}{Z} \int \prod_{i\neq 0,\sigma} \mathcal{D}c^{\dagger}_{i\sigma} \mathcal{D}c_{i\sigma} e^{-S} \tag{2.4}$$

Here Z_{eff} is the partition function of S_{eff}, whose formal expression can be obtained by first

splitting the original action into three parts: $S = S_0 + S^{(0)} + \Delta S$ where

$$S_0 = \int_0^\beta d\tau \left(\sum_\sigma c^\dagger_{0\sigma}(\tau)(\partial_\tau - \mu)c_{0\sigma}(\tau) + U n_{0\uparrow}(\tau) n_{0\downarrow}(\tau) \right) \tag{2.5a}$$

$$S^{(0)} = \int_0^\beta d\tau \left(\sum_{i\neq 0,\sigma} c^\dagger_{i\sigma}(\tau)(\partial_\tau - \mu)c_{i\sigma}(\tau) - t \sum_{\langle i,j\neq 0\rangle,\sigma} (c^\dagger_{i\sigma}(\tau)c_{j\sigma}(\tau) + H.c.) + U n_{i\uparrow}(\tau) n_{i\downarrow}(\tau) \right) \tag{2.5b}$$

$$\Delta S = -t \int_0^\beta d\tau \sum_{i\sigma} (c^\dagger_{i\sigma}(\tau)c_{0\sigma}(\tau) + H.c.) \tag{2.5c}$$

S_0 is the action of the selected site 0 decoupled from the rest of the lattice, $S^{(0)}$ is the lattice action to which site 0 and all the bonds connecting to it have been removed leaving a "cavity", ΔS is the action that describes the hybridization between site 0 and the lattice. In order to carry the integration in (2.4) it is useful to recognize that ΔS with $\eta_i \equiv t_{i0} c_{0\sigma}$ act as sources coupled to the fields $c^\dagger_{i\sigma}$, and the integration over fermions for $i \neq 0$ brings in the generating functional of the connected Green's function $G^{(0)}$ of the cavity Hamiltonian.

$$\begin{aligned} S_{eff} = cte + S_0 + \sum_{n=1}^{\infty} \sum_{\substack{i_1 \cdots i_n \\ j_1 \cdots j_n}} \int_0^\beta d\tau_{i_1} \cdots d\tau_{i_n} d\tau_{j_1} \cdots d\tau_{j_n} \\ \times \eta^\dagger_{i_1}(\tau_{i_1}) \cdots \eta^\dagger_{i_n}(\tau_{i_n}) \eta_{j_1}(\tau_{j_1}) \cdots \eta_{j_n}(\tau_{j_n}) \\ \times G^{(0)}_{\substack{i_1 \cdots i_n \\ j_1 \cdots j_n}}(\tau_{i_1}, \cdots, \tau_{i_n}, \tau_{j_1}, \cdots, \tau_{j_n}) \end{aligned} \tag{2.6}$$

The function $G^{(0)}$ describes the process of an electron that leaves the site 0 to propagate into the lattice and then returns back to the site 0. This result is not too useful because the cavity Green's function $G^{(0)}$ is not available. Up to now no approximation has been made and finding the cavity functional is as hard as solving the original problem itself. Nevertheless, in the limit of large dimension, the hopping t has to be rescaled at $t \propto 1/\sqrt{d}^{|i-j|}$ to have the interaction and kinetic terms of the same order and obtain a non-trivial model Metzner and Vollhardt [1989]. A consequence of this scaling is that $G^{(0)} \propto 1/\sqrt{d}^{|i-j|}$, therefore only the leading order term, the 2-point Green's function remains from the sum and is of order 1 provided $i = j$, all the higher orders of the cavity Green's function vanish in the infinite dimension limits as they decay at least as fast as $1/d$. This dramatic simplification reduces the effective action into:

$$S_{\text{eff}} = \int_0^\beta d\tau \left(\sum_\sigma c^\dagger_{0\sigma}(\tau)(\partial_\tau - \mu)c_{0\sigma}(\tau) + U n_{0\uparrow}(\tau) n_{0\downarrow}(\tau) \right) - \int_0^\beta d\tau \int_0^\beta d\tau' \sum_\sigma c^\dagger_{0\sigma}(\tau) c_{0\sigma}(\tau') \sum_{\langle ij,0\rangle} t_{i0} t_{0j} G^{(0)}_{ij\sigma}(\tau,\tau') \tag{2.7}$$

In this notation $\langle ij, 0\rangle$ are the nearest neighbors of the cavity. This effective action allows to introduce an effective propagator, which reads in Matsubara frequency space:

$$\mathcal{G}_0^{-1}(i\omega_n) = i\omega_n + \mu - \sum_{\langle ij,0\rangle} t_{i0} t_{0j} G^{(0)}_{ij}(i\omega_n) \tag{2.8}$$

This function is the Weiss field of our dynamical mean-field theory, it is the quantum analogous of the effective magnetic field in the context of the Ising model. On the Bethe lattice, schematically shown in Fig. 2.3 for a connectivity of 4 neighbors, the Weiss field can be restricted to the $i = j$ case since the neighbors of the tagged site 0 are completely disconnected in this lattice once the cavity is created in it. Also, in the limit of infinite connectivity ($z \to \infty$) removing one site does no change the Green's function, thus the full lattice propagator and the one holding the cavity are equal such that $G^{(0)}_{ii} = G_{ii} \equiv G_{\text{loc}}$. This reduces the Weiss function on the lattice (eq. 2.8) to:

$$\mathcal{G}_0^{-1}(i\omega_n) = i\omega_n + \mu - t^2 G_{\text{loc}}(i\omega_n) \tag{2.9}$$

It is relevant to remark that this construction is exact and is only due to renormalization of scales in the limit of infinite coordination.

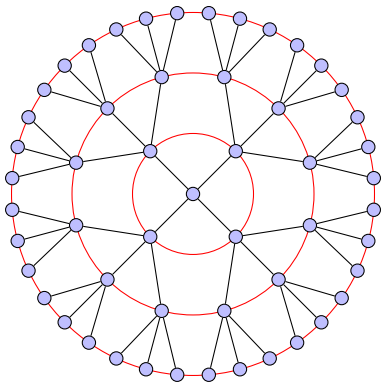

Figure 2.3: Drawing of the Bethe lattice with a connectivity $z = 4$

2.2.1 Connection to the impurity problem

A crucial step forward in the implementation of the DMFT equations (2.8) is obtained by observing that the effective action of the isolated site from equation 2.7 corresponds to the one obtained for the single impurity Anderson Model Anderson [1961], that describes a magnetic impurity coupled to a conduction bath Georges and Kotliar [1992]. This is written in therms of second quantization operators as:

$$\mathcal{H}_{\text{AIM}} = \sum_{k\sigma} \epsilon_k c^\dagger_{k\sigma} c_{k\sigma} + \sum_{k\sigma} (V_k c^\dagger_{k\sigma} d_\sigma + H.c.) + \epsilon_d \sum_\sigma d^\dagger_\sigma d_\sigma + U n_{d\uparrow} n_{d\downarrow} \tag{2.10}$$

where $d^\dagger_\sigma$ (d_σ) create (annihilate) an electron in the impurity orbital d with on-site energy ϵ_d and spin σ, $c^\dagger_{k\sigma}$ ($c_{k\sigma}$) create (annihilate) electrons in the conduction bath with quantum numbers of momentum k and spin σ. The conduction electrons are hybridized to the impurity by a hopping amplitude V_k, and on the impurity electrons experience the Coulomb repulsion $U > 0$.

The action of this Hamiltonian is given by:

$$\begin{aligned} S_{\text{AIM}} = \int_0^\beta d\tau \Bigg(& \sum_{k\sigma} c^\dagger_{k\sigma}(\tau)(\partial_\tau + \epsilon_k) c_{k\sigma}(\tau) + (V_k c^\dagger_{k\sigma}(\tau) d_\sigma(\tau) + H.c.) \\ & + \sum_\sigma d^\dagger_\sigma(\tau)(\partial_\tau + \epsilon_d) d_\sigma(\tau) + U n_{d\uparrow}(\tau) n_{d\downarrow}(\tau) \Bigg) \end{aligned} \tag{2.11}$$

The terms corresponding to the conduction bath and the hybridization to the impurity are quadratic, so that one can perform the Gaussian integral over all Grassmann variables Negele and Orland [1988] corresponding to the conduction electrons c to obtain and effective action for the impurity:

$$S_{\text{AIM-eff}} = cte. + \int_0^\beta d\tau \int_0^\beta d\tau' \left(\sum_\sigma d^\dagger_\sigma(\tau) \mathcal{G}_0^{-1}(\tau, \tau') d_\sigma(\tau') + \int_0^\beta d\tau U n_{d\uparrow}(\tau) n_{d\downarrow}(\tau) \right) \tag{2.12}$$

where $\mathcal{G}_0^{-1}$ is the Green's function of a non-interacting impurity in a conduction bath, also known as the resonant-level model, which in Matsubara frequencies is given by:

$$\mathcal{G}_0^{-1} = i\omega_n - \epsilon_d - \Delta(i\omega_n) = i\omega_n - \epsilon_d - \sum_k \frac{V_k^2}{i\omega_n - \epsilon_k} \tag{2.13}$$

here $\Delta(i\omega_n)$ is the retarded hybridization function of the impurity with the bath of conduction

electrons. The eq. (2.12) is the same action as (2.7), confirming the exact mapping that exist between the DMFT impurity in infinite dimensions and the Anderson impurity problem Georges and Kotliar [1992]. The dynamical mean field comes into play by a retarded interaction between the impurity and an uncorrelated conduction bath, provided that the parameters of the impurity problem V_k and ϵ_k can be found to match the same propagator from equation 2.13 to 2.8.

2.2.2 Self-consistency condition

The DMFT framework enables us to study the impurity problem given by the effective action in equation (2.7). We solve the Anderson impurity model from eq. (2.12) to extract the impurity Green's function.

$$G_{\text{imp}}(\tau - \tau') = -\langle T_\tau c(\tau) c^\dagger(\tau') \rangle_{S_{eff}} \tag{2.14}$$

In the non-interacting case $U = 0$, the local lattice Green's function equals the impurity propagator $G_{\text{loc}}(i\omega_n) = \mathcal{G}_0(i\omega_n)$. This can be our initial guess to fix the effective impurity problem, and then use any available method to obtain the solution for the impurity Green's function (eq. 2.14). The local self-energy of the problem is defined via Dyson's equation:

$$\Sigma(i\omega_n) = \mathcal{G}_0^{-1}(i\omega_n) - G_{\text{imp}}^{-1}(i\omega_n) \tag{2.15}$$

The DMFT approximation comes into play when one attempts to represent finite dimensional systems and lattices. The impurity self-energy has no spatial dependence, and under the DMFT approximation it is set equal to the lattice self-energy neglecting any momentum dependence. This claim is nevertheless exact in the limit of infinite coordination in which DMFT was formulated. In order to relate back to the lattice Green's function we can thus insert this self-energy directly into the lattice Green's function again by the use of Dyson's equation for the lattice.

$$G^{-1}(\vec{k}, i\omega_n) = G_0^{-1}(\vec{k}, i\omega_n) - \Sigma(i\omega_n) \tag{2.16}$$

The momentum average of the lattice Green's function has to restore the local quantity

$$G_{\text{loc}}(i\omega_n) = \sum_{\vec{k}} \left[i\omega + \mu - \epsilon_k - \Sigma(i\omega_n) \right]^{-1} = \int \frac{d\epsilon \rho_0(\epsilon)}{i\omega + \mu - \epsilon - \Sigma(i\omega_n)} \tag{2.17}$$

where ϵ_k is the non-interacting lattice dispersion, and $\rho_0(\epsilon)$ is the non-interacting density of states of the lattice. This local Green's function must be equal to the impurity one (eq.

(2.14)). We can use it again in the Dyson equation to construct a new Weiss field and fix a new bath for the effective impurity problem (eq. (2.10)).

$$\mathcal{G}_0^{-1}(i\omega_n) = G_{\text{loc}}^{-1}(i\omega_n) + \Sigma(i\omega_n) \tag{2.18}$$

The steps enunciated by equations (2.15) (2.16) (2.17) and (2.18) together with the impurity problem in equation (2.7) provide an iterative scheme for the DMFT self-consistent solution of the lattice problem. At convergence the impurity Green's function corresponds to the local Green's function of the original lattice model.

When working on an infinite coordination Bethe lattice. This particular set of equations is simplified as enunciated before by the self-consistency equation (2.9) together with the impurity problem in eq. (2.7).

2.2.3 Methods of Solution for the impurity problem

In this section we describe the methods to solve the quantum impurity problem required at each iteration of the DMFT loop. The reader not interested in this technical detail is encouraged to go ahead to section 2.2.4

2.2.3.1 Iterated Perturbation Theory Solver

The simplest approach to solve the DMFT equation is by use of the Iterated Perturbation Theory (IPT). Under this approximation one calculates the self-energy of the impurity problem by only using the second order diagrammatic expansion in the interaction Georges and Kotliar [1992]. This allows to construct the self-energy as a function of the bare propagators of the impurity problem known in the DMFT context as the Weiss field $\mathcal{G}_0$. It then reads:

$$\Sigma^{IPT}(i\omega_n) \equiv -U^2 \int_0^\beta \mathcal{G}^0(\tau)\mathcal{G}^0(-\tau)\mathcal{G}^0(\tau)e^{i\omega_n\tau}d\tau \tag{2.19}$$

The advantage of this method is that it allows for extremely fast numerically stable and precise calculations, at the expense of neglecting all other terms in the expansion. Therefore, it is always necessary to cross validate its results with exact methods such as quantum Monte Carlo. By construction this perturbative method is valid in the small U limit, but in spite of that this expression also corresponds to the atomic limit $t \to 0$ in the half-filled Hubbard model Zhang et al. [1993], Lange [1998]. Consequently it provides a connection between the weak and strong coupling limits and is well suited to study the metal insulator transition at half-filling. A second advantage of this method is that the analytical continuation can be

performed directly in the iterative scheme and we can obtain as well a real frequency solver at finite temperatures, refer to appendix C for details.

2.2.3.2 Continuous Time Quantum Monte Carlo in Hybridization expansion

Monte Carlo methods depart from the idea of performing a statistical sampling over a configuration space in order to solve the high dimensional integrals encountered in the treatment of thermodynamic systems Metropolis et al. [1953]. Quantum Monte Carlo algorithms focus on solving problems in quantum mechanical systems by the use of statistical sampling over an observable. In our specific problem we focus on sampling over the action of the many-body problem (2.7), to measure the expected value of the relevant physical observable, in our case the single particle impurity Green's function (2.14). In this work we use the Hybridization expansion approach Werner and Millis [2006] as implemented in the software packages TRIQS/CTHYB Seth et al. [2016], and in the following I'll introduce the general view of the algorithm as presented in the review by Gull et al. [2011].

The basic idea in continuous time quantum Monte Carlo methods is to split the impurity Hamiltonian in two parts $H = H_a + H_b$ and then write the partition function in the interaction representation Fetter and Walecka [2003] with respect to H_a and expand in powers of H_b:

$$\begin{aligned} Z =& \mathrm{Tr}\; T_\tau e^{-\beta H_a} \exp\left[-\int_0^\beta d\tau H_b(\tau)\right] \\ =& \sum_k (-1)^k \int_0^\beta d\tau_1 \ldots \int_{\tau_{k-1}}^\beta d\tau_k \\ & \times \mathrm{Tr}\left[e^{-\beta H_a} H_b(\tau_k) H_b(\tau_{k-1}) \ldots H_b(\tau_1)\right] \end{aligned} \tag{2.20}$$

In the hybridization expansion algorithm (CT-HYB) developed by Werner et al. [2006], Werner and Millis [2006] the starting point is to split the AIM Hamiltonian (2.10) to conform with eq. (2.20) where H_b is the hybridization term H_{hyb} and $H_a = H_{\mathrm{bath}} + H_{\mathrm{loc}}$. The advantage of this approach is that the average expansion order for a typical problem near the Mott transition is much smaller than in the interaction expansion methods and therefore lower temperatures are accessible Gull et al. [2007]. Since $H_{hyb} = \sum_{pj}(V_p^j c_p^\dagger d_j + V_p^{j*} d_j^\dagger c_p) = \tilde{H}_{hyb} + \tilde{H}_{hyb}^\dagger$ contains two terms which respectively create and annihilate electrons on the impurity only even powers of the expansion and contributions with equal numbers of $\tilde{H}_{hyb}$ and $\tilde{H}_{hyb}^\dagger$ can yield a non-zero trace. The partition function therefore becomes

$$Z = \sum_{k=0}^{\infty} \int_0^\beta d\tau_1 \dots \int_{\tau_{k-1}}^\beta d\tau_k \int_0^\beta d\tau'_1 \dots \int_{\tau_{k'-1}}^\beta d\tau'_k \\ \times \mathrm{Tr}\left[T_\tau e^{-\beta H_a} \tilde{H}_{hyb}(\tau_k)\tilde{H}^\dagger_{hyb}(\tau'_k)\dots\tilde{H}_{hyb}(\tau_1)\tilde{H}^\dagger_{hyb}(\tau'_1)\right]. \tag{2.21}$$

Inserting the $\tilde{H}_{hyb}$ and $\tilde{H}^\dagger_{hyb}$ operators explicitly yields

$$Z = \sum_{k=0}^{\infty} \int_0^\beta d\tau_1 \dots \int_{\tau_{k-1}}^\beta d\tau_k \int_0^\beta d\tau'_1 \dots \int_{\tau'_{k-1}}^\beta d\tau'_k \\ \sum_{\substack{j_1,\cdots j_k \\ j'_1,\cdots j'_k}} \sum_{\substack{p_1,\cdots p_k \\ p'_1,\cdots p'_k}} V^{j_1}_{p_1} V^{j'_1 *}_{p'_1} \cdots V^{j_k}_{p_k} V^{j'_k *}_{p'_k} \\ \times \mathrm{Tr}\Big[T_\tau e^{-\beta H_a} d_{j_k}(\tau_k) c^\dagger_{p_k}(\tau_k) c_{p_{k'}}(\tau'_k) d^\dagger_{j'_k}(\tau'_k) \\ \cdots d_{j_1}(\tau_1) c^\dagger_{p_1}(\tau_1) c_{p'_1}(\tau'_1) d^\dagger_{j'_1}(\tau'_1)\Big]. \tag{2.22}$$

Separating the bath and impurity operators we obtain

$$Z = \sum_{k=0}^{\infty} \int_0^\beta d\tau_1 \dots \int_{\tau_{k-1}}^\beta d\tau_k \int_0^\beta d\tau'_1 \dots \int_{\tau'_{k-1}}^\beta d\tau'_k \\ \sum_{\substack{j_1,\cdots j_k \\ j'_1,\cdots j'_k}} \sum_{\substack{p_1,\cdots p_k \\ p'_1,\cdots p'_k}} V^{j_1}_{p_1} V^{j'_1 *}_{p'_1} \cdots V^{j_k}_{p_k} V^{j'_k *}_{p'_k} \\ \times \mathrm{Tr}_d \left[T_\tau e^{-\beta H_{\mathrm{loc}}} d_{j_k}(\tau_k) d^\dagger_{j'_k}(\tau'_k) \cdots d_{j_1}(\tau_1) d^\dagger_{j'_1}(\tau'_1)\right] \\ \times \mathrm{Tr}_c \left[T_\tau e^{-\beta H_{\mathrm{bath}}} c^\dagger_{p_k}(\tau_k) c_{p_{k'}}(\tau'_k) \cdots c^\dagger_{p_1}(\tau_1) c_{p'_1}(\tau'_1)\right]. \tag{2.23}$$

We can now integrate out the bath operators $c_p(\tau)$, since they are non-interacting and the time-evolution (given by H_a) no longer couples the impurity and the bath. Defining the bath partition function

$$Z_{\mathrm{bath}} = \mathrm{Tr} e^{-\beta H_{\mathrm{bath}}} = \prod_\sigma \prod_p (1 + e^{-\beta \varepsilon_p}), \tag{2.24}$$

and the anti-periodic hybridization function $\mathbf{\Delta}(i\omega_n)$ (introduced in eq. (2.13))

$$\Delta_{lm}(\tau) = \sum_p \frac{V_p^{l*} V_p^m}{e^{\varepsilon_p \beta} + 1} \times \begin{cases} -e^{-\varepsilon_p(\tau-\beta)}, & 0 < \tau < \beta \\ e^{-\varepsilon_p \tau}, & -\beta < \tau < 0 \end{cases}, \tag{2.25}$$

we obtain the determinant

$$\begin{aligned} &\frac{1}{Z_{\text{bath}}} \text{Tr}_c \Big[T_\tau e^{-\beta H_{\text{bath}}} \sum_{p_1, \cdots p_k} \sum_{p'_1, \cdots p'_k} V_{p_1}^{j_1} V_{p'_1}^{j'_1 *} \cdots V_{p_k}^{j_k} V_{p'_k}^{j'_k *} \\ &\times c^\dagger_{p_k}(\tau_k) c_{p_{k'}}(\tau'_k) \cdots c^\dagger_{p_1}(\tau_1) c_{p'_1}(\tau'_1) \Big] = \det \mathbf{\Delta}, \end{aligned} \tag{2.26}$$

for an arbitrary product of bath operators. Here, $\mathbf{\Delta}$ is a $k \times k$ matrix with elements $\Delta_{lm} = \Delta_{j_l j_m}(\tau_l - \tau_m)$. In practice, and in analogy to the algorithms in previous sections, it will be more convenient to handle the inverse of this matrix $\mathbf{\Delta}$, which we denote by $\mathbf{M} = \mathbf{\Delta}^{-1}$.

The partition function expansion for the hybridization algorithm now reads (for time-ordered configurations)

$$\begin{aligned} Z \;\; = Z_{\text{bath}} \sum_k \;\; &\iiint d\tau_1 \cdots d\tau'_k \sum_{j_1, \cdots j_k} \sum_{j'_1, \cdots j'_k} \\ &\times \text{Tr}_d \left[T_\tau e^{-\beta H_{\text{loc}}} d_{j_k}(\tau_k) d^\dagger_{j'_k}(\tau'_k) \cdots d_{j_1}(\tau_1) d^\dagger_{j'_1}(\tau'_1) \right] \det \mathbf{\Delta}. \end{aligned} \tag{2.27}$$

The CT-HYB algorithm generates configurations with the weight that they contribute to the partition function Z. The most relevant observable for quantum Monte Carlo impurity solvers is the finite temperature imaginary time Green's function $G_{lm}(\tau) = -\langle T_\tau d_l(\tau) d^\dagger_m(0) \rangle$. The series for this observable is

$$\begin{aligned} G_{lm}(\tau_l, \tau_m) = &- Z_{\text{bath}} \sum_{k, \substack{j_1, \cdots j_k \\ j'_1, \cdots j'_k}} \int d\tau_1 ... d\tau'_k \det \mathbf{\Delta}_k \\ &\times \text{Tr}_d \Big[T_\tau e^{-\beta H_{\text{loc}}} \; d_l(\tau_l) d^\dagger_m(\tau_m) \; d_{j_k}(\tau_k) d^\dagger_{j'_k}(\tau'_k) \ldots d_{j_1}(\tau_1) d^\dagger_{j'_1}(\tau'_1) \Big]. \end{aligned} \tag{2.28}$$

This shows that Green's function configurations at expansion order k are partition function configurations at expansion order k with additional d_l and $d^\dagger_m$ operators or, alternatively, partition function operators at order $k+1$ with no hybridization line connecting to $d_l(\tau_l)$ and $d^\dagger_m(\tau_m)$. In practice we obtain an estimator of $G_{lm}(\tau_l, \tau_m)$ by identifying two operators $d_l(\tau_l), d^\dagger_m(\tau_m)$ in a partition function configuration that are an imaginary time distance

$\tau = \tau_l - \tau_m$ apart, and removing the hybridization line connecting them.

The size $(k-1) \times (k-1)$ hybridization matrix $\mathbf{\Delta}_{k-1}^{\tau_l,\tau_m}$ of all hybridization operators except for $d_l(\tau_l)$ and $d_m^\dagger(\tau_m)$ corresponds to $\mathbf{\Delta}$ with the column(row) s_l (s_m) corresponding to the operators d_l and $d_m^\dagger$ removed, and the weight of a Green's function configuration $G_{lm}(\tau_l, \tau_m)$ is

$$\frac{p_{G_{lm}}}{Z} = \frac{\det \mathbf{\Delta}_{k-1}^{\tau_l,\tau_m}}{\det \mathbf{\Delta}}. \tag{2.29}$$

An expansion by minors describes how such a determinant ratio is computed:

$$\frac{p_{G_{lm}}}{Z} = (\mathbf{\Delta})^{-\mathbf{1}}_{\mathbf{s_m s_l}} = \mathbf{M}_{\mathbf{s_m s_l}}. \tag{2.30}$$

We can bin this estimate into fine bins to obtain the Green's function estimator

$$G_{lm}(\tau) = \frac{1}{\beta} \left\langle \sum_{ij}^{k} M_{ji} \tilde{\delta}(\tau, \tau_m - \tau_l) \delta_{t(i)l} \delta_{t(j)m} \right\rangle_{\text{MC}}, \tag{2.31}$$

$$\tilde{\delta}(\tau, \tau') = \begin{cases} \delta(\tau - \tau'), & \tau' > 0 \\ -\delta(\tau - \tau' - \beta), & \tau' < 0, \end{cases} \tag{2.32}$$

with $t(i)$ denoting the orbital index of the operator at row or column i. For a configuration at expansion order k we obtain a total of k^2 estimates for the Green's function – or one for every creation-annihilation operator pair or every single element of the $(k \times k)$-matrix $\mathbf{M} = \mathbf{\Delta}^{-1}$.

Quantum Monte Carlo sampling is formulated in the imaginary time and can treat exactly a wide range of energy scales. But it requires the analytical continuation to obtain real frequency information. Quantum Monte Carlo are most effective for imaginary-time simulation. Many observables can be directly obtained from the simulated data. But it is also useful to obtain the spectral function. The standard method for performing the analytical continuation in the Maximum-entropy method Jarrell and Gubernatis [1996]. In this thesis all continuations of data are done using the library PyMaxent referenced in the appendix E.

2.2.4 Visualization of Spectral functions

Solution of a Hamiltonian implies finding it eigen-states and eigen-energies. Take a 1D tight binding model for example,

$$\mathcal{H} = -t \sum_l c_l^\dagger c_{l+1} \tag{2.33}$$

in this case momentum k_x is a good quantum number which allow to diagonalize this Hamiltonian and find the eigen-energies are given by:

$$\epsilon_k = -2t \cos k_x a \tag{2.34}$$

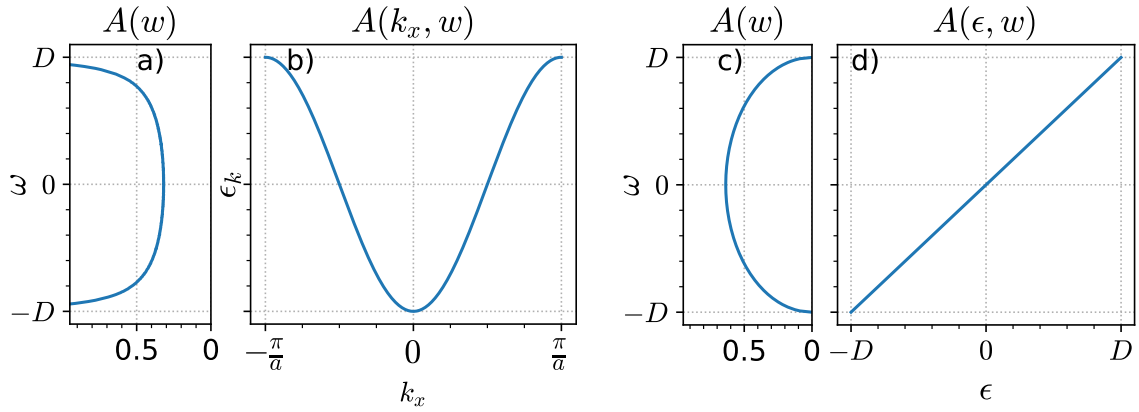

Figure 2.4: a) Density of states (DOS) of 1D tight-binding model. b) Corresponding electronic dispersion ϵ_k as a function of momentum k_x c) Density of states of a Bethe lattice d) Energy resolved spectral function of an arbitrary lattice with bounded band edges.

Quantity (2.34) is known as the dispersion relation of our model and is displayed in Fig. 2.4 b). It is also possible to obtain the density of states of this model

$$\rho(\epsilon) = \frac{1}{N}\sum_k \delta(\epsilon - \epsilon_k) \tag{2.35}$$

plotted in Fig. 2.4 a). This way of visualizing the spectral structure of a Hamiltonian can be extended to represent other less intuitive lattices. The Green's function of the Hamiltonian is

$$G(k,w) = \frac{1}{w - \mathcal{H}} = \mathcal{PV}\frac{1}{w-\epsilon_k} - i\pi\delta(\omega - \epsilon_k) \tag{2.36}$$

Notice, how the dispersion relation of the model ϵ_k represents the excitations of the system. We call the quantity $A(k,\omega) = -\frac{1}{\pi}\Im mG(k,\omega) = \delta(\omega - \varepsilon_k)$ the momentum resolved spectral function and in the $\omega - k$ plane represents the same dispersion relation of the model as presented in Fig. 2.4 b).

For lattices where momentum is not a good quantum number, the Bethe lattice for example, the Hamiltonian has nevertheless eigen-states and one can simply trade the momentum and dispersion relation for energy $k \to \epsilon_k \to \epsilon$, and present a energy resolved spectral function, shown in Fig. 2.4 d). In this case it is just a straight line in the ω, ϵ plane for all lattices. The density of states remains nevertheless lattice dependent, in the case of the Bethe lattice is a semi-circle as presented in Fig. 2.4 c)

In the context of interacting systems one represents the Green's function from equation (2.36) into an explicit form where one separates the contribution of the non-interacting part of the Hamiltonian in $\mathcal{H}_0$ and encapsulates all effects of interactions in the self-energy Σ,

obtaining the expression:

$$G(k,w) = \frac{1}{w - \mathcal{H}_0 - \Sigma(k,w)} \tag{2.37}$$

The definition of the spectral function remains unmodified, but one now talks about the single particle excitations. The nature of this excitations can be coherent or incoherent. In the first case the imaginary part of the self-energy is vanishinly small, so the excitations are long-lived, like quasi-particles in Fermi liquid theory Pines and Nozières [1966]. If on the contrary the imaginary part of the self-energy is large, the excitation is short lived. The entire aim of the study of interaction effects is to track how the self-energy renormalizes the non-interacting energy level of the Hamiltonian. In this thesis I'll use many figures of the electronic structure in the form of Fig. 2.4 c and d, which will be presented with intensity plots, as the energy resolved spectral function $A(\epsilon,\omega)$ is not anymore composed of sharp δ functions but of a more complex structure.

2.2.5 Solution of the half-filled single band Hubbard model

The DMFT solution for the single band Hubbard model has been very well studied in the infinite dimensions limit Georges et al. [1996]. Here we shall review the key features of this solution. At half-filling it reveals the phase diagram already illustrated in Fig. (1.2 right) where metallic and insulating solutions are found.

In the metallic state, Fermi-liquid theory applies beneath a low energy scale ε_F^*, which can be interpreted as the coherence-scale for quasiparticles (i.e long-lived quasiparticles exist only for energies and temperature smaller than ε_F^*). This low-energy coherence scale is given by $\varepsilon_F^* \sim ZD$, with D the half-bandwidth, also equal to the Fermi energy of the non-interacting system at half-filling. Here Z is the quasiparticle weight. In this regime in fact the self-energy can be expanded around $\omega = 0$

$$\Sigma(\omega) \simeq \Re e\Sigma(\omega = 0) + \alpha\omega + O(\omega^2)$$

and the interacting Green's function of eq. (2.37) reduced to a non-interacting one at low energies, but weighted by $Z = 1/(1-\alpha)$:

$$G(k, w \to 0) = \frac{Z}{w - \tilde{\varepsilon}_k} \tag{2.38}$$

In the strongly correlated metal close to the transition, $Z \ll 1$, so that ε_F^* is strongly reduced as compared to the bare Fermi energy.

In addition to low-energy quasiparticles (carrying a fraction Z of the spectral weight), the one-particle spectrum of the strongly correlated metal contains high-energy excitations carrying a spectral weight $1 - Z$. These are associated to the atomic-like transitions corresponding to

the addition or removal of one electron on an atomic site, which broaden into Hubbard bands in the solid. As a result, the momentum-integrated spectral function $A(\omega) = \sum_{\mathbf{k}} A(\mathbf{k}, \omega)$ (density of states DOS) of the strongly correlated metal is predicted Georges and Kotliar [1992] to display a three-peak structure, made of a quasiparticle band of weight Z at the Fermi energy surrounded by lower and upper Hubbard bands of weight $1 - Z$ (Fig. 2.5). The quasiparticle part of the DOS has a reduced width of order $ZD \sim \varepsilon_F^*$. Notice the pinning condition of the DOS at its non-interacting value ($A(w = 0) = A_0(w = 0)$). The spectral density at the Fermi surface is not renormalized by the interactions, which is a strong implication of the self-energy being momentum independent Müller-Hartmann [1989a], as long as there is no broken symmetry. One recognizes, as the strength of the Hubbard interaction U is increased, that spectral weight is transferred from low energy to higher energy giving origin to the Upper and Lower Hubbard bands. The lower and upper Hubbard bands are separated by an energy scale $\Delta \sim U - 2D$.

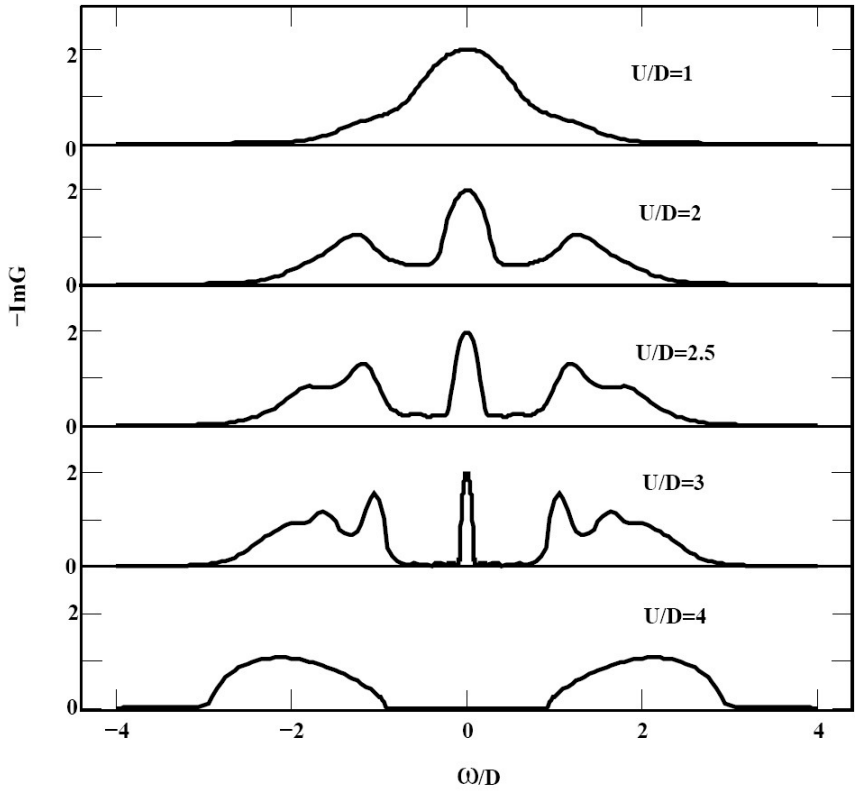

Figure 2.5: Local spectral function for several values of the interaction strength in DMFT. These results have been obtained using the IPT approximation, for the half-filled Hubbard model with a semi-circular DOS (from Ref. Georges et al. [1996]). Close to the transition, the separation of scales between the quasiparticle coherence energy (ε_F^*) and the distance between Hubbard bands (Δ) is clearly seen.

At strong enough coupling, the paramagnetic solution of the DMFT equations is a Mott insulator, with a gap Δ in the one-particle spectrum. This phase is characterized by unscreened local moments, associated with a Curie law for the local susceptibility $\sum_q \chi_q \propto$

$1/T$, and an extensive entropy. Note however that the uniform susceptibility $\chi_{q=0}$ is finite, of order $1/J \sim U/D^2$. As temperature is lowered, these local moments order into an antiferromagnetic phase Georges and Krauth [1993], Jarrell [1992]. The Néel temperature is however strongly dependent on frustration Georges et al. [1996] and can be made vanishingly small for fully frustrated models.

Within DMFT, a separation of energy scales holds close to the Mott transition. The dynamical mean-field solution corresponding to the paramagnetic metal at $T = 0$ disappears at a critical coupling U_{c_2}. At this point, the quasiparticle weight vanishes ($Z \propto 1 - U/U_{c_2}$) as in the Brinkman and Rice [1970] theory for the Metal-Insulator transition. On the other hand, a mean-field insulating solution is found for $U > U_{c_1}$, with the Mott gap Δ opening up at this critical coupling (Mott-Hubbard transition). As a result, Δ is a finite energy scale for $U = U_{c_2}$ and the quasiparticle peak in the DOS is well separated from the Hubbard bands in the strongly correlated metal.

These two critical couplings extend at finite temperature into two spinodal lines $U_{c_1}(T)$ and $U_{c_2}(T)$, which delimit a region of the $(U/D, T/D)$ parameter space in which two mean-field solutions (insulating and metallic) are found (Fig. 1.2 right). Hence, within DMFT, a first-order Mott transition occurs at finite temperature even in a purely electronic model. The corresponding critical temperature T_c^{el} is of order $T_c^{el} \sim \Delta E/\Delta S$, with ΔE the energy difference and $\Delta S \sim \ln(2S+1)$ the entropy difference between the metal and the insulator states, $S = 1/2$ is the spin of the impurity. Because the energy difference is small ($\Delta E \sim (U_{c_2} - U_{c_1})^2/D$), the critical temperature is much lower than D and U_c (by almost two orders of magnitude). Indeed, in V_2O_3 as well as in the organics, the critical temperature corresponding to the endpoint of the first-order Mott transition line is a factor of 50 to 100 smaller than the bare electronic bandwidth.

2.2.5.1 Optical conductivity

In order to make a realistic connection between our calculations and materials, in the following we shall study the optical conductivity, which can reveal non-trivial aspects of the underlying electronic structure. Our result can be then linked to the experimental measure of optical conductivity. The optical conductivity of a given system is defined by

$$\sigma(\omega) = \frac{1}{\mathcal{V}\,\omega} \Im m \int_0^\infty \langle [\mathcal{J}(t), \mathcal{J}(0)] \rangle e^{i\omega t} dt \tag{2.39}$$

where $\mathcal{V}$ is the volume, $\mathcal{J}$ is the current operator and $\langle\,\rangle$ indicates an average over a finite temperature ensemble or over the ground state at zero temperature.

In infinite dimensions, $\sigma(\omega)$ can be expressed in terms of the one particle spectrum of the current carrying electrons Khurana [1990], Pruschke et al. [1993]:

$$\sigma(\omega) = \frac{1}{\omega}\frac{2e^2t^2a^2}{\nu\hbar^2}\int_{-\infty}^{\infty} d\epsilon\ \rho_0(\epsilon)\int_{-\infty}^{\infty}\frac{d\omega'}{2\pi} A_\epsilon(\omega')A_\epsilon(\omega'+\omega)(n_f(\omega')-n_f(\omega'+\omega)) \tag{2.40}$$

with $A_\epsilon(\omega) = -2\Im m[G(\epsilon,\omega)]$ being the spectral representation of the Green function of the lattice conduction electrons, ρ_0 the non-interacting density of states of the lattice, a the lattice constant, ν the volume of the unit cell, and e the electrons bare charge.

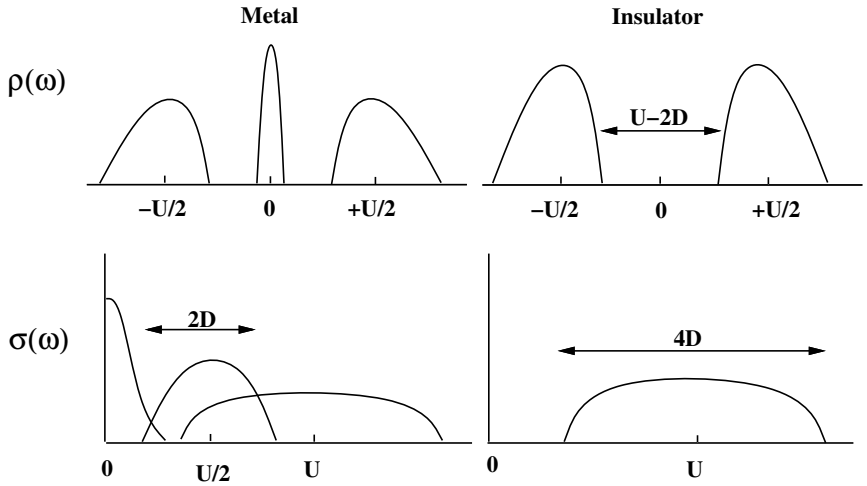

Figure 2.6: Schematic DOS for the Hubbard model (1/2 filling) and their corresponding optical spectra for the metallic and insulator solutions from Rozenberg et al. [1996]. The width of the incoherent peaks in the DOS is $\approx 2D$ and the one of central peak in the metal is $\approx ZD \equiv \varepsilon_F^*$.

The solution of the DMFT equations shows that at low temperatures the model has a metal insulator transition (Mott-Hubbard transition) at an intermediate value of the interaction. The different structures of the DOS (Fig. 2.6) give rise to very different optical responses. Let's first consider the insulator, which is simpler. In this case, optical transitions are possible from the lower to the upper Hubbard band. We therefore expect the optical spectrum that results from the convolution (2.40) to display a single broad feature that extends approximately from $U-2D$ to $U+2D$ (Fig. 2.6). A negligible temperature dependence of the spectra is expected, as long as $T \ll \Delta$. On the other hand, in the metallic case, the low temperature optical spectrum displays various contributions: *i*) A narrow low frequency peak that is due to transitions within the quasiparticle band which crosses the Fermi level. In the $T = 0$ limit this peak becomes a δ-function and is the Drude part of the optical response. *ii*) At frequencies of order $U/2$ an incoherent feature of width $\sim 2D$ emerges due to transitions between the Hubbard bands and the central peak. *iii*) A last contribution at frequency $\sim U$ appears due to transitions between the Hubbard bands. This is a broad feature of width $\sim 4D$. Therefore, we expect an optical spectrum like the one schematically drawn

in (Fig. 2.6). It is important to realize that, unlike the insulator, a notable temperature dependence of the spectra is to be expected. There is a low energy scale T_{coh} that corresponds to the temperature below which coherent quasiparticle excitations are sustained. It roughly corresponds to the the width of the resonance at the Fermi energy $\varepsilon_F^* \equiv ZD$. As T is then increased and becomes comparable to T_{coh}, the quasiparticles are destroyed, and as consequence, the contributions to the optical spectra associated with them, (i) and (ii), rapidly decrease.

It should be clear that in our previous discussion we have assumed that the system does not order magnetically, as paramagnetic solutions were considered. This situation can in fact be realized by introduction of disorder (e.g. a random distribution of t_{ij}) or next nearest neighbor hopping, and avoids the artificial nesting property of the bipartite lattice Georges and Krauth [1993], Rozenberg et al. [1994].

2.3 The Dimer Hubbard Model

2.3.1 The Model

In the scope of this work I'll focus on the *dimer* Hubbard Model(DHM), which is a natural extension of the single band Hubbard Model. The key feature is that in the former case there is a single site in the unit cell, while in the latter case there is a dimer. This materializes a system where two copies of the Hubbard model have been coupled at every site by an intra-dimer hopping $t_\perp$. In the limit of $t_\perp \to 0$ the two copies become independent and one recovers physics of the conventional single site Hubbard model Georges et al. [1996], Moeller et al. [1999], Nájera et al. [2017]. This two site cluster, as the unit cell of the lattice, is the fundamental choice to imitate VO_2 dimerized behavior. On a general context the presence of a preferential direction in all vanadium compounds is non negligible Schwingenschlögl and Eyert [2004]. The *dimer* Hubbard model in terms of second quantization operators reads:

$$H = \left[-t \sum_{\langle i,j \rangle \alpha\sigma} c^\dagger_{i\alpha\sigma} c_{j\alpha\sigma} + \; t_\perp \sum_{i\sigma} c^\dagger_{i1\sigma} c_{i2\sigma} + H.c. \right] + U \sum_{i\alpha} n_{i\alpha\uparrow} n_{i\alpha\downarrow} \tag{2.41}$$

where $\langle i, j \rangle$ denotes next-neighbor lattice sites, $\alpha = \{1, 2\}$ denote the dimer orbitals, σ is the spin, t is the lattice (i.e. inter-site) hopping and $(t_\perp)$ is the intra-dimer hopping. The parameter U is the on-site Coulomb repulsion.

The non-interacting limit of the DHM has two bands which are locally hybridized at every lattice site. This leads to a direct splitting of two parallel bands by $2t_\perp$. When this splitting is large enough, the system experiences a metal insulator transition. This is considered a Peierls-like mechanism, as it is driven by the increase of the intra dimer hopping amplitude

$t_\perp$, where dimers in the unit cell form a molecular bond that locks the conduction degrees of freedom from the lattice. This transition is clearly of second order. Another way to see this is by starting with local dimers that form a bonding (B) and an anti-bonding (A) orbital at every 1-2 link. These molecular orbitals become bands in the lattice environment of a solid where the lattice hopping t is switched on. A large enough lattice hopping t will produce the overlap of the B and A bands separated by a fixed $t_\perp$, hence an insulator to metal transition will take place.

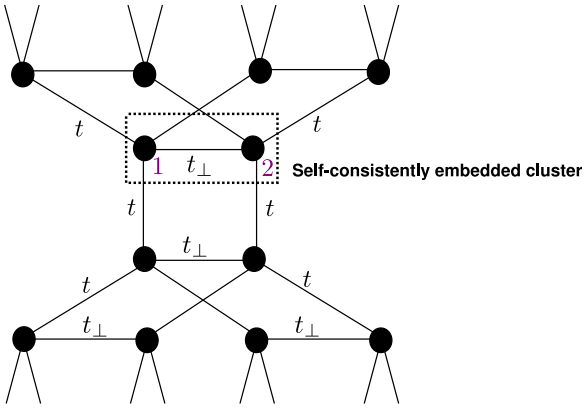

Figure 2.7: Lattice structure of the Dimer Bethe Lattice with dimer coordination $z = 3$. Delimited the effective dimer impurity cluster.

Before proceeding, we should avoid any confusion here by noting that the model (2.41) is only fully defined after its lattice is specified. For instance, if dimers are arranged as a one dimensional system, the model is a "ladder" (the dimer rungs are perpendicular to the direction of the lattice). In two dimensions, one would get a "bi-layer" model, where the dimer rungs connect at every site the two parallel layers Kancharla and Okamoto [2007], Golor et al. [2014], Lee et al. [2014]. Those systems have qualitatively different behaviors from the one that concerns us here, namely, the physics of the three dimensional system. For these 3D systems that have strong local interactions one may expect the DMFT to be a reasonable approximation Emery [1993]. In fact DFT+DMFT methods are implicitly based on such assumption. In this work we shall neglect the specific details of a lattice structure and adopt a Bethe lattice to construct the lattice of dimers as shown in figure 2.7. The Bethe lattice is not only convenient from the mathematical point of view, but it can be viewed as treating a translationally invariant lattice with a semi-circular density of states (DOS). This is a good starting point for working with generic spectral densities since it is has a finite bandwidth given by $4t$ where t is the lattice hopping amplitude defined in equation (2.41) and it possesses square-root singularities at the band edges such as three-dimensional densities of states have, otherwise it is featureless Georges et al. [1996], Economou [2006], Karski et al. [2008]. For this work we adopt as unit of energy the half bandwidth $D = 2t = 1$. It is important to emphasize here that the physics of models treated within DMFT in general do not depend on specific geometry of the lattice, but on the nature of the quantum impurity

model as DMFT yields the generic behavior of a high-dimensional lattice.

2.3.2 Non-interacting Solution of the DHM: Electronic structure and optical conductivity

To start it is most useful to study the local Green's function of the non-interacting Bethe lattice. A matrix formulation of the DHM is obtained by introducing the vector operators $\mathbf{c}^{\dagger}_{i\sigma} = (c^{\dagger}_{i1\sigma}, c^{\dagger}_{i2\sigma})$, producing a matrix form to the Green's function which will be written as function of this vector and described by 2×2 matrices:

$$\mathbf{G}_{ij\sigma}(\tau - \tau') = \langle T_\tau \mathbf{c}_{i\sigma}(\tau)\mathbf{c}^{\dagger}_{i\sigma}(\tau')\rangle = \begin{bmatrix} -\langle T_\tau c_{i1\sigma}(\tau)c^{\dagger}_{i1\sigma}(\tau')\rangle & -\langle T_\tau c_{i1\sigma}(\tau)c^{\dagger}_{i2\sigma}(\tau')\rangle \\ -\langle T_\tau c_{i2\sigma}(\tau)c^{\dagger}_{i1\sigma}(\tau')\rangle & -\langle T_\tau c_{i2\sigma}(\tau)c^{\dagger}_{i2\sigma}(\tau')\rangle \end{bmatrix} \tag{2.42}$$

In the Bethe lattice the self-consistent condition of the local Matsubara Green's function reads:

$$\mathbf{G}^{0;-1}_{\sigma} = \begin{bmatrix} \mu + i\omega_n & -t_\perp \\ -t_\perp & \mu + i\omega_n \end{bmatrix}_\sigma - t^2 \begin{bmatrix} G_{11} & G_{12} \\ G_{21} & G_{22} \end{bmatrix}_\sigma \tag{2.43}$$

In this non-interacting case we take $\mathbf{G} = \mathbf{G}^0$. Taking advantage of the symmetry that any site within the dimer is equivalent to each-other, we set: $G_{11} = G_{22}$ and $G_{12} = G_{21}$. The self-consistent equation is then easily solvable as a quadratic set of equations. One can transform this problem into diagonal form by the use of the rotation matrix:

$$P = \frac{\sqrt{2}}{2}\begin{bmatrix} 1 & 1 \\ 1 & -1 \end{bmatrix} = P^{-1} = P^{\dagger} \tag{2.44}$$

Which transforms the non-interacting Green's function into

$$P\mathbf{G}^{0;-1}_{\sigma}P^{\dagger} = \begin{bmatrix} G^0_{AA} & 0 \\ 0 & G^0_{BB} \end{bmatrix}_\sigma = \begin{bmatrix} i\omega_n - t_\perp + \mu - t^2(G^0_{11} + G^0_{12}) & 0 \\ 0 & i\omega_n + t_\perp + \mu - t^2(G^0_{11} - G^0_{12}) \end{bmatrix}_\sigma \tag{2.45}$$

and as expected the dimerized unit cell forms the 2 bands. For the notation in this thesis, they will be labeled as anti-bonding (A) and bonding (B), and the corresponding Green's function G_{AA} and bonding G_{BB} respectively. Solving these equations restores the well known

semi-circular density of states in each of the bands, with the center of the semi-circles split by $2t_\perp/D$.

$$G^0_{AA} = \frac{1}{2t^2}\left(i\omega_n - t_\perp + \mu - \sqrt{(i\omega_n - t_\perp + \mu)^2 - 4t^2}\right) \tag{2.46a}$$

$$G^0_{BB} = \frac{1}{2t^2}\left(i\omega_n + t_\perp + \mu - \sqrt{(i\omega_n + t_\perp + \mu)^2 - 4t^2}\right) \tag{2.46b}$$

In order to return to the local basis is easy to remember that the local Green's function $G_{11} = \frac{1}{2}(G_{AA} + G_{BB})$ is the average of the composing bands. From equations (2.46) we can again resume the discussion of the band insulator transition and visualize it in figure 2.8. The Bethe lattice density of states is a semi-circle. When $t_\perp = 0$ the two lattices are decoupled. However, as dimerization is activated ($t_\perp \neq 0$) a gap opens between the bonding and anti-bonding bands. This can be seen as a Peierls transition as is purely a band structure effect only due to the change in hopping amplitude $t_\perp$ as the dimers are formed. This transition is completely absent in the $t_\perp = 0$ case that we discussed in figure 2.5.

The optical conductivity has to be extended in the case of the dimer lattice having two atoms per unit cell Tomczak and Biermann [2009]. The explicit derivation for our model is presented in appendix B in particular section B.3. The optical response of this system starts with a single Drude peak when the system is undimerized, but when inequivalent orbitals exist(the BB in blue and AA bands in orange) there can be an inter band transition between those, such optical excitation appears at $2t_\perp$, this is a local molecular excitation. In the Peierls transition this molecular excitation drifts to higher energies as dimerization is increased and the centers' of each bands separate even further.

2.3.3 DMFT treatment of the Dimer Hubbard Model

The DMFT in the single band Hubbard model develops around a single quantum impurity with a completely local self-energy. In the scope of this thesis the cavity construction isolates two atoms (the dimer) and the lattice has this dimer as its motif for the unit cell. In this case we can reformulate the cavity construction from the DMFT formalism introduced in the previous section and construct a theory that remains exact in the limit of infinite coordination of dimers Moeller et al. [1999]. Here the self-energy of the system is constrained to the quantum dimer impurity with a component for short range spatial correlations encoded in the intra dimer hopping, now inherent of the impurity problem.

The DMFT equations become particularly simple and easy to derive in the case of a Bethe lattice(Fig. 2.7) and reduce in this case to:

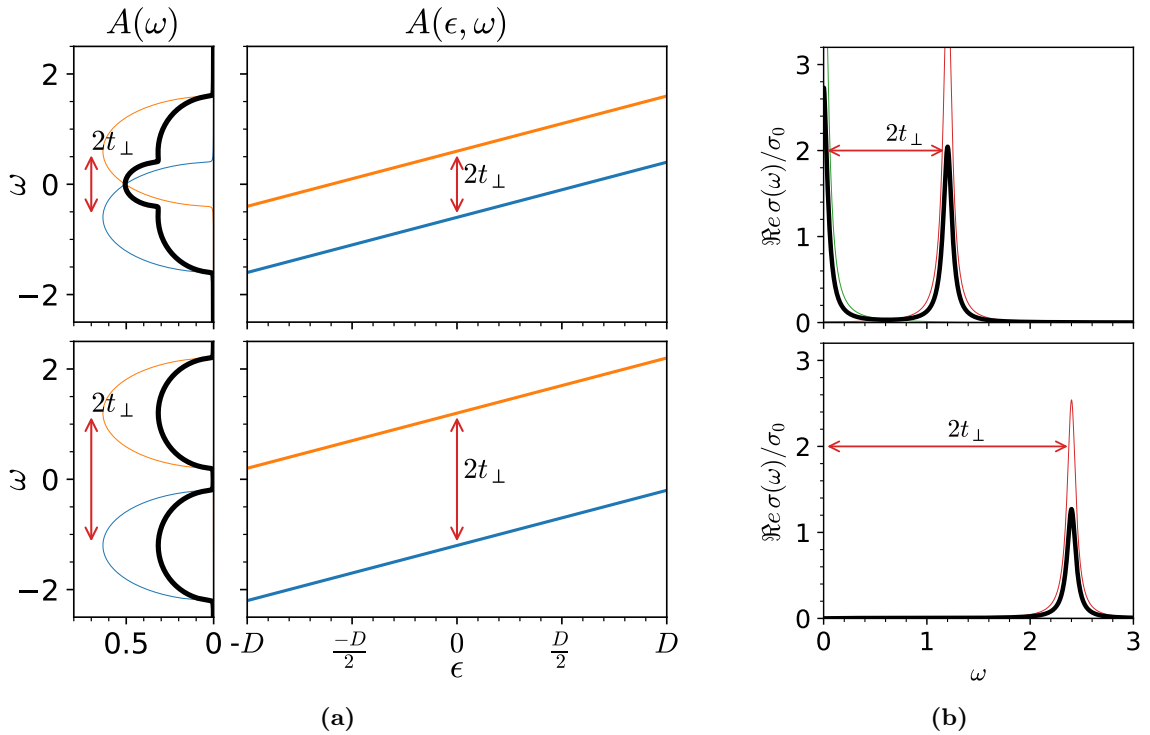

Figure 2.8: Band insulator transition of the non-interaction dimer Hubbard model. a) Left column) Spectral function $A(\omega) = -\Im m G(\omega)/\pi$ displaying the opening of a band insulating gap by enhanced dimerization, local spectral function (A_{11}) in bold black lines, Bonding (A_{BB}) in light blue, and anti-bonding (A_{AA})in orange. Right column) Electronic structure or energy resolved spectral function $A(\epsilon,\omega)$. b) Real part of the optical conductivity, total in black, intra band in green and inter band in red. The optical conductivity is ploted using and exagerated broadening $\gamma = 0.025$ to show lorenzian peaks for display purposes, for the non-interacting system where bands are rigid, only delta peaks exist.

$$S_{\text{eff}} = \int_0^\beta d\tau \int_0^\beta d\tau' \sum_\sigma \mathbf{c}^\dagger_{0\sigma}(\tau)\mathcal{G}_0^{-1}(\tau-\tau')\mathbf{c}_{0\sigma}(\tau') + U\int_0^\beta d\tau \left(n_{1\uparrow}(\tau)n_{1\downarrow}(\tau) + n_{2\uparrow}(\tau)n_{2\downarrow}(\tau)\right) \tag{2.47}$$

$$\mathcal{G}_0^{-1}(i\omega_n) = \begin{pmatrix} i\omega_n + \mu & -t_\perp \\ -t_\perp & i\omega_n + \mu \end{pmatrix} - t^2\mathbf{G}(i\omega_n), \tag{2.48}$$

The DMFT procedure to find a self-consistent solution remains exactly the same as specified in the previous section one is only solving for a matrix Green's function at each step of the iterative problem. The DMFT approach to the DHM with a dimer unit cell is, strictly speaking, a cluster-DMFT calculation, possibly the simplest instance of CDMFT Kotliar et al. [2001] and other cluster extensions of DMFT Maier et al. [2005].

The dimer Hubbard model has already been studied by few authors, but has surprisingly received little attention in general and only partial solutions have been obtained. The main results have been focused on the identification of a Metal-Insulator transition, which is of first order, presenting an hysteresis region where metallic and insulating solution can be stabilized at moderate U and small $t_\perp$. This was lead by calculations in the paramagnetic solution at zero temperature under the IPT approximation by Moeller et al. [1999] and at finite temperature Fuhrmann et al. [2006] $T/t = 0.025$ using quantum Monte Carlo Hirsch and Fye [1986], those phase diagrams are presented in figure 2.9. The anti-ferromagnetic solution was studied in Hafermann et al. [2009] at even higher temperatures $T/t = 0.1$ by use of the continuous time quantum Monte Carlo Rubtsov et al. [2005].

In this thesis we obtain the detailed solution of the problem paying special attention to the MIT and the nature of the coexistent solutions as well as the change in character of the insulating phases. We solve the DMFT equations with hybridization-expansion continuous-time quantum Monte Carlo (CT-QMC) Werner and Millis [2006], Seth et al. [2016] and exact diagonalization Georges et al. [1996], which provide (numerically) exact solutions. We also adopt the IPT approximation Moeller et al. [1999] which, remarkably is exact in the atomic limit $t = 0$, refer to appendix C.1.2, therefore provides reliable solutions of comparable quality as in the single-band Hubbard model Georges et al. [1996]. Furthermore, IPT is extremely fast and efficient to explore the large parameter space of the model and provides accurate solutions on the real frequency axis. This model can be considered as one of the first cluster extensions to DMFT Kotliar et al. [2001], Maier et al. [2005] and it remains the simplest cluster extension retaining the exact infinite dimensional limit of single site DMFT.

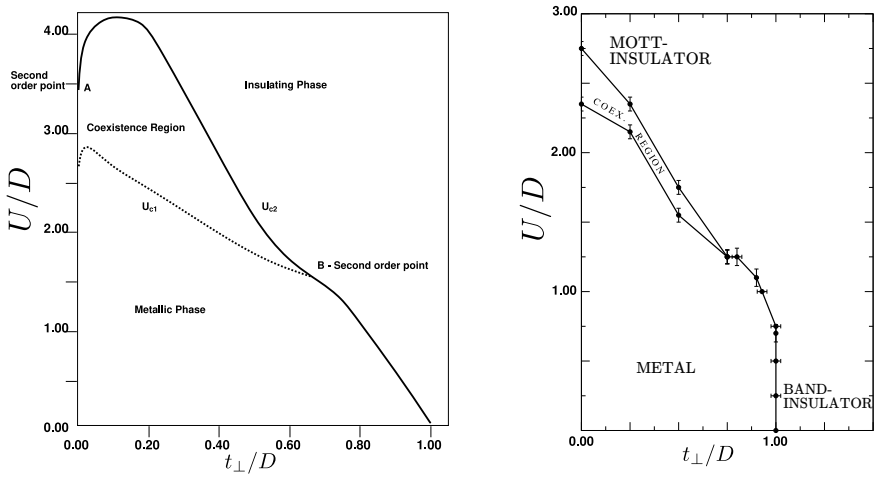

Figure 2.9: Phase diagrams from the dimer Hubbard model. left) T=0 using IPT solver Moeller et al. [1999] and right) β/t=40 using QMC solver Fuhrmann et al. [2006].

Chapter 3

DMFT Solution of the Dimer Hubbard Model

This section describes our main results on the study of Dimer Hubbard Model. We shall describe the electronic phases it sustains at zero and finite temperatures and the transitions between them, as well.

3.1 Metal Insulator transition at $T = 0$ in the DHM

We first reproduce the work of Moeller et al. [1999] in Fig. 3.1, with our numerical implementation of the IPT solver. The results are essentially the same, though our implementation shown better numerical stability when portraying the ground state solutions especially when $t_\perp \to 0$. The phase diagram shows a metallic phase for $t_\perp/D < 1$, and an insulator phase at high enough U. The metal-insulator transition changes character depending on the value of $t_\perp$. At values higher than $t_\perp \approx 0.7$ the transition is continuous (2nd order) along a line U_{c_3} indicated in green in Fig. 3.1. At smaller values of $t_\perp$ there are two lines U_{c_1} and U_{c_2} respectively indicated in blue and red in the figure. These are two spinodal lines of the mean field theory's self-consistent solution. The metal state is destabilized above U_{c_2} while, coming down from higher values of U, the insulator state is destabilized along U_{c_1}. Thus, in between the two spinodal lines there are two different solutions of the DMFT equations, one metallic and one insulating. The phase diagram at $T = 0$ is obtained with IPT but all its main features have been validated by extensive CT-QMC calculations.

3.1.1 Metal to insulator transition: U_{c_2} and U_{c_3} lines

The paradigmatic scenario for the Mott transition follows the idea from Brinkman and Rice [1970] where as correlations are increased the effective mass of conduction electrons diverges at the Mott transition marking the disappearance of quasiparticles at the Fermi energy and destroying the metallic state. This scenario has been validated within DMFT in the single band Hubbard model Georges et al. [1996]. In the DHM this is not the case as first identified by Moeller et al. [1999] where it was shown that the quasiparticle weight remained finite at the Mott transition even at zero temperature. It was also identified that

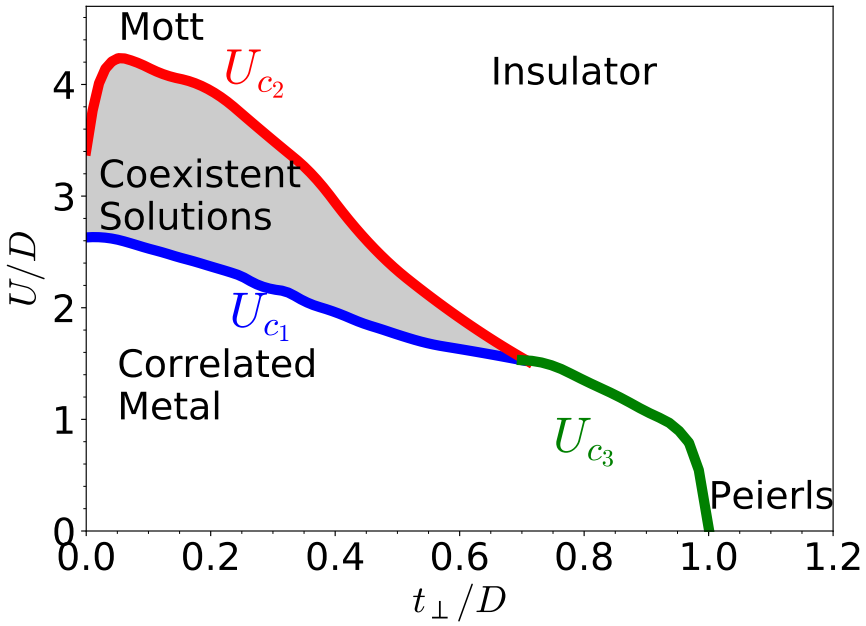

Figure 3.1: Zero temperature $T = 0$ phase diagram of the dimer Hubbard Model. The Metal-Insulator transition takes place at U_{c_2} and U_{c_3}(red and green lines respectively), U_{c_1} marks the spinodal line where the Mott insulator vanishes to reestablish the correlated metal phase. The Mott insulator is continuously connected to the Peierls insulator, however different crossover behaviors can be identified.

there was violation of the "pinning condition" for the density of states at the Fermi level in comparison to the $t_\perp = 0$ case. We remind the reader that in the $t_\perp = 0$ one has two independent copies of the single band Hubbard Model. At the same time the mechanism for the metal to insulator transition remained unresolved, and as we shall present here, the MIT when electronic correlations are increased dramatically changes its character as a function of $t_\perp$, the lattice dimerization. In Fig. 3.2 we illustrate this by showing the evolution of the frequency-dependent DOS with increasing U, for two representative values $t_\perp = 0.3$ and 0.8, that respectively cross the U_{c_2} and the U_{c_3} lines, where the transition is of first order in the first case and second order in the latter.

Here I'll present a unifying view for the Metal Insulator Transition, evolving from the paradigmatic Mott insulating state at $t_\perp = 0$ and U_{c_2} to the band insulating state at $U = 0$ and $t_\perp/D = 1$. The behavior at high $t_\perp/D = 0.8$ is rather simple, it retains all the characteristic of the Band insulating transition. To illustrate this we show the partial DOS for the two bonding (B) and anti-bonding (A) bands of the system (B in dotted blue and A in dot-dashed orange), which average into the local density of states (shown in thick black lines). In this case the two bands barely change their shape, their mass is remains essentially un-renormalized. As U is increased bands drift apart and continuously open a band insulating gap. We can identify this state with a correlation assisted Peierls insulator,

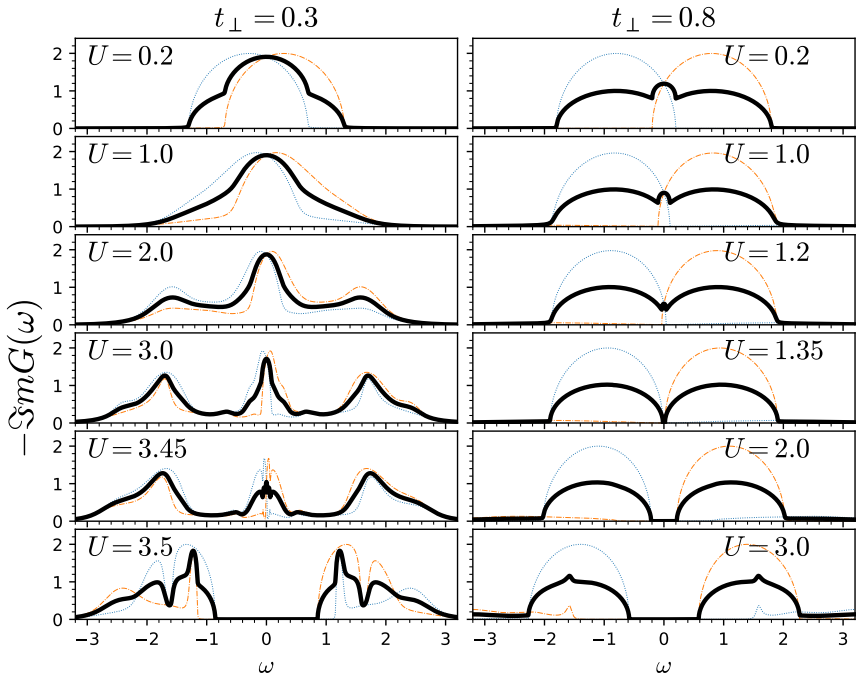

Figure 3.2: DOS for increasing values of U. Black lines represent the local$(-\Im mG_{11})$ Spectral function, which is the average of the bonding (dashed blue) and anti-bonding (dot dashed orange) bands. Calculated at $T = 0$ (IPT).

as it occurs at a large molecular hybridization and relatively low interaction $U_c \simeq 1.35$. In this situation the Bonding band is almost completely filled and the anti-bonding band has been depleted. It is relevant to keep in mind that this intuitive picture does not hold as one moves further in the correlated regime by increasing U. In such case there is a continuous transfer of spectral weight across the gap, which aims to balance the participation of each of the bands. The discussion of this effects is left to forthcoming section 3.2.1.

The metal-insulator transition within the region of coexistence, such as for $t_\perp = 0.3$ in this example, is less intuitive. In this case the local spectral function first evolves following the well known pattern described from the single site DMFT studies of the single band Hubbard Model. There is a redistribution of spectral weight, transferring low energy states to higher energies of order $U/2$ developing the Hubbard bands and the characteristic 3-peak structure of a Mott system. What is different is that the central peak does not continuously shrink until its disappearance at $U_{c_2}(t_\perp = 0.3) \approx 3.47$, in clear contrast to the Brinkman and Rice [1970] scenario. It actually remains finite and contrary to the single band Hubbard model case, there is no pinning condition for the central quasiparticle peak Moeller et al. [1999]. This quasiparticle also develops a non-trivial structure in the DOS at low frequencies as the critical value U_{c2} is approached. This is an essential difference to the single site$(t_\perp = 0)$ case where the transition is of second order at $T = 0$ and U_{c_2}. One can nevertheless see from

the two bands crossing E_F that the disappearance of the metallic state here does not seem linked to a divergence in the quasiparticles' effective mass. We shall address this point in detail next.

3.1.1.1 Low energy behavior: the renormalized two band (R2B) parametrization

The character of the Mott MIT transition is significantly affected by the dimer structure of the system as it is sharply different form the $t_\perp = 0$ case. However, as I'll argue it resembles a renormalized band-insulating mechanism for the low energy features. To pinpoint this, it is convenient to adopt a low-energy Fermi liquid parametrization of the DOS, which is always possible in the metallic phase, because the low frequency behavior of the self-energy is of a local Fermi liquid. In such regime the real part of self-energy can be well represented up to linear order, thus one can provide a minimal set of parameters to described the low energy behavior of the spectral function where the quasiparticle residue Z is given by:

$$Z^{-1} \equiv 1 - \left.\frac{\partial \Re\Sigma_{AA/BB}(\omega)}{\partial\omega}\right|_0 = 1 - \left.\frac{\partial \Re e\Sigma_{11}(\omega)}{\partial\omega}\right|_{\omega=0} \tag{3.1}$$

and we may define the renormalized intra-dimer hopping

$$\tilde{t}_\perp \equiv t_\perp \pm \Re\Sigma_{AA/BB}(0) = t_\perp + \Re\Sigma_{12}(0) \tag{3.2}$$

The equalities in eqs. (3.1) and (3.2) are only valid at half-filling, when the system is particle-hole symmetric. With this two low energy parameters one obtains a renormalized two-band (R2B) representation of the electronic structure at low frequencies in terms of two quasiparticle bands. Their corresponding DOS is composed of two narrowed semicircles of width $2\tilde{D} = 2ZD$ and split by $2Z\tilde{t}_\perp$,

$$\rho^{R2B}_{AA/BB}(\omega) = \frac{2}{\pi D^2}\sqrt{D^2 - (\frac{\omega}{Z} \mp \tilde{t}_\perp)^2} \tag{3.3}$$

that corresponds to two heavy effective bands with dispersion $E_\epsilon^{AA/BB} = \pm Z\tilde{t}_\perp + Z\epsilon$, where the effective mass renormalization is $m^*/m = 1/Z$. The overlap between the two bands is given by 2η, where

$$\eta = ZD - Z\tilde{t}_\perp. \tag{3.4}$$

Thus, for $\eta > 0$ we have a metal state, and for $\eta < 0$ the DOS opens a gap (see Fig. 3.3). The renormalized two-band (R2B) model may describe both metallic and insulating states, so long the self-energy Σ remains well behaved, according to the parametrization. As it

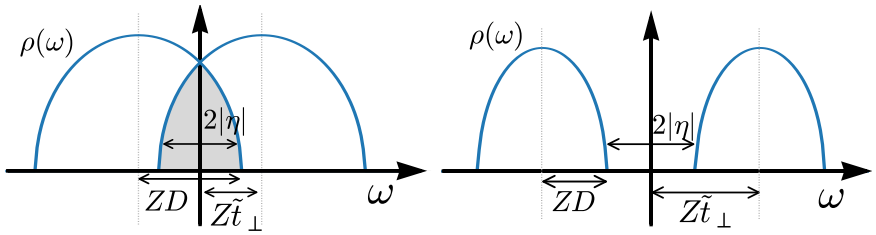

Figure 3.3: Schematic representation of the two bands in the R2B model. This model is a simple renormalization of the non-interacting case where $Z = 1$ and the intra-dimer hopping is $\tilde{t}_\perp = t_\perp$.

turns out this description will be valid at low frequencies throughout the metallic phase, which is a Fermi liquid. In the insulator, we shall see that it is a good approximation only within the Peierls limit, where the interaction and thus the Σ are small.

To test the goodness of the description of a low energy renormalized two band system, we replot in Fig. 3.4 the low frequency part of the spectra of Fig. 3.2 (l.h.s.), for the $t_\perp/D = 0.3$ case as a function of the rescaled frequency ω/ZD. We can observe a new emerging picture, where the central peak in the local density of states can be understood as composed of two heavy bands. Their bandwidth has been renormalized down by the interactions but also their splitting has been renormalized down. The R2B model parametrization (in red dashed line in figure 3.4 for the anti-bonding band) provides an good description of the low energy part of the spectra which in this case corresponds to the low energy band edges of the bonding and anti-bonding quasiparticle peaks. It looses accuracy at *higher* energies, but it provides enough information to track the breakdown of the metallic state.

Unlike the Brinkman-Rice scenario Brinkman and Rice [1970], where $Z \to 0$, here the transition occurs at a finite effective mass. The opening of the gap results from the combined effect of the renormalization of the bandwidth and of the splitting. Both decrease as $U \to U_{c2}(t_\perp)$ for the metal within the coexistence region, but the quantity that becomes zero is not Z but the renormalized bonding/anti-bonding bands overlap $\eta = ZD - Z\tilde{t}_\perp$. This means that the low-energy contributions to the quasi-particle peak separate. This behavior is similar to the MIT reported in a correlated two orbital model Mazza et al. [2016]. Nevertheless, the transition does share a similarity with the MIT in the single band case, namely, that as the DOS($\omega = 0$) becomes zero the Kondo effect at the two impurity sites can no longer be sustained and the impurities loose their respective Kondo screening clouds. In the single band (single-site) case one is left with almost free local moments, however, in the present case a strong RKKY-like magnetic interaction between the two sites takes over and one has intra-dimer screening. This dramatic enhancement of the intra-dimer magnetic interaction translates to the concomitant sharp increase of intra-dimer effective hopping $\tilde{t}_\perp = t_\perp + \Re\Sigma_{12}(0)$, which opens a large gap (see Fig. 3.2) Nájera et al. [2017].

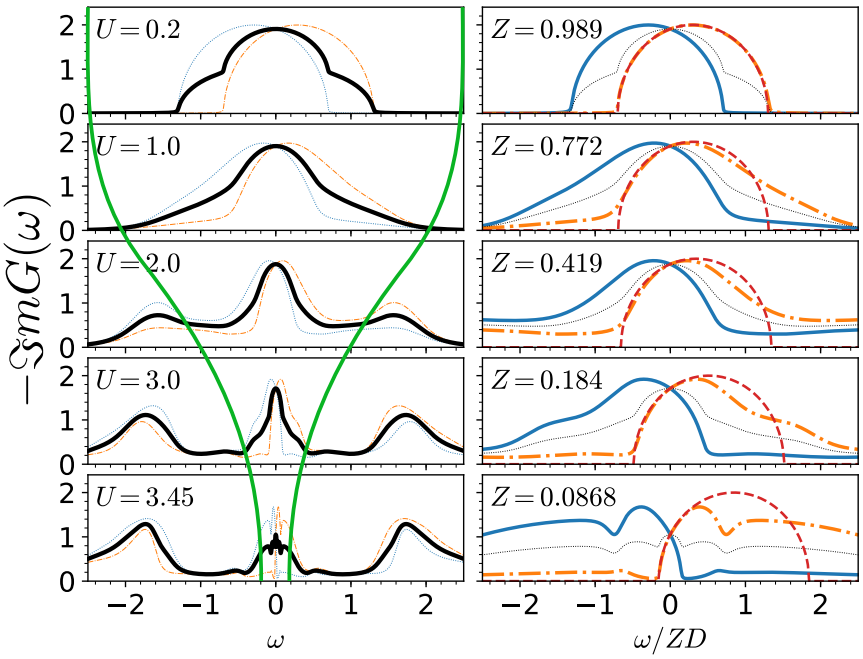

Figure 3.4: Left panel: Metallic DOS for $t_\perp/D = 0.3$, reproduction of Fig. 3.2. Right panel: Rescaled view of low frequency part of the DOS as a function of ω/ZD for increasing U at fixed $t_\perp = 0.3$, representing the region within the green lines in left panel. The local spectral function (black dotted line) is decomposed in the Bonding Spectral function (Blue line) and Anti-bonding Spectral function(orange dot dashed line). The dashed red line is the renormalized parametrization of the low energy quasiparticle from equation (3.3)

The renormalization of the intra-dimer hopping driving the IMT originates in the loss of Kondo screening and the concomitant boost of the magnetic interaction. These competing mechanisms are well known in strongly correlated systems tracing back to Doniach's Kondo lattice Doniach [1977].

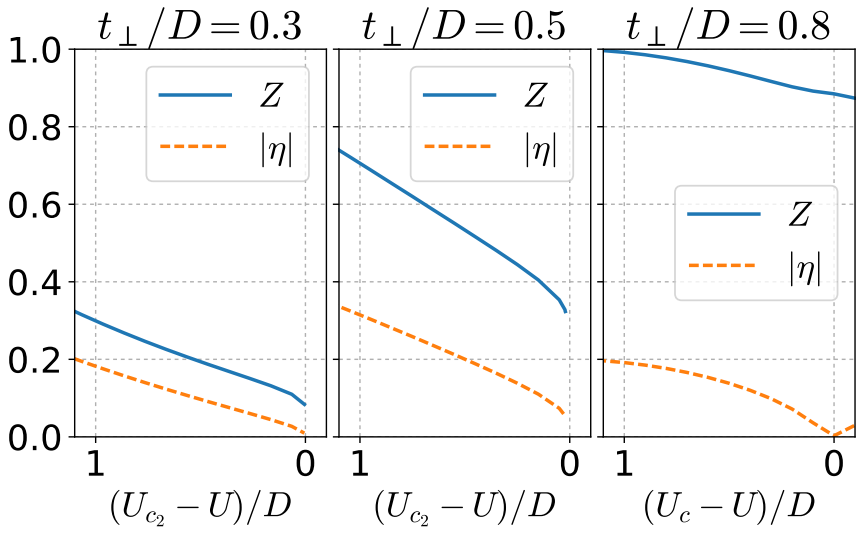

Figure 3.5: Z and $|\eta|$ as a function of U for various values of dimerization $t_\perp$. The left and central panels correspond to the behavior as the $U_{c_2}(t_\perp)$ red spinodal line is approached (cf. Fig.3.1), where the metal-insulator transition is discontinuous. The right panel shows the behavior when the green 2$^{\text{nd}}$ order line is crossed (cf. Fig.3.1). The R2B parametrization works on either side of the transition. Note that η is negative on the insulating side in the last panel.

In figure 3.5 we show the behavior of the low energy parameters that describe the metal insulator transition. Consistent with the previous discussion we see that the parameter $|\eta|$ decreases much faster than the quasiparticle residue Z as U is increased towards U_{c_2}. For $t_\perp/D = 0.3$ the mass renormalization ($\propto 1/Z$) is very large. Thus the metal state is strongly correlated with heavy quasiparticles resulting from two "Kondo" states at each one of the atomic impurity sites. Each one of the sites is independently screened by conduction electrons, and also by each other. When $\eta \to 0$ the DOS at E_F decreases, the Kondo-screening cannot be sustained and the MIT takes place. As one increases the values of $t_\perp/D$ to 0.5, we observe that the Z parameter does not experience such a strong renormalization and appears to be finite at the transition point. When $t_\perp/D = 0.8$, in contrast, there is little change in the quasiparticle weight Z, which indicates an almost negligible mass enhancement. Nevertheless the band overlap $|\eta|$ decreases continuously up to the metal insulator transition and for $U > U_{c_3}$ it becomes a measure of the insulating gap. The insulator just above U_{c_3} is a weakly renormalized band insulator and the R2B parametrization still holds. In contrast, the insulator above U_{c_2}, as discussed above, is a Mott insulator and the R2B parametrization fails completely. There is a discontinuous change in the spectral functions at the transition at U_{c_2}.

We should mention for completeness that this intuitive picture of the metal-insulator transition holds almost everywhere along the $U_{c_2} - U_{c_3}$ lines and would provide a unifying picture of the breakdown of the metallic state. However, we noted that the vanishing of η is not complete within the IPT approximation around intermediate values of $t_\perp/D$, as explicitly shown in figure 3.5 for the case of $t_\perp/D = 0.5$. We have also compared with results from exact methods like CT-QMC at the lowest possible temperatures but results where inconclusive. This is due to the very small energy scales being in competition with the low temperature. This issue might be resolved with better adapted methods such as NRG-DMFT Bulla et al. [1998] or DMRG-DMFT García et al. [2004].

3.1.2 Insulator to Metal transition: U_{c_1} line

We have described above how the metallic solution collapses discontinuously as one increases the interaction U along the U_{c_2} line. Here we shall consider the collapse of the insulator one as we come down from high U towards U_{c_1}. The systematic behavior of the DOS is shown in Fig. 3.6 for two values of $t_\perp$. A smaller value $t_\perp = 0.4$ and, for comparison, a larger value $t_\perp = 0.6$ closer to the starting point of the continuous transition line U_{c_3} (cf. Fig.3.1).

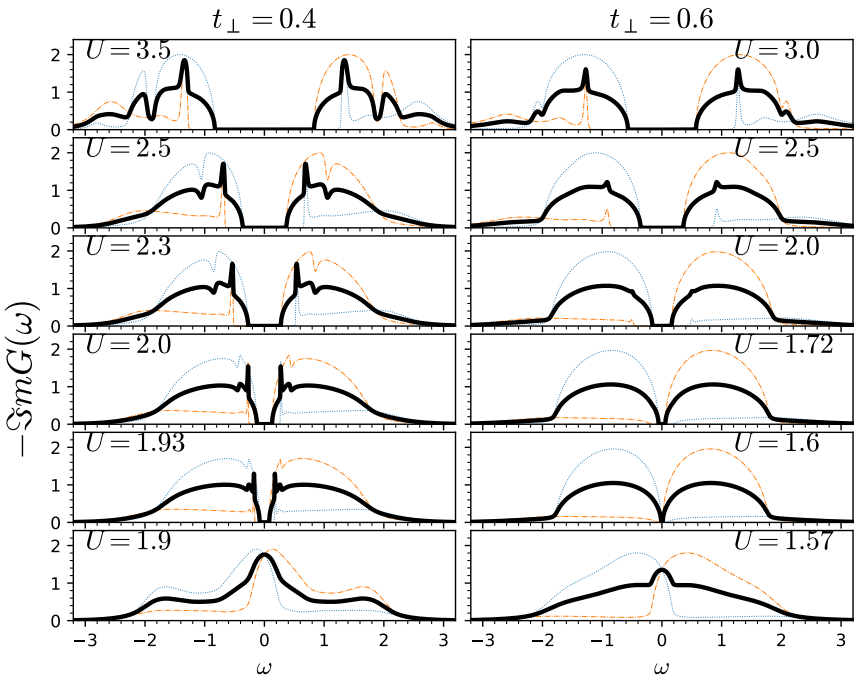

Figure 3.6: DOS for decreasing values of U as the system crosses the U_{c1} transition line. Black lines represent the local$(-\Im mG_{11})$ Spectral function, which is the average of the bonding (dashed blue) and anti-bonding (dot dashed orange) bands. Calculated at $T = 0$

At the lower value of $t_\perp$ we observe that the DOS does not seem to close the gap at the transition. Notice the values of U close to the critical point. The transition is very discontinuous, as just below U_{c_1} the DOS is qualitatively different, displaying a metallic state

that has a large quasiparticle peak. The line-shape of the Hubbard bands is quite peculiar and we shall consider that feature later on. At the larger value of $t_\perp$ the system is still crossing the U_{c_1} line. However, and in contrast to the previous data, the gap seems to close continuously. Nevertheless, and different to the behavior across the U_{c_3} line that we described before (cf Fig. 3.2), the transition from insulator to metal remains very discontinuous. Indeed, the line-shape of the DOS changes quite significantly for a tiny variation of U (lower two panels on the r.h.s. of Fig. 3.6). Also in contrast to the lower $t_\perp$ case, we see that the line-shape of the DOS in the insulator has significantly less structure, it mostly resembles the two independent semi-circular bands. This is due to the proximity of the parameters to those of the continuous transition, therefore the first order character gets weakened as one approaches the *tri-critical* transition point where the U_{c_1}, U_{c_2} and U_{c_3} lines meet.

3.1.2.1 Discontinuous closing of the gap

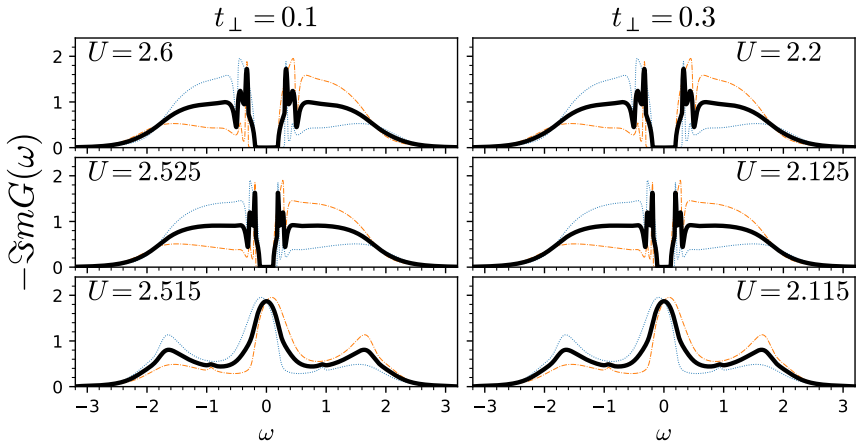

Figure 3.7: DOS for decreasing values of U as the system crosses the U_{c1} transition line. Black lines represent the local$(-\Im mG_{11})$ Spectral function, which is the average of the bonding (dashed blue) and anti-bonding (dot dashed orange) bands. Calculated at $T = 0$

The closing of the gap at U_{c_1} for $t_\perp \to 0$ is more involved than close to the tri-critical endpoint that we discussed before. The spectral function close to U_{c_1} for $t_\perp/D < 0.4$, as shown in Fig. 3.7, has a finite gap before the transition and the band edges become sharper as $t_\perp \to 0$.

The finite gap at the transition at U_{c_1} could be an artifact of the IPT approximation as does happen in the single band case. Therefore, we investigate this issue using QMC data at the lowest available temperatures. To study the disappearance of the insulating state at U_{c_1} the analytical continuation of QMC data is performed for the lowest temperature insulator ($\beta = 1/T = 200$) as close as possible to U_{c_1} and is shown in Fig. 3.8.

Our data show that at low temperatures the gap remains sharply defined upon approaching U_{c_1} at low $t_\perp$. It is interesting to note that the imaginary part of the Matsubara self-energy

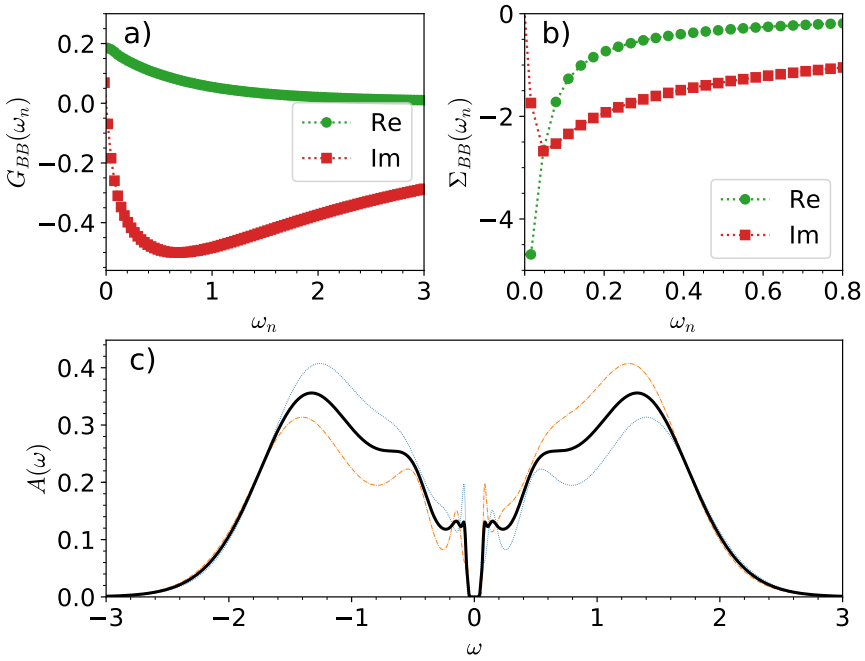

Figure 3.8: QMC solution at $U_{c_1} = 2.315$ for $t_\perp/D = 0.1$ and $\beta D = 200$. a) Matsubara Bonding Green's function, b) Matsubara Bonding self-energy, c) Density of states: black lines local DOS, dotted blue Bonding DOS, dashed orange Anti-Bonding DOS. The reader is reminded that $\Re G_{12}(i\omega_n) = -\Re G_{BB}(i\omega_n)$ and $\Im G_{11}(i\omega_n) = \Im G_{BB}(i\omega_n)$ and equally for Σ

does not diverge as it does in the half-filled single band case. As can be seen in panel (b), the first Matsubara frequency is significantly lower that the others. On the other hand, the real part shows a rather smooth behavior and becomes very large at low frequencies. This large value of $\Re\Sigma_{12}(\omega = 0)$ denotes the enhancement of the intra-dimer dimer hopping driven by magnetic coupling that we mentioned before (cf. eq.(3.2)). At this low temperature we observe the sharp band edges of the gap and a gap that seems to remain finite up to U_{c_1}, in excellent qualitative agreement with the results from IPT of Fig. 3.7. This good agreement is also important as it provides crucial support for the IPT approximation. We shall provide further validation of IPT in later sections.

While the data at $t_\perp = 0.1$ are convincing, we also explored higher values of inter-dimer hopping. Fig. 3.9 shows the insulating solution at $t_\perp/D = 0.3$ approaching as much as possible the value of U_{c_1}. The spectral function has the same qualitative behavior, displaying large and narrow features at the inner edges of the Hubbard bands. The Green's function shows clearly the presence of the gap and the self-energy is relatively smaller compared to the $t_\perp/D = 0.1$ case. As before, the imaginary part shows no divergence and actually extrapolates to zero at low frequencies. The real part of the self-energy remains large and much larger than the bare intra-dimer hopping $t_\perp$, which remind us that this insulator has gap due to a correlation boosted intra-dimer effective hopping.

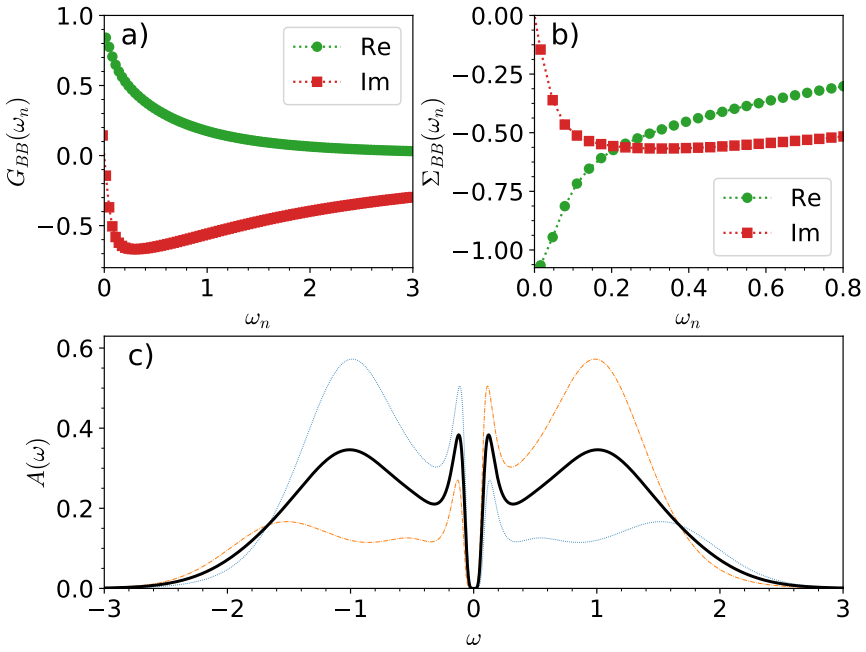

Figure 3.9: QMC solution at $U_{c_1} = 1.92$ for $t_\perp/D = 0.3$ and $\beta D = 200$. a) Matsubara Bonding Green's function, b) Matsubara Bonding self-energy, c) Density of states: black lines local DOS, dotted blue Bonding DOS, dashed orange Anti-Bonding DOS. The reader is reminded that $\Re G_{12}(i\omega_n) = -\Re G_{BB}(i\omega_n)$ and $\Im G_{11}(i\omega_n) = \Im G_{BB}(i\omega_n)$ and equally for Σ

3.1.3 Electronic structure in the coexistence region

In this section I'll compare the spectral functions between the correlated metal and Mott insulator within the coexistence region. Figure 3.10 superposes the metal and insulator spectral functions in the local basis in the top panels and, for comparison, also for the bonding basis in the bottom panel. To obtain the anti-bonding contribution one reflects the bonding spectra around the $\omega = 0$, and to obtain the local spectra one takes the average of the two.

The upper left panel (a) is a reminder of the single site DMFT spectral functions, which also corresponds to the $t_\perp = 0$ case in the present model. The metal has the quasiparticle resonance at the Fermi level whereas the insulator has completely incoherent Hubbard bands. If we then move into the (b) panel where $t_\perp/D = 0.2$, the metal spectral function is not too different from the single band case. The 3 peak structure is still present but the metal Hubbard bands do not show as much structure. The insulating spectral function, in contrast, presents marked changes. Sharp resonances appear at the inner band edges, which are absent in the single band case. The system is half-filled and particle-holy symmetric, but the bonding/anti-bonding bands have each one a different filling as evidenced by the panel (f) below. The metallic phase does not show as much of an asymmetry in the spectral function

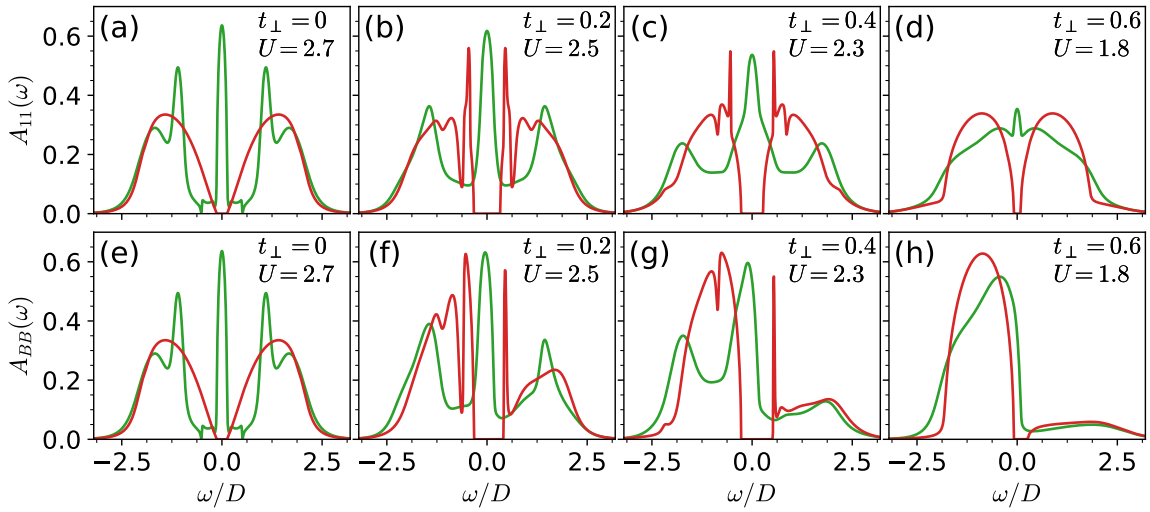

Figure 3.10: Top panels: Comparison of the local spectral function for selected points inside the coexistence region. Green is Metallic solution, Red is insulating. Bottom panels: Comparison of the bonding spectral function for the same points as top panel

as the insulator, this may be linked to the insulator having an enhanced intra-dimer hopping by the correlations that increases the asymmetry.

The (c) and (d) panels of figure 3.10 are at higher dimerization and one is forced to decrease the strength of the interaction U in order to remain within the region of coexistent solutions. A remarkable fact is that despite the reduced interaction in the metal the distance between the Hubbard bands and the central quasiparticle is of order $\sim U$ and not $U/2$ as in the single band case. The Mott insulator, however, does have its lower Hubbard band center of mass located at energies of order $\sim U/2$

In the rightmost panels we show data for $t_\perp/D = 0.6$, close to the tri-critical endpoint. The Coulomb repulsion is lower and the high dimerization prevents the metal to develop its characteristic three peak structure close to the Mott transition. One can only see a noticeable redistribution of spectral weight in the metal phase. The insulator is perhaps surprisingly close to the non-interacting state. In this case one can say that the Mott insulator at high dimerization is qualitatively close to the band insulator, while the correlated metal is close to a weakly renormalized two band system.

Finally, for higher $t_\perp$ beyond the tri-critical endpoint, the transition is continuous. There is no coexistence of solutions and the metal and the insulator evolve continuously into each other as function of U. Across the transition, the spectra is approximately described as the overlap of two semi-circles, cf. Fig. 3.2.

Further detail can be obtained from the comparison of the electronic structure of the metal and the insulator within the coexistence region shown in Fig. 3.11. In the correlated metallic

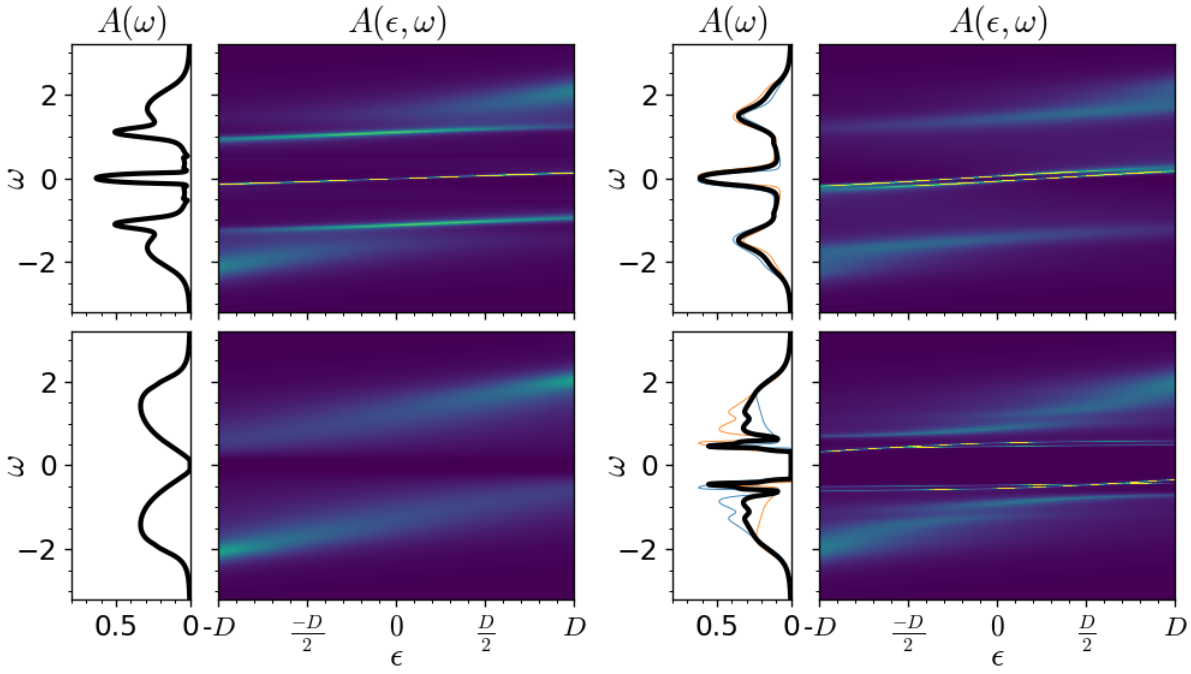

(a) $t_\perp = 0$ - $U = 2.7$ **(b)** $t_\perp = 0.2$ - $U = 2.5$

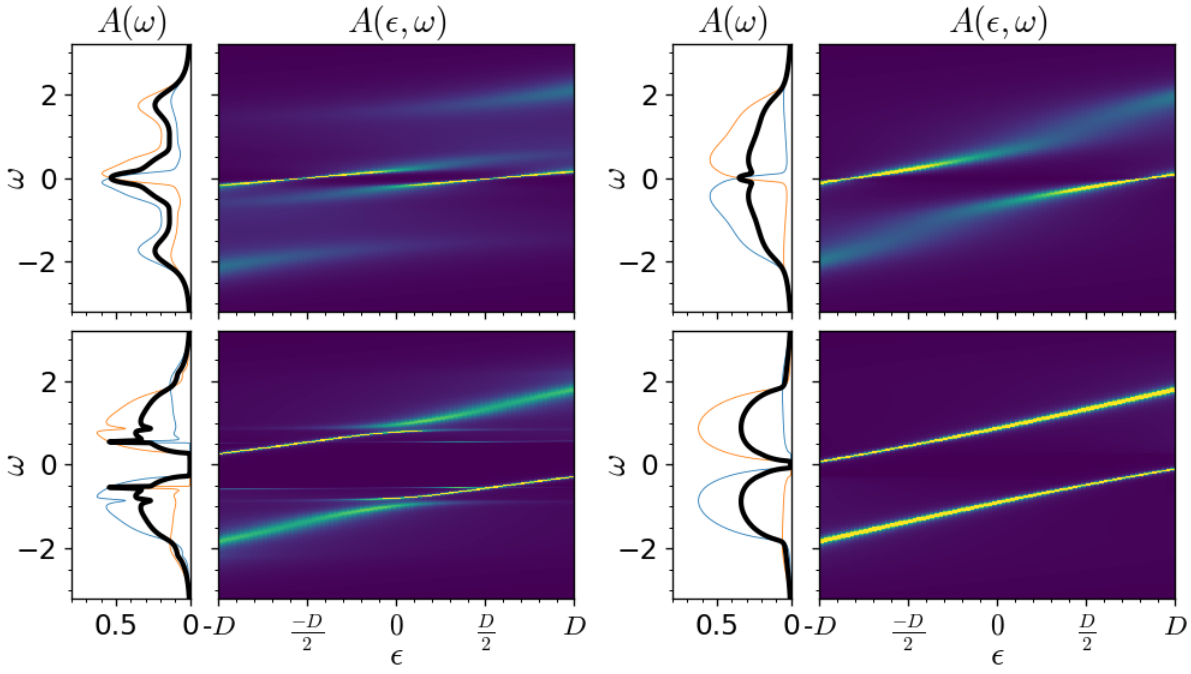

(c) $t_\perp = 0.4$ - $U = 2.3$ **(d)** $t_\perp = 0.6$ - $U = 1.8$

Figure 3.11: Electronic structure in the local basis for points in the coexistence region as in figure 3.10 . Panels with the integrated density of states display the total in black, bonding in blue and anti-bonding in orange

state, plotted in panels (a) and (b), we find at high energies ($\sim \pm U/2$) the incoherent Hubbard bands, which are signatures of Mott physics. The incoherent nature is denoted by their diffuse line-shape. At lower energies, we also observe a sharp pair of heavy quasiparticle bands crossing the Fermi energy at $\omega = 0$. Consistent with our previous discussion, this pair of quasiparticle bands can be though of as the renormalization of the non-interacting band-structure. Unlike the single-band Hubbard model, the effective mass of these metallic bands does not diverge at the MIT at the critical U, even at $T = 0$ (cf. 3.1.1). In fact, the finite $t_\perp$ cuts off the effective mass divergence as expected in a model that incorporates spin-fluctuations.

In Fig. 3.11 we also show the results for the insulator electronic dispersion at the same values of the parameters. The comparison of the insulator and the metal illustrate the significant changes that undergo at the 1st order MIT. We see in (a) the single band Hubbard model ($t_\perp = 0$) that only has incoherent Hubbard bands. The low dimerization case in (b) shows the metallic pair of quasiparticle bands that suddenly open a large gap. More precisely, in contrast to the one-band case, here the Hubbard bands acquire a non-trivial structure, with sharp coherent features coexisting with incoherent ones. The coherent part dispersion can be traced to those of a lattice of singlet-dimers (cf. appendix A.6). Hence, the insulator can be characterized as a novel type of Mott-singlet state where the Hubbard bands have a mix character with both coherent and incoherent electronic-structure contributions.

At larger dimerization strength shown in the panels (c) and (d) of figure 3.11 the metallic quasiparticles do not remain coherent throughout the entire energy spectra, this will have consequences in the optical conductivity due to their inter-band excitations. The insulator in (c) also opens a large gap as in panel (b) but the coherent features at the inner edge of the Hubbard bands become more dispersive. Finally close to the tri-critical point the insulator in (d) has quite coherent bands.

In Fig.3.12 we show the electronic structure of the coexistent solutions obtained by CT-QMC and exact diagonalization impurity solvers. These two methods are in principle numerically exact up to their respective precision. As we can observe, they are both consistent with the data from IPT. This provides an important benchmark of our calculations.

3.1.4 Frequency dependent conductivity across the metal-insulator transition

In this section we discuss the metal insulator transition from the perspective of a different spectral function. Figure 3.13 shows the optical conductivity of the dimer Hubbard model as the local interaction U is increased across the MIT for various values of $t_\perp$. The results were obtained at a low $T = 1/200$ using IPT. Let's first recall the discussion from the non-interacting limit regarding the optical response. When the system is metallic there is the Drude peak at zero frequency, and in addition there is a molecular dimer optical

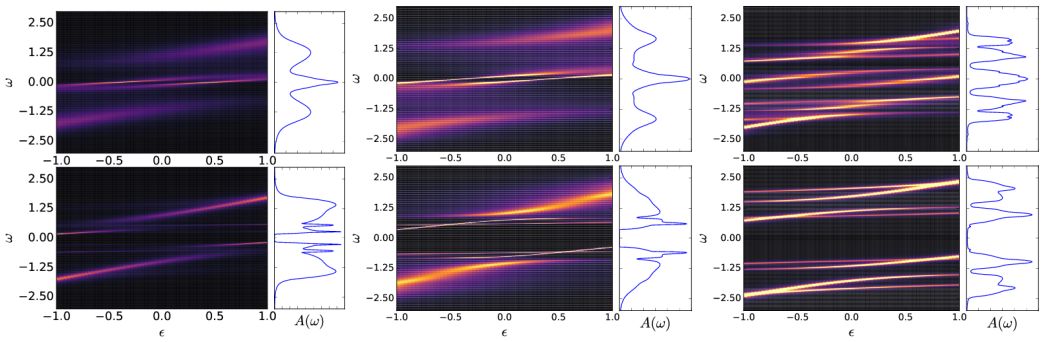

Figure 3.12: Comparison of the electronic structures in the Metal and Insulator phases at $t_\perp = 0.3$. Left CT-QMC in the coexistence $U = 2.15$, center IPT taken from main text $U = 2.5$, right results from ED metal at $U = 1.8$, insulator at $U = 3$

contribution at $\omega \sim 2t_\perp$ (cf. Fig. 2.8). In the top left the panel of Fig. 3.13 we show the response of the system at $t_\perp/D = 0.3$ as U is increased. One may observe how the Drude peak reduces its weight, similarly to the single site Hubbard model, as it corresponds to the transitions within the heavy quasiparticles at low energy. The second contribution is at finite $\omega \sim 2t_\perp$ due to excitations between the quasiparticles of the bonding and anti-bonding bands. The frequency of this features depends on the value of U. As discussed in the previous section the interaction renormalize the band splitting down at small hybridization thus one appreciates how this excitation drifts towards lower frequencies. This feature is a mid-infra-red contribution and will turn to be key to account for experimental near-field optical data obtained in VO_2, as we shall describe in the next chapter. Similarly as in the previous case this excitation originates only from transitions within the quasiparticles and it also looses weight as states are transferred to higher energies to form the Hubbard bands. At frequencies of order $\sim U/2$ an incoherent response emerges. These are transitions between the quasiparticles and the Hubbard bands. Finally, at energies of order $\sim U$ the transitions between Hubbard bands also come into play. These last two features are also well known from the single band Hubbard model. Once the Mott insulating state is realized there is correspondingly a large optical gap followed by an optical response centered at frequencies of order $\sim U$, as it corresponds to transitions between the Hubbard bands. The particular structure in this response originates from the complex structure of the Hubbard bands that the dimer Mott insulator realizes(cf. Fig. 3.2). As we shall discuss in later sections, the dimer insulator the Hubbard bands support a mixed structure with coherent and incoherent features.

For intermediate $t_\perp/D$, but still within the coexistence region, in the top right panel of figure 3.13 we show data that follows the same trend as interactions are increased. The ever heavier quasiparticles reduce the weight of the Drude peak. The inter-band transition drifts to lower energies as the band splitting is renormalized down, but in this case and unlike for lower

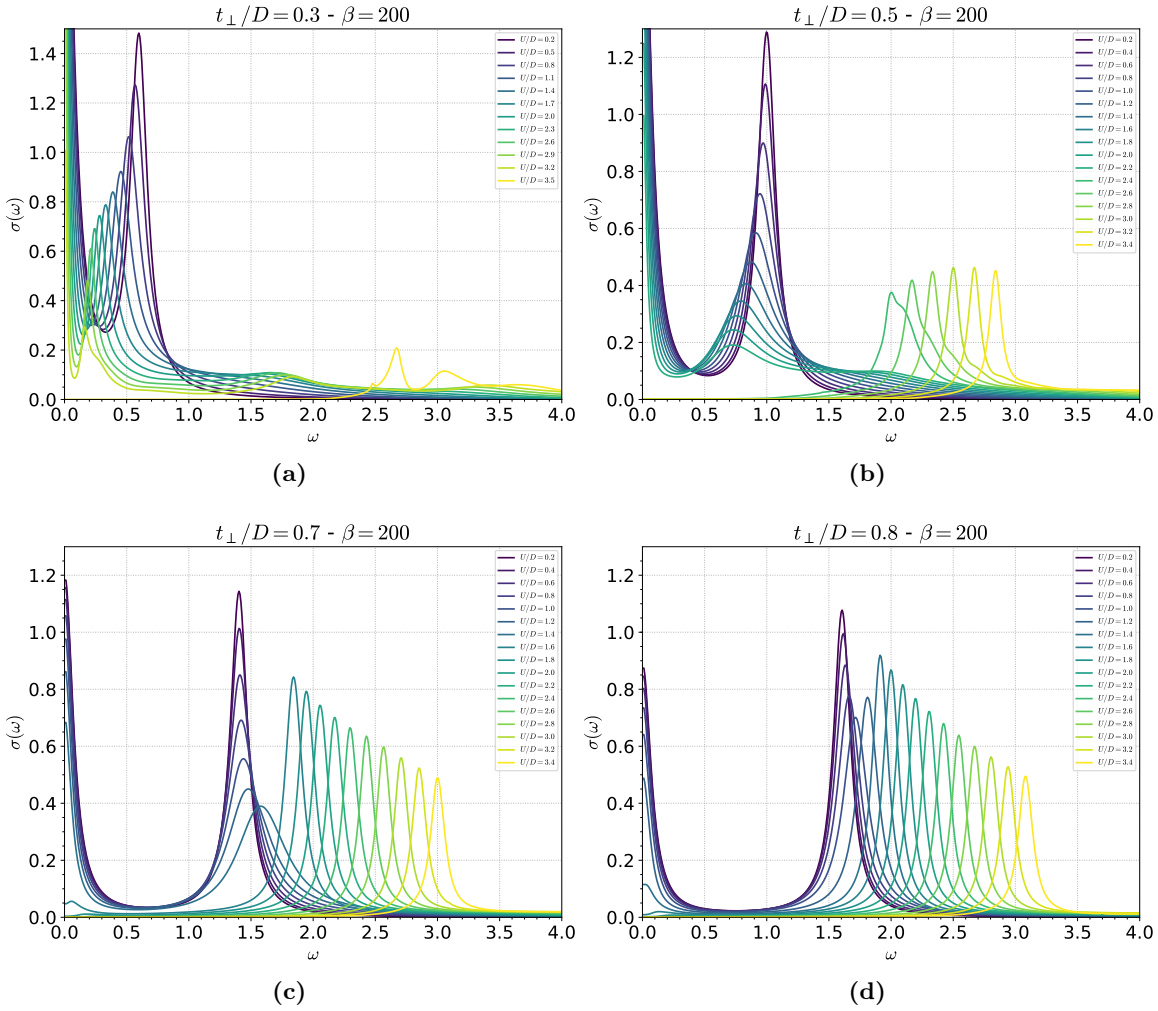

Figure 3.13: a) Metal Mott-insulator transition of the weakly dimerized system. Correlations reduce the bandwidth of the non-interacting bands and brings them closer to the Fermi Energy. The Insulator at $U_{c_2}^+$ is completely disconected. b) MIT when dimerization has the same strength as the renormalized lattice hopping. The non-interacting band structure also gets reduced and the insulator is disconected from the metal. c) Transition at the tri-critical end point. Composing bands do not appear to get closer together as interaction is increased. Insulator is closely connected to metal before the transition. d) MIT after the tri-critical end point. Metal and insulator have a connected response, transition is the lost of overlap of composing bands.

$t_\perp/D$, it becomes broader. This is because the electronic structure bands, including the quasi-particle ones, are more incoherent. Lastly, there is still an incoherent feature appearing at energies of order U as before. In the insulating state the main response is given by an optical gap originated in the excitations between the inner coherent edges of the Hubbard bands and also between the transitions of the incoherent parts at higher frequencies.

The inferior panels of figure 3.13 at higher $t_\perp$ do not entirely follow the same trend. At $t_\perp/D = 0.7$ one goes approximately across the tri-critical end point where the U_{c_1}, U_{c_2} and U_{c_3} lines meet. In this case there is little transfer of spectral weight and mass enhancement evidenced by the small change of the Drude response. The inter-band transition do not experience a notable drift to lower energies, however, there is a smearing of this response due to the increased incoherent character of the Hubbard bands. Finally, in the insulator, the response is of course gapped, but otherwise relatively close to the high frequency part described for the metal case.

3.2 Mott-Peierls insulator-insulator crossover

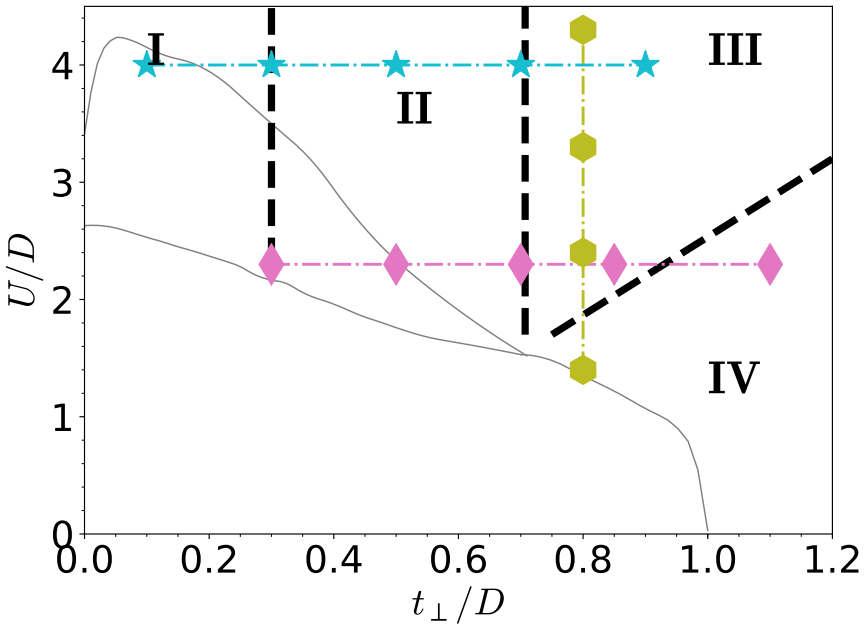

Figure 3.14: The phase diagram of the model with the various crossover regimes **I-IV** that are described in the text. The black dashed lines separating the different zones are for reference only, since the evolution is continuous. The colored dash-dotted lines denote the various paths and points across the diagram whose evolution we describe in the text. For reference, we draw in gray lines the U_{c1}, U_{c2} and U_{c3} transitions (cf Fig. 3.1)

We now turn to one of the central parts of our study, namely, the discussion of the multiple insulator crossover regimes in the DHM. We shall characterize in this section the rich physics and subtle behavior changes that the DHM exhibits as it crosses-over from pure Mott to

pure Peierls. We may define the former with respect to the prototypical Mott insulator that is realized in the one band Hubbard model. As we already mentioned before the DHM in the $t_\perp = 0$ limit becomes two independent copies of the single-band Hubbard model. In such case, at large U, the electrons become localized because of the strong on-site Coulomb repulsion. This creates "free local moments" at every site, and the electronic structure is, accordingly, that of *incoherent Hubbard bands* split by a large energy scale $\sim U$ Georges et al. [1996]. The other extreme case, the pure "Peierls" insulator, may be identified in the DHM with the $U = 0$ and $t_\perp \geq D$ limit. There, the anti-bonding / bonding (A/B) bands have a $2t_\perp$ separation, which is larger that the bandwidth $2D$. Hence, a gap in the DOS spectra opens by virtue of the momentum-independent strong dimerization hopping amplitude. This is a pure "band-structure" effect as the interaction U is set to zero. In this insulator state, the bonding and anti-bonding bands are separated and the former is fully filled with two electrons per dimer site. The system is a "band-insulator", which is non-magnetic and its electronic structure shows two parallel *coherent Bloch bands*. We shall explore in this section how the system transmutes from one regime to the other.

In Fig. 3.14 we show the various regimes that the systems exhibits as it crosses-over from the Mott to the Peierls limit. There are four different zones, which can be well characterized. The understanding of Zone I will be discussed later in section 3.3.1. Its important feature is an interesting *thermal* crossover where spin degrees of freedom are active. These magnetic moments are due to the Coulomb interaction and emerge as the result of Mott localization above the U_{c1} line at low $t_\perp$. Zone IV is characterized by the insulating Peierls state. As we shall see, we can think of that state as "orbitally polarized" in the A/B basis, with correlations playing a relatively minor role. The Zones II and III have a mix character and the evolution of the electronic structure is quite subtle. We have therefore explored the evolution of the system across the different zones by following the color lines that are indicated in Fig. 3.14. We consider two parallel lines at fixed values of U and varying $t_\perp$. The relatively smaller U line tracks the systematic evolution from within the Mott coexistence region towards the Peierls one. At a larger value of U we shall argue that we remain within a Mott state even for relatively large values of $t_\perp$. The main feature is an interesting evolution of the electronic structure, going from incoherent Hubbard bands (Zone I) to coherent ones (Zone III) and passing through a *mixed* state with the coexistence of coherent and incoherent contributions (Zone II). We shall describe these in detail in the following subsections.

3.2.1 Zone IV-III and IV-I crossovers: building correlations on the Peierls state

We will discuss how from the Peierls non-magnetic state (large $t_\perp$ and $U = 0$) the magnetic moments gradually emerge as the correlations are increased. To illustrate that, we plot in Fig. 3.15 the evolution of the bonding orbital DOS, i.e. the $A_{BB}(\omega)$ spectral function for

increasing U along with its corresponding self-energy $\Sigma_{BB}(\omega)$. At weak correlations, for $t_\perp = 0.8$ and $U = 1.4$, the system is still within the Peierls insulating state in Zone IV. We observe that the R2B model parametrization (red dashed line corresponds to eq.3.3) provides a rather good description. The occupation of the bonding band is almost complete, so we may consider this state as fully orbitally polarized in the A/B basis. Accordingly, the self-energy remains smooth and small.

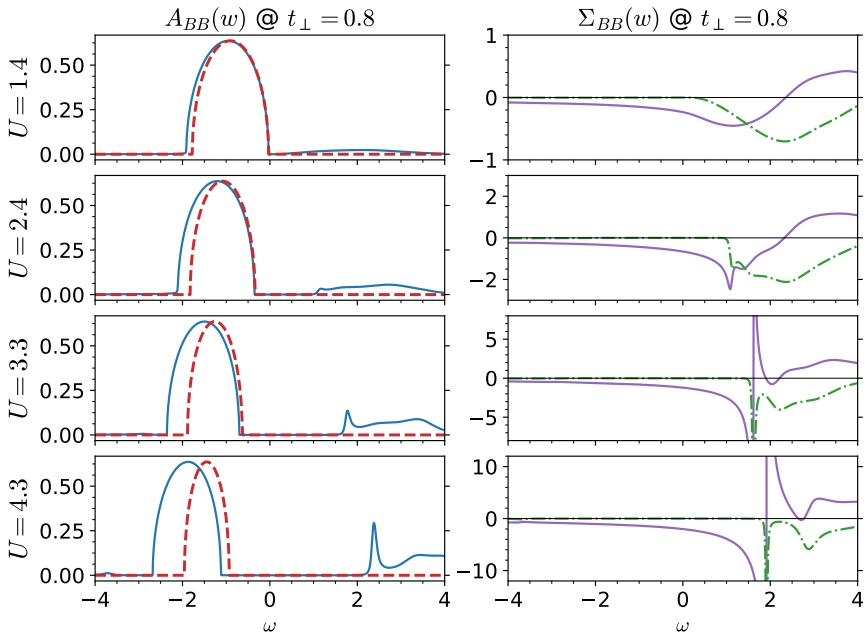

Figure 3.15: Evolution of the bonding DOS(ω) and corresponding change in the bonding self-energy at fixed $t_\perp = 0.8$ for increasing U, yellow line with hexagon marker in Fig.3.14. The location of this crossover path is indicated by one of the black dash-dotted lines in Fig. 3.14. Red dashed lines correspond to the R2B model parametrization.

By increasing U the system crosses-over from Zone IV to III and we observe qualitative changes in both, the DOS and Σ. For $U = 2.4$ we already see an incipient structured spectral weight developing at $\omega \approx 1$ in the lower band edge of the upper Hubbard band. Accordingly, the self-energy begins to develop a rapidly varying wiggle at the same frequency. These incipient structures become apparent at a higher interaction strength $U = 3.3$. We clearly observe the emergence of a quasiparticle-like resonance in the DOS, with a concomitant pole in the self-energy. This signals the emergence of a well-defined excitation and the narrowness of the peak indicates that is essentially a localized state. This excitation is in fact due to local moments building up at each of the dimer sites Nájera et al. [2017]. Here the moments are strongly coupled by the large $t_\perp$. Therefore, they remain Mott-localized *within* the dimer and establish a local coherent (singlet) state. Further increasing the interaction U the resonance gains spectral weight and the strength of the pole in the self-energy also grows. The "Mottness" character of the state increases as we see that the simple renormalized two band parametrization fully breaks down. Notice, however, that in contrast to the pure Mott

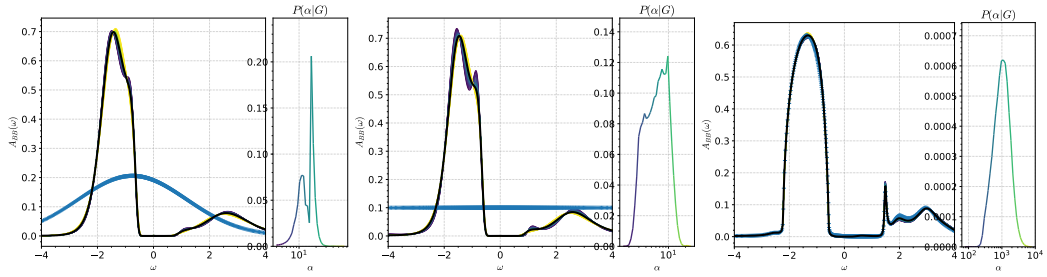

(a) (b) (c)

Figure 3.16: Most probable analytically continuated QMC spectral function at $U = 3$ - $t_\perp = 0.75$ in thick black lines, other color lines are possible fits and their prior probability is shown in the narrow panels. At this high values of U and $t_\perp$ the statistical sampling is of low quality as the system is very close to the isolated dimer limit. In this case the IPT solution looks identical to the one obtained from the QMC solution within the statistical error. Extra care is taken during the continuation in this case, and we present the results obtained by using different default models. (a) Uses a Gaussian default model, (b) uses a uniform model, (c) uses the IPT solution as default model, marked in thick blue lines.

insulator with incoherent Hubbard bands, here the lower Hubbard band in $A_{BB}(\omega)$ remains fully coherent as in the Peierls insulator case, Tomczak et al. [2008]. This is evident from the imaginary part of the self-energy (bottom right panel of Fig. 3.15), which is negligible on the full $\omega < 0$ frequency range. We thus begin to observe the coexistence of incoherent and coherent features in the electronic structure, which are respectively connected to Mott and Peierls physics.

In Fig.3.16 we show the DOS of a high U and high $t_\perp$ insulator. The Monte Carlo sampling at this point is not appropriate for a reliable analytical continuation and in this case the system approaches the isolated dimer limit. In the Matsubara axis the solution from QMC and IPT match, the analytical continuation to the real axis recovers some features, like showing the uncorrelated band at $\omega < 0$, and it hints to the development of the resonance at the inner band edge at $\omega > 0$.

We now turn to the crossover behavior from zone IV to zone I (cf Fig. 3.14). The systematic behavior is shown for $A_{BB}(\omega)$ and $\Sigma_{BB}(\omega)$ in Fig. 3.17. We observe that all the features that we described before in the zone IV to III crossover as a function of U are also present here as a function of the model parameter $t_\perp$. The system evolves from the Peierls insulator in zone IV along a path towards the Mott state in zone I. Similarly as before, we observe the emergence of a narrow resonance in the $\omega > 0$ part of the spectra. However, a difference with the previous crossover is that the evolution now ends close to the pure Mott state and we see that the $\Sigma_{BB}(\omega)$ is non negligible at $\omega < 0$. One may notice that the second crossover path traverses the zone II. The clear characterization of that regime requires the discussion of the spectral function $A(\epsilon, \omega)$, which we shall consider in the next subsection. Nevertheless,

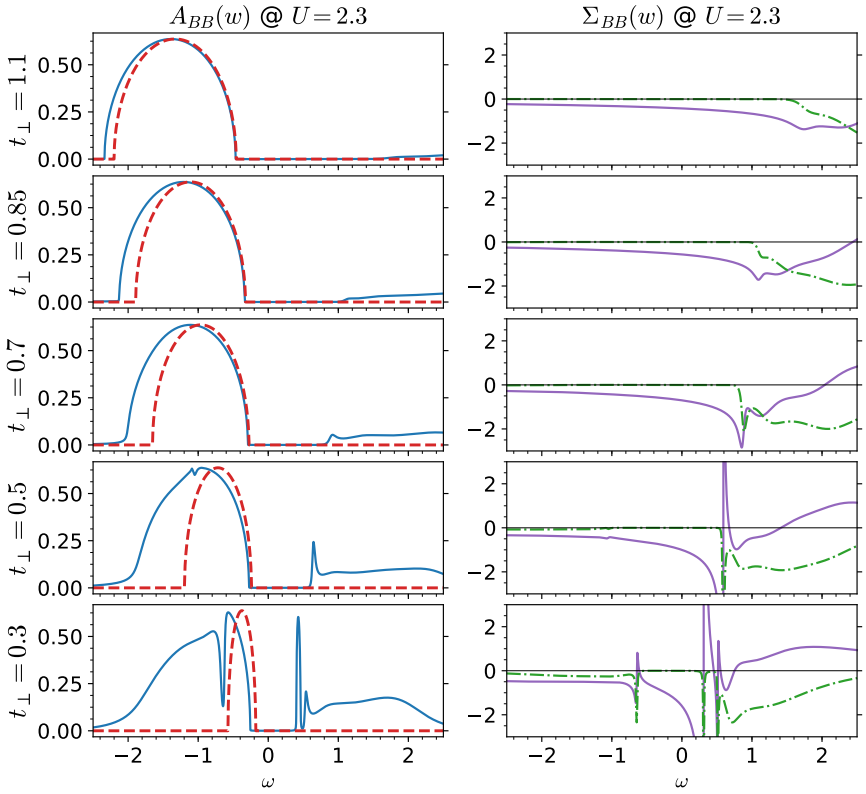

Figure 3.17: Evolution of the bonding DOS(ω) and corresponding change in the bonding self-energy at fixed $U = 2.3$ for decreasing $t_\perp$, pink line with diamond marker in Fig.3.14. The location of this crossover path is indicated by one of the black dash-dotted lines in Fig. 3.14. Red dashed lines correspond to the R2B model parametrization.

we want to emphasize that these IPT results are validated by QMC (cf. in later sections in Fig.3.32 lower panel)

We now consider a strongly correlated regime set by a relatively large value of the interaction $U = 4$. We shall discuss the systematic changes of the insulator state as it evolves as a function of increasing intra-dimer hopping $t_\perp$. As we did before, we begin considering the bonding DOS $A_{BB}(\omega)$ and the corresponding self-energy $\Sigma_{BB}(\omega)$, which unveils details of its mathematical structure. The data is shown in Fig. 3.18. We recall that the same quantities on the anti-bonding band are obtained by reflection around $\omega = 0$, and that the total DOS corresponds to the average of them. The main feature is that there is always a large gap with two main contributions at $\omega \sim \pm U/2$. Thus for all $t_\perp$ we have a large insulating gap controlled by U, which is an indication of Mott physics having a dominant role. We also see, consistent with that observation and previous discussion, that the unoccupied part of $A_{BB}(\omega)$ always has a sharp resonance that we associated to emergent magnetic moments. Moreover, in $\Sigma_{BB}(\omega)$ we always observe the presence of a strong pole. Interestingly we see that the position of the pole is almost at the center of the gap at lower $t_\perp$. In fact, it must reach $\omega = 0$ in the limit of $t_\perp \to 0$ as the system becomes two independent copies of a single-band Mott insulator Georges et al. [1996]. Thus, this strong pole is a hallmark of the opening of a Mott gap. As we increase $t_\perp$ we see that the pole remains strong but evolves towards the upper edge of the gap. This has the effect of strongly affecting the $\omega > 0$ part of the spectrum while we observe that the $\omega < 0$ in contrast evolves towards the semi-circular density of states. This apparent weakening of correlations in the lower Hubbard band can be also understood by the fact that this band is further filled up, hence effectively moving away from the half-filled situation. However, it would be a mistake to simply consider this a weakly correlated state since, as we already emphasized, the gap is large and set by the Coulomb interaction U. In fact, we observe that the R2B model parametrization (red dashes line in the Fig. 3.18) is inappropriate in all cases, as we are not dealing with Fermi Liquids in the insulator.

Another interesting feature revealed by the $\Sigma_{BB}(\omega)$ is that the imaginary part, which is related to the inverse life-time is always relatively large on the $\omega > 0$ side of the spectra while is much smaller, or even negligible for larger $t_\perp$ on the $\omega < 0$ side. This indicates that the positive frequency excitations have incoherent character (save for the sharp resonance state that we discussed earlier) while the negative frequency ones are coherent.

3.2.2 The evolution of the dimer Mott insulator: coexistent incoherent and coherent contributions in the electronic structure

One additional interesting feature that we would like to point out is the complex evolution of the line shape of $A_{BB}(\omega)$ at small $t_\perp$, where $\Im\Sigma_{BB}$ is still non-negligible. This regime corresponds to the crossover zone II (cf. Fig. 3.14). In order to gain further insight into

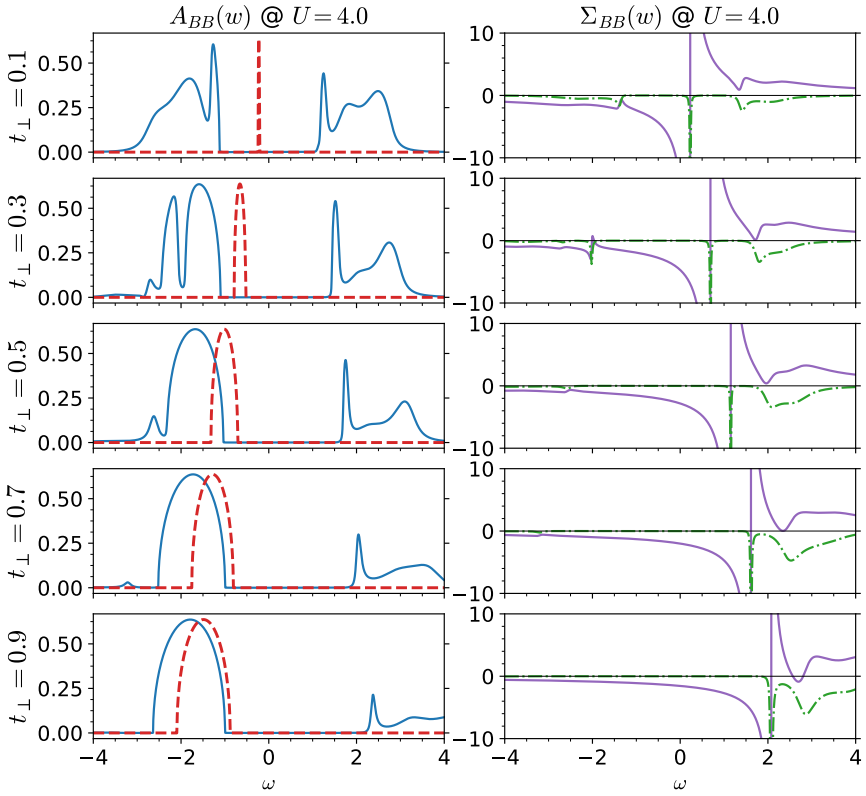

Figure 3.18: Evolution of the bonding DOS(ω) and corresponding change in the bonding self-energy at fixed $U = 4$ for increasing $t_\perp$, cyan line with star marker in Fig.3.14. The location of this crossover path is indicated by one of the black dash-dotted lines in Fig. 3.14. Red dashed lines correspond to the R2B model parametrization, which is always poor in this case.

these issues we shall consider the energy resolved spectral function $A(\epsilon, \omega)$ along with the local DOS, $A(\omega) = \int d\epsilon A(\epsilon, \omega)$.

For the sake of clarity we consider, both, the total (i.e. site basis) and bonding orbital spectral functions. Their evolution is shown, respectively, in Figs. 3.19 and 3.20. As we increase the $t_\perp$ in Figs. 3.19 and 3.20 we observe the systematic evolution of the electronic structure. It always shows two roughly parallel lower and upper Hubbard bands split by U. These bands gain in coherence as $t_\perp$ is increased. At the end state, i.e., higher $t_\perp$, two well-defined and coherent contributions dominate the electronic structure. As can be seen in the last panel of Fig. 3.20 the main contribution comes from the bonding band for the lower Hubbard band, and correspondingly from the anti-bonding for the upper Hubbard one. However, some incoherent weak intensity and weakly dispersive states can still be observed. This state resembles the Hubbard I solution, with 2 coherent bands, that are split by U. This can be rationalized noting that in the A/B basis the system is strongly orbitally polarized.

More interesting are the states at lower values of $t_\perp$. As displayed in the first two panels we observe that the Hubbard bands develop a unique characteristic, which is their mixed character. In fact, we observe sharper and more coherent quasiparticle-like contributions to the electronic structure in the inner edges of the Hubbard bands, which upon integration lead to a peculiar line-shape for the local DOS(ω). The outer part of the Hubbard bands, in contrast, is strongly incoherent. The physical interpretation of the quasiparticle states stems from the intra-dimer magnetic coupling of the emergent moments. Within the dimer they develop a coherent singlet state, which is continuously connected to the non-interacting bonding/anti-bonding states of the Peierls insulator. Electronic correlations enhance the local character with a large effective heavy mass. The propagation of the remaining states through the lattice remains very incoherent, as signaled by the diffuse spectral intensity which is broad on a scale of $\sim D$. This insulating state with a mixed character in the dispersion of the Hubbard bands is an original feature of the DHM and absent in the single band model case. It is important to mention here that these results obtained by IPT have been validated also by QMC. An example of coexistent coherent and incoherent character of Hubbard bands can be seen in the data of Fig.3.12.

3.3 Finite Temperature effects: 1^{st} order transition and crossovers

3.3.1 Zone I: the singlet to free-moment crossover in the Mott state

This regime at $U > U_{c1}$ and small $t_\perp$ is crucial to understand the physical behavior of the Dimer Hubbard model. The large value of the on-site Coulomb repulsion U creates a local magnetic moment at each site of the dimer. Then, the interaction between these moments undergoes a *thermal crossover* from a singlet ground state at $T \to 0$ to a free-moment regime above a low temperature scale T^*. This temperature is a low energy scale of the model,

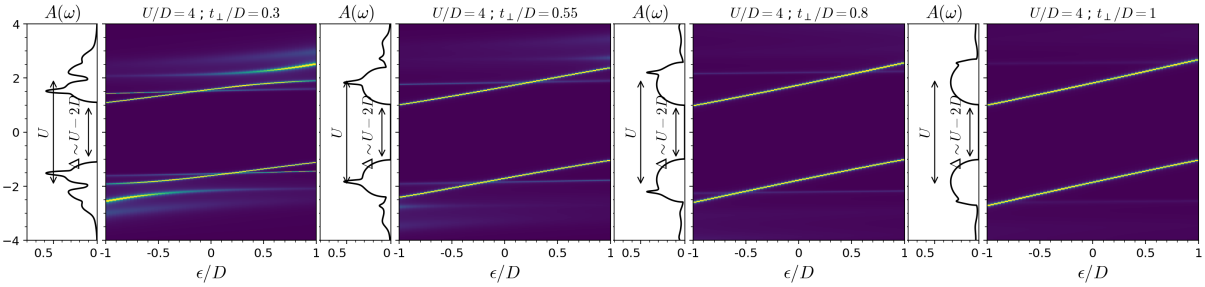

Figure 3.19: Local density of states $A(\omega)$ (vertical panels) and intensity plots of the spectral function $A(\epsilon, \omega)$ of the Mott insulating state at large $U = 4$ and increasing $t_\perp$.

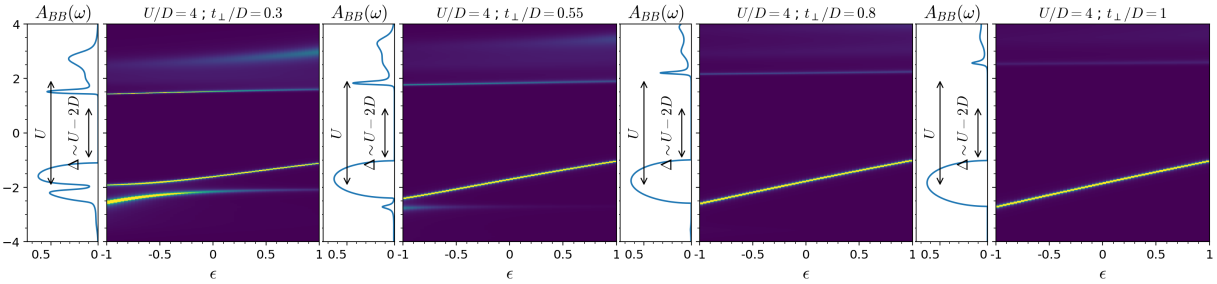

Figure 3.20: Bonding density of states $A_{BB}(\omega)$ (vertical panels) and intensity plots of the bonding spectral function $A_{BB}(\epsilon, \omega)$ of the Mott insulating state at large $U = 4$ and increasing $t_\perp$.

which indicates the singlet pair formation and is two orders of magnitude smaller than the bare parameters. In the Fig. 3.21 we show the behavior of the total magnetic moment formation $\langle (N_\uparrow - N_\downarrow)^2 \rangle = \langle [(n_{1\uparrow} + n_{2\uparrow}) - (n_{1\downarrow} + n_{2\downarrow})]^2 \rangle$ as a function of $t_\perp$ at different fixed temperatures. At any given temperature, we observe that the moment formation goes from a very small value at large $t_\perp$ to suddenly display a dramatic increase upon lowering that parameter. The reason is that the magnetic coupling between the local moments at the two sites of the dimer is large at bigger $t_\perp$ so they lock into a singlet state which is non-magnetic. When, this magnetic interaction is reduced at lower $t_\perp$ the magnetic binding energy ($\propto t_\perp^2/D^2$) falls below the thermal energy and the singlet state breaks down. The two local moments unbind and behave as local free spins analogous to the Mott insulator state of the single band Hubbard model.

This behavior can also be clearly seen by its dramatic effect on the electronic structure. In Fig. 3.22 we show in a color intensity plot the *bonding* spectral function dispersion $A_{BB}(\epsilon, \omega)$ for the system at a fixed T and two values of $t_\perp$. One larger $t_\perp = 0.3$ with the two moments locked into the singlet and a smaller one $t_\perp = 0.1$ with two unbound free-moments, which shows the very low $t_\perp$ regime (zone I) where the system is deep in the Mott phase with decoupled magnetic moments (at finite $T > T^*$). At larger $t_\perp$ the spectral function follows the behavior already shown in Fig. 3.20, as the magnetic fluctuations are quenched.

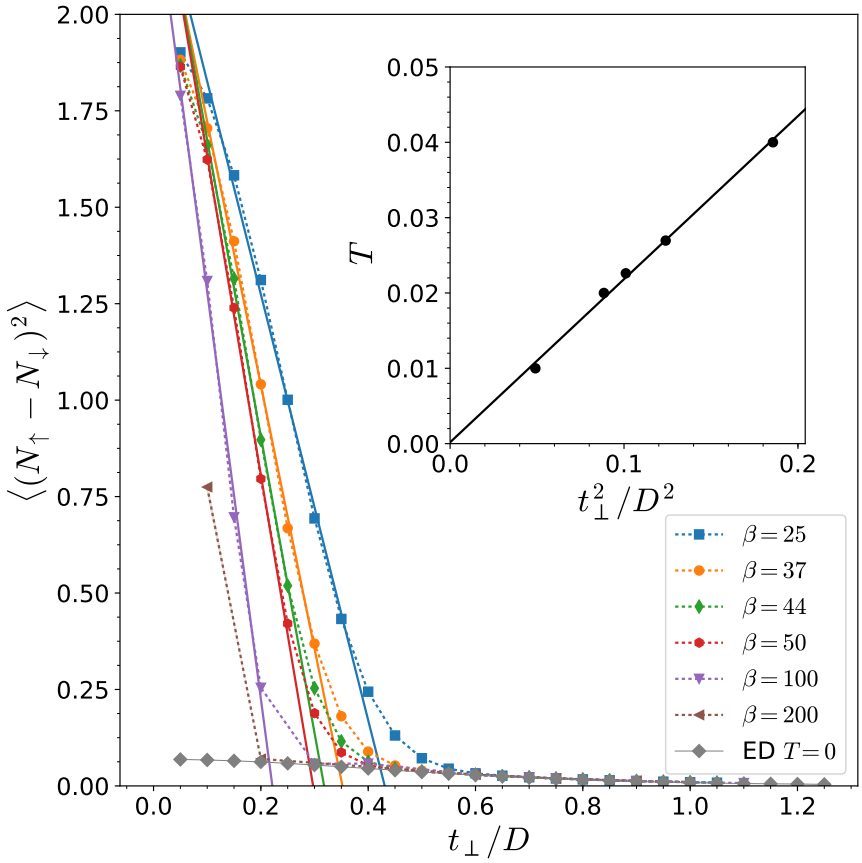

Figure 3.21: Total magnetic moment formation as a function of $t_\perp$ at different temperatures. Finite temperature calculation done with CTHYB, and zero temperature with ED. Inset: Temperature crossover scale for singlet pairing of the two site moments T^*. This scale is proportional to the square of $t_\perp$ consistent with its magnetic origin.

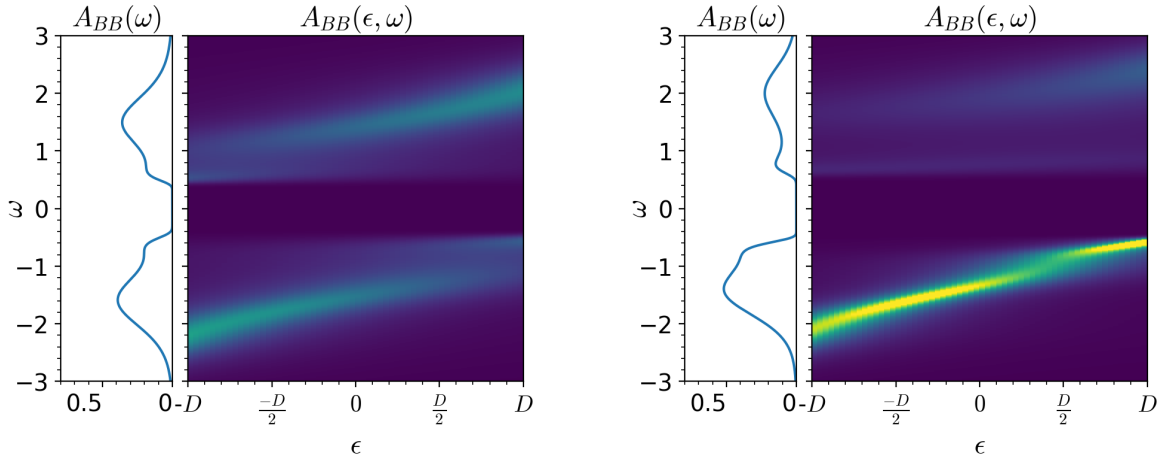

(a) $\beta = 50$ - $U = 3$ - $t_\perp = 0.1$ **(b)** $\beta = 50$ - $U = 3$ - $t_\perp = 0.3$

Figure 3.22: Intensity plot of the *bonding* spectral function $A_{BB}(\epsilon, \omega)$ at U=3 and $t_\perp$=0.1 and 0.3 calculated at T=0.02, using CTHYB. In side panels we show the corresponding DOS(ω), i.e. the integrated *bonding* spectral function. We recall that in the Bethe lattice the single particle *energy* plays an analogous role as the lattice momentum k. The non-interacting dispersion is $\epsilon - t_\perp$, with $-D < \epsilon < D$.

The change in the spectral function is very significant and consistent with the magnetic state. To display the effect more explicitly we focus on the bonding spectral function. We recall that the anti-bonding is obtained by reflection around $\omega = 0$, and the site-basis one is the average of the two. At the higher value of $t_\perp$ the spectra is not symmetric, we see that the low energy band has most of the spectral weight. This signals, consistently with the magnetic state, that the system is locked in the singlet bound state, which is almost fully occupied. In contrast, at lower $t_\perp$ the state is not magnetically bound and correspondingly we obtain a symmetric spectrum. The anti-bonding state is virtually identical to the bonding one, so both have a similar occupation, which indicates that the magnetic states are decoupled and free to fluctuate as in the Mott insulator in the single band case. In fact, the spectral function of the low $t_\perp$ case that is above T^* is very similar to the incoherent Hubbard bands of the single band Mott-Hubbard insulator Georges et al. [1996], which is nothing but the $t_\perp = 0$ one. This physical insight is a key reference to guide the discussion of how dimerization fundamentally changes the ground state of the system.

3.3.2 $U - T$ phase diagram and its dependence on $t_\perp$

In this subsection we shall discuss the thermal phase diagram of the model. Specifically we shall consider its evolution as a function of $t_\perp$. We shall focus on the evolution of the shape of the coexistence region, since it is related to the the thermally driven 1^{st} order insulator to metal transition.

For reference we may recall the situation in the single band Hubbard model, which corresponds to the $t_\perp = 0$ limit of the present one. In that case, the coexistence region in the $U - T$ plane had a triangular shape with the segment U_{c_1} to U_{c_2} at the base, and a critical endpoint T_{MIT} at finite temperature. In that model, the ground-state is metallic, therefore, upon warming there is a 1^{st} order metal to insulator transition. We shall see that here this situation remains qualitatively similar for very small values of $t_\perp$, however it dramatically changes upon increasing this "dimerization" parameter. We shall see that the triangular shape changes its tilt as the insulator takes over as the ground-state and we find an insulator to metal transition upon warming. The increased stability of the insulator is due to the energy gain of the dimer magnetic moments that can lock into a singlet, a phenomenon that is absent in the single site Hubbard model. Interestingly, this transition is qualitatively similar to that observed in actual compounds such as VO_2. We shall consider a more detail comparison later in chapter 4.

Fig. 3.24 shows the single-site double occupation of the system at $t_\perp/D = 0.1$ within the coexistence region. This observable computes the double occupation at a given site of the dimer, which is also related to the so called "moment formation" $\langle(n_\uparrow - n_\downarrow)^2\rangle = 1 - 2\langle n_\uparrow n_\downarrow\rangle$. Thus it indicates how much of a local magnetic moment is created on a given lattice site by the correlations. This observable is relatively easy to compute and can be used as a reliable way to differentiate between a metal and an Mott insulator state Georges et al. [1996]. It is relatively high in the former and smaller in the latter. In the figure, one clearly sees the two regimes and the overlap of values within the coexistence region. In the weakly dimerized case the Mott insulator has a weak dependence in temperature for the on-site double occupation. It only depends on the interaction U, like in the single site DMFT solution. Here the electrons become localized on each lattice site. On the other hand, the metal solution increases its on-site double occupation as the temperature is lowered Kotliar et al. [2000]. Besides the on-site moment formation, in the present dimerized model case it is also useful to look at the total magnetic moment formation of the dimer $\langle(N_\uparrow - N_\downarrow)^2\rangle$, already introduced in previous section 3.3.1, because it provides insight into the magnetic state within the dimer. We recall that if this quantity is large the moments within the dimer are rather decorrelated, while if it is low they are locked into a singlet.

The effect of Coulomb correlations is to suppress the double occupation on a lattice site and induce local magnetic moments. However, the way these moment organize into a quantum state is different in each phase. In the metal each moment is independently Kondo-screened by the environment and thus the spins on each site of the dimer are almost uncorrelated. Their screening happens with the bath. On the insulator at high temperatures the singlets unlock as was explained before. Thus the state is conformed of free spin that keep a large magnetic moment but remain uncorrelated. At low temperatures these free magnetic moments can quench their entropy by locking into a singlet and decrease their magnetic fluctuation. A pictorial representation of this is illustrated in Fig.3.23.

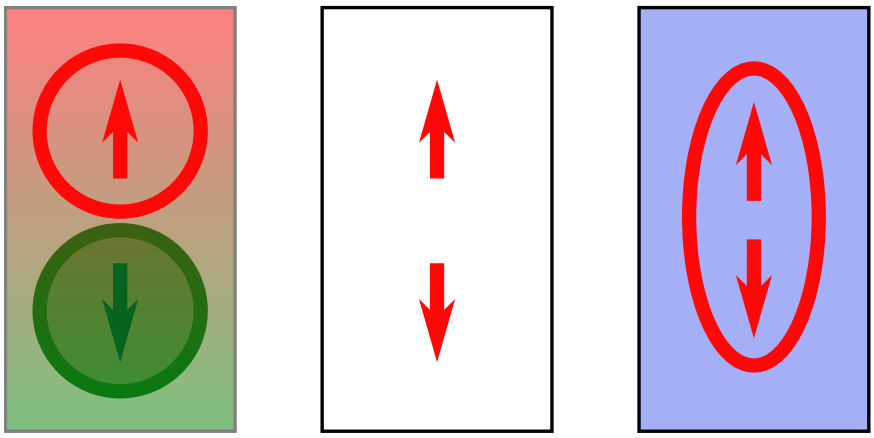

Figure 3.23: Pictorial representation of the competing electronic phases. On the left the metallic phase where each impurity is Kondo screened by the environment. Center has the free electronic moments in the high temperature Mott insulator. Right is the low temperature dimer Mott insulating phase where localized electronic moments bind into a singlet.

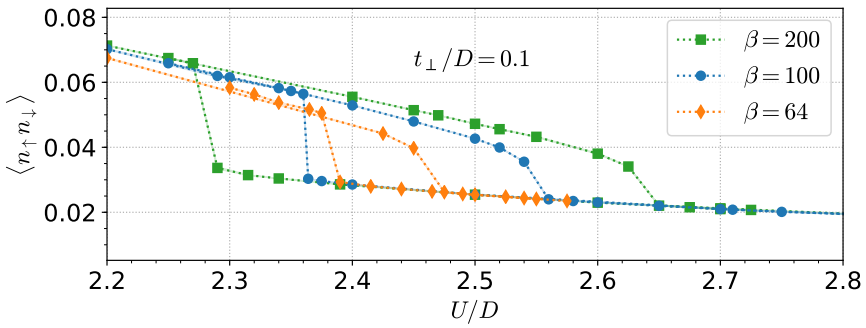

Figure 3.24: QMC Double occupation of the dimer system upon lowering temperature for the $t_\perp/D = 0.1$ case. The coexistence region is evidenced by the existence of two well defined different solutions and it grows to both sides as temperature is lowered.

We used the computed double occupation data from QMC (cf. Fig. 3.24) at different temperatures to construct a phase diagram for the dimer case at low $t_\perp/D = 0.1$. It is shown in Fig. 3.25. We see that the coexistence region is a triangle tilted to left like in the single site DMFT solution but at very low temperature the coexistence region seems to extend to lower values of U. This far edge for U_{c_1} has been hinted for the single band Hubbard model from results from Exact Diagonalization Joo and Oudovenko [2001] and random dispersion approximation Noack and Gebhard [1999], but it is not achievable from high temperature calculations on QMC or from IPT estimates for the single band model. The dimer model for this value of dimerization $t_\perp = 0.1$ directly demonstrates this change in the stability of the coexistence region at low temperatures.

The total magnetic moment formation $\langle (N_\uparrow - N_\downarrow)^2 \rangle$ in Fig. 3.26 shows how the free electronic moments that are now localized on each site contribute to the magnetic response of the system. As the system is cooled down, the insulating phase drastically quenches its magnetic fluctuations. The Mott localized electrons can quench the entropy of its two free magnetic moments by forming a singlet state within the dimer. These correlation-localized electrons couple with their respective neighboring electron within the dimer to form a singlet.

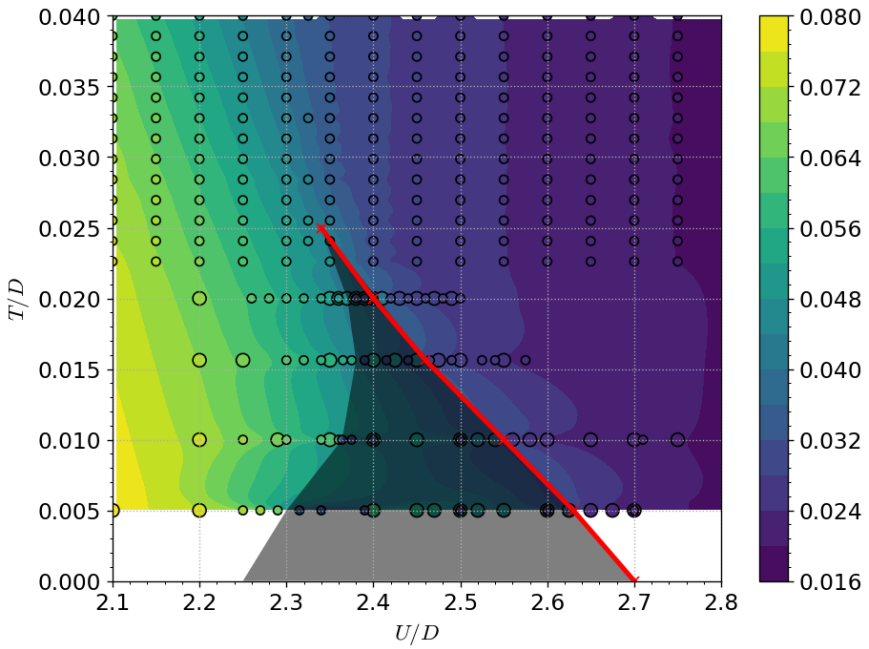

Figure 3.25: $t_\perp/D = 0.1$ QMC phase diagram, colored circles are calculated points for on-site double occupation. Colormap is for visual aid only, coexistence region neighboring points of distinct phases distorts the interpolation algorithm. Shaded region is coexistence region and red line marks equal internal energy. $U_{c_1}(T = 0) \approx 2.25$ and $U_{c_2}(T = 0) \approx 2.7$.

As one increases dimerization to $t_\perp/D = 0.3$ the coexistence region changes its tilt with from a triangle leaning to the left (cf. Fig. 3.24) to one towards the right as shown in Fig. 3.27. This diagram is constructed with data from Fig. 3.28 and 3.29, which also provide insight into the physical states. Here the finite $t_\perp$ permits a large energy gain in the Mott insulator by

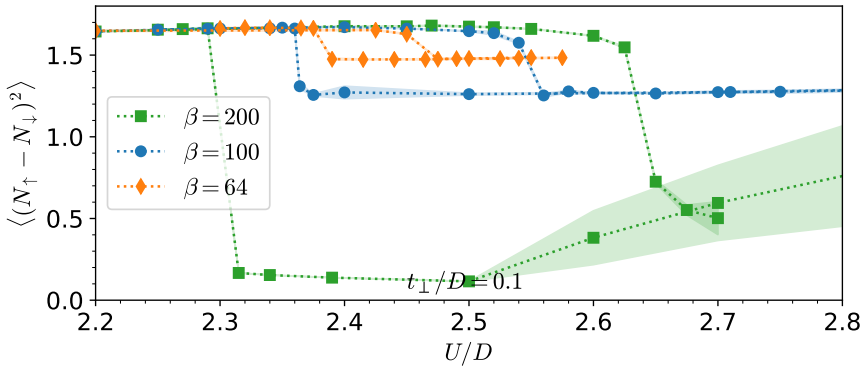

Figure 3.26: QMC Total magnetic moment formation of the dimer system upon lowering temperature for the $t_\perp/D = 0.1$ case in the coexistence region. At low temperatures and large values of U the QMC sampling promotes anti-ferromagnetism. When averaging for the paramagnetic solution noticeable uncertainty is measured in this region.

quenching the degenerate entropy. This mechanism, already observed in other cluster-DMFT models Parcollet et al. [2004], Park et al. [2008], Balzer et al. [2009] stabilizes the insulator within the coexistence region, leading to the change in the tilt. This also implies that upon *warming* an insulator undergoes a 1$^{\text{st}}$ order transition to a (bad) correlated metal at finite-T. IPT calculations also show the exact same behavior inverting the stability of the coexistence region. It appears from IPT and QMC calculations that the temperature at which this end point occurs, is rather independent of the strength of dimerization $t_\perp$.

The difference between metallic and insulating on-site double occupation for more dimerized lattices does not seem to experience a large dependence with temperature as is shown in Fig. 3.28. This is clear in comparison to the lower $t_\perp$ case of Fig. 3.24 where the metal gains in double occupation as temperatures are lowered. One could be tricked to think the on-site double occupations is considerably higher almost by a factor of 2 for the larger dimerization strength, because the numerical values within the coexistence are much higher. Nevertheless in a fair comparison for a common value of interaction as $U \approx 2.2$ the on-site double occupation for the metallic phase is not too different for both values of dimerization $t_\perp = 0.1$ and 0.3. This is to highlight that not only has the coexistence region changed its shape, but that it has entirely drifted to lower values of U as well. At this point both coexistence regions for $t_\perp/D = 0.1$ and $t_\perp/D = 0.3$ do not overlap at all (cf. Fig. 3.25 and 3.27).

Increasing the dimerization $t_\perp$ continues this trend. It drifts the coexistence region to lower interaction values, but is also reduces its lateral extension. Around the tri-critical endpoint where U_{c_1}, U_{c_2} and U_{c_3} meet the coexistence region is so narrow that it becomes hard to distinguish between the phases at finite temperatures. To illustrate this point we show in Fig. 3.30 a phase diagram obtained from IPT at a $t_\perp = 0.5$.

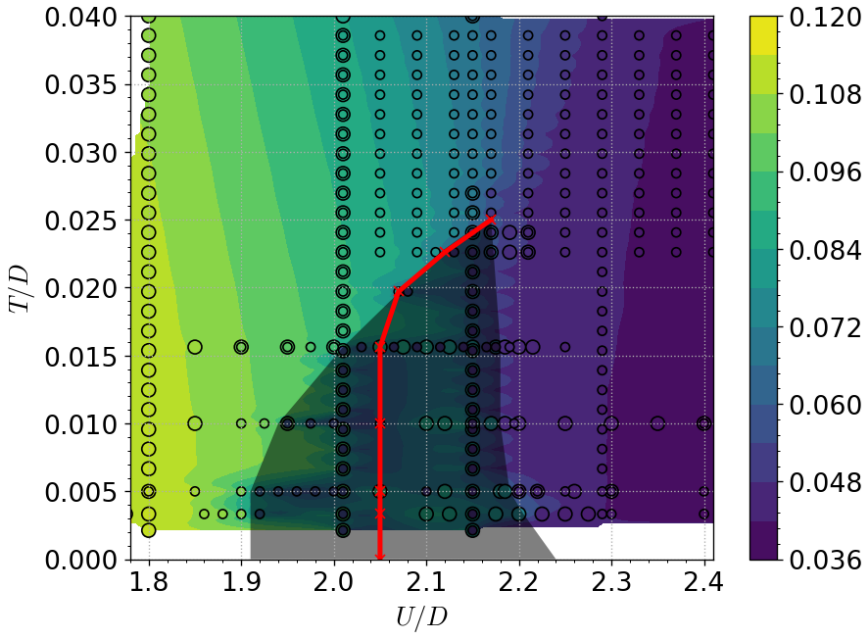

Figure 3.27: $t_\perp/D = 0.3$ QMC phase diagram, colored circles are calculated points for on-site double occupation. Colormap is for visual aid only, coexistence region neighboring points of distinct phases distorts the interpolation algorithm. Shaded region is coexistence region and red line marks equal internal energy. $U_{c_1}(T=0) \approx 1.9$ and $U_{c_2}(T=0) \approx 2.25$.

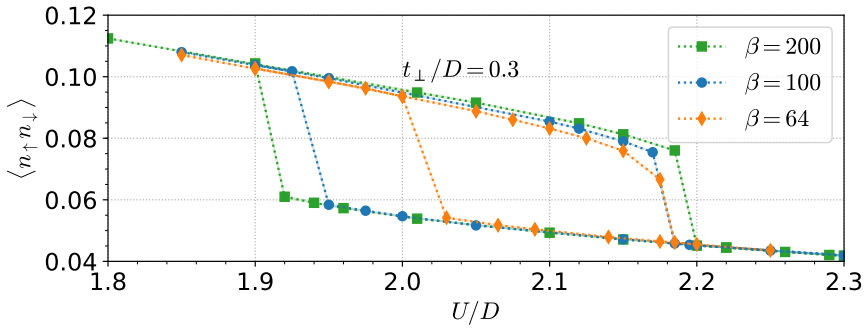

Figure 3.28: QMC Double occupation of the dimer system upon lowering temperature for the $t_\perp/D = 0.3$ case. The coexistence region is evidenced by the existence of two well defined different solutions and it grows to both sides as temperature is lowered.

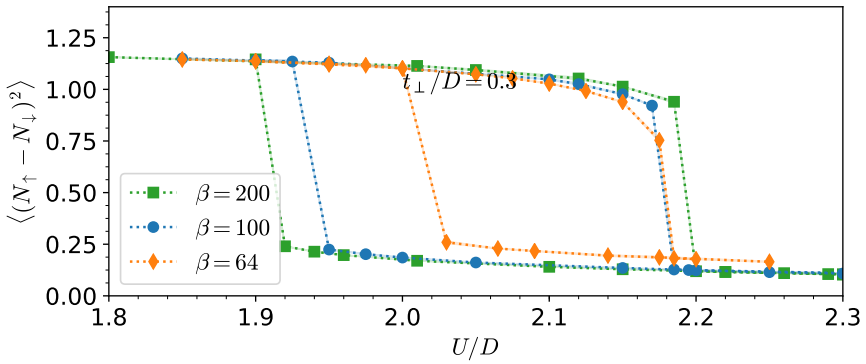

Figure 3.29: QMC Total magnetic moment formation of the dimer system upon lowering temperature for the $t_\perp/D = 0.3$ case in the coexistence region.

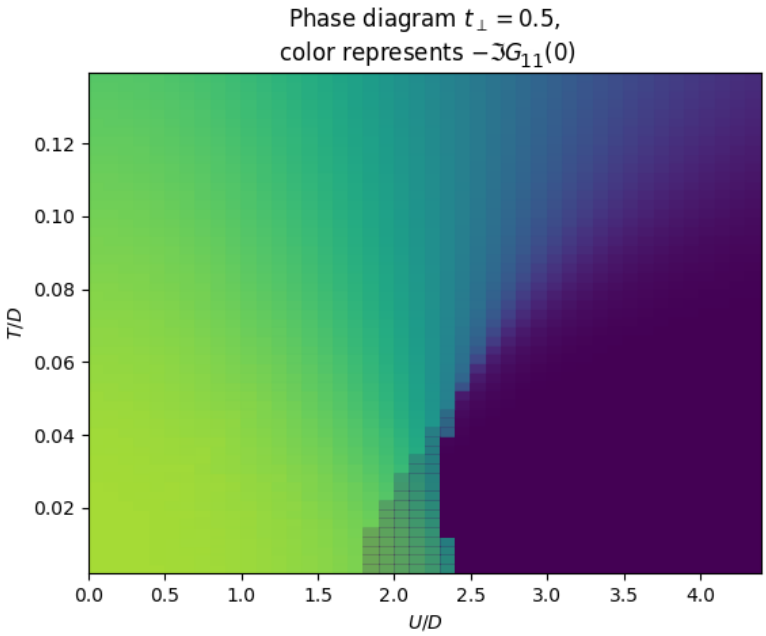

Figure 3.30: IPT phase diagram established by the spectral density at the Fermi energy. Coexistence region narrows in comparison to the $t_\perp = 0.3$ case and drifts to even lower values of U (cf. Fig.3.31).

Before leaving this subsection we would like to briefly illustrate that IPT does provide a reliable approximation for this model, which is in good agreement with QMC data. Fig.3.31 shows the direct comparison of the QMC and IPT phase diagrams in the $U-T$ plane and also in the $U-t_\perp$ plane at two different temperatures.

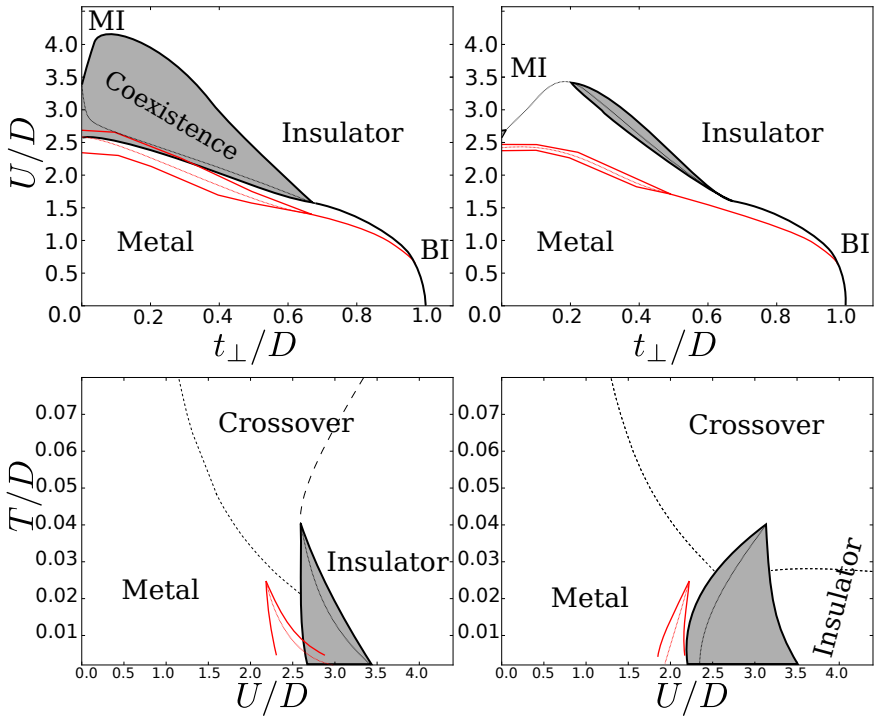

Figure 3.31: Phase diagram showing the coexistence (grayed) of metal and insulator states (black lines from IPT and red from QMC), where the approximate position of the 1$^{\text{st}}$ order lines is indicated. MI denotes Mott insulator and BI band insulator, the crossover regions have bad metal behavior. Top panels show $t_\perp - U$ plane. Left one shows lower temperatures $T = 0.001$ (IPT) and $1/200$ (CT-QMC), and right one shows higher temperature $T = 0.03$ (IPT) and $1/64$ (CT-QMC). Lower panels show the $U-T$ plane. Left one is for fixed $t_\perp = 0$ (i.e. single-band Hubbard model), and right one for $t_\perp = 0.3$. From Nájera et al. [2017]

3.3.3 Temperature driven Insulator to Metal transition: Melting of quasi-particles and filling of the gap

We shall now describe the 1^{st} order thermal transition from the perspective of the DOS and electronic structure to gain further insight.

In figure 3.32 we show the evolution of the spectral function for Bonding orbitals on the left panels and the local spectral on the right ones. The temperature is increased from bottom to top panels and the data can be correlated to the phase diagram in Fig. 3.27. We follow the insulator solution until it reaches the spinodal line $U_{c_1}(T)$ where there is a discontinuous jump of the spectra.

The main feature to notice is that the sharp features at the inner band edges are not stable

upon heating up the system. Their origin can be traced to the magnetic bonding, and as T is increased their excitations create in-gap states. As they singlet moments unbind and the system crosses the U_{c_1} line there is a dramatic reorganization of the quantum state and the system becomes a metal. There is the emergence of a Kondo-like quasiparticle peak at the Fermi energy, which is indicative that the screening of the moments of the dimer is now provided by the environment (i.e. the rest of the lattice). Actually since there are two sites, there are two quasiparticle peaks (repelled by $\sim t_\perp$) at the Fermi energy.

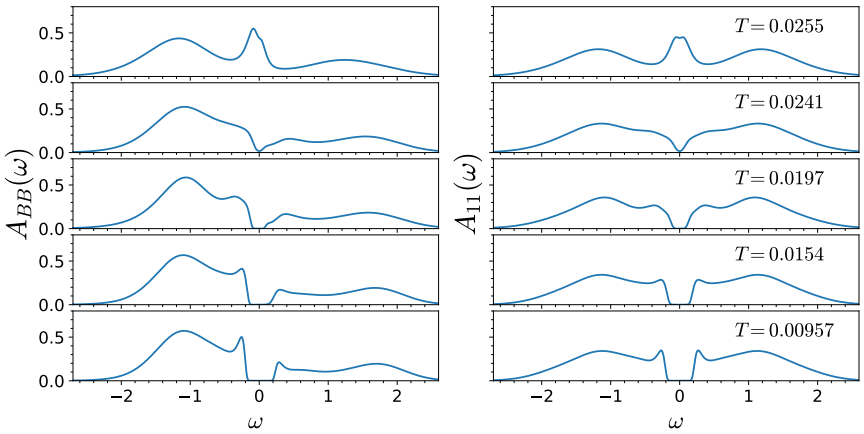

Figure 3.32: Change of the Spectral function as the temperature is increased from bottom to top panels. The data were obtained by CTHYB plus analytic continuation for $U/D = 2.15$ and $t_\perp/D = 0.3$. The gap fills up with temperature and leads to a (bad) metallic state at finite T.

We can gain further insight on this transition by computing the self-energy. In Fig. 3.33 we show the imaginary part of the real frequency self-energy obtained by analytic continuation.

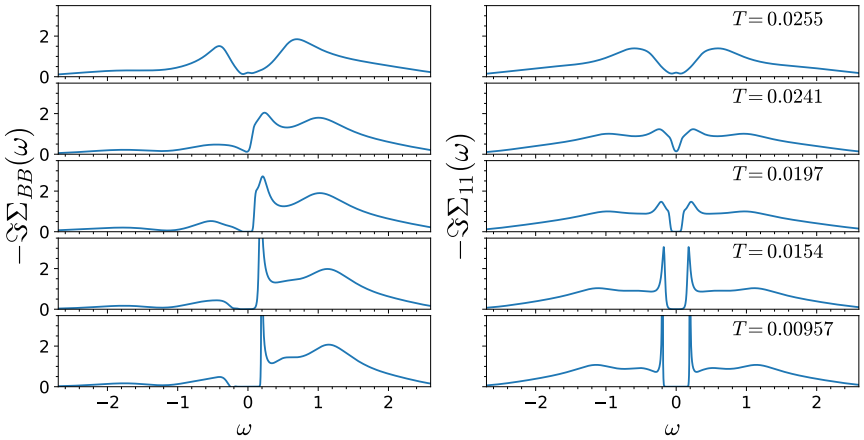

Figure 3.33: Change of the self-energy with temperature. The pole inside the Mott gap is broadened until disappearance. There is no connection between metal and insulator self-energy, their structures change drastically. Transition from a Mott insulator to a Fermi liquid

It is interesting to observe from the bonding basis data (left panels) that the two quasiparticle

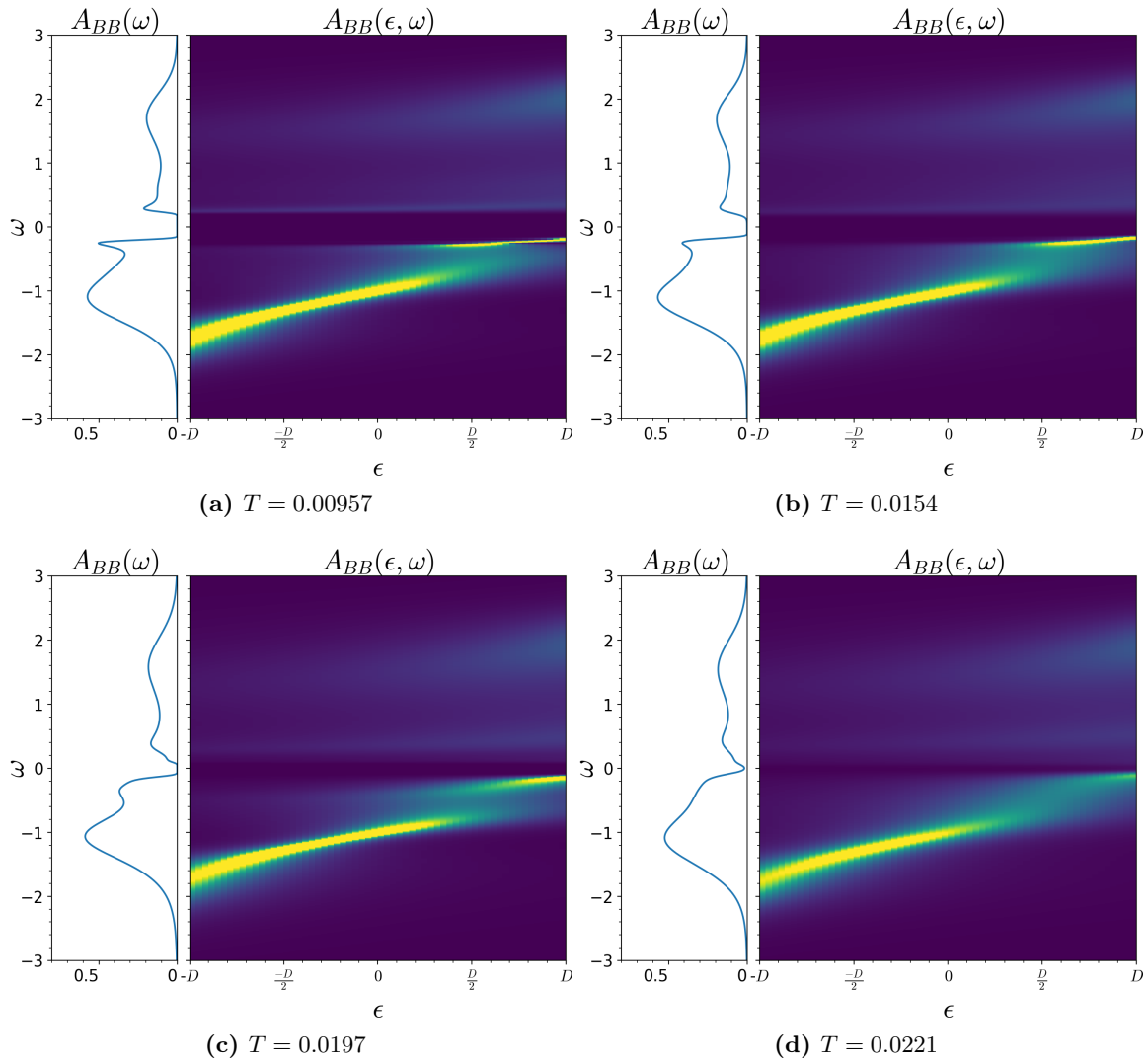

(a) $T = 0.00957$ **(b)** $T = 0.0154$

(c) $T = 0.0197$ **(d)** $T = 0.0221$

Figure 3.34: Bonding Spectral function dispersion of dimer Hubbard model at $t_\perp/D = 0.3$ and $U/D = 2.15$. Dissolution of Mott insulator upon warming

peaks on the sides of the gap have very different nature. The self-energy reveals that the $\omega < 0$ has a small $\Im\Sigma$ while the $\omega > 0$ one has very large value. Since $\Im\Sigma$ provides the inverse lifetime of the states (or its scattering rate) we conclude that the negative frequency peak is a coherent quasiparticle excitation, while the positive energy is a very incoherent one. Since these are QMC data, we would also like to draw the attention to the lower panel of Fig. 3.17, which have qualitatively similar data obtained from IPT. Thus, this provides further validation of the excellent quality of the IPT approximation.

We can gain further insight on the nature and thermal evolution of these excitations by considering the ϵ-resolved spectral functions. The data is shown in the panels of Fig. 3.34.

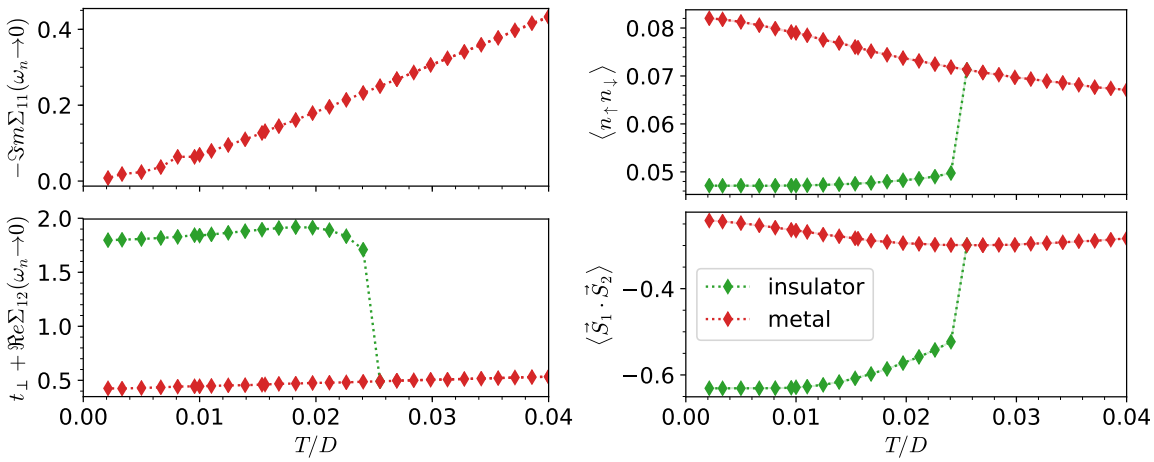

(a) (b)

Figure 3.35: (a) Temperature evolution of the linear extrapolation from the Matsubara self-energy to the Fermi level. (b) Temperature evolution of local observables single-site double occupation and intra-dimer spin-spin correlation.

Starting at low temperatures we observe that the $\omega < 0$ part of the spectra has a quasiparticle-like state at the inner part of the insulating gap. This coherent excitation of the Hubbard band broadens and fade away as temperature is increased and its weight fills up the gap.

We shall end this subsection with the discussion of the thermal behavior of a few observables that shed additional light on the dramatic transmutation of the quantum state as the first order transition takes place.

In Fig. 3.35a we plot the extrapolation of the Matsubara self-energy to $\omega = 0$ for the metallic and insulating phases. The top panel shows the imaginary part of the on-site self-energy, whose y-axis intercept indicates the scattering rate (i.e. inverse scattering time) of the metal. The anomalously high scattering rate indicates that the metal is characterized as a *bad metal* Gunnarsson et al. [2003]. In fact, we observe the it rapidly reaches values the order of the lattice hopping $\Im\Sigma_{11}(\omega = 0) \sim t$ after the insulator to metal transition point at $T_c \approx 0.0245$. In the insulating phase the zero frequency behavior of the imaginary part of the local self-energy is gaped (equal to zero) for all temperatures except at high temperatures close to the transition, thus it is not shown.

On the other hand, further information on the mechanism driving the transition can be obtained from the behavior of the intra-dimer self-energy Σ_{12}. From the low energy parametrization presented in section 3.1.1.1, equation (3.2) shows how the effective hopping amplitude inside the dimer is effectively renormalized as $\tilde{t}_\perp = t_\perp + \Re\Sigma_{12}(0)$. This behavior is shown in Fig.3.35a lower panel. We see that in the metallic state it remains unrenormalized $\sim t_\perp$, while it becomes large $\gg t_\perp$ at low temperatures in the insulator. This effect boosts

the splitting of the double quasiparticle peak and opens the gap at low T.

We should also mention here that these non-trivial behaviors of the self-energy obtained from QMC data is also very well captured by IPT, as we show in Fig.3.36. Therefore this provides additional support to the excellent quality of the approximation.

To complete our discussion of thermal effect, in the top panel of Fig.3.35b we show the on-site double occupation as a function of temperature. As expected, in the insulating phase there is a weak variation with temperature, consistent with a Mott insulator state. In contrast, the metal is relatively large and thus there is a big jump of this quantity at the insulator to metal transition. Consistent with the picture described so far, the spin-spin correlation between the two dimer sites shown in the lower panel has a large (negative) value at low temperature in the insulator as the two spins are locked into a singlet. They begin to unbind upon heating for $T > 0.01$. In contrast, in the metal, the correlation is relatively low, as each spin is independently Kondo-screened by the rest of the lattice.

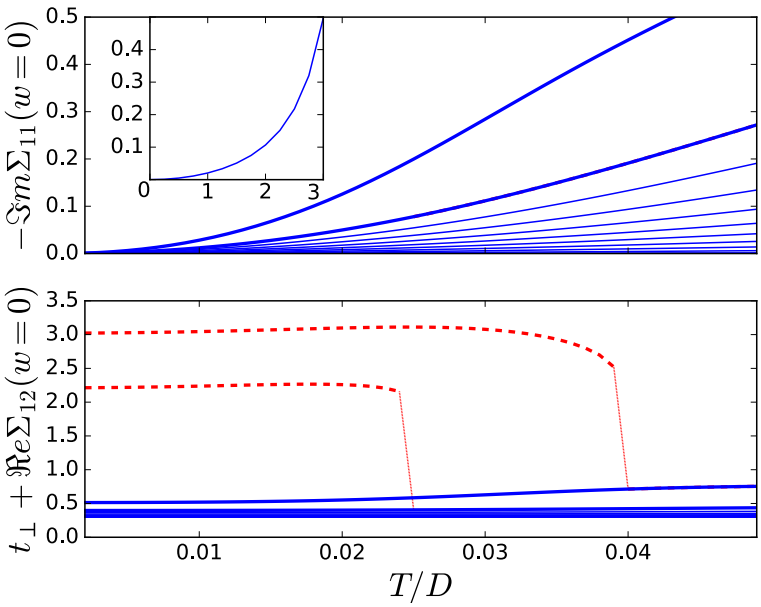

Figure 3.36: Top: The scattering rate $\mathrm{Im}[\Sigma_{11}(\omega = 0)]$ for the metal (solid) at fixed $t_\perp/D = 0.3$ values of U from 0 to 3 in steps of 0.5 (upwards). The relevant values $U = 2.5$ and 3, are highlighted with thick lines. Inset shows the U dependence at fixed $T = 0.04$. Bottom: The effective intra-dimer hopping $\tilde{t}_\perp = t_\perp + \Re e[\Sigma_{12}](0)$ (bottom) as a function of T for the same parameters as the top panel. Metal states are in solid (blue) lines and the insulator in dashed (red) lines for $U = 2.5$ and 3. The calculation are done with IPT.

Chapter 4

The Dimer Hubbard model and experiments in VO_2

In this chapter we shall discuss the relevance of the dimer Hubbard model for the interpretation of experiments in VO_2. As we discussed already in the Introduction, the physical characterization of the VO_2 as Mott, Peierls or "in-between" has been a debated issue. This problem has been mainly considered within the framework of so called DFT+DMFT approaches, which are numerically heavy and of high technical complexity. Here, we are adopting a different strategy, we consider a schematic model Hamiltonian where we trade the realistic aspect for a detailed physical solution, including at finite temperatures. Of course the hope is that the model remains applicable to capture the basic physics of the material. In fact, it is important to emphasize again, that the DHM in DMFT has the same time of impurity problem as the one in the monoclinic phase of VO_2 in DFT+DMFT. Therefore, we are giving up the multi-orbital aspect and crystal fields, but retaining the crucial dimerization-correlation competition, which we have already study in great detail in the previous chapter. Now, we shall explore how the insights that we obtained may shed light into some standing open issues in recent experiments done on VO_2.

We shall first determine the energy scales of the model parameters in regard to results of DFT calculations. Specifically, we shall then discuss the possibility and evidence for a purely electronic insulator-metal transition in VO_2. We shall address this point by considering various recent experiments that seem to provide strong indications of an IMT purely driven by electronic effects and decoupled from the lattice. We shall try to correlate those observations with the "monoclinic" metal that is predicted by our model calculations.

Therefore, one of the key question that shall concern us, and has been the goal of many recent experiments, is: can the electronic transition be decoupled from the structural one? and more specifically: can the system thermally collapse the insulating gap without removing dimerization, producing an intermediate monoclinic metallic phase as predicted by our model calculations? If this is the case, one may argue that the "chicken-and-egg" problem of VO_2 is thus resolved. We advance that we shall present evidence for this and we shall thus conclude that the IMT is driven by correlations that collapse the insulator into a metal within the monoclinic phase, which eventually no longer profits from the lattice monoclinic distortion

and hence evolves to the rutile structure Nájera et al. [2017].

The experiments that we shall describe are of different types. A common feature of them is the realization of an intermediate metallic electronic phase that is different from the rutile, or where the structural transition apparently has not yet taken place. They may be observed by either heating Qazilbash et al. [2007, 2011], Laverock et al. [2014], Liu et al. [2015], or applying pressure Arcangeletti et al. [2007], Marini et al. [2010], or by photo excitation in pump-probe experiments Kim et al. [2006], Cocker et al. [2012], Yoshida et al. [2014], Morrison et al. [2014], Wegkamp et al. [2014].

4.1 The energy scale of model parameters

We first consider the energy scales and compare the parameters of the DHM to those of electronic structure calculations. The dimer Hubbard Model has three parameters: inter-dimer (or lattice) hopping t, intra-dimer hopping $t_\perp$, local Coulomb repulsion U. The lattice hopping provides the bandwidth of our model Hamiltonian $W = 4t$ Georges et al. [1996], Moeller et al. [1999], Nájera et al. [2017]. In the case of VO_2, LDA calculations show that the t_{2g} states of the V atoms in either the Rutile or Monoclinic structures have an approximate bandwidth of 2eV Biermann et al. [2005], Lazarovits et al. [2010], Belozerov et al. [2012], Brito et al. [2016], refer to Fig. 4.1. This corresponds in our model to $4t$ and hence we set $t = 0.5eV$. This is convenient, since the half-bandwidth of the model is $D = 2t$ and was used as unit of energy in our results of the previous chapter. Then, with $D = 1eV$ we may simply read the numerical energy value of the figures directly in physical units (eV) and compare to experimental data of VO_2.

The intra-dimer hopping quoted from Biermann et al. [2005] is ~ 0.68eV, that value concerns solely the a_{1g} orbital. There are in fact also two additional intra-dimer hopping amplitudes (associated to e_g states), which are 0.22eV and a smaller value Lazarovits et al. [2010]. Since we are considering a unit cell with two sites and one orbital each, we have a single intra-dimer hopping parameter. Therefore, and in the spirit of a mean field theory, we chose a value that is the approximate average of the 3 hopping amplitudes and adopt the value of $t_\perp = 0.3eV$, in a reduced simplification of a 3 orbital model into a single orbital. This is in contrast to using the single orbital of the dimer model to express only one of the orbitals present in the lattice Tomczak and Biermann [2007], Tomczak et al. [2008]. Nevertheless, we should also mention that our results and conclusion would remain qualitatively valid even if we had adopted a somewhat larger value of $t_\perp$ so long it is within the coexistence region. The values for the hopping amplitudes found in later works Belozerov et al. [2012], Brito et al. [2016] use consistent values with the multi orbital formulation, we continue to use the average in our reduced model.

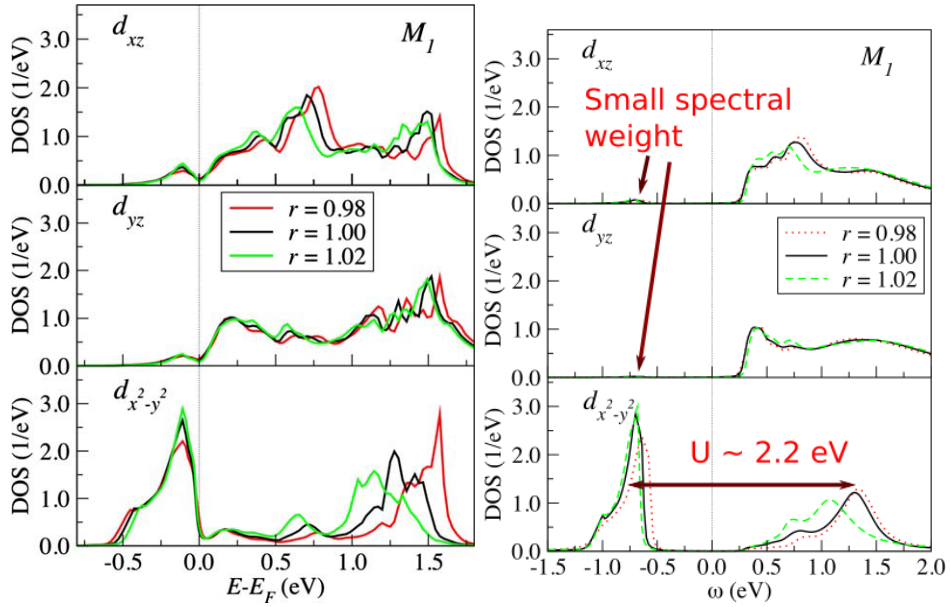

Figure 4.1: (a) LDA (b) LDA+CDMFT. Local density of states around the Fermi level for t_{2g} bands under strain r in the M_1 lattice. Adapted from Lazarovits et al. [2010]

4.2 Phase diagram and thermally driven insulator to metal transition

The choice of $t_\perp = 0.3eV$ gives the phase diagram shown in Fig. 4.2 in physical units. We observe that at low T there is a large coexistent region at moderate U. This region gradually shrinks as T is increased and fully disappears at a critical end point. This is consistent with the well known single-band Hubbard model result, where the coexistent region also extends in a triangular region defined by the lines $U_{c_1}(T)$ and $U_{c_2}(T)$ Georges et al. [1996]. In that model ($t_\perp = 0$) the triangle is tilted to the left, which indicates that upon warming the correlated metal undergoes a first order transition to a finite-T Mott insulator, cf. Fig.1.2. Such behavior was immediately associated to the famous 1st order MIT observed in *Cr-doped* V_2O_3 Rozenberg et al. [1994], Georges et al. [1996], which has been long considered a prime example of a Mott Hubbard transition Imada et al. [1998]. It is noteworthy that this physical feature has remained relevant even in recent LDA+DMFT studies, where the full complexity of the lattice and orbital degeneracy is considered Grieger et al. [2012], Hansmann et al. [2013]. In the present case as $t_\perp$ is increased the tilt of the triangular region evolves towards the right (cf. discussion in Chapter 3). This signals that $t_\perp$ fundamentally changes the stability of the ground-state. Thus, upon warming, the insulator undergoes a 1st order transition to a (bad) correlated metal at finite-T.

The IPT results for the coexistence region are shown in black lines in Fig. 4.2. It is centered around $U \approx 2.5 - 3eV$, which is a value consistent with those adopted for the Coulomb

interaction strength in the LDA+DMFT studies Biermann et al. [2005], Lazarovits et al. [2010]. The QMC results are also indicated in the figure in red lines. They are both quantitatively consistent upon a slightly different choice of the parameter $D = 2t = 1.2eV$ starting from the results shown in the phase diagram of Fig.3.27. They both give a coexistence region located around a similar value of $U \approx 2.5eV$, and importantly, they also coincide to give a 1st order transition line close to the spinodal $U_{c_1}(T)$. Thus, it is also significant that these results predict an electronic first order insulator to metal transition by heating in the range of $300 \sim 400K$, which is very consistent with the experimental value of $T_c \approx 340K$ for the transition in VO_2 (indicated by a horizontal line in the figure). This agreement is rather remarkable, since this energy scale is about two orders of magnitude smaller than the bare parameters of the model.

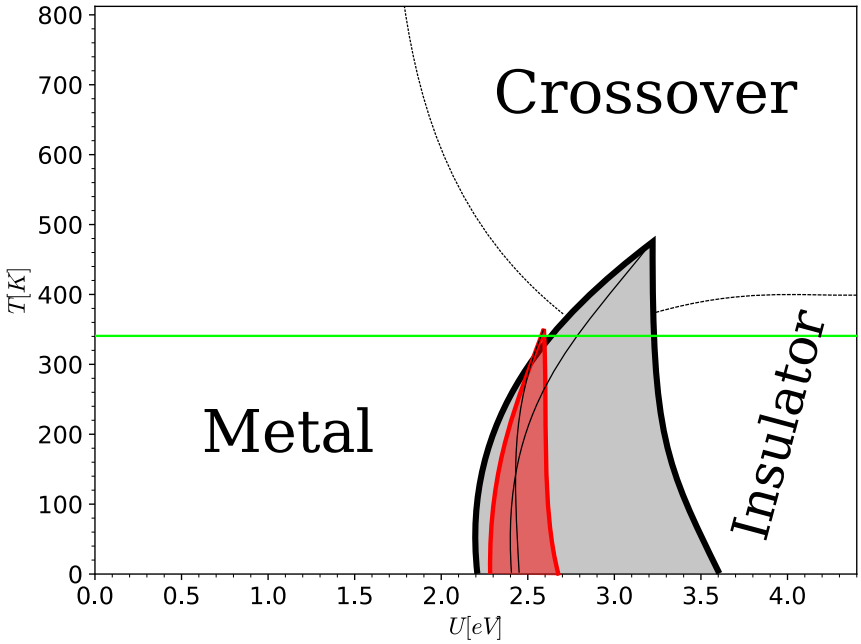

Figure 4.2: $U - T$ Phase diagram for $t_\perp/D = 0.3$ showing the coexistence (filled region) of metal and insulator states (black lines from denote IPT solution with $D = 1eV$ and red lines denote QMC solution with $D = 1.2eV$). Green horizontal line $T = 340K$ experimental VO_2 transition temperature. Approximate position of the 1st order lines is indicated as black lines inside the coexistence region.

We may add that the choice of the value of $U = 2.5eV$ for the semi-quantitative comparison with experiments is also quite consistent with the values considered in Lazarovits et al. [2010], who systematically explored the range of $U = 2.2$ to 3.5eV, and settled for the former to better match experimental data, cf. Fig. 4.1. The values adopted by Biermann et al. [2005], Belozerov et al. [2012] are $U = 4eV$ and $J = 0.68$. These values are in fact higher than ours, however, Biermann et al. pointed out that a choice of values of U and J significantly smaller, such as $U = 2eV$, would also compatible with their findings.

It is noteworthy that in our model the values $U = 2.5$ and $t_\perp = 0.3$ lead to Hubbard bands

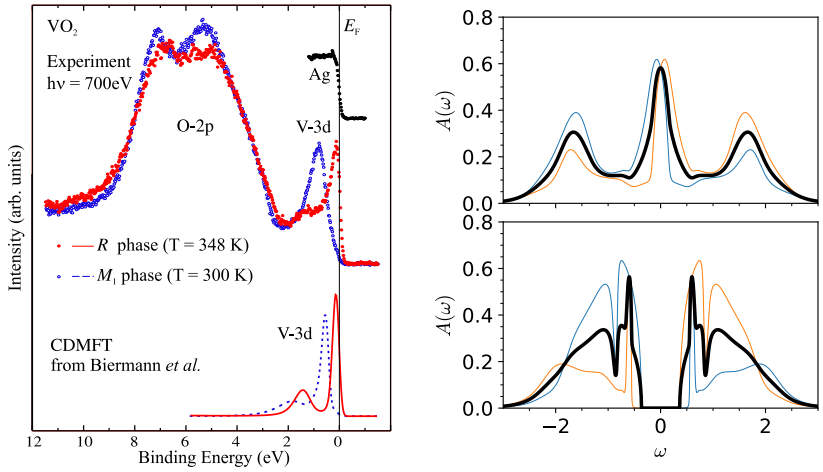

Figure 4.3: Left:Valence band photoemission spectra of VO_2 from Koethe et al. [2006]. Right: DHM Spectra for metal(top)- insulator(bottom).

that are centered at $\approx \pm 1.5eV$ and a quasiparticle residue $Z \approx 0.4$, both consistent with photoemission experiments of Koethe et al. [2006], shown in Fig.4.3.

4.3 Spectroscopic and finite frequency experimental probes across the insulator metal transition

Using scattering near-field optical microscopy (SNOM) Keilmann and Hillenbrand [2004], Novotny and Hecht [2012] to measure the nanoscale optical response through the MIT of VO_2 one is able to discriminate between metallic and insulating domains. VO_2 phase separates into metallic and insulating domains near the transition temperature T_c, consistent with the first order nature of the phase transition. The detected metallic puddles that form in the sample close to the transition temperature display a different optical signal than the high temperature rutile metal. In the next two sections we describe how our results on the dimer Hubbard model can account for the unusual experimental behavior of the VO_2 system at the phase transition. Then, in the two final section we shall describe pump-probe experimental results that are also remarkably accounted by our model calculations. Moreover, we also make predictions, which can be experimentally tested.

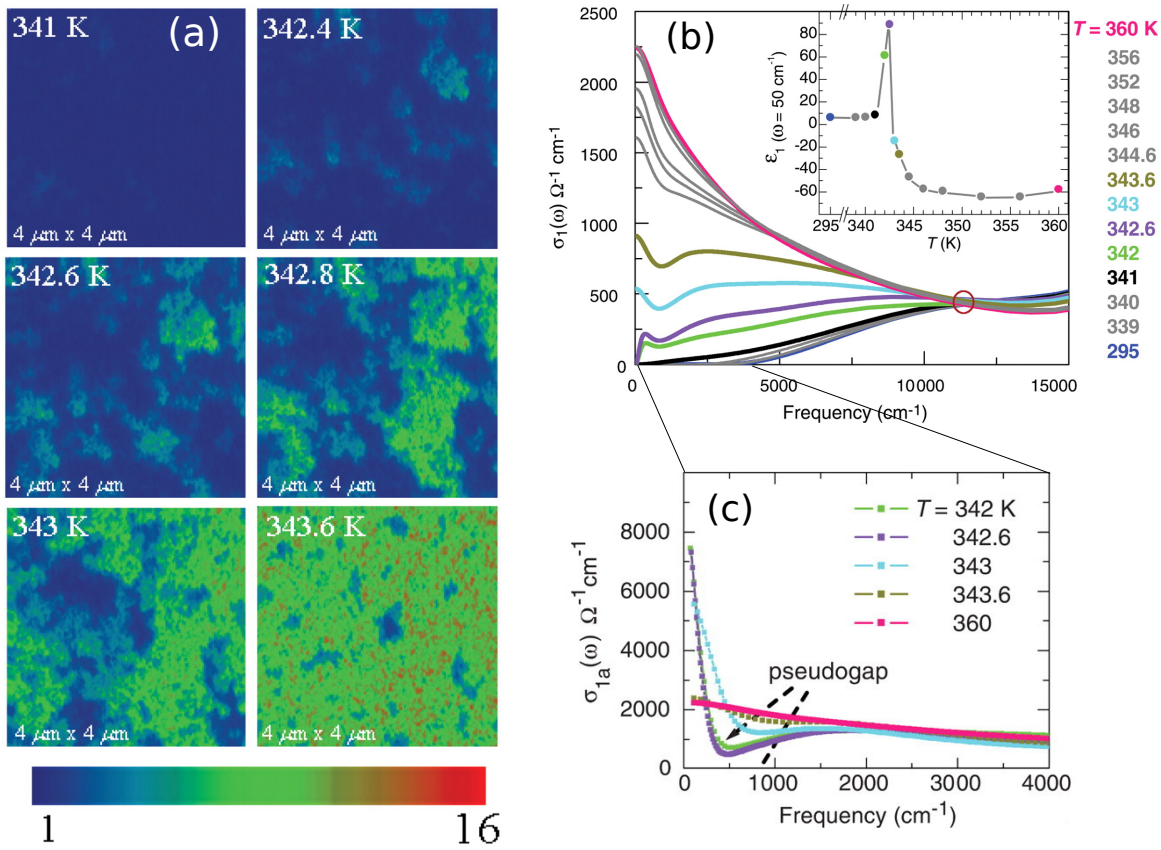

Figure 4.4: (a) Images of the the near-field scattering amplitude of a VO_2 sample upon heating across the insulator to metal transition. The metallic regions(light blue, green and red colors) give a higher response compared to the insulating phase in dark blue. (b) Real part of the Optical conductivity of the macroscopic sample of VO_2 for various temperatures(inset temperature dependence of the real part of the dielectric function at $\omega = 50cm^{-1}$). (c) Optical conductivity of the metallic nano-domains of VO_2 as a function of temperature. From Qazilbash et al. [2007]

4.3.1 Optical conductivity of nanoscale metallic puddles at the insulator metal transition of VO_2

In a notable experiment Qazilbash et al. [2007] investigated the spatially resolved optical response of a VO_2 sample as a function of temperature. Upon heating from the low temperature monoclinic phase and within the hysteresis region, they clearly identified the emergence of nanoscale correlated metallic domains near the transition temperature. A remarkable surprise was that the electronic properties of the metallic puddles were unlike those of the rutile metal. The measured images are shown in Fig.4.4. The lattice structure of these puddles was not identified at that time and their interpretation remained a puzzle. Subsequent investigation form Qazilbash et al. [2011] showed that the system does not show any signature of a structural transition when the non-percolating nanoscale metallic puddles develop. Therefore, these domains have undergone an insulator to metal transition without structural change. Additionally, the work of Nag et al. [2012] demonstrated that the insulator metal transition and structural phase transition can occur non-congruently when initiated thermally, suggesting the presence of a metal-like, M_1 phase of VO_2. Further experiments continued to promote the identification of an intermediate monoclinic metallic state at the transition Tao et al. [2012], Liu et al. [2013].

This transition must, therefore, have a purely electronic character. Upon further heating the system percolates and eventually reaches the homogeneous rutile metal.

To interpret these experiments we can go back to our results for the electronic structure of the Dimer Hubbard model within the coexistence region for the parameters appropriate for VO_2. The DOS spectra and the electronic structure are shown in Fig. 4.5. We recall that the figure panels may be directly read in physical units (eV). In order to gain further insight about the consequences of the dimer metal phase with its split quasiparticles bands at low energy and make contact with this key experiments, we now consider the optical conductivity response $\sigma(\omega)$ within the MIT coexistence region. Comparing to the set of remarkable data obtained in this regime by Qazilbash et al. [2007], the key point that we want to emphasize here is that $\sigma(\omega)$ in the putative M1-metallic state was characterized by a intriguing mid-infra-red (MIR) peak $\omega_{mir} \approx 1800 cm^{-1} = 0.22eV$, whose origin was not understood. From our results on the electronic structure, we find a natural interpretation for the puzzling MIR peak. It should correspond to excitations between the split metallic quasiparticle bands. Since they are parallel, they would produce a significant contribution to $\sigma(\omega)$, which enabled its detection. In Fig. 4.6 we show the calculated optical conductivity response that results from the electronic spectra presented in Fig. 4.5. In the metal we see that, in fact, a prominent MIR peak is present at $\omega_{mir} \approx 0.22eV$, in excellent agreement with the experimental value. On the other hand, the optical conductivity of the insulator shows a maximum at $\omega_{ins} \approx 2eV$ in both, theory and experiment. Moreover, we also note the good agreement of the relative spectral strengths of the main features in the two phases.

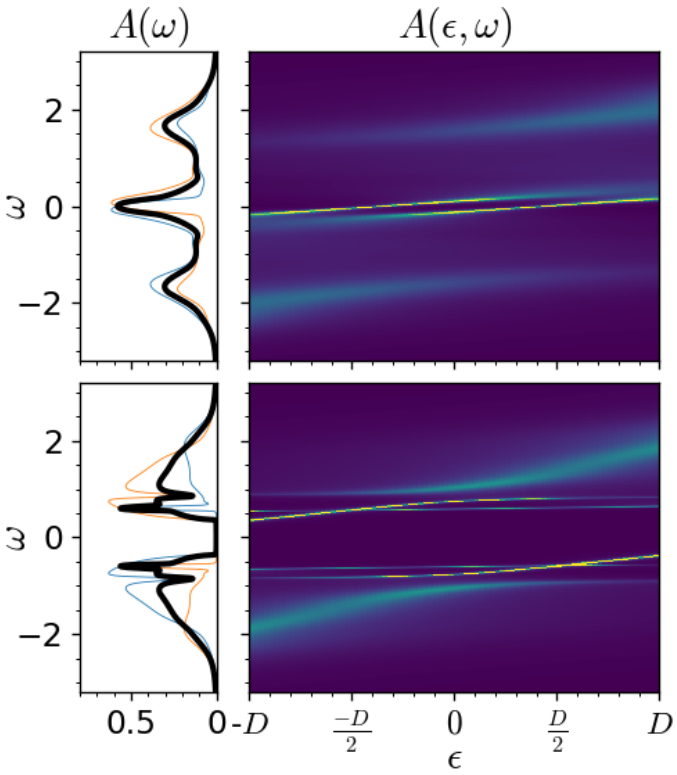

Figure 4.5: Electronic dispersion for the metal (left top) and insulator (left bottom) in the coexistence region for parameter values $t_\perp/D = 0.3$, $U/D = 2.5$ and $T = 0.01$. Right panels show the respective DOS(ω). The calculations are done with IPT

However, we should also mention that our results do seem to miss on the size of the optical gap in the insulating phase by a factor of ~ 2. We will come to this issue again in the next section. We should also remind the reader that because we are treating an reduced single band dimer model only the optical transitions of its composing bands are present and the optical response continues to decay for $\omega > 3$ in the metal and insulator states. The real material's optical conductivity would also include inter-band transitions to the oxygen bands resulting in a higher response at higher frequencies. For comparison refer to Tomczak and Biermann [2009] for the optical conductivity of the stable phases. We remind the reader our results focus on the meta-stable phase of the mono-clinic metal with the signature of a mid-infra-red peak at $\omega_{mir} \approx 1800cm^{-1} = 0.22eV$.

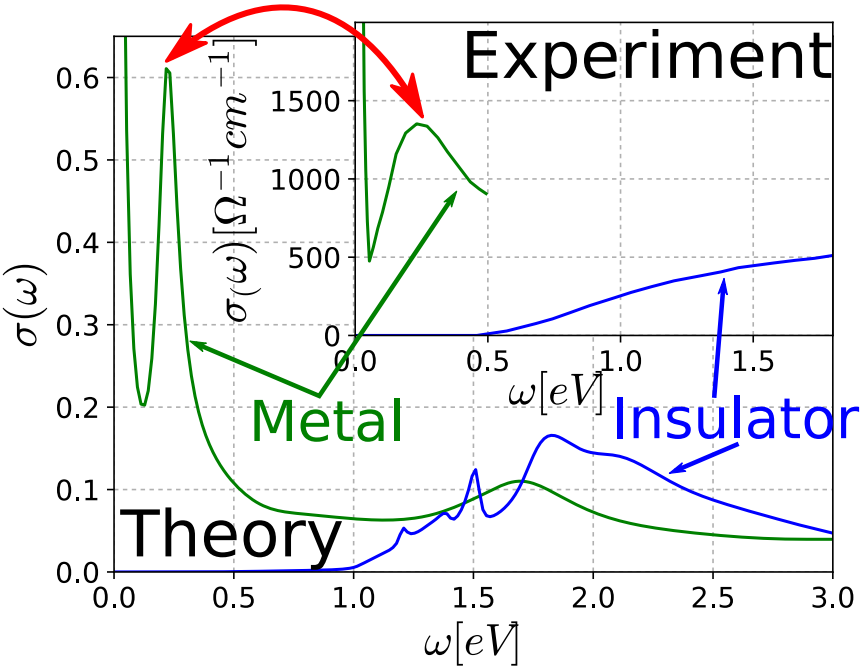

Figure 4.6: The optical conductivity $\sigma(\omega)$ of the metastable monoclinic metal and monoclinic insulator within the coexistence region for parameters $t_\perp = 0.3$, $U = 2.5$ and $T = 0.01$. The calculations are done with IPT, the optical conductivity is within a renormalized unit σ_0. Inset: The experimental optical conductivity adapted from Qazilbash et al. [2007] containig the data shown in Fig.4.4 (b) and (c), insulator data is at $T = 340K$, metal data is at $T = 342.6K$.

4.3.2 Simultaneous tera-Hertz and mid-infrared spatial imaging at the transition. (Work done in collaboration with Basov's group at UCSD.)

Like in the previous experiment the near-field scattering amplitude of VO_2 films is measured. The key innovation compared to the previously described experiment is that they perform the measurement of the near-field scatting amplitude at both mid-infrared (MIR) and terahertz

(THz) frequencies. In comparison to the phase-separated MIR images, which display an abrupt change in signal level between insulating and metallic domains, the THz images appear homogeneous at the transition with a continuously evolving signal level through the transition. This is a surprising and intriguing feature. Fig. 4.7 shows the experimental data: images at MIR and THz frequencies of the near-field response of a 100 nm granular VO_2 thin film. The top row images the film at THz frequencies, and the images in the bottom row are taken in the MIR. In both the THz and MIR images, the signal S is shown normalized to that from a region of gold in the same field of view. Contrast in near-field signal S, which is a measure of local reflectivity, has been shown to reliably discriminate between metallic and insulating regions at both MIR and THz frequencies. Here we choose a linear color scale with red corresponding to high S metallic regions, and blue to low S insulating regions of the sample. The MIR images are clearly phase-separated and show the emergence of strong spatial inhomogeneity by the appearance of well defined metallic domains similar to previous observations Qazilbash et al. [2007]. In stark contrast, the THz images evolve homogeneously and continuously from insulating to metallic signal levels through the same temperature region.

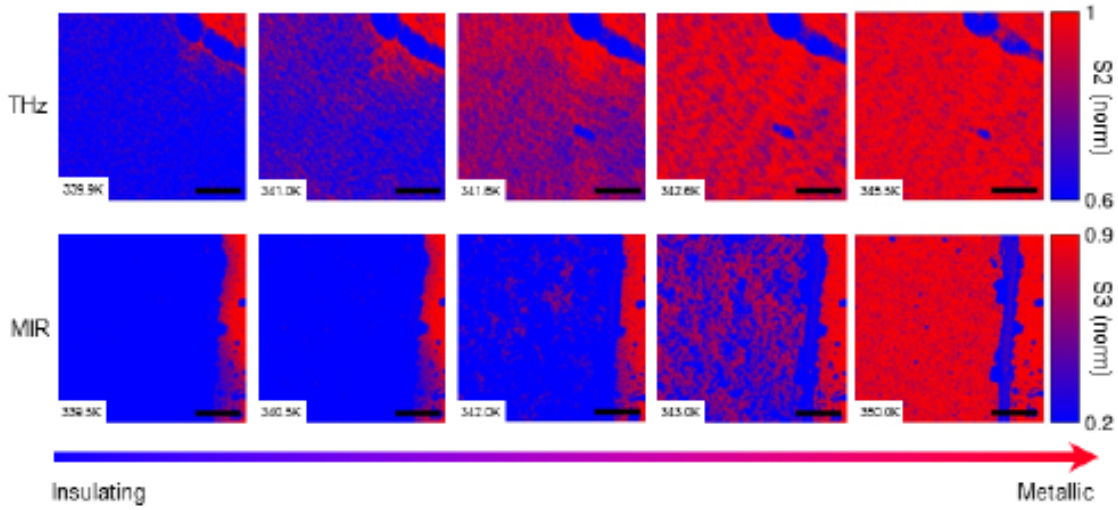

Figure 4.7: SNOM images of the VO_2 MIT taken at THz (top row) and MIR (bottom row) frequencies. The THz images are taken at 339.9K, 341.0K, 341.6K, 342.6K, and 345.5K, while the MIR images are at 339.5K, 340.5K, 342.0K, 343.0K, and 350.0K, reading from left to right. In all images, the signal at every temperature is normalized to the signal obtained on gold (bright red region in the upper right or right of the image, for THz and MIR respectively). The THz and MIR data are S2 and S3, which is the detected signal demodulated at the second and third harmonic of the tip tapping frequency, respectively. Scale bar, $2\mu m$.

The distribution of the pixels' intensity values in each image, shown in Fig.4.8 (a), elucidates this distinction. These histograms exclude the pixels in the gold region of each image. The MIR histograms are bimodal at the transition temperatures; they show an abrupt change in

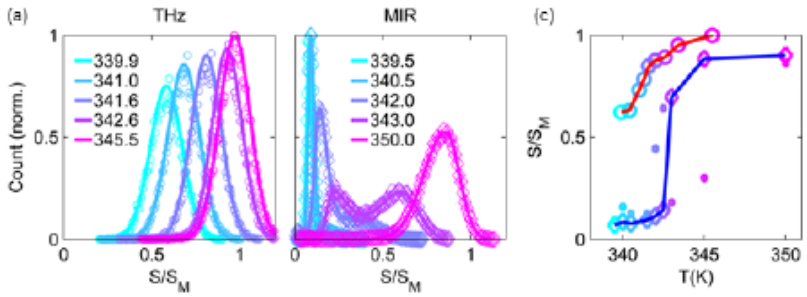

Figure 4.8: (a) Histograms of the THz (left) and MIR (right) images shown in Fig.4.7. The density of pixels in each signal intensity is plotted as circles (THz) or diamonds (MIR). The solid line is a fit to the data, which is a single Gaussian for the THz and a skewed bimodal Gaussian for the MIR. Right panel: peak signal level as a function of temperature in the THz (red line, circles) and MIR (blue line, diamonds) extracted from single or bi-modal Gaussian fits to the histograms.

signal level between metallic and insulating domains at a single temperature, represented by the separation between the two peaks. However, the pixels in the THz images are distributed according to a single Gaussian at all temperatures; there is a continuous variation in signal level across the image at any given temperature through the transition. We plot the mean THz near-field signal as a function of temperature in Fig.4.8 (c) as circles, connected by a red line as a guide to the eye. The THz near-field signal increases smoothly and homogeneously upon heating. Similarly, we fit the MIR histograms to the sum of two skewed Gaussians, whose means trace the insulating and metallic signal levels at each temperature. These extracted mean signals are presented in Fig.4.8 (c) as diamonds, of which there are two for each temperature. The larger is the signal of the taller Gaussian, corresponding to the signal level of the majority of pixels (insulating or metallic) in the image, the smaller diamonds represent the minority signal. We connect the majority signal levels with a blue line, which shows the abrupt jump in magnitude at the transition temperature and the minor signal changes within the metallic and insulating phases, whose signal intensity drifts as a function of temperature.

We may now attempt to understand these experimental observations by means of the DHM results. In previous section 3.3 we introduced the temperature evolution of the DOS, upon heating, of the DHM preceding the IMT. The DHM predicts both an abrupt first order IMT with a noticeable change in the density of states between the insulating and metallic phases with a precursor appearance of in-gap states before the transition. As it turns out, these incoherent states filling the gap at finite temperatures are responsible for the relatively large near field signal at THz frequencies in the insulating state just below T_c that, within the experimental noise, smoothly evolves into the metallic state just above T_c.

In Fig.4.9 we show representative electronic spectra of the DHM for two different values of

the ratio $t_\perp/U$, which are prototypical sets of data that can portray the behavior seen in experiment. Panels (a)-(c) correspond to a case with small $t_\perp/U$, and panels (d)-(f) are for large $t_\perp/U$. Both sets of values of $t_\perp/U$ are within the coexistence region of the phase diagram and support a first order insulator to metal transition by heating. However, the temperature dependence of the electronic spectra is strongly affected by changing $t_\perp/U$.

The case of small $t_\perp/U$, in Fig.4.9 (a), shows that the density of states (DOS) abruptly shifts from insulating to metallic character at a specific temperature T_c, with a minor filling of the large charge gap. The optical conductivity, in panel (b), for the insulating state is vanishingly small and barely presents a perturbation in this frequency range as a function of temperature. The metallic conductivity shows a large Drude-like metallic conductivity, with the characteristic MIR resonance, but no perceptible change with temperature. In Fig.4.9 (c) we show the near-field signal that arises from the optical conductivity. We model the near field signal using a lightning-rod model for the tip-sample interaction McLeod et al. [2014]. The modeled near-field signal recreates the same general trends as the DOS and the optical conductivity. It is low for $T < T_c$ and high for $T > T_c$, with an abrupt jump in signal level between the two states at all frequencies. There is very little temperature dependence otherwise. This data also shows that the near-field signal, close to $\omega \to 0$ experiences a sharp increase in the insulating phase. This is a consequence of the semi-conducting gap being slightly filled by incoherent states, which result in a finite, though small, conductivity at very low frequencies. This effect is dramatically magnified at larger $t_\perp/U$ ratio as we shall see next.

Indeed, the spectral temperature dependence is markedly different for the case of large $t_\perp/U$, as shown in Fig.4.9 (d). There is still an abrupt change in the DOS at T_c, but the DOS below and above T_c show a stronger temperature evolution. We see that the gap is continuously filling at temperatures below T_c. This is due to the break down of the intra-dimer singlet as temperature is increased. As discussed in section 3.3.3, the sharp insulating gap is reduced and filled with incoherent states from the now free fluctuating magnetic moments of the localized electrons. Accordingly, in Fig.4.9 (e) the optical conductivity at $T < T_c$ already has a noticeable spectral strength at low frequencies in the insulating state, which grows in magnitude as temperature increases. There is then an abrupt jump in conductivity at T_c to a Drude-like metallic response and as temperature continues to rise for $T > T_c$ the conductivity continues to increase. For the choice of $t_\perp/U$ shown in the bottom row of Fig.4.9, the low-frequency conductivity changes by an order of magnitude across the transition.

Notably, in the high $t_\perp/U$ case the optical conductivity of the insulator has a significant strength at all frequencies and even roughly follows the behavior of the upper lying metal at higher temperatures. Crucially, this finite optical conductivity in the insulating state translates to a $1/\omega$ behavior in reflectivity. SNOM is essentially a measure of local reflectivity and the calculated near-field signal, shown in figs.4.9 (c & f), demonstrates that at THz frequencies even a small optical conductivity translates into a large near-field signal that

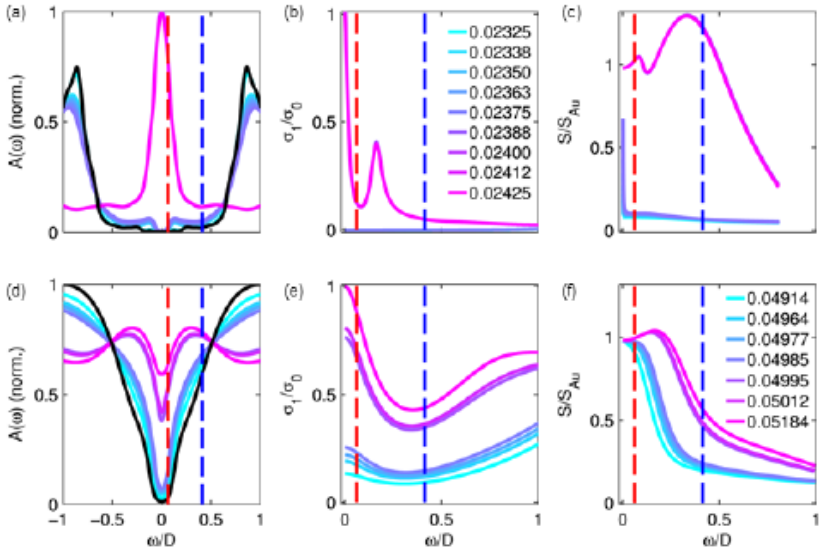

Figure 4.9: Spectra at different temperatures around T_c, for the dimer Hubbard model with parameters $t_\perp = 0.2$, $U = 3.1$ (a-c) and $t_\perp = 0.5$, U = 2.405 (d-f) as a function of energy normalized to the bandwidth D. The temperatures (normalized to the bandiwdth D) of each curve for small $t_\perp/U$ (a-c) are shown in the legend in panel (b). The temperatures used for large $t_\perp/U$ (d-f) are shown in the legend in panel (f). The left column shows the local density of states (LDOS) at different temperatures as a function of energy for small $t_\perp/U$ (a) and large $t_\perp/U$ (d). The black line is the LDOS at T $\approx$ 0. The middle column shows the real part of the optical conductivity at different temperatures for small $t_\perp/U$ (b) and large $t_\perp/U$ (e). All conductivities curves are normalized to the DC conductivity at the highest temperature shown (i.e., the DC conductivity of the metallic state). The right column shows the calculated near-field signal at different temperatures as a function of frequency for small $t_\perp/U$ (c) and large $t_\perp/U$ (f). The dashed vertical lines in all figures indicate the THz (red) and MIR (blue) frequencies.

can match the metallic signal, which has a saturation limit. In panel (c), the vanishingly small optical conductivity produces a flat near-field signal for almost all frequencies, except at $\omega \to 0$. In contrast, in panel (f), due to the optical weight at low frequencies, there is a larger frequency window where the near-field signal is comparable to the metallic one. Thus, we can find a region at low frequencies (red dashed-line), where the change in signal at the IMT looks essentially continuous. In contrast, at higher frequencies (blue dashed-line) there is a large region where the signal presents an evident jump in intensity.

Thus, the DHM appears to provide a framework for understanding the apparently conflicting results of our THz and MIR near-field images. Increased intra-dimer hopping and weaker Coulomb interaction (large $t_\perp/U$) leads to the formation of intra-dimer singlets, which break down at a characteristic temperature and below the IMT, consequently the insulating gap is filled with incoherent states at finite $T < T_c$. Gap filling in the insulating state at finite temperature is consistent with previous measurements of both bulk and thin film VO_2 Ladd and Paul [1969], Liu et al. [2011]. The smooth filling of the gap for $T < T_c$ leads to a small but finite THz conductivity in the insulating state. This small optical conductivity in turn generates a reflectivity which is low at most finite frequencies, but rapidly increases as the frequency approaches 0. Thus, the increased $t_\perp/U$ generates a small, finite THz optical conductivity for $T \leq T_c$, which translates into a relatively large THz reflectivity in the insulating state compared to the MIR. In other words, the THz reflectivity is especially sensitive to small changes of the optical conductivity in the insulating state. At temperatures very close to the transition, the insulating THz near-field signal is already within the experimental detection limit of the metallic signal. Even though there is an abrupt first-order jump in the optical conductivity at T_c, the relative change in THz nearfield signal across the MIT is very small. Therefore, the transition appears relatively more spatially homogeneous in the THz images with respect to the MIR ones. The transition at T_c from insulating to metallic remains abrupt in the MIR near-field signal, which evidences the phase segregation.

4.4 Femto-second pump-probe spectroscopies

The observation that the insulator to metal transition can be stimulated by an ultra fast optical pulse Becker et al. [1994] has promoted a new field of experimental investigation in photo-induced phase transitions in VO_2. In VO_2 the transition to the metallic phase is accompanied by a structural transition from a monoclinic phase (with dimers) to a rutile phase (where the dimers have relaxed). The comparison with our dimer metal phase cannot be traced then, *unless the structural transition is preempted*. Here we shall explore in detail the consequenses of our predicted correlated monoclinic metal and show that they are in excellent qualitative and even quantitative agreement with a variety of recent pump-probe experiments.

The unique possibility to increase the temperature of the electronic gas without affecting the lattice degrees of freedom is offered by recent ultra-fast pump-probe experiments, which could photo-induce a MIT in VO_2. The transition can be triggered with pump pulses that energetic enough to overcome the optical gap Kübler et al. [2007], Nakajima et al. [2008], Wall et al. [2012], Cocker et al. [2012], Wall et al. [2013], Morrison et al. [2014], Wegkamp et al. [2014], Yoshida et al. [2014], O'Callahan et al. [2015] and as well with pump pulses in the THz regime with energies below the semi-conducting gap but that are intense enough Pashkin et al. [2011], Mayer et al. [2015]. Unlike in the previous section, experiments here are out of equilibrium. However, they present a very fast thermalization to meta-stable states. Our main goal is to focus on the intermediate meta-stable monoclinic metal and present a clear physical description of the electronic structure of both, the correlated insulator and metal states. In other words, the femto-second pump-probe experiments open a window to decouple the electronic state from the lattice. This is achieved by probing the system at a shorter time that what it takes for the lattice ions to move. In this section we shall consider three interesting experiments.

4.4.1 Photo-induced phase transitions

Cocker et al. [2012] studied the photo-induced transition to construct a entire phase diagram. They excite the sample with 1.55eV photons, which are powerful enought to overcome the optical gap in VO_2. Their probe is in the THz region which corresponds to meV, thus much smaller than the gap energy, so is a faithful measure of the IMT. They find that there is a threshold fluence above which the sample presents a long lived metallic state, and thus confirm an insulator to metal transition. They find evidence that the transition is not due to laser heating of the lattice and that there exist a non-thermal threshold to trigger the transition. Moreover, at low temperatures they argue for the existence of an intermediate metallic state where the Peierls distortion remains intact.

Fig.4.10 shows the photo-induced phase diagram of VO_2. In region A (green colored), the incident fluence in incapable of triggering a transition into a long-lived metallic state. Region B (cyan colored) only exists below 180K, in this case the THz absorption of the sample is long-lived but it presents a slowly decaying conductivity. This region shows the surprising feature that the threshold fluence to trigger the IMT is approximately constant (i.e. independent of T) and appears to be solely linked to the fluence needed to photo exited and electronic density equal to the metallic state electron density. The metallic regions promoted by the photo-excitation do not grow, consequently there is no increase in the transient THz conductivity. This state suggests an intermediate monoclinic metallic state without a lattice relaxation. The Mott localization is defeated but the Peiels distortion remains intact. This behavior is consistent with our theory of the dimer Hubbard model where we keep the lattice geometry fixed but are able to find a coexistence region where the

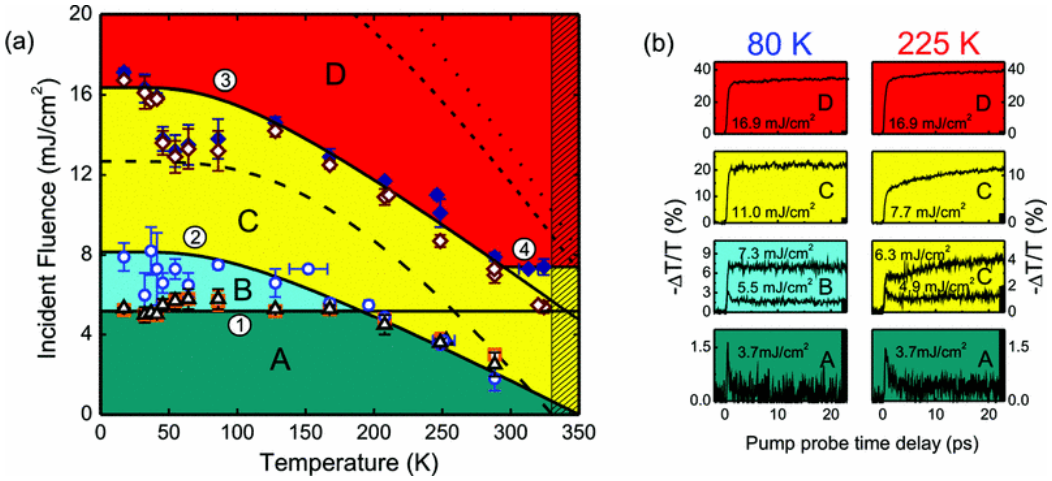

Figure 4.10: (a) Phase-diagram of the photo-induced insulator to metal transition in VO_2. Region A does not transition to a metallic state, Region B has long-lived THz dynamics but a decaying conductivity over time. Region C shows slow-rise dynamics. Region D presents a complete metallic modulation. Long dashed line is the fluence necessary to heat the surface of the sample to 330K(start thermal transition), Short dashed line raises the average temperature of the sample to 350K, dotted line raises the back surface of the sample to 350K. (b) THz conductivity dynamics, drop in transmission of the THz pulse. From Cocker et al. [2012]

(metastable) metallic state below $U_{c_1}(T)$ exist up to $T = 0$, cf. Fig.3.27 and Fig.4.2.

Region C in Fig.4.10 characterizes a IMT where the THz absorption of the VO_2 sample present a slow-rise behavior. Here one may argue that not only electrons are excited but also phonons are on a slower time-scale. This allows for the metallic domains to percolate in the insulating matrix of the sample. As this lattice relaxation is a slow process this slow-rise response can be seen over 100-ps time frame. This is inline with the idea that once the electronic system has turned metallic the lattice relaxation (i.e. a monoclinic to rutile transition) can happen as a consequence Pergament [2003]. At high pump fluence, region D, one achieves full metallic THz pulse modulation ($-\Delta T/T \geq 33.5\%$). In this case the macroscopic electron density has saturated and is identical to the high temperature metal. This supports the assumption that the metallic state formed by the steady state heating and the photo induced by intense optical pumping are the same and that the lattice has relaxed to its high temperature phase.

4.4.2 Pump-probe photoemission

Yoshida et al. [2014] investigated the photoemission spectra of VO_2 upon photo-excitation in a pump-probe experiment. They use a powerful pump with 3.15eV photon, which is enough to overcome the optical gap of VO_2 and also to overcome the entire bandwidth of

the low energy states of d-orbitals of the V atoms. The photoemission probe uses 28.3eV photons, thus are still quite surface sensitive appropriate for the thin film being probed. It is experimentally found that only beyond a threshold pump fluence of $\phi_t \approx 5\text{mJ/cm}^2$ an IMT is observed. Interestingly, it is also reported that the photoemission spectra of the photo-excited metallic state is long lived ($>$ 10ps) and is different from the high temperature rutile metal.

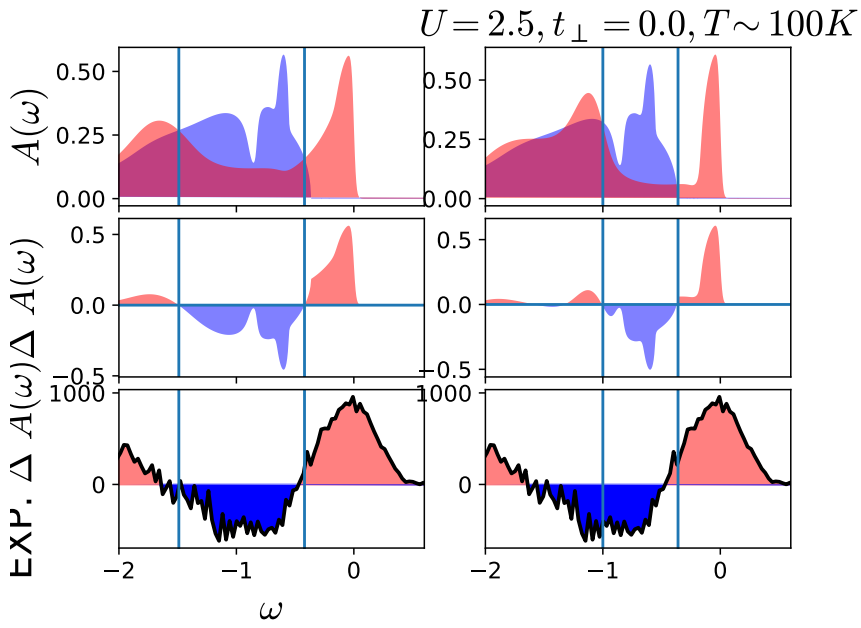

Figure 4.11: (top) Comparison of spectral functions for the dimer insulator into a dimerized Metal(left) and from a dimerized insulator to a single band Metal(right). (Middle) difference of spectral weight and (bottom) comparison to experimental data from photo-excited VO_2 sample reproduced from Yoshida et al. [2014].

Remarkably, we shall show now that this long-lived photo-induced metallic state can be naturally explained within the DHM. The IMT in the experimental pump-probe results from ref. Yoshida et al. [2014] put in evidence the transfer of the spectral weight from the insulating to the metallic phase upon photo-excitation, as reported in Fig. 4.11, bottom panels. Our results for the Mott IMT into a dimer metal with the same parameters adopted in section 4.3 and Fig.4.6 are shown in the top panel of the figure and their difference in the mid panel. The agreement is very good. A key point is that a spectral weight redistribution takes place from the Hubbard bands of the insulator (around $\omega \sim -1$) to form the bonding/anti-bonding structure of the low energy peak in the dimerized metal, when $t_\perp \neq 0$ (left panel of Fig. 4.11). This spectral weight transfer is at the origin of the negative (blue) depression in the spectral difference. We also considered, for comparison, the transfers of spectral weight for a non-dimerized model (i.e. $t_\perp = 0$) that mimics the rutile metal. In that case the agreement is less satisfactory. This is because the low energy peak is thinner, as is just renormalized by Z and has no splitting. Also the spectral weight transfer from the

Hubbard bands takes place on a smaller energy interval (as pointed out in the right panel in Fig. 4.11). We might then predict, that if the same experiment of ref. Yoshida et al. [2014] is repeated at a much higher fluence, sufficient to relax the lattice to a rutile metal, then the the negative blue-interval should reduce, as shown in the right hand side panels of Fig. 4.11

4.4.3 Simultaneous electronic MIR transmittance and structural changes

In a very beautiful experiment, Morrison et al. [2014] studied the photo-induced insulator to metal transition with a strong focus on the changes in the lattice structure. Using a pump pulse of $1.55eV$ photons they determined, similarly as in other experiments that a threshold fluence is necessary to induce the a metallic response in the transmittance. The specificity of their experiment was that it used two probes simultaneously. One to measured the time-resolved infra-red transmittance and, at the same time they observed the ultra-fast electron diffraction data to track any change in the lattice structure.

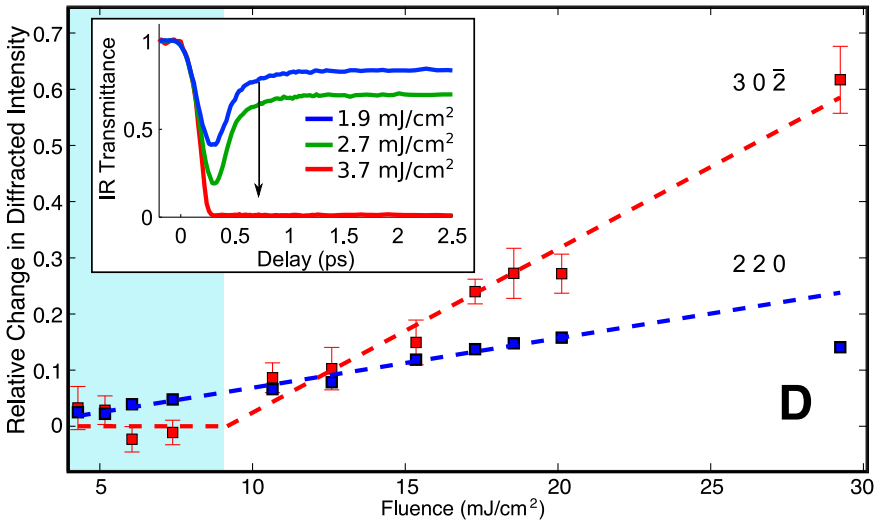

Figure 4.12: Fluence dependence of the fast and slow signal amplitudes as measured for the reflection peaks: $(30\bar{2})$ which is only allowed in the M_1 phase of VO_2 and (220) is present in both equilibrium phases. Inset) Time resolved IR (5 μ m, 0.25 eV) transmissivity in the light blue fluence region (3.7 mJ/cm^2 (red), 2.7 mJ/cm^2 (green) and 1.9 mJ/cm^2 (blue)) display a persistent decrease to a very long-lived plateau ($>$ 100 ps). The amplitude of this decrease reaches $>$ 99% at 3.7 mJ/cm^2, indicating a significant closing of the semiconducting gap and a transition to a metallic-like state. From Morrison et al. [2014].

Their main result is shown in Fig.4.12 where the change in the intensity of the lattice diffraction peaks was measured 20ps after photo-excitation pump pulse. The weak reflection of peak $(30\bar{2})$, which is only present in the monoclinic structure shows two regimes. In the first, with the excitation fluence below 9mJ/cm^2, it remains unchanged, thus the M_1 lattice structure remains intact. In the second, with larger fluence, there is a fast change in the lattice peak, as its reflection intensity drops with a half-life of 300fs. This corresponds to the dissolution of the lattice dimerization, which inevitably happens when a large energy is

deposited by the pump pulse on the sample. Extrapolating this response the authors estimate that ~ 43 mJ/cm^2 would be required to dissolve the dimerization in the entire sample. For reference, the dynamics of the reflection peak (220) present on both lattice structures was also measured. This reflection does not correspond to a structural rearrangement of the lattice, but is associated with a collective reorganization of the valence charge density in the M_1 phase that increases the electron density in the Vanadium dimer bonds Morrison et al. [2014].

Importantly, simultaneously with the change in the lattice structure, the experiment also probe the infra-red transmittance that is shown in the inset of Fig.4.12. The data reveal that, rather remarkably, the threshold fluence required to observe a transition in the transmittance $3.7mJ/cm^2$ is much lower than the one required for structural changes ($9mJ/cm^2$). The transmittance is probed at a frequency of $0.25eV$, which coincidentally is the same frequency of the MIR feature in the optical conductivity of the nano-size puddles that was captured by our model in the dimerized metallic state (cf. sec. 4.3.1). Thus, there is a range of pump-pulse fluence, between $3.7 \lesssim \phi_t \lesssim 9$ mJ/cm^2, where the absorption at 0.25eV is complete but the lattice structure has not changed. Thus, the experiment unambiguously demonstrates a photo-induced transformation to a long-lived state with metal-like mid IR optical properties, where the lattice structure remains in the low-temperature monoclinic M_1 phase. This state differs from the equilibrium rutile metal crystallographically, in that it only involves a reorganization of charge density rather than a transition to the isotropic 3D electronic state of the high temperature phase Haverkort et al. [2005], Koethe et al. [2006].

We have shown in sec. 3.1.4 that an optical transition from the bonding to the anti-bonding band should follow from the double-peak structure of the low-energy part of the density of states (cf. inset fig.4.13). This produces a mid-infra-red (MIR) peak in the optical conductivity, which was detected in the near-field data of Qazilbash et al. [2007], cf. sec. 4.3.1. In a remarkable coincidence, Morrison et al. [2014] use the same frequency to probe for a metallic state. It would be very interesting to test how the infra-red transmittance may eventually change at larger time scales and at higher fluences, which can trigger the structural transition.

In such a case, our model has specific predictions, which are shown in Fig. 4.13. We superpose on the left hand side panels the optical spectra for the dimer metal and the insulator along with their difference. On the right hand side we show the corresponding calculations for the "rutile' (i.e. $t_\perp = 0$) metal. Thus, as seen from the spectra, the transmittance at $0.25eV$ is expected to recover as the MIR peak should disappear upon the lattice structural change.

Moreover, from our model we may predict the changes in the full frequency range for fluences between 3.7 and 9 mJ/cm^2. This prediction could in principle be tested by measuring the transmittance (or reflectivity) at different frequencies. This would be an exciting test for the further validation of our model.

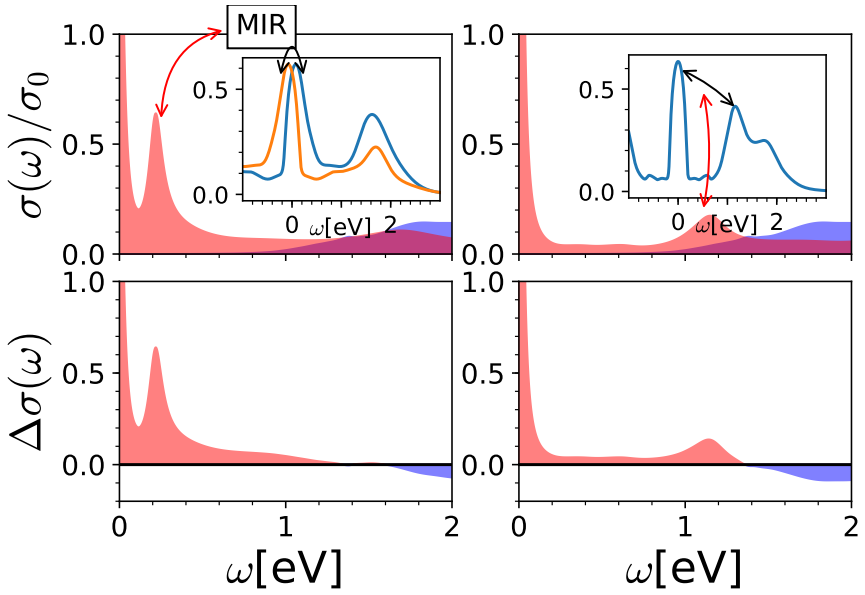

Figure 4.13: Optical conductivity with a mid-infrared resonance in the left panel corresponding to the dimer metal. On the right is the comparison to the optical response where one to find a non-dimerized metal.

Chapter 5

Conclusions

In this thesis we have studied in detail the solution of a basic strongly correlated model, namely, the dimer Hubbard model. From a large perspective, our work's systematic investigation of the model parameter space should shed light for the classification of a large variety of monoclinic transition metal oxide systems with the MO_2 formula Hiroi [2015] and more generally structures with a dominating bond between a pair of correlated metallic ions. Important cases are, of course, VO_2, which we considered in detail in the present thesis, and also NbO_2, which is also of great interest as it has a similar IMT at significantly higher temperature.

This model is also interesting in its own right as is arguably the simplest realization of a cluster DMFT problem. It is rather surprising that after almost 20 years from its original formulation Moeller et al. [1999] this basic model has remained poorly understood. Understanding it turned out to be a challenge and the emerging physical behavior that we found is rich, subtle and experimentally relevant, as we have argued.

We provided a detailed description of the solutions in the "coexistent region" where two (meta)stable states of the DMFT equations are found, one a metal and the other an insulator. Moreover, we described in detail how these states break down at their respective critical lines. We have clarified the key role played by the intra-dimer correlation, which here acts in addition to the familiar onsite Coulomb correlations (Mott-Hubbard) already present in the one-band case. Their interplay (i.e. Kondo screening vs RKKY) determines the physics of the metal-to-insulator transition line as the instance where the renormalized low-energy composing bonding and anti-bonding bands separate. This transition bears resemblance then with a band-transition, however here one deals with strongly renormalized quasiparticle bands. The transition point is determined by the intra-dimer correlation renormalizing the intra-dimer hopping $t_\perp$, rather than by the usual local correlation producing a quasiparticle residue Z, which does not vanish at the transition point. This was made explicit by means of our R2B model parametrization, which is always applicable in the metallic side on the full $t_\perp - U$ phase diagram at low enough frequencies.

The simplicity of the DHM provides new and detailed physical insight and allows us to clarify the important issue of the Mott-Peierls insulator crossover. We find a surprisingly

subtle evolution of the electronic structure with the systematic change of model parameters. In fact, the crossover from the Mott to the Peierls limit is non-trivial and we characterized a variety of physical regimes. Interestingly, we found that the Hubbard bands evolve from purely incoherent (Mott) to purely coherent (Peierls) through a state with unexpected mixed character. This feature can be understood as follows: in the Mott limit, at low intra-dimer hopping $t_\perp$, one has emergent magnetic degrees of freedom that remain freely fluctuating above a (low) spin singlet pairing temperature T^*. Increasing the intra-dimer hopping binds these free moments into a spin singlet state and they acquire coherence (i.e. a well-defined quantum state) within the dimer. However, higher energy excitations of such a state still lack coherence through the lattice and give origin to the Hubbard bands. We may think of this insulator state as Mott-localized singlet-dimers. Upon further increase of the intra-dimer hopping the bonding orbital becomes fully occupied as one may consider the $t_\perp$-dimerization as an effective crystal field. Hence, the system becomes orbitally polarized in the bonding/anti-bonding basis, which renders the electronic structure coherent as quantum fluctuations are frozen out. Nevertheless, even in this large $t_\perp$ limit the gap remains controlled by the interaction U. Therefore, the system remains a Mott insulator at high enough U (zone III on Fig. 3.14), although it is in an orbitally polarized state, in the bonding/anti-bonding basis.

The finite temperature study of this model allows us to find a singlet pairing temperature T^* below which the localized electrons at each atomic site can bind into a singlet and quench their entropy, this uncovers a new paradigm of a non-magnetic Mott insulator. We also investigated the evolution of the insulator's spectral function features as a function of temperature. In particular, we studied in detail the question of the closing of the gap and how the insulator turns into a finite temperature bad metal. We also showed how the shape of the coexistence region depends on the dimerization parameter $t_\perp$, which could turn the well known thermal metal-to-insulator transition of the single band Hubbard model ($t_\perp = 0$) into an insulator-to-metal one as occurs in VO_2.

The studied dimer Hubbard model under DMFT has an impurity problem which is simpler (i.e. no multi orbital and crystal field) but, nevertheless, has an analogue form (i.e. correlated dimer in a medium) to that of technically complex LDA+DMFT approaches used for the theoretical characterization of VO_2. We think that the present solution of the DHM may bring the equivalent physical insight for VO_2, as the DMFT studies of the single band Hubbard model dealing with the Mott transition have provided for that of experimental paramagnetic Cr-doped V_2O_3, which is one of the significant achievements of DMFT Georges et al. [1996], Kotliar and Vollhardt [2004]. Specifically, our work contributes to shed light on the longstanding question of the driving force behind the Mott transition of VO_2, where we show that the monoclinic structure can support a purely electronic a first order transition from a monoclinic insulator to a monoclinic metal.

To this aim we have discussed the relevance of our results for the interpretation of various

experimental studies in VO_2. Several physical mechanisms have clearly emerged from our study: The first is a Mott insulator where the magnetic entropy of the localized moments is quenched by a boosted super-exchange, which may provide an extra binding energy to stabilize the lattice deformation. The second, is a correlated metal with two heavy quasiparticle bands that are split by the intra-dimer hopping, which gives rises to particular feature in the optical conductivity of the correlated metallic state observed in the thermally activated phase transition. Third, the insulator's spectral function is not conformed of rigid bands, temperature can induce drastic changes in the optical response of the material allowing for a more detailed characterization of the material at the transition, as the scattering near-field optical microscopy shows. Fourth, the fact that the metallic nano-regions that form close to the transition are non-percolating shows the clear enthalpy of formation between these phases but also the coexistence character between both. Fifth, the coexistence of these phases can extent up to zero temperature as found by Cocker et al. [2012], with a transition threshold independent of temperature, proving further information on the nature of the coexistent character of these two phases. We have presented a variety of arguments that allow us to advance the conclusion that the long-lived (meta-stable) metallic phase induced in pump-probe experiments and the thermally activated M_1 meta-stable metallic state in nano-domains accessed optically are the same, and that they may all be qualitatively described by the dimerized correlated metal state of our model.

Our work has provided some answers but also opened new interesting questions, which are worth considering into the future. For instance, with respect to the transition in VO_2 we provided a rationalization for the thermally induced insulator-to-metal transition by heating. We discussed the electronic driven instability of the dimerized lattice. Once the transition to the higher temperature monoclinic metallic state takes place, the lattice clearly has no advantage in keeping the distortion. Thus, this promotes the structural transition into the less distorted rutile phase, which should improve the kinetic energy. This interpretation is very consistent with the experimental pump-probe data. However, it also opens the question of whether there are any precursor features of a metal-to-insulator transition upon cooling. An eventual asymmetry observed in the dynamics of the growth of one phase into the other by cooling versus heating may provide interesting information in this respect. Studies of this sort have already been done in the related V_2O_3 system McLeod et al. [2016].

Another important direction for future work is the study of the effect of doping. Experimentally it is quite a challenge to dope VO_2. Therefore, studies of the doped DHM may provide very useful insights. Our preliminary studies hint at various unexpected behaviors, which certainly call for further study and verification. For instance, similarly as we have seen how small temperature variations can melt the narrow quasiparticles at the Hubbard band edges, we have observed that small variations the chemical potential can also have a large effect. Since we have characterized our gap as correlated-dimerization driven and producing local singlets, we may speculate that doping may bear some similarities to the physics of cuprate

superconductors. This is certainly an exciting direction worth pursuing.

References

C. H. Ahn, A. Bhattacharya, M. D. Ventra, J. N. Eckstein, C. D. Frisbie, M. E. Gershenson, A. M. Goldman, I. H. Inoue, J. Mannhart, A. J. Millis, A. F. Morpurgo, D. Natelson, and J.-M. Triscone. Electrostatic modification of novel materials. *Reviews of Modern Physics*, 78(4):1185–1212, 2006. doi: 10.1103/revmodphys.78.1185. URL https://doi.org/10.1103/revmodphys.78.1185.

P. W. Anderson. Localized magnetic states in metals. *Physical Review*, 124(1):41–53, 1961. doi: 10.1103/physrev.124.41. URL https://doi.org/10.1103/physrev.124.41.

E. Arcangeletti, L. Baldassarre, D. D. Castro, S. Lupi, L. Malavasi, C. Marini, A. Perucchi, and P. Postorino. Evidence of a pressure-induced metallization process in monoclinic VO_2. *Physical Review Letters*, 98(19):196406, May 2007. ISSN 0031-9007, 1079-7114. doi: 10.1103/physrevlett.98.196406. URL https://doi.org/10.1103/physrevlett.98.196406.

M. Balzer, B. Kyung, D. Sénéchal, A.-M. S. Tremblay, and M. Potthoff. First-order Mott transition at zero temperature in two dimensions: Variational plaquette study. *EPL (Europhysics Letters)*, 85(1):17002, 2009. doi: 10.1209/0295-5075/85/17002. URL http://dx.doi.org/10.1209/0295-5075/85/17002.

M. F. Becker, A. B. Buckman, R. M. Walser, T. Lépine, P. Georges, and A. Brun. Femtosecond laser excitation of the semiconductor-metal phase transition in VO_2. *Applied Physics Letters*, 65(12):1507–1509, 1994. doi: 10.1063/1.112974. URL https://doi.org/10.1063/1.112974.

A. S. Belozerov, M. A. Korotin, V. I. Anisimov, and A. I. Poteryaev. Monoclinic M_1 phase of VO_2 : Mott-Hubbard versus band insulator. *Phys. Rev. B*, 85(4):045109, 2012. doi: 10.1103/physrevb.85.045109. URL http://dx.doi.org/10.1103/PhysRevB.85.045109.

S. Biermann, A. Poteryaev, A. I. Lichtenstein, and A. Georges. Dynamical singlets and correlation-assisted Peierls transition in VO_2. *Physical Review Letters*, 94(2):26404, 2005. ISSN 0031-9007. doi: 10.1103/physrevlett.94.026404. URL https://doi.org/10.1103/physrevlett.94.026404.

W. F. Brinkman and T. M. Rice. Application of gutzwiller's variational method to the metal-insulator transition. *Physical Review B*, 2(10):4302–4304, nov 1970. ISSN 0556-2805. doi: 10.1103/physrevb.2.4302. URL https://doi.org/10.1103/physrevb.2.4302.

W. H. Brito, M. C. O. Aguiar, K. Haule, and G. Kotliar. Metal-insulator transition in VO_2: A DFT+DMFT perspective. *Phys. Rev. Lett.*, 117(5), July 2016. ISSN 0031-9007,

1079-7114. doi: 10.1103/physrevlett.117.056402. URL http://dx.doi.org/10.1103/PhysRevLett.117.056402.

R. Bulla, A. C. Hewson, and T. Pruschke. Numerical renormalization group calculations for the self-energy of the impurity anderson model. *Journal of Physics: Condensed Matter*, 10(37):8365–8380, 1998. doi: 10.1088/0953-8984/10/37/021. URL https://doi.org/10.1088/0953-8984/10/37/021.

T. L. Cocker, L. V. Titova, S. Fourmaux, G. Holloway, H.-C. Bandulet, D. Brassard, J.-C. Kieffer, M. A. E. Khakani, and F. A. Hegmann. Phase diagram of the ultrafast photoinduced insulator-metal transition in vanadium dioxide. *Physical Review B*, 85(15):155120, 2012. doi: 10.1103/physrevb.85.155120. URL https://doi.org/10.1103/physrevb.85.155120.

S. Doniach. The kondo lattice and weak antiferromagnetism. *Physica B+C*, 91(Supplement C):231–234, 1977. doi: 10.1016/0378-4363(77)90190-5. URL https://doi.org/10.1016/0378-4363(77)90190-5.

E. N. Economou. *Green's Functions in Quantum Physics*. Number 7 in Springer series in solid-state sciences. Springer, Berlin, 3. ed edition, 2006. ISBN 978-3-540-28838-1.

V. J. Emery. Correlated electron systems. In *Correlated Electron Systems: Proceedings of the 9th Jerusalem Winter School for Theoretical Physics*, pages 1–364, 8 1993. doi: 10.1142/9789814536363. URL https://doi.org/10.1142/9789814536363.

V. Eyert. The metal-insulator transitions of VO_2: A band theoretical approach. *Annalen der Physik*, 11(9):650–704, 2002.

V. Eyert. VO_2 : A novel view from band theory. *Physical Review Letters*, 107(1):016401, 2011. doi: 10.1103/physrevlett.107.016401. URL http://dx.doi.org/10.1103/physrevlett.107.016401.

A. L. Fetter and J. D. Walecka. *Quantum theory of many-particle systems*. Courier Corporation, 2003.

A. Fuhrmann, D. Heilmann, and H. Monien. From Mott insulator to band insulator: A dynamical mean-field theory study. *Physical Review B*, 73(24):245118, 2006. doi: 10.1103/physrevb.73.245118. URL https://doi.org/10.1103/physrevb.73.245118.

D. J. García, K. Hallberg, and M. J. Rozenberg. Dynamical mean field theory with the density matrix renormalization group. *Physical Review Letters*, 93(24):246403, 2004. doi: 10.1103/physrevlett.93.246403. URL https://doi.org/10.1103/physrevlett.93.246403.

F. Gebhard, K. Bott, M. Scheidler, P. Thomas, and S. W. Koch. Optical absorption of non-interacting tight-binding electrons in a Peierls-distorted chain at half band-filling. *Philosophical Magazine Part B*, 75(1):1–12, Jan. 1997. ISSN 1364-2812, 1463-6417. doi: 10.1080/13642819708205700.

A. Georges and G. Kotliar. Hubbard model in infinite dimensions. *Physical Review B*, 45 (12):6479–6483, 1992. doi: 10.1103/physrevb.45.6479. URL https://doi.org/10.1103/physrevb.45.6479.

A. Georges and W. Krauth. Physical properties of the half-filled hubbard model in infinite dimensions. *Physical Review B*, 48(10):7167–7182, 1993. doi: 10.1103/physrevb.48.7167. URL https://doi.org/10.1103/physrevb.48.7167.

A. Georges, G. Kotliar, W. Krauth, and M. J. Rozenberg. Dynamical mean-field theory of strongly correlated fermion systems and the limit of infinite dimensions. *Reviews of Modern Physics*, 68(1):13–125, 1996. doi: 10.1103/revmodphys.68.13. URL https://doi.org/10.1103/revmodphys.68.13.

M. Golor, T. Reckling, L. Classen, M. M. Scherer, and S. Wessel. Ground-state phase diagram of the half-filled bilayer Hubbard model. *Physical Review B*, 90(19):195131, 2014. doi: 10.1103/physrevb.90.195131. URL https://doi.org/10.1103/physrevb.90.195131.

J. B. Goodenough. Direct Cation- -Cation Interactions in Several Oxides. *Physical Review*, 117(6):1442–1451, 1960. doi: 10.1103/physrev.117.1442. URL https://doi.org/10.1103/physrev.117.1442.

D. Grieger, C. Piefke, O. E. Peil, and F. Lechermann. Approaching finite-temperature phase diagrams of strongly correlated materials: A case study for v2o3. *Physical Review B*, 86 (15):155121, 2012. doi: 10.1103/physrevb.86.155121. URL https://doi.org/10.1103/physrevb.86.155121.

E. Gull, P. Werner, A. Millis, and M. Troyer. Performance analysis of continuous-time solvers for quantum impurity models. *Physical Review B*, 76(23):1–9, dec 2007. ISSN 10980121. doi: 10.1103/physrevb.76.235123. URL https://doi.org/10.1103/physrevb.76.235123.

E. Gull, A. J. Millis, A. I. Lichtenstein, A. N. Rubtsov, M. Troyer, and P. Werner. Continuous-time monte carlo methods for quantum impurity models. *Reviews of Modern Physics*, 83 (2):349–404, 2011. doi: 10.1103/revmodphys.83.349. URL https://doi.org/10.1103/revmodphys.83.349.

O. Gunnarsson, M. Calandra, and J. E. Han. Colloquium: Saturation of electrical resistivity. *Reviews of Modern Physics*, 75(4):1085–1099, Oct 2003. doi: 10.1103/revmodphys.75.1085. URL https://doi.org/10.1103/revmodphys.75.1085.

M. C. Gutzwiller. Effect of correlation on the ferromagnetism of transition metals. *Physical Review Letters*, 10(5):159–162, 1963. doi: 10.1103/physrevlett.10.159. URL https://doi.org/10.1103/physrevlett.10.159.

H. Hafermann, M. I. Katsnelson, and A. I. Lichtenstein. Metal-insulator transition by suppression of spin fluctuations. *EPL (Europhysics Letters)*, 85(3):37006, 2009. doi: 10.1209/0295-5075/85/37006. URL https://doi.org/10.1209/0295-5075/85/37006.

P. Hansmann, A. Toschi, G. Sangiovanni, T. Saha-Dasgupta, S. Lupi, M. Marsi, and K. Held. Mott-Hubbard transition in V_2O_3 revisited. *physica status solidi (b)*, 250(7):1251–1264, 2013. doi: 10.1002/pssb.201248476. URL https://doi.org/10.1002/pssb.201248476.

M. W. Haverkort, Z. Hu, A. Tanaka, W. Reichelt, S. V. Streltsov, M. A. Korotin, V. I. Anisimov, H. H. Hsieh, H.-J. Lin, C. T. Chen, D. I. Khomskii, and L. H. Tjeng. Orbital-assisted metal-insulator transition in VO_2. *Physical Review Letters*, 95(19):196404, 2005. doi: 10.1103/physrevlett.95.196404. URL https://doi.org/10.1103/physrevlett.95.196404.

Z. Hiroi. Structural instability of the rutile compounds and its relevance to the metal-insulator transition of VO_2. *Progress in Solid State Chemistry*, 43(1-2):47–69, 2015. doi: 10.1016/j.progsolidstchem.2015.02.001. URL https://doi.org/10.1016/j.progsolidstchem.2015.02.001.

J. E. Hirsch and R. M. Fye. Monte carlo method for magnetic impurities in metals. *Physical Review Letters*, 56(23):2521–2524, 1986. doi: 10.1103/physrevlett.56.2521. URL https://doi.org/10.1103/physrevlett.56.2521.

J. Hubbard. Electron correlations in narrow energy bands. *Proceedings of the Royal Society A: Mathematical, Physical and Engineering Sciences*, 276(1365):238–257, 1963. ISSN 1364-5021. doi: 10.1098/rspa.1963.0204. URL https://doi.org/10.1098/rspa.1963.0204.

T. J. Huffman, C. Hendriks, E. J. Walter, J. Yoon, H. Ju, R. Smith, G. L. Carr, H. Krakauer, and M. M. Qazilbash. Insulating phases of vanadium dioxide are Mott-Hubbard insulators. *Physical Review B*, 95(7):075125, 2017. doi: 10.1103/physrevb.95.075125. URL https://doi.org/10.1103/physrevb.95.075125.

M. Imada, A. Fujimori, and Y. Tokura. Metal-Insulator transitions. *Reviews of Modern Physics*, 70(4):1039–1263, oct 1998. ISSN 0034-6861. doi: 10.1103/RevModPhys.70.1039. URL http://link.aps.org/doi/10.1103/RevModPhys.70.1039.

M. Jarrell. Hubbard model in infinite dimensions: A quantum monte carlo study. *Physical Review Letters*, 69(1):168–171, 1992. doi: 10.1103/physrevlett.69.168. URL https://doi.org/10.1103/physrevlett.69.168.

M. Jarrell and J. Gubernatis. Bayesian inference and the analytic continuation of imaginary-time quantum monte carlo data. *Physics Reports*, 269(3):133–195, 1996. doi: 10.1016/0370-1573(95)00074-7. URL https://doi.org/10.1016/0370-1573(95)00074-7.

J. Joo and V. Oudovenko. Quantum monte carlo calculation of the finite temperature Mott-Hubbard transition. *Physical Review B*, 64(19):193102, 2001. ISSN 0163-1829. doi: 10.1103/physrevb.64.193102. URL https://doi.org/10.1103/physrevb.64.193102.

S. S. Kancharla and S. Okamoto. Band insulator to Mott insulator transition in a bilayer

Hubbard model. *Physical Review B*, 75(19):1–4, 2007. doi: 10.1103/physrevb.75.193103. URL https://doi.org/10.1103/physrevb.75.193103.

M. Karski, C. Raas, and G. S. Uhrig. Single-particle dynamics in the vicinity of the Mott-Hubbard metal-to-insulator transition. *Physical Review B*, 77(7):075116, 2008. doi: 10.1103/physrevb.77.075116. URL https://doi.org/10.1103/physrevb.77.075116.

F. Keilmann and R. Hillenbrand. Near-field microscopy by elastic light scattering from a tip. *Philosophical Transactions of the Royal Society A: Mathematical, Physical and Engineering Sciences*, 362(1817):787–805, 2004. doi: 10.1098/rsta.2003.1347. URL https://doi.org/10.1098/rsta.2003.1347.

A. Khurana. Electrical conductivity in the infinite-dimensional hubbard model. *Physical Review Letters*, 64(16):1990–1990, 1990. doi: 10.1103/physrevlett.64.1990. URL https://doi.org/10.1103/physrevlett.64.1990.

H.-T. Kim, Y. W. Lee, B.-J. Kim, B.-G. Chae, S. J. Yun, K.-Y. Kang, K.-J. Han, K.-J. Yee, and Y.-S. Lim. Monoclinic and correlated metal phase in VO_2 as evidence of the Mott transition: Coherent phonon analysis. *Physical Review Letters*, 97(26):266401, 2006. doi: 10.1103/physrevlett.97.266401. URL https://doi.org/10.1103/physrevlett.97.266401.

T. C. Koethe, Z. Hu, M. W. Haverkort, C. Schüßler-Langeheine, F. Venturini, N. B. Brookes, O. Tjernberg, W. Reichelt, H. H. Hsieh, H.-J. Lin, C. T. Chen, and L. H. Tjeng. Transfer of spectral weight and symmetry across the metal-insulator transition in VO_2. *Physical Review Letters*, 97(11), 2006. doi: 10.1103/physrevlett.97.116402. URL https://doi.org/10.1103/physrevlett.97.116402.

G. Kotliar and D. Vollhardt. Strongly correlated materials: Insights from dynamical mean-field theory. *Physics Today*, 57(3):53–59, 2004. doi: 10.1063/1.1712502. URL https://doi.org/10.1063/1.1712502.

G. Kotliar, E. Lange, and M. J. Rozenberg. Landau theory of the finite temperature Mott transition. *Physical Review Letters*, 84(22):5180–5183, 2000. doi: 10.1103/physrevlett.84.5180. URL http://dx.doi.org/10.1103/physrevlett.84.5180.

G. Kotliar, S. Y. Savrasov, G. Pálsson, and G. Biroli. Cellular dynamical mean field approach to strongly correlated systems. *Physical Review Letters*, 87(18):186401, 2001. doi: 10.1103/physrevlett.87.186401. URL https://doi.org/10.1103/physrevlett.87.186401.

C. Kübler, H. Ehrke, R. Huber, R. Lopez, A. Halabica, R. F. Haglund, and A. Leitenstorfer. Coherent structural dynamics and electronic correlations during an ultrafast insulator-to-metal phase transition in VO_2. *Physical Review Letters*, 99(11):116401, 2007. doi: 10.1103/physrevlett.99.116401. URL https://doi.org/10.1103/physrevlett.99.116401.

L. A. Ladd and W. Paul. Optical and transport properties of high quality crystals of

V_2O_4 near the metallic transition temperature. *Solid State Communications*, 7(4):425–428, 1969. doi: 10.1016/0038-1098(69)90888-6. URL https://doi.org/10.1016/0038-1098(69)90888-6.

E. Lange. Renormalized versus unrenormalized perturbation-theoretical approaches to the Mott transition. *Modern Physics Letters B*, 12(22):915–919, 1998. doi: 10.1142/s0217984998001050. URL https://doi.org/10.1142/s0217984998001050.

J. Laverock, S. Kittiwatanakul, A. A. Zakharov, Y. R. Niu, B. Chen, S. A. Wolf, J. W. Lu, and K. E. Smith. Direct observation of decoupled structural and electronic transitions and an ambient pressure monocliniclike metallic phase of VO_2. *Phys. Rev. Lett.*, 113 (21), Nov. 2014. ISSN 0031-9007, 1079-7114. doi: 10.1103/physrevlett.113.216402. URL http://dx.doi.org/10.1103/PhysRevLett.113.216402.

B. Lazarovits, K. Kim, K. Haule, and G. Kotliar. Effects of strain on the electronic structure of VO_2. *Physical Review B*, 81(11):115117, 2010. doi: 10.1103/physrevb.81.115117. URL https://doi.org/10.1103/physrevb.81.115117.

H. Lee, Y.-Z. Zhang, H. O. Jeschke, and R. Valentí. Competition between band and Mott insulators in the bilayer Hubbard model: A dynamical cluster approximation study. *Physical Review B*, 89(3):3–8, 2014. ISSN 10980121. doi: 10.1103/physrevb.89.035139. URL https://doi.org/10.1103/physrevb.89.035139.

M. Liu, A. J. Sternbach, M. Wagner, T. V. Slusar, T. Kong, S. L. Bud'ko, S. Kittiwatanakul, M. M. Qazilbash, A. McLeod, Z. Fei, E. Abreu, J. Zhang, M. Goldflam, S. Dai, G.-X. Ni, J. Lu, H. A. Bechtel, M. C. Martin, M. B. Raschke, R. D. Averitt, S. A. Wolf, H.-T. Kim, P. C. Canfield, and D. N. Basov. Phase transition in bulk single crystals and thin films of VO_2 by nanoscale infrared spectroscopy and imaging. *Physical Review B*, 91(24), Jun 2015. ISSN 1550-235X. doi: 10.1103/physrevb.91.245155. URL http://dx.doi.org/10.1103/physrevb.91.245155.

M. K. Liu, M. Wagner, E. Abreu, S. Kittiwatanakul, A. McLeod, Z. Fei, M. Goldflam, S. Dai, M. M. Fogler, J. Lu, S. A. Wolf, R. D. Averitt, and D. N. Basov. Anisotropic electronic state via spontaneous phase separation in strained vanadium dioxide films. *Physical Review Letters*, 111(9):096602, 2013. doi: 10.1103/physrevlett.111.096602. URL http://dx.doi.org/10.1103/PhysRevLett.111.096602.

W.-T. Liu, J. Cao, W. Fan, Z. Hao, M. C. Martin, Y. R. Shen, J. Wu, and F. Wang. Intrinsic optical properties of vanadium dioxide near the insulator-metal transition. *Nano Letters*, 11 (2):466–470, 2011. doi: 10.1021/nl1032205. URL https://doi.org/10.1021/nl1032205.

T. Maier, M. Jarrell, T. Pruschke, and M. H. Hettler. Quantum cluster theories. *Reviews of Modern Physics*, 77(3):1027–1080, 2005. doi: 10.1103/revmodphys.77.1027. URL https://doi.org/10.1103/revmodphys.77.1027.

C. Marini, L. Baldassarre, M. Baldini, A. Perucchi, D. D. Castro, L. Malavasi, S. Lupi, and P. Postorino. Evidence for a monoclinic metallic phase in high-pressure VO_2. *High Pressure Research*, 30(1):55–59, Mar. 2010. ISSN 0895-7959, 1477-2299. doi: 10.1080/08957951003600756. URL http://dx.doi.org/10.1080/08957951003600756.

B. Mayer, C. Schmidt, A. Grupp, J. Bühler, J. Oelmann, R. E. Marvel, R. F. Haglund, T. Oka, D. Brida, A. Leitenstorfer, and A. Pashkin. Tunneling breakdown of a strongly correlated insulating state in VO_2 induced by intense multiterahertz excitation. *Physical Review B*, 91(23):235113, 2015. doi: 10.1103/physrevb.91.235113. URL https://doi.org/10.1103/physrevb.91.235113.

G. Mazza, A. Amaricci, M. Capone, and M. Fabrizio. Field-driven Mott gap collapse and resistive switch in correlated insulators. *Physical Review Letters*, 117(17):176401, 2016. doi: 10.1103/physrevlett.117.176401. URL https://doi.org/10.1103/physrevlett.117.176401.

A. S. McLeod, P. Kelly, M. D. Goldflam, Z. Gainsforth, A. J. Westphal, G. Dominguez, M. H. Thiemens, M. M. Fogler, and D. N. Basov. Model for quantitative tip-enhanced spectroscopy and the extraction of nanoscale-resolved optical constants. *Physical Review B*, 90(8):085136, 2014. doi: 10.1103/physrevb.90.085136. URL https://doi.org/10.1103/physrevb.90.085136.

A. S. McLeod, E. van Heumen, J. G. Ramirez, S. Wang, T. Saerbeck, S. Guenon, M. Goldflam, L. Anderegg, P. Kelly, A. Mueller, M. K. Liu, I. K. Schuller, and D. N. Basov. Nanotextured phase coexistence in the correlated insulator V_2O_3. *Nature Physics*, 13(1):80–86, 2016. doi: 10.1038/nphys3882. URL https://doi.org/10.1038/nphys3882.

N. Metropolis, A. W. Rosenbluth, M. N. Rosenbluth, A. H. Teller, and E. Teller. Equation of state calculations by fast computing machines. *The Journal of Chemical Physics*, 21(6):1087–1092, 1953. ISSN 00219606. doi: 10.1063/1.1699114. URL https://doi.org/10.1063/1.1699114.

W. Metzner and D. Vollhardt. Correlated lattice fermions in $d = \infty$ dimensions. *Physical Review Letters*, 62(3):324–327, 1989. doi: 10.1103/physrevlett.62.324. URL https://doi.org/10.1103/physrevlett.62.324.

A. J. Millis. *Optical Conductivity and Correlated Electron Physics*. Physics and chemistry of materials with low-dimensional structures. Kluwer Academic Publishers, July 2004. doi: 10.1007/978-1-4020-3463-3_7. URL https://doi.org/10.1007/978-1-4020-3463-3_7.

G. Moeller, V. Dobrosavljević, and A. E. Ruckenstein. RKKY interactions and the Mott transition. *Physical Review B*, 59(10):6846–6854, mar 1999. ISSN 0163-1829. doi: 10.1103/physrevb.59.6846. URL https://doi.org/10.1103/physrevb.59.6846.

F. J. Morin. Oxides which show a metal-to-insulator transition at the neel temperature.

Physical Review Letters, 3(1):34–36, 1959. doi: 10.1103/physrevlett.3.34. URL https://doi.org/10.1103/physrevlett.3.34.

V. R. Morrison, R. P. Chatelain, K. L. Tiwari, A. Hendaoui, A. Bruhács, M. Chaker, and B. J. Siwick. A photoinduced metal-like phase of monoclinic VO_2 revealed by ultrafast electron diffraction. *Science*, 346(6208):445–448, 2014. doi: 10.1126/science.1253779. URL https://doi.org/10.1126/science.1253779.

E. Müller-Hartmann. The hubbard model at high dimensions: Some exact results and weak coupling theory. *Zeitschrift für Physik B Condensed Matter*, 76(2):211–217, 1989a. doi: 10.1007/bf01312686. URL https://doi.org/10.1007/bf01312686.

E. Müller-Hartmann. Correlated fermions on a lattice in high dimensions. *Zeitschrift für Physik B Condensed Matter*, 74(4):507–512, 1989b. doi: 10.1007/bf01311397. URL https://doi.org/10.1007/bf01311397.

J. Nag, R. F. Haglund, E. Andrew Payzant, and K. L. More. Non-congruence of thermally driven structural and electronic transitions in VO_2. *Journal of Applied Physics*, 112(10): 103532, 2012. ISSN 00218979. doi: 10.1063/1.4764040.

O. Nájera, M. Civelli, V. Dobrosavljević, and M. J. Rozenberg. Resolving the VO_2 controversy: Mott mechanism dominates the insulator-to-metal transition. *Physical Review B*, 95 (3):035113, 2017. doi: 10.1103/physrevb.95.035113. URL https://doi.org/10.1103/physrevb.95.035113.

M. Nakajima, N. Takubo, Z. Hiroi, Y. Ueda, and T. Suemoto. Photoinduced metallic state in VO_2 proved by the terahertz pump-probe spectroscopy. *Applied Physics Letters*, 92(1): 011907, 2008. doi: 10.1063/1.2830664. URL https://doi.org/10.1063/1.2830664.

J. Negele and H. Orland. *Quantum many-particle systems*. Frontiers in physics. Addison-Wesley Pub. Co., 1988. ISBN 9780201125931. URL https://books.google.fr/books?id=EV8sAAAAYAAJ.

R. M. Noack and F. Gebhard. Mott-Hubbard transition in infinite dimensions. *Physical Review Letters*, 82(9):1915–1918, 1999. doi: 10.1103/physrevlett.82.1915. URL https://doi.org/10.1103/physrevlett.82.1915.

L. Novotny and B. Hecht. *Principles of Nano-Optics*. Cambridge University Press, 2. ed edition, 2012.

B. T. O'Callahan, A. C. Jones, J. H. Park, D. H. Cobden, J. M. Atkin, and M. B. Raschke. Inhomogeneity of the ultrafast insulator-to-metal transition dynamics of VO_2. *Nature Communications*, 6:6849, Apr. 2015. ISSN 2041-1723. doi: 10.1038/ncomms7849. URL http://dx.doi.org/10.1038/ncomms7849.

O. Parcollet, G. Biroli, and G. Kotliar. Cluster dynamical mean field analysis of the Mott transition. *Physical Review Letters*, 92(22), June 2004. ISSN 0031-9007, 1079-7114.

doi: 10.1103/physrevlett.92.226402. URL http://dx.doi.org/10.1103/PhysRevLett.92.226402.

H. Park, K. Haule, and G. Kotliar. Cluster Dynamical Mean Field Theory of the Mott transition. *Physical Review Letters*, 101(18):186403, 2008. ISSN 00319007. doi: 10.1103/PhysRevLett.101.186403. URL https://doi.org/10.1103/PhysRevLett.101.186403.

A. Pashkin, C. Kübler, H. Ehrke, R. Lopez, A. Halabica, R. F. Haglund, R. Huber, and A. Leitenstorfer. Ultrafast insulator-metal phase transition in $V0_2$ studied by multiterahertz spectroscopy. *Physical Review B*, 83(19):195120, 2011. doi: 10.1103/physrevb.83.195120. URL https://doi.org/10.1103/physrevb.83.195120.

A. Pergament. Metal-insulator transition: the Mott criterion and coherence length. *Journal of Physics: Condensed Matter*, 15(19):3217–3223, 2003. doi: 10.1088/0953-8984/15/19/322. URL https://doi.org/10.1088/0953-8984/15/19/322.

D. Pines and P. Nozières. *The Theory of Quantum Liquids: Normal Fermi liquids*. The Theory of Quantum Liquids. W.A. Benjamin, 1966. URL https://books.google.fr/books?id=263vAAAAMAAJ.

A. I. Poteryaev, J. M. Tomczak, S. Biermann, A. Georges, A. I. Lichtenstein, A. N. Rubtsov, T. Saha-Dasgupta, and O. K. Andersen. Enhanced crystal-field splitting and orbital-selective coherence induced by strong correlations inv2o3. *Physical Review B*, 76(8):085127, 2007. doi: 10.1103/physrevb.76.085127. URL https://doi.org/10.1103/physrevb.76.085127.

J. P. Pouget, H. Launois, T. M. Rice, P. Dernier, A. Gossard, G. Villeneuve, and P. Hagenmuller. Dimerization of a linear heisenberg chain in the insulating phases of $V_{1-x}Cr_xO_2$. *Physical Review B*, 10(5):1801–1815, 1974. doi: 10.1103/physrevb.10.1801. URL https://doi.org/10.1103/physrevb.10.1801.

B. J. Powell and R. H. McKenzie. Strong electronic correlations in superconducting organic charge transfer salts. *Journal of Physics: Condensed Matter*, 18(45):R827–R866, 2006. doi: 10.1088/0953-8984/18/45/r03. URL https://doi.org/10.1088/0953-8984/18/45/r03.

T. Pruschke, D. L. Cox, and M. Jarrell. Hubbard model at infinite dimensions: Thermodynamic and transport properties. *Physical Review B*, 47(7):3553, 1993.

M. M. Qazilbash, M. Brehm, B.-G. Chae, P.-C. Ho, G. O. Andreev, B.-J. Kim, S. J. Yun, A. V. Balatsky, M. B. Maple, F. Keilmann, H.-T. Kim, and D. N. Basov. Mott transition in VO_2 revealed by infrared spectroscopy and nano-imaging. *Science*, 318(5857):1750–1753, 2007. doi: 10.1126/science.1150124. URL http://dx.doi.org/10.1126/science.1150124.

M. M. Qazilbash, A. Tripathi, A. A. Schafgans, B.-J. Kim, H.-T. Kim, Z. Cai, M. V. Holt, J. M. Maser, F. Keilmann, O. G. Shpyrko, and D. N. Basov. Nanoscale imaging of the electronic

and structural transitions in vanadium dioxide. *Phys. Rev. B*, 83(16):165108, 2011. doi: 10.1103/physrevb.83.165108. URL http://dx.doi.org/10.1103/physrevb.83.165108.

M. J. Rozenberg, G. Kotliar, and X. Y. Zhang. Mott-Hubbard transition in infinite dimensions. II. *Physical Review B*, 49(15):10181–10193, 1994. doi: 10.1103/physrevb.49.10181. URL https://doi.org/10.1103/physrevb.49.10181.

M. J. Rozenberg, G. Kotliar, and H. Kajueter. Transfer of spectral weight in spectroscopies of correlated electron systems. *Physical Review B*, 54(12):8452–8468, 1996. doi: 10.1103/physrevb.54.8452. URL https://doi.org/10.1103/physrevb.54.8452.

A. N. Rubtsov, V. V. Savkin, and A. I. Lichtenstein. Continuous-time quantum monte carlo method for fermions. *Physical Review B*, 72(3):035122, jul 2005. ISSN 1098-0121. doi: 10.1103/physrevb.72.035122. URL https://doi.org/10.1103/physrevb.72.035122.

U. Schwingenschlögl and V. Eyert. The vanadium magnéli phases V_nO_{2n-1}. *Annalen der Physik*, 13(9):475–510, 2004. ISSN 0003-3804. doi: 10.1002/andp.200410099. URL https://doi.org/10.1002/andp.200410099.

P. Seth, I. Krivenko, M. Ferrero, and O. Parcollet. TRIQS/CTHYB: A continuous-time quantum Monte Carlo hybridisation expansion solver for quantum impurity problems. *Computer Physics Communications*, 200:274–284, mar 2016. doi: 10.1016/j.cpc.2015.10.023. URL https://doi.org/10.1016/j.cpc.2015.10.023.

Z. Tao, T.-R. T. Han, S. D. Mahanti, P. M. Duxbury, F. Yuan, C.-Y. Ruan, K. Wang, and J. Wu. Decoupling of structural and electronic phase transitions in VO_2. *Physical Review Letters*, 109(16):166406, 2012. doi: 10.1103/physrevlett.109.166406. URL https://doi.org/10.1103/physrevlett.109.166406.

J. M. Tomczak and S. Biermann. Effective band structure of correlated materials: the case of VO_2. *Journal of Physics: Condensed Matter*, 19(36):365206, 2007. doi: 10.1088/0953-8984/19/36/365206. URL https://doi.org/10.1088/0953-8984/19/36/365206.

J. M. Tomczak and S. Biermann. Optical properties of correlated materials: Generalized peierls approach and its application to VO_2. *Physical Review B*, 80(8), Aug. 2009. ISSN 1098-0121, 1550-235X. doi: 10.1103/physrevb.80.085117. URL http://dx.doi.org/10.1103/PhysRevB.80.085117.

J. M. Tomczak, F. Aryasetiawan, and S. Biermann. Effective bandstructure in the insulating phase versus strong dynamical correlations in metallic VO_2. *Physical Review B*, 78 (11):115103, 2008. ISSN 10980121. doi: 10.1103/physrevb.78.115103. URL https://doi.org/10.1103/physrevb.78.115103.

S. Wall, D. Wegkamp, L. Foglia, K. Appavoo, J. Nag, R. Haglund, J. Stähler, and M. Wolf. Ultrafast changes in lattice symmetry probed by coherent phonons. *Nature*

Communications, 3:721, Mar. 2012. ISSN 2041-1723. doi: 10.1038/ncomms1719. URL http://dx.doi.org/10.1038/ncomms1719.

S. Wall, L. Foglia, D. Wegkamp, K. Appavoo, J. Nag, R. F. Haglund, J. Stähler, and M. Wolf. Tracking the evolution of electronic and structural properties of VO_2 during the ultrafast photoinduced insulator-metal transition. *Phys. Rev. B*, 87(11):115126, 2013. doi: 10.1103/physrevb.87.115126. URL http://dx.doi.org/10.1103/PhysRevB.87.115126.

C. Weber, D. D. O'Regan, N. D. M. Hine, M. C. Payne, G. Kotliar, and P. B. Littlewood. Vanadium dioxide: A Peierls-Mott insulator stable against disorder. *Physical Review Letters*, 108(25):256402, jun 2012. ISSN 0031-9007. doi: 10.1103/physrevlett.108.256402. URL https://doi.org/10.1103/physrevlett.108.256402.

D. Wegkamp, M. Herzog, L. Xian, M. Gatti, P. Cudazzo, C. L. McGahan, R. E. Marvel, R. F. Haglund, A. Rubio, M. Wolf, and J. Stähler. Instantaneous band gap collapse in photoexcited monoclinic VO_2 due to photocarrier doping. *Physical Review Letters*, 113(21), 2014. doi: 10.1103/physrevlett.113.216401. URL https://doi.org/10.1103/physrevlett.113.216401.

R. M. Wentzcovitch, W. W. Schulz, and P. B. Allen. VO_2: Peierls or Mott-Hubbard? a view from band theory. *Phys. Rev. Lett.*, 72(21):3389–3392, 1994. doi: 10.1103/physrevlett.72.3389. URL https://doi.org/10.1103/physrevlett.72.3389.

P. Werner and A. J. Millis. Hybridization expansion impurity solver: General formulation and application to kondo lattice and two-orbital models. *Physical Review B*, 74(15):1–13, oct 2006. ISSN 10980121. doi: 10.1103/physrevb.74.155107. URL https://doi.org/10.1103/physrevb.74.155107.

P. Werner, A. Comanac, L. de' Medici, M. Troyer, and A. J. Millis. Continuous-time solver for quantum impurity models. *Physical Review Letters*, 97(7):076405, aug 2006. ISSN 0031-9007. doi: 10.1103/physrevlett.97.076405. URL https://doi.org/10.1103/physrevlett.97.076405.

R. Yoshida, T. Yamamoto, Y. Ishida, H. Nagao, T. Otsuka, K. Saeki, Y. Muraoka, R. Eguchi, K. Ishizaka, T. Kiss, S. Watanabe, T. Kanai, J. Itatani, and S. Shin. Ultrafast photoinduced transition of an insulating VO_2 thin film into a nonrutile metallic state. *Physical Review B*, 89(20):205114, 2014. doi: 10.1103/physrevb.89.205114. URL http://dx.doi.org/10.1103/physrevb.89.205114.

X. Y. Zhang, M. J. Rozenberg, and G. Kotliar. Mott transition in the d=∞ Hubbard model at zero temperature. *Physical Review Letters*, 70(11):1666–1669, 1993. doi: 10.1103/physrevlett.70.1666. URL https://doi.org/10.1103/physrevlett.70.1666.

Appendix A

The isolated molecule

> In almost all textbooks, even the best, this principle is presented so that it is impossible to understand. I do not choose to break with tradition.
>
> V. I. Arnold, *Mathematical Methods of Classical Mechanics*, footnote on p. 246

A.1 The Eigen system

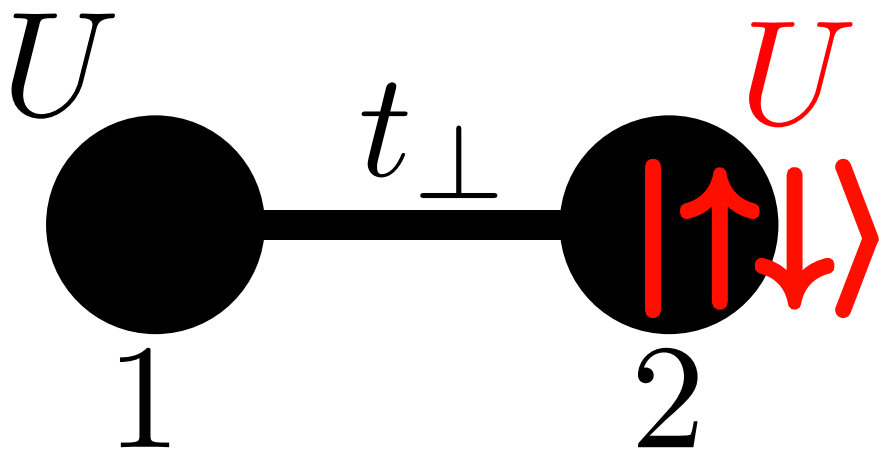

Figure A.1: Abstaction of the Hydrogen molecule. Two isolated atoms close together so that their hybridization is strong enough to bind them.

Let's devote our initial focus to the first extension to the atomic limit to study correlated behavior. Starting with a di-atomic molecule or better said the Hydrogen molecule and further referred here as the dimer, one has two neighboring atoms each with one electronic orbital which then hybridize to form a chemical bond as shown in figure A.1. It can be very easily modeled by the next Hamiltonian:

$$H = t_\perp \sum_\sigma (c^\dagger_{1\sigma} c_{2\sigma} + c^\dagger_{2\sigma} c_{1\sigma}) + U(n_{1\uparrow} n_{1\downarrow} + n_{2\uparrow} n_{2\downarrow}) - \mu \sum_{\alpha,\sigma} n_{\alpha\sigma} \tag{A.1}$$

where $c_{\alpha\sigma}$ annihilates and electron from the atomic orbital $\alpha = \{1, 2\}$ and of spin $\sigma = \{\uparrow, \downarrow\}$. $U > 0$ is the on-site repulsive Hubbard interaction and $t_\perp > 0$ the dimer hybridization. One fixes the chemical potential to ensure half-filling $\mu = U/2$. The Hamiltonian of equation (A.1) can be rewritten as:

$$\mathcal{H} = -\frac{U}{2}\left[(n_{1\uparrow} - n_{1\downarrow})^2 + (n_{2\uparrow} - n_{2\downarrow})^2\right] + t_\perp \sum_\sigma (c^\dagger_{1\sigma} c_{2\sigma} + H.c.) = \mathcal{H}_{int} + \mathcal{H}_{dim} \tag{A.2}$$

This compact form allows us to recognize that the system gains energy by localizing single electron with high spin polarization on each site. To present a solution in this work the fermionic arrangement convention is to order states by their spin projection on the z axis[1]. Thus the full occupation state vector is:

$$|1\uparrow 2\uparrow 1\downarrow 2\downarrow\rangle = c^\dagger_{1\uparrow} c^\dagger_{2\uparrow} c^\dagger_{1\downarrow} c^\dagger_{2\downarrow} |\emptyset\rangle \tag{A.3}$$

The single particle sector has 4 states, evidently as one has 4 particles. Diagonalizing this block we only find 2 distinct energy levels as up and down spin are degenerate. This 2 levels are called the bonding(B) and anti-bonding(A) levels.

$$|A\sigma\rangle = \frac{1}{\sqrt{2}}(|1\sigma\rangle + |2\sigma\rangle) \qquad E_A = -\frac{U}{2} + t_\perp \tag{A.4a}$$

$$|B\sigma\rangle = \frac{1}{\sqrt{2}}(|1\sigma\rangle - |2\sigma\rangle) \qquad E_B = -\frac{U}{2} - t_\perp \tag{A.4b}$$

Figure A.2 displays the eigen-energies of the molecule, and we can see, this single particle levels, being accounted in the $N = 1$ block. The groundstate energy is in the $N = 2$ sector and is non-degenerate $\forall U > 0$ and $t_\perp > 0$. It's value is expressed as follows:

$$E_{GS} = -\frac{U}{2} - \frac{1}{2}\sqrt{U^2 + 16t_\perp^2} \tag{A.5}$$

[1]This particular choice allows for a simple block diagonalization of Hamiltonian and thus is preferred to the usual convention to order the particles by their position.

which corresponds to the quantum state of a weighted singlet given by:

$$|GS\rangle = \frac{1}{\sqrt{\frac{32t_\perp^2}{\left(U+\sqrt{U^2+16t_\perp^2}\right)^2}+2}}\left((|2\uparrow 1\downarrow\rangle + |1\uparrow 2\downarrow\rangle) - \frac{4t_\perp}{U+\sqrt{U^2+16t_\perp^2}}(|1\uparrow\downarrow\rangle + |2\uparrow\downarrow\rangle)\right) \tag{A.6}$$

where one can directly see that for an non interacting case all terms will have equal weight. As interactions are included the double occupation is penalized by the local Coulomb interaction. To simplify the notation in the following text I'll replace $c = \sqrt{U^2+16t_\perp^2}$ and the normalization of the groundstate by $a = \sqrt{\frac{32t_\perp^2}{(U+c)^2}+2}$. In this case equation (A.6) is expressed in:

$$|GS\rangle = \frac{1}{a}\left((|1\uparrow 2\downarrow\rangle + |2\uparrow 1\downarrow\rangle) - \frac{4t_\perp}{U+c}(|1\uparrow\downarrow\rangle + |2\uparrow\downarrow\rangle)\right) \tag{A.7}$$

It is clear to follow that on increasing the local interaction $U \to \infty$ the double occupation becomes forbidden.

The fundamental excitations are the triplet states located at energies $E_T = -U$

$$|T_1\rangle = \frac{1}{\sqrt{2}}(|1\uparrow 2\downarrow\rangle - |2\uparrow 1\downarrow\rangle) \tag{A.8a}$$

$$|T_2\rangle = |1\uparrow 2\uparrow\rangle \tag{A.8b}$$

$$|T_3\rangle = |1\downarrow 2\downarrow\rangle \tag{A.8c}$$

Finally there are high energy excitations

$$|D\rangle = \frac{1}{\sqrt{2}}(|1\uparrow\downarrow\rangle - |2\uparrow\downarrow\rangle) \qquad E_D = 0 \tag{A.9a}$$

$$|DS\rangle = \frac{1}{b}\left((|1\uparrow 2\downarrow\rangle + |2\uparrow 1\downarrow\rangle) - \frac{4t_\perp}{U-c}(|1\uparrow\downarrow\rangle + |2\uparrow\downarrow\rangle)\right) \quad E_{DS} = -\frac{U}{2} + \frac{1}{2}\sqrt{U^2+16t_\perp^2} \tag{A.9b}$$

where $b = \sqrt{\frac{32t_\perp^2}{(U-c)^2}+2}$.

The three particle states are the particle-hole symmetric states to the single particle ones and have the same energy and levels.

$$|^3B\uparrow\rangle = \frac{1}{\sqrt{2}}(|1\uparrow 2\uparrow 1\downarrow\rangle - |1\uparrow 2\uparrow 2\downarrow\rangle) \qquad E_B = -\frac{U}{2} - t_\perp \tag{A.10a}$$

$$|^3B\downarrow\rangle = \frac{1}{\sqrt{2}}(|1\uparrow 1\downarrow 2\downarrow\rangle - |2\uparrow 1\downarrow 2\downarrow\rangle) \qquad E_B = -\frac{U}{2} - t_\perp \tag{A.10b}$$

$$|^3A\uparrow\rangle = \frac{1}{\sqrt{2}}(|1\uparrow 2\uparrow 1\downarrow\rangle + |1\uparrow 2\uparrow 2\downarrow\rangle \qquad E_A = -\frac{U}{2} + t_\perp \tag{A.10c}$$

$$|^3A\downarrow\rangle = \frac{1}{\sqrt{2}}(|1\uparrow 1\downarrow 2\downarrow\rangle + |2\uparrow 1\downarrow 2\downarrow) \qquad E_A = -\frac{U}{2} + t_\perp \tag{A.10d}$$

An energy level diagram is shown in figure A.2, where each eigenstate label its eigenenergy. The diagram is also sectioned in each total particle number sector. Particle-hole excitation which are described by green's functions move between particle number sectors. In the diagram shown the ration $U/t_\perp = 6$. For this intuitive case the ground state of the system is below the degenerate triplet states. If $U \to \infty$ the ground state becomes less distinguishable to the triplets and in the undimerized case($t_\perp = 0$) it is 4-fold degenerate. The study when $t_\perp$ is comparable to U is also interesting. When the ratio $U/t_\perp = 2$, the single particle states of the bonding levels are degenerate with the triplet states and for even higher values of $U/t_\perp < 2$ the triplet excitation is higher in energy than the bonding energy levels, meaning that the system would spontaneously prefer by thermal excitations to ionize rather and develop a magnetic moment of $S = 1/2$ rather than form a triplet state and have a magnetic moment $S = 1$. That is to say that charge excitations would become more likely than those of spin type.

A.2 Ground state Green's Functions

The zero temperature Green's function of the Dimer can be expressed through the Lehmann representation by:

$$G_{\alpha\beta\sigma}(z) = \sum_m \frac{\langle GS|c_{\alpha\sigma}|m_{N=3}\rangle\langle m_{N=3}|c^\dagger_{\beta\sigma}|GS\rangle}{z - (E_m - E_{GS})} + \sum_m \frac{\langle m_{N=1}|c_{\alpha\sigma}|GS\rangle\langle GS|c^\dagger_{\beta\sigma}|m_{N=1}\rangle}{z - (E_{GS} - E_m)} \tag{A.11}$$

In this case because the ground state is non degenerate the partition function is $Z = 1$ and this expression is normalized as presented. $|m_N\rangle$ represents the eigenstates at fixed number of particles. z is a complex frequency, which can be taken on the real frequency axis or along the Matsubara axis. Evaluating this formula for the relevant entries of the Green's function

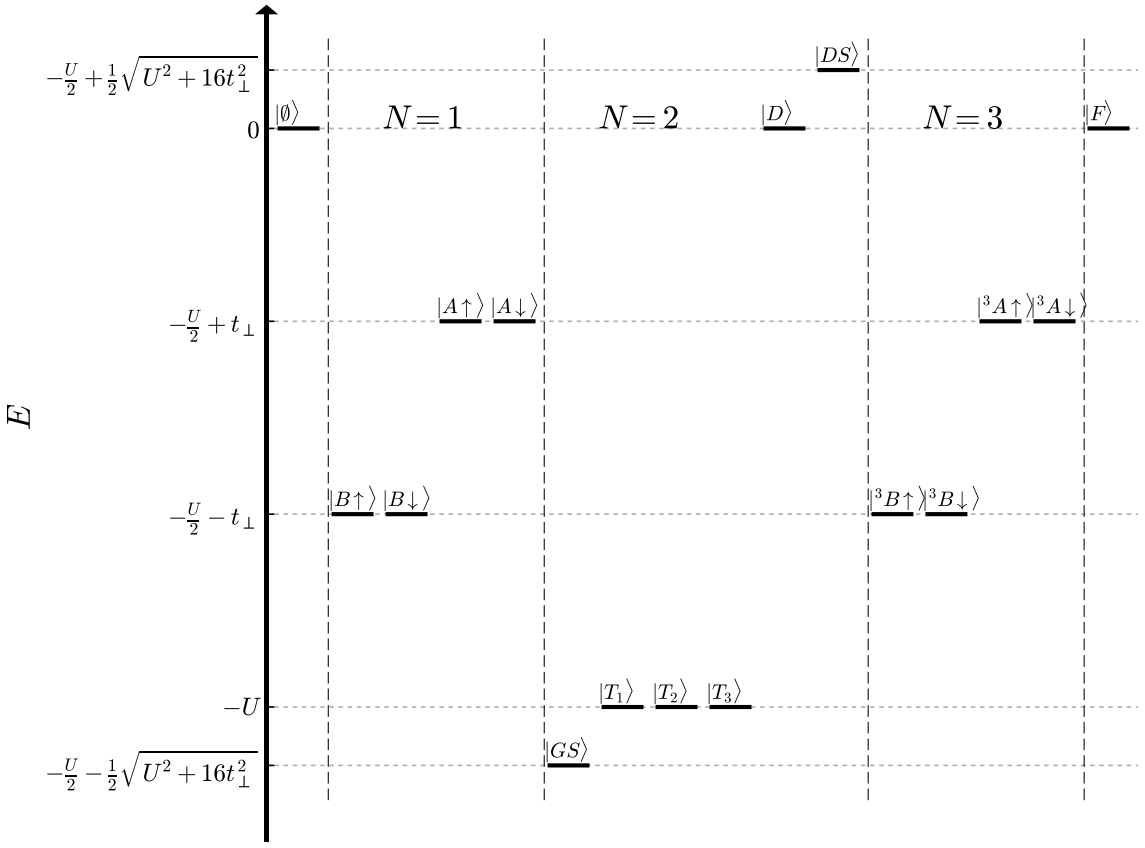

Figure A.2: Molecule Energy levels

we obtain.

$$G_{11\sigma} = \frac{1}{2a^2}\left[\frac{\left(1-\frac{4t_\perp}{U+c}\right)^2}{\left(z+t_\perp+\frac{c}{2}\right)} + \frac{\left(1-\frac{4t_\perp}{U+c}\right)^2}{\left(z-t_\perp-\frac{c}{2}\right)} + \frac{\left(1+\frac{4t_\perp}{U+c}\right)^2}{\left(z-t_\perp+\frac{c}{2}\right)} + \frac{\left(1+\frac{4t_\perp}{U+c}\right)^2}{\left(z+t_\perp-\frac{c}{2}\right)}\right] \tag{A.12a}$$

$$G_{12\sigma} = \frac{1}{2a^2}\left[\frac{\left(1-\frac{4t_\perp}{U+c}\right)^2}{\left(z+t_\perp+\frac{c}{2}\right)} - \frac{\left(1-\frac{4t_\perp}{U+c}\right)^2}{\left(z-t_\perp-\frac{c}{2}\right)} - \frac{\left(1+\frac{4t_\perp}{U+c}\right)^2}{\left(z-t_\perp+\frac{c}{2}\right)} + \frac{\left(1+\frac{4t_\perp}{U+c}\right)^2}{\left(z+t_\perp-\frac{c}{2}\right)}\right] \tag{A.12b}$$

The spectral function for the dimer is expressed in the in terms of the local Green's function G_{11} and it covers the excitations of removing particles from the groundstate for them to leave the system in the Bonding and Anti-bonding levels, conversely to add a particle and reach the corresponding levels of the $N = 3$ sector. This Spectral function is shown in figure A.3, where it clearly reflects the 4 pole structure and to which transition the response is associated. Transitions to Bonding levels are energetically less expensive.

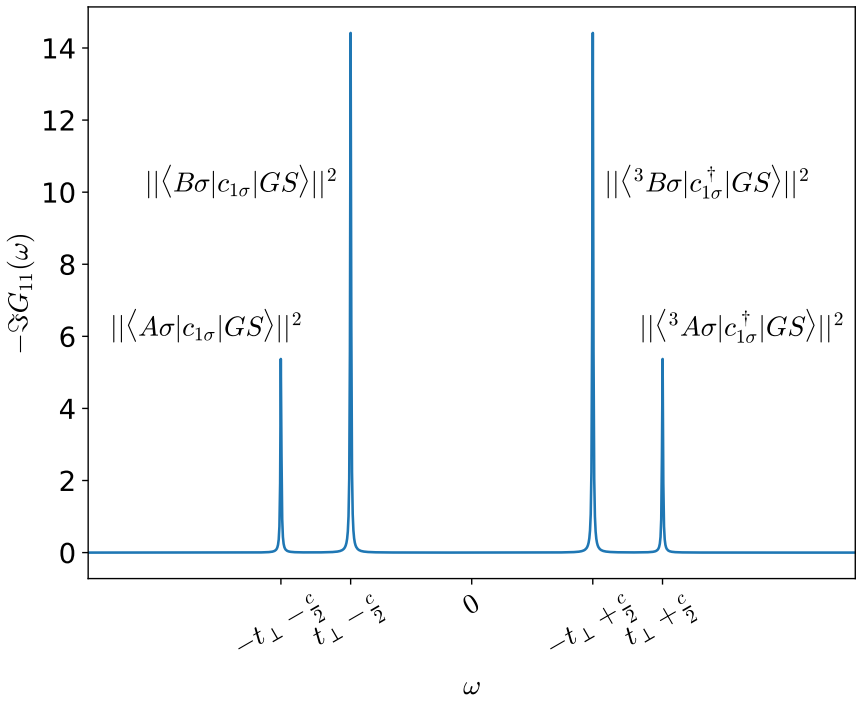

Figure A.3: Zero temperature isolated Molecule Spectral function. Each excitation response is labeled from the generating transition. (In this plot $U/t_\perp = 8$)

A.3 self-energy

It is now possible to directly extract the self-energy of the dimer through Dyson equation

$$\mathbf{G}_\sigma^{-1} = \begin{bmatrix} z & -t_\perp \\ -t_\perp & z \end{bmatrix}_\sigma - \begin{bmatrix} \Sigma_{11} & \Sigma_{12} \\ \Sigma_{21} & \Sigma_{22} \end{bmatrix}_\sigma \tag{A.13}$$

Keeping in mind that by symmetry $G_{11} = G_{22}$, $G_{12} = G_{21}$, $\Sigma_{11} = \Sigma_{22}$ and $\Sigma_{12} = \Sigma_{21}$ it becomes trivial to diagonalize this equation using the rotation matrix

$$P = \frac{\sqrt{2}}{2} \begin{bmatrix} 1 & 1 \\ 1 & -1 \end{bmatrix} = P^{-1} = P^\dagger \tag{A.14}$$

With this transformation we obtain and diagonal form of the Green's function which entries belong to the Anti-bonding and bonding functions.

$$P\mathbf{G}_\sigma^{-1}P = \begin{bmatrix} z - t_\perp & 0 \\ 0 & z + t_\perp \end{bmatrix}_\sigma - \begin{bmatrix} \Sigma_{11} + \Sigma_{12} & 0 \\ 0 & \Sigma_{11} - \Sigma_{12} \end{bmatrix}_\sigma = \begin{bmatrix} G_{AA} & 0 \\ 0 & G_{BB} \end{bmatrix}_\sigma \tag{A.15}$$

After that extracting the self-energy is trivial from equation (A.15) and one is left with:

$$\Sigma_{11} = \frac{U^2}{4} \frac{z}{z - 9t_\perp^2} = \frac{U^2}{8} \left(\frac{1}{z + 3t_\perp} + \frac{1}{z - 3t_\perp} \right) \tag{A.16a}$$

$$\Sigma_{12} = \frac{U^2}{4} \frac{3t_\perp}{9t_\perp^2 - z^2} = \frac{U^2}{8} \left(\frac{1}{z + 3t_\perp} - \frac{1}{z - 3t_\perp} \right) \tag{A.16b}$$

The self-energy has a 2 pole structure.

A.4 The Diagonal Basis

Because the single particle Green's function and self-energy have a diagonal form it is convenient to work on the problem in this particular basis where the single particle states are eigenstates of the system too. It is possible to further block diagonalize the matrix representation of equation (A.2) by proposing a change of basis using the rotation matrix of eq. (A.14). This in turn means that my original creation and annihilation operators are no longer in the site basis but in the one of the Bonding and Anti-Bonding basis given by:

$$\begin{bmatrix} c_1 \\ c_2 \end{bmatrix} = P^\dagger \begin{bmatrix} c_A \\ c_B \end{bmatrix}_\sigma = \frac{1}{\sqrt{2}} \begin{bmatrix} c_A + c_B \\ c_A - c_B \end{bmatrix}_\sigma ; \qquad \begin{bmatrix} c_A \\ c_B \end{bmatrix} = P \begin{bmatrix} c_1 \\ c_2 \end{bmatrix}_\sigma = \frac{1}{\sqrt{2}} \begin{bmatrix} c_1 + c_2 \\ c_1 - c_2 \end{bmatrix}_\sigma \tag{A.17}$$

Notice how it corresponds to equation (A.4), where we build my single particle eigen-states. This Transforms the non-interacting part of the Hamiltonian (A.2) into a diagonal form, where one can directly see that the Anti-bonding operators give the upper energy level and the Bonding ones the lower energy level.

$$\mathcal{H}_{dim} = t_\perp \left(c^\dagger_{A\downarrow} c_{A\downarrow} + c^\dagger_{A\uparrow} c_{A\uparrow} - c^\dagger_{B\downarrow} c_{B\downarrow} - c^\dagger_{B\uparrow} c_{B\uparrow} \right) = t_\perp \sum_\sigma (n_{A\sigma} - n_{B\sigma}) \tag{A.18}$$

The local interaction has to be transformed to this new basis where it spreads along both bands and gives to many cross-terms between these bands.

$$H_{int} = \frac{U}{2} \begin{pmatrix} c^\dagger_{A\uparrow} c^\dagger_{A\downarrow} c_{A\uparrow} c_{A\downarrow} + c^\dagger_{A\uparrow} c^\dagger_{A\downarrow} c_{B\uparrow} c_{B\downarrow} + c^\dagger_{A\uparrow} c^\dagger_{B\downarrow} c_{A\uparrow} c_{B\downarrow} + c^\dagger_{A\uparrow} c^\dagger_{B\downarrow} c_{B\uparrow} c_{A\downarrow} + \\ c^\dagger_{B\uparrow} c^\dagger_{A\downarrow} c_{A\uparrow} c_{B\downarrow} + c^\dagger_{B\uparrow} c^\dagger_{A\downarrow} c_{B\uparrow} c_{A\downarrow} + c^\dagger_{B\uparrow} c^\dagger_{B\downarrow} c_{A\uparrow} c_{A\downarrow} + c^\dagger_{B\uparrow} c^\dagger_{B\downarrow} c_{B\uparrow} c_{B\downarrow} \end{pmatrix} \tag{A.19}$$

Despite this more complicate structure the matrix structure of this Hamiltonian is much more reduced. Consisting of 14 blocks instead of the 9 blocks in the site basis.

The single particle basis is exactly as described in the previous section with equation (A.4) as that is the starting point of the eigenvectors. The ground state has to be visualized differently

$$|GS\rangle = \frac{1}{f} \left(\frac{U}{4t_\perp - c} |B\uparrow B\downarrow\rangle + |A\uparrow A\downarrow\rangle \right) = \beta |B\uparrow B\downarrow\rangle + \alpha |A\uparrow A\downarrow\rangle \tag{A.20}$$

where $f = \sqrt{\frac{U^2}{(4t_\perp - c)^2} + 1}$. In this case there are much less terms, but is harder to form an intuition in the interacting case. At $U = 0$ the groundstate is uniquely conformed by the double occupation of bonding states, because as in any non-interacting system one orderly occupies fermionic energy levels stating from the lowest single particle states. The probability amplitude of each 2-particle state do, verify this limit: $\lim_{U\to 0} \frac{1}{f} \frac{U}{4t_\perp - c} = -1$ and $\lim_{U\to 0} \frac{1}{f} = 0$. When interactions are turned on the Anti-bonding level becomes part of the state admixture to destructively interfere and reduce the onsite double occupation, see for comparison equation (A.7). Figure A.4 shows the probability of the doubly occupied bonding levels to the ground state.

The triplet states are a mixture of bonding and antibonding states.

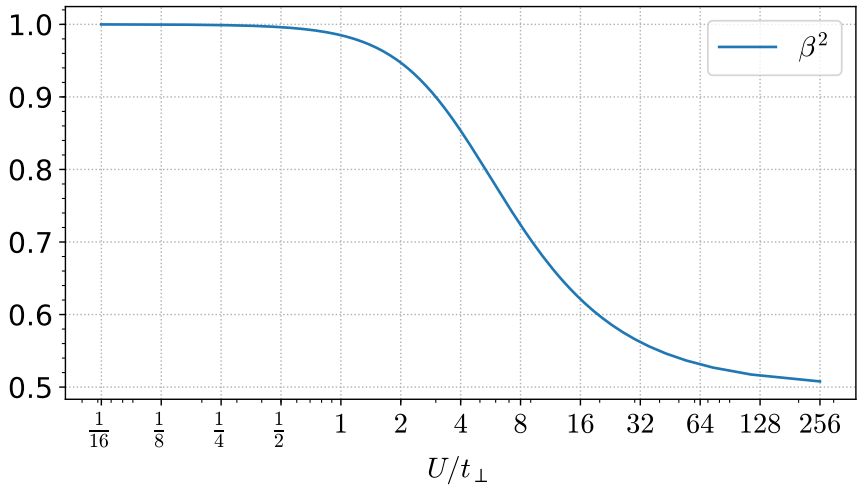

Figure A.4: Contribution of the doubly occupied bonding level to the dimer ground state. Here $\beta^2 = \frac{U^2}{f^2(4t_\perp - c)^2}$, refer to eq. (A.20).

$$|T_1\rangle = \frac{\sqrt{2}}{2}(|A\uparrow B\downarrow\rangle - |B\uparrow A\downarrow\rangle) \tag{A.21a}$$

$$|T_2\rangle = |A\uparrow B\uparrow\rangle \tag{A.21b}$$

$$|T_3\rangle = |A\downarrow B\downarrow\rangle \tag{A.21c}$$

The three particle states are similar to the single particle ones and have the same energy and levels, they are describes in equation (A.10)

A.4.1 Constructing the zero temperature Green Functions

The spectral function has a much simpler reform in this basis, as firstly shown in equation (A.15). The spectral function from equation (A.11) is reduced to a diagonal form:

$$G_{\alpha\beta\sigma}(z) = \sum_m \frac{\delta_{\alpha\beta}||\langle m_{N=3}|c^\dagger_{\alpha\sigma}|GS\rangle||^2}{z-(E_m - E_{GS})} + \sum_m \frac{\delta_{\alpha\beta}||\langle m_{N=1}|c_{\alpha\sigma}|GS\rangle||^2}{z-(E_{GS} - E_m)} \tag{A.22}$$

One can construct first the Anti-bonding zero temperature Green's function, which has only two non-zero terms:

$$G_{AA\sigma}(z) = \frac{||\langle^3 B\sigma|c^\dagger_{A\sigma}|GS\rangle||^2}{z-(E_B-E_{GS})} + \frac{||\langle A\bar{\sigma}|c_{A\sigma}|GS\rangle||^2}{z-(E_{GS}-E_A)} \tag{A.23a}$$

$$= \frac{\beta^2}{z+t_\perp-\frac{c}{2}} + \frac{\alpha^2}{z+t_\perp+\frac{c}{2}} \tag{A.23b}$$

$$= \frac{1}{z-t_\perp-\frac{U^2}{4}\frac{1}{z+3t_\perp}} \tag{A.23c}$$

An analogous procedure gives the Bonding Green's function

$$G_{BB\sigma}(z) = \frac{||\langle^3 A\sigma|c^\dagger_{B\sigma}|GS\rangle||^2}{z-(E_A-E_{GS})} + \frac{||\langle B\bar{\sigma}|c_{B\sigma}|GS\rangle||^2}{z-(E_{GS}-E_B)} \tag{A.24a}$$

$$= \frac{\alpha^2}{z-t_\perp-\frac{c}{2}} + \frac{\beta^2}{z-t_\perp+\frac{c}{2}} \tag{A.24b}$$

$$= \frac{1}{z+t_\perp-\frac{U^2}{4}\frac{1}{z-3t_\perp}} \tag{A.24c}$$

With special attention to equations (A.23) and (A.24) one can see that they do not differ much in structure from the Green's functions of a half-filled isolated atom, which is $G(z) = [z-U^2/(4z)]^{-1}$. It is the same excitation only that now there is $t_\perp$ shifting the non-interacting energy level and the pole of the self-energy is now shifted away of zero frequency by $3t_\perp$. The presence of the of the on-site Hubbard interaction is to redistribute the excitation spectra in order to induce a charge gap.

To visualize the Green functions in the real axis we take $z \to \omega + i\eta$. Figure A.5 shows each of the excitations out of the groundstate for the dimer and the self-energy, for the anti-bonding response. Excitations in the diagonal basis are very easily traceable. Because in the ground state of the system the 2 particle wave functions are only composed of a doubly occupied bonding levels and a doubly occupied anti-bonding levels. There are only 2 possible excitations on the system. It is only possible to add an anti-bonding particle to the part of the wave function with the pure bonding character which also has the largest weight, the adding to other component is forbidden by the Pauli exclusion principle as we cannot have more than one electron in the same quantum state. The same holds for the removal of the anti-bonding particle which can only be taken away from the pure anti-bonding contribution of the wave function. This asymmetry in the the form of the wave function and final energy level gives rise to the asymmetry in the response function, which nevertheless composes into a particle-hole symmetric local Green's function.

Notice that the divergence of the self-energy is asymmetrically spaced form each of the excitations and that the one that is closer to the divergence in the self-energy has as smaller

spectral weight. This asymmetry is also evidenced on the probed states, equation (A.24a) when probing the response of the anti-bonding particle ($c_{A\sigma}$) one reaches the anti-bonding state in the single particle sector but a bonding state in the 3 particle sector. This clearly indicates the excitation asymmetry but also explains the different weights. Since the ground state of the system is mainly composed of the Bonding state contributions.

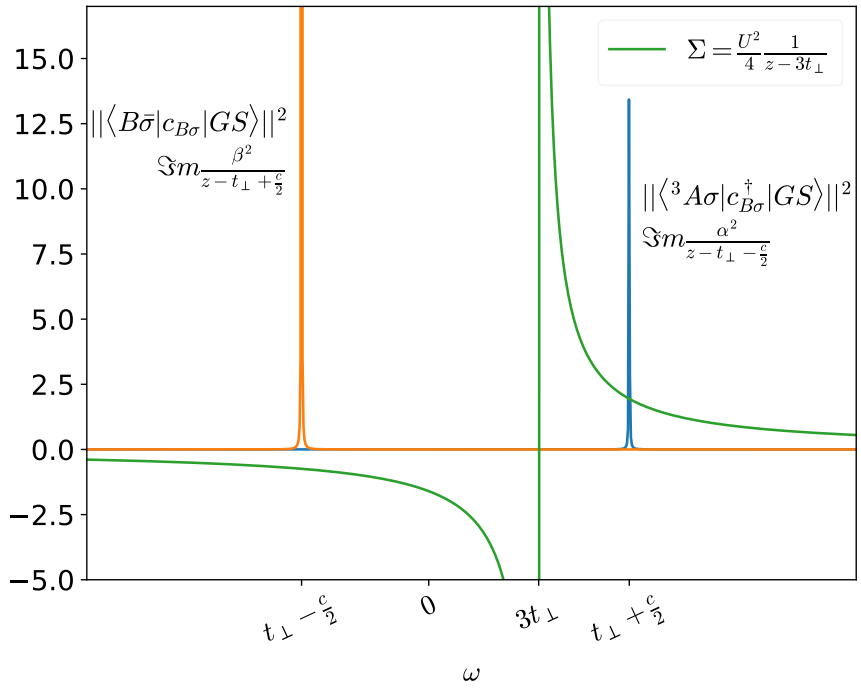

Figure A.5: Composition of the bonding spectral function and self-energy separating the components given in equation (A.24). (In this plot $U/t_\perp = 8$) Compare to figure A.3.

A.5 Finite temperature Green Functions

The dimer at zero temperature only resides on its ground state, but at finite temperature one has a thermal population. Figure A.6 presents the thermal occupation of each of the eigenstates of the dimer at a given temperature. There is of course a temperature range where only the ground state is the unique contributor to the systems wave function, but little temperature can induce the spin excitations of the triplet states. Further increase in temperature induces population of single and 3 particle bonding states and as expected at high temperatures all states are equiprobable.

The finite temperature Green's functions is given by the Lehmann representation, where the thermal occupation comes into play.

$$G_{\alpha\beta\sigma}(z) = \frac{1}{\mathcal{Z}}\sum_{m,n}\frac{\langle n|c_{\alpha\sigma}|m\rangle\langle m|c^\dagger_{\beta\sigma}|n\rangle}{z-(E_m-E_n)}(e^{-\beta E_n}+e^{-\beta E_m}) \tag{A.25}$$

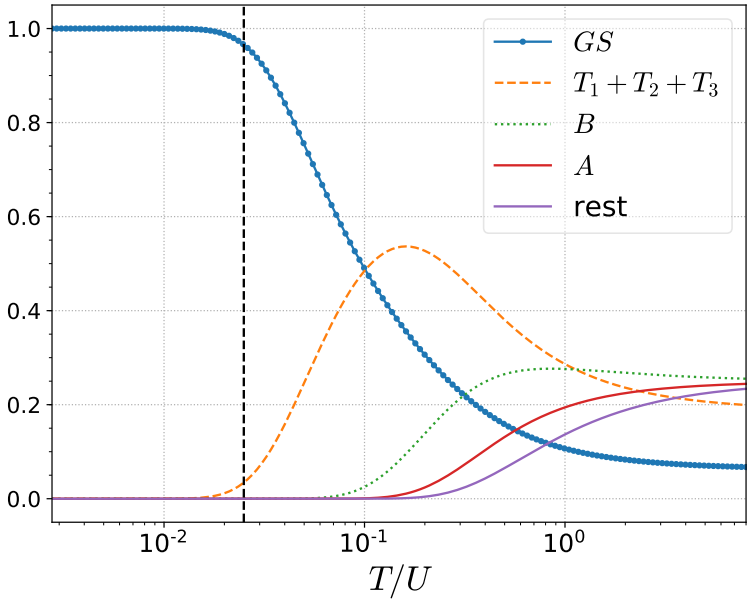

Figure A.6: Thermal occupation of states for the setup $U/t_\perp = 5.7$. B (A) represent the sum of all (anti-)bonding levels. Vertical dashed line is $T/U = 0.025$.

here $\mathcal{Z}$ is the Grand canonical Partition function, and n, m enumerate all the eigenstates of the Hamiltonian. The analytical description of the entire Green function is to complicated to track. Thus contributions to it will be traced in relevant steps. The first case study will restrict to the excitations out of the triplet states. The only eigen states first allowed to contribute to the wave function are $\Psi \in \{|GS\rangle, |T_1\rangle, |T_2\rangle, |T_3\rangle\}$, and this approximations can be made:

$$\mathcal{Z} \approx e^{-\beta E_{GS}} + 3e^{-\beta E_T} = e^{\beta(\frac{U}{2} + \frac{1}{2}\sqrt{U^2+16t_\perp^2})} + 3e^{\beta U} \tag{A.26}$$

$$G_{BB\sigma}(z) = \sum_{m,\Psi} \left[\frac{e^{-\beta E_\Psi} + e^{-\beta E_m}}{\mathcal{Z}} \frac{||\langle m_{N=3}|c^\dagger_{B\sigma}|\Psi\rangle||^2}{z - (E_m - E_\Psi)} + \frac{e^{-\beta E_\Psi} + e^{-\beta E_m}}{\mathcal{Z}} \frac{||\langle m_{N=1}|c_{B\sigma}|\Psi\rangle||^2}{z - (E_\Psi - E_m)} \right] \tag{A.27}$$

Excitation out of the ground state will only gain an extra thermal weight but the allowed transition are the ones already described in the zero temperature Green function as shown in equation (A.24).

$$G^{GS}_{BB\sigma} = \frac{\alpha^2}{\mathcal{Z}} \frac{\left(e^{\beta(\frac{U}{2}+t_\perp)} + e^{\beta(\frac{U}{2}+\frac{c}{2})}\right)}{\left(z - t_\perp - \frac{c}{2}\right)} + \frac{\beta^2}{\mathcal{Z}} \frac{\left(e^{\frac{\beta}{2}(U-2t_\perp)} + e^{\beta(\frac{U}{2}+\frac{c}{2})}\right)}{\left(z - t_\perp + \frac{c}{2}\right)} \tag{A.28}$$

All the triplet subspace contributes to the thermal Green's function. For presentation purposes lets focus first on the triplet Green's function of the Bonding spin up function.

$$G^T_{BB\uparrow} = \frac{e^{U\beta} + e^{\beta(\frac{U}{2}+t_\perp)}}{\mathcal{Z}} \frac{||\langle {}^3B\uparrow|c^\dagger_{B\uparrow}|T_1\rangle||^2}{z-(E_B-E_T)} \tag{A.29a}$$

$$+ \frac{e^{U\beta} + e^{\beta(\frac{U}{2}-t_\perp)}}{\mathcal{Z}} \frac{||\langle A\downarrow|c_{B\uparrow}|T_1\rangle||^2}{z-(E_T-E_A)} \tag{A.29b}$$

$$+ \frac{e^{U\beta} + e^{\beta(\frac{U}{2}-t_\perp)}}{\mathcal{Z}} \frac{||\langle A\uparrow|c_{B\uparrow}|T_2\rangle||^2}{z-(E_T-E_A)} \tag{A.29c}$$

$$+ \frac{e^{U\beta} + e^{\beta(\frac{U}{2}+t_\perp)}}{\mathcal{Z}} \frac{||\langle {}^3B\downarrow|c^\dagger_{B\uparrow}|T_3\rangle||^2}{z-(E_B-E_T)} \tag{A.29d}$$

$$= \frac{e^{U\beta} + e^{\beta(\frac{U}{2}-t_\perp)}}{\mathcal{Z}} \frac{3/2}{z+t_\perp+\frac{U}{2}} + \frac{e^{U\beta} + e^{\beta(\frac{U}{2}+2t_\perp)}}{\mathcal{Z}} \frac{3/2}{z+t_\perp-\frac{U}{2}} \tag{A.29e}$$

Figure A.7 presents each of this contributions and the numerical self-energy obtained by Dyson's equation. The poles of the Green's function retain their predictable shape but the self-energy is much more complex and even the main divergence has changes its position, deviating from the value $-3t_\perp$ as given by the Ground state excitation.

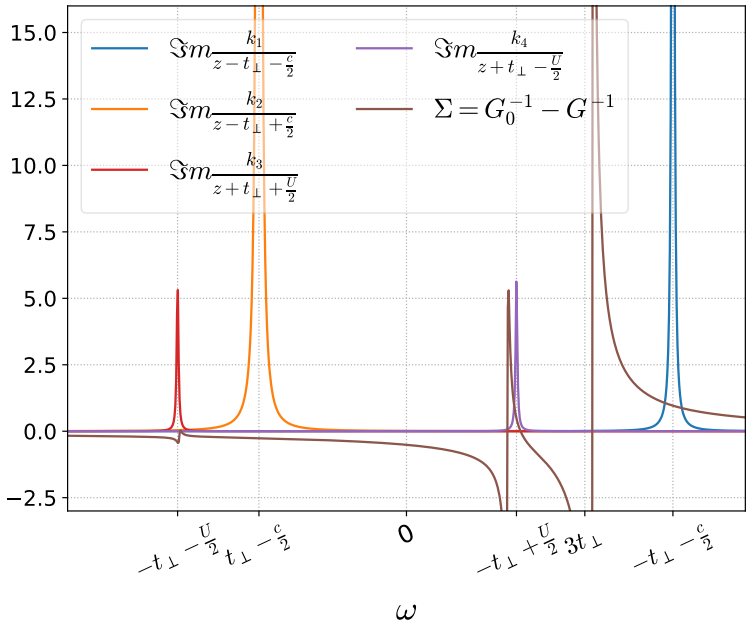

Figure A.7: Thermal Green's function for the dimer where only the groundstate and triplets are populated, refer to figure A.6, $U/t_\perp = 5.7$ and $T/U = 0.025$. Blue peaks are excitations out of the Ground state(compare to figures A.5 and A.3), orange peaks are excitations out of the triplet states.

A.6 Hubbard Approximations

When interactions have to be considered the model becomes untraceable and one needs to rely on approximations to be able to study the problem. Most of ours insight into the correlated electron problem and the Metal-insulator transition arises from directly including the local behavior of the system, the atomic like view, into the approximation. In appendix The isolated molecule we describe the solution of the dimer molecule. Those results will be directly used here for the next lattice approximations.

One can use this known shape of the spectral function to view extra approximations to the lattice Dimer model.

The first approximation is the crude Hubbard I approximation Hubbard [1963], which describes the coherent propagation of holes or double occupations and reduces itself into inserting the isolated molecule self-energy into the lattice Green's function.

This approximation can be directly obtained by including the lattice dispersion in equation (A.24c)

$$G_{BB\sigma}(\epsilon,\omega) = \frac{1}{\omega + i\eta - \epsilon + t_\perp - \frac{U^2}{4}\frac{1}{z-3t_\perp}} \tag{A.30}$$

where ϵ is the lattice dispersion. In the case of the Bethe lattice one does not have a momentum description thus $\epsilon \in [-D, D]$ is taken, where D is the half-bandwidth. It is unfortunately not evident how to use this same approximation for the individual contributions as replacing $z \to \omega - \epsilon$ directly into (A.24a) gives the wrong behavior. In figure A.8 one can visualize this approximation where there is a upper Hubbard band that has a large dispersion and a lower one which is a rather heavier band.

It is also possible to do a Hubbard III approximation in order to give the incoherent behavior into the spectral function. for this we start from equation (A.24a) and replace $z \to {\mathcal{G}^0_{BB}}^{-1}$ which is the DMFT Weiss field. Also introducing the DMFT self-consistency condition for this field in the Anti-bonding band

$${\mathcal{G}^0_{BB}}^{-1} = \omega - t_\perp - t^2 G_{BB} \tag{A.31}$$

One has to solve for this field, and then construct the Green's function and recover the self-energy by Dyson's equation. The resulting spectral function is presented in figure A.8, where the one has under the Hubbard III approximation where it is clear that the lower Hubbard band is highly incoherent but the upper Hubbard band has also lost much of its coherence. This spectra gives the local spectral function in blue. For comparison the Hubbard I solution is plotted on top corresponding to this sharp lines showing how the lower

Hubbard band rather flat whereas the upper one is highly dispersive, the corresponding density of states in this approximation is on the left green curve.

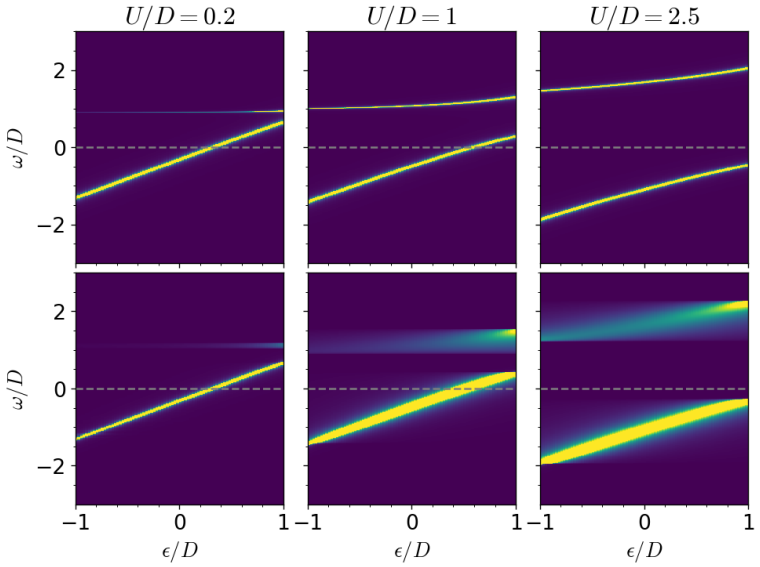

Figure A.8: Zero temperature bonding spectral dispersion calculated with the Hubbard approximations for various values of Hubbard interaction U. Top panels are Hubbard I approximation, bottom ones are Hubbard III. The Fermi level is plotted for visual guide.

A.7 Thermal Hubbard approximations

When constructing the lattice spectral functions under the Hubbard I and III approximation like in the previous section but incorporation the thermal Green's functions we obtain figure A.9. This structure has a strong resemblance to the DMFT solutions. I'll enumerate from top to bottom under the name we have previously given when analyzing the DMFT data. Whether, the naming is accurate to the physical process is still under debate. Thus we have 4 *bands*, the upper Hubbard band, the long lived quasiparticle, the heavy quasiparticle and the lower Hubbard band. When comparing this bands to the zero temperature response of figure A.8 that the upper Hubbard band has detached from the long lived quasiparticle and even there is an avoided crossing between the two. A note worthy remark is that we can read directly from this plot the composition and origin of this bands, that is in figure A.9 left panel one is at $\beta = 16$ and the system is 75% groundstate (view Fig. A.6). The long lived quasiparticle disperses equally 75% of the bandwidth $\epsilon \in [-1; 0.5]$ before becoming flat. This repeats itself in the right panel where the Ground state contribution to the wavefunction is only 50% and the dispersion of the quasiparticle is only half the bandwidth. It is then well identified that this long lived quasiparticle is the anti-bonding excitations out of the dimer groundstate. Why this band in the DMFT solution will retain an infinite lifetime is still unclear. Second unclear case is that the dimer insulator according to the DMFT QMC

solution is largely dominated by the dimer groundstate, but the long lived quasiparticle band does not disperse in the same contribution along the bandwidth. The Hubbard III approximation does not give clear hint of the avoided band crossing to actually happen although their is a drop in the sharpness of the spectra in that region. The lower Hubbard band has not changed much from the zero temperature form. It just loses weight depending on the temperature of the system. What does change is the heavy quasiparticle, which comes from removing the anti-bonding particle out of the triplet states. This is a very flat band when it first appears. It does not seem to ever mix with the lower Hubbard band and as temperature is elevated it gains spectral weight and according to the Hubbard I approximation also a dispersion.

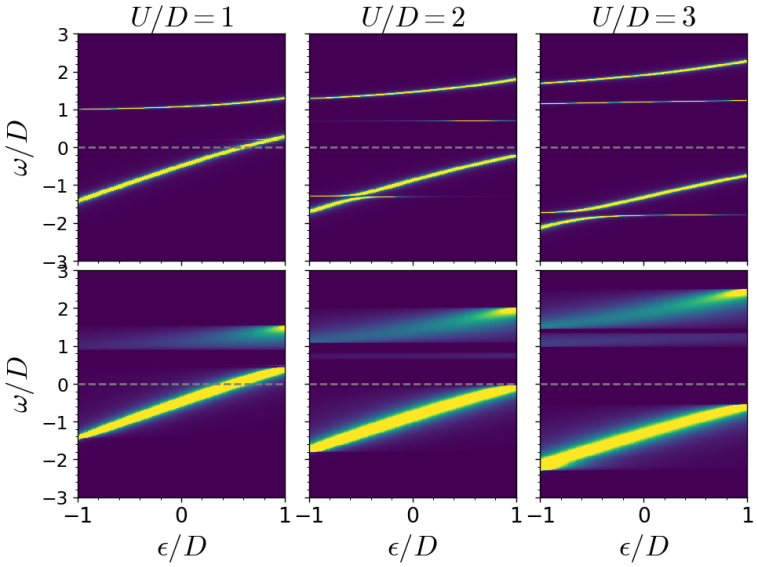

Figure A.9: Thermal bonding spectral dispersion calculated with the Hubbard approximations for various values of Hubbard interaction U at $\beta/D = 30$. Top panels are Hubbard I approximation, bottom ones are Hubbard III. The Fermi level is plotted for visual guide.

Appendix B

Optical Conductivity

B.1 1D case

The connected graph geometrical representation of the dimer ladder that of each unit cell consisting of the dimer which has both ends liked by a hopping integral proportional to $t_\perp$ and all dimer ends are linked along a chain by $-t$. The unit cell is of length a and the projection of the dimer length on the chain is $\eta \in [-\frac{a}{2}, \frac{a}{2})$. As this model is 1D is shall also be interpreted as a system where the dimers are all colinear and they experience a strange next nearest hopping between them. Figure B.1 provides the graphical representation of both alternatives.

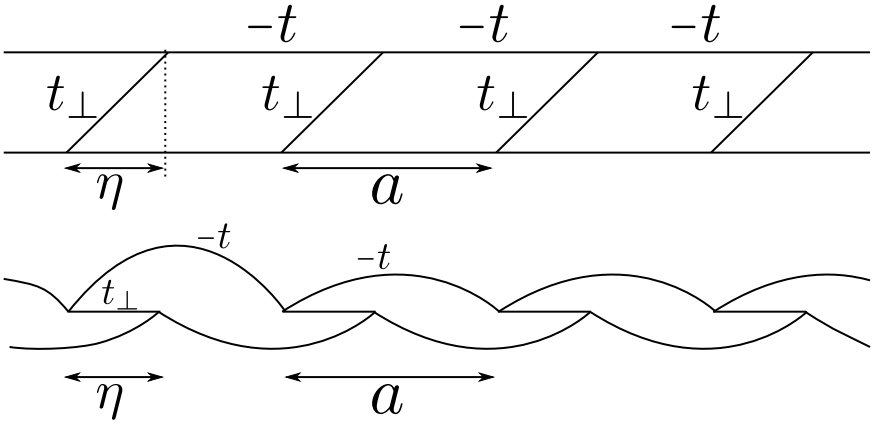

Figure B.1: The dimer ladder

The Hamiltonian for this problem reads:

$$H = t_\perp \sum_{i,\sigma} (c^\dagger_{i,1,\sigma} c_{i,2,\sigma} + H.c.) - t \sum_{i,\alpha,\sigma} (c^\dagger_{i,\alpha,\sigma} c_{i+1,\alpha,\sigma} + H.c.) \tag{B.1}$$

where $c^\dagger_{i,\alpha,\sigma}$ creates a fermion on the ladder site i, in the $\alpha = \{1, 2\}$ ion of the dimer and with spin $\sigma = \{\uparrow, \downarrow\}$. One can bring this problem into momentum space by the Fourier transform of the creation-annihilation operators:

$$c_i^\dagger = \frac{1}{\sqrt{N}} \sum_{\vec{k}} e^{i\vec{k}\cdot\vec{r}_i} c_k^\dagger \tag{B.2}$$

inserting B.2 in B.1 one obtains:

$$H = t_\perp \sum_{k,\sigma} (e^{-ik\eta} c_{k,1,\sigma}^\dagger c_{k,2,\sigma} + H.c.) + \sum_{k,\alpha,\sigma} \epsilon_k c_{k,\alpha,\sigma}^\dagger c_{k,\alpha,\sigma} \tag{B.3}$$

where $\epsilon_k = -2t\cos(ka)$. One can rewrite this Hamiltonian in matrix form as:

$$H = \sum_{k,\sigma} \Psi_{k,\sigma}^\dagger \begin{bmatrix} \epsilon_k & t_\perp e^{-ik\eta} \\ t_\perp e^{ik\eta} & \epsilon_k \end{bmatrix} \Psi_{k,\sigma} \tag{B.4}$$

where $\Psi_{k,\sigma}^\dagger = [c_{k,1,\sigma}^\dagger, c_{k,2,\sigma}^\dagger]$. It is then possible to diagonalize this Hamiltonian in momentum space by introducing new fermion quasiparticles $\{a_{k,-,\sigma}^\dagger, a_{k,+,\sigma}^\dagger\}$

$$\begin{bmatrix} a_{k,-,\sigma}^\dagger \\ a_{k,+,\sigma}^\dagger \end{bmatrix} = \frac{1}{\sqrt{2}} \begin{bmatrix} -e^{ik\eta} & 1 \\ e^{ik\eta} & 1 \end{bmatrix} \begin{bmatrix} c_{k,1,\sigma}^\dagger \\ c_{k,2,\sigma}^\dagger \end{bmatrix}; \begin{bmatrix} c_{k,1,\sigma}^\dagger \\ c_{k,2,\sigma}^\dagger \end{bmatrix} = \frac{1}{\sqrt{2}} \begin{bmatrix} -e^{-ik\eta} & e^{-ik\eta} \\ 1 & 1 \end{bmatrix} \begin{bmatrix} a_{k,-,\sigma}^\dagger \\ a_{k,+,\sigma}^\dagger \end{bmatrix} \tag{B.5}$$

The Hamiltonian then reads:

$$H = \sum_{k,\sigma} \left[(\epsilon_k - t_\perp) a_{k,-,\sigma}^\dagger c_{k,-,\sigma} + (\epsilon_k + t_\perp) a_{k,+,\sigma}^\dagger c_{k,+,\sigma} \right] \tag{B.6}$$

Where the first term will be called the lower Peierls band or bonding band, and the second is the upper Peierls band or antibonding band. This two bands run parallel along the Brillouin zone as plotted in Fig.B.2.

The total bandwidth is $W = 4t + 4t_\perp$ and the direct gap is $\Delta = 2t_\perp$. At zero temperature the ground state is the half-filled system which is occupied below the Fermi energy. In figure B.2 we have marked the bounds of the window of optical transitions, which is bounded to the regions $[-k_{F_1}; -k_{F_2}] \bigcup [k_{F_2}; k_{F_1}]$.

B.2 Optical conductivity finite dimensions

The aim is to perturb the system with an Electric field to induce transitions between the bands. There are some methods to study the coupling of the system to the electric field

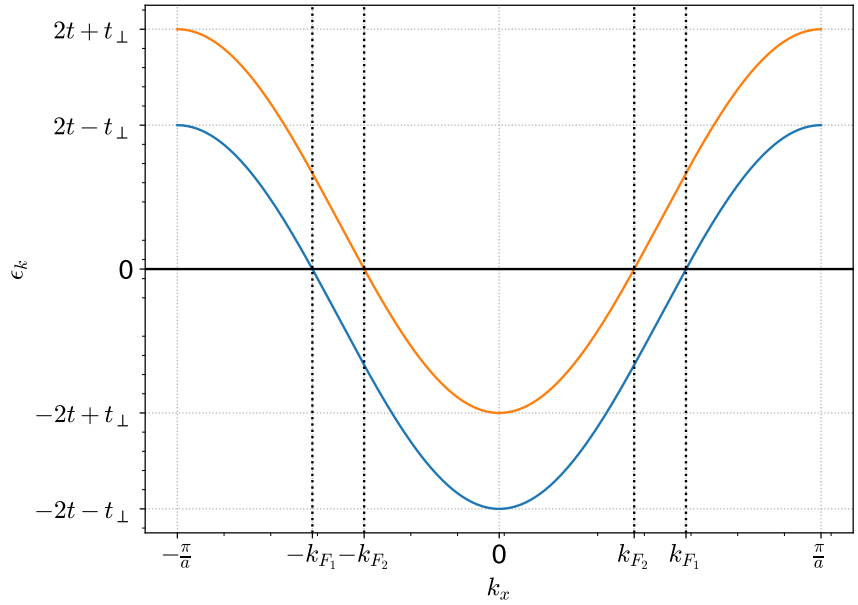

Figure B.2: Band structure of the dimer chain, with lower (upper) Peierls band in blue(green). Region is marked for optical transition window

which is described by the term

$$H_{EM} = -\hat{j}\frac{\mathcal{A}(t)}{c} \tag{B.7}$$

which couples the external vector potential $\mathcal{A}(t)$ to the current operator $\hat{j}$ of the system.

B.2.1 Peierls Ansatz

To find the current operator one works in the Coulomb gauge and sets the scalar potential to zero. Then the electric field is is given by the vector potential alone $\mathcal{A}(t)$, $E(t) = -1/c\partial\mathcal{A}(t)/\partial t$ or upon Fourier transform $\mathcal{A}(\omega)/c = E(\omega)/(i\omega)$. The electrical field shall be taken constant over lattice distances in the regime we study the optical transitions. The presence of the vector potential changes the hopping amplitudes for the electron transfer between neighboring unit cells. But one can perform a gauge transformation to eliminate the the vector potential from the Hamiltonian and letting the Wannier functions acquire a field dependence Millis [2004], Gebhard et al. [1997] $c_i^\dagger \to c_i^\dagger \exp\left(i\frac{e}{c}\int^{R_i}\vec{\mathcal{A}}\cdot d\vec{r}\right)$ now one can rewrite the hopping amplitude under the know Peierls substitution:

$$t(\delta) \to t(\delta)\exp\left(i\frac{e}{c}\vec{\mathcal{A}}\cdot\vec{\delta}\right) \tag{B.8}$$

where $t(\delta) = \{t, t_\perp\}$ is the hopping between two atoms, e is the electron charge, c the speed of light, $\vec{\delta}$ is the vector that joint the neighboring atoms. Replacing B.8 in B.1 and expanding for small $\mathcal{A}$ in the linear response regime one obtains:

$$\begin{aligned} H(\mathcal{A}) &= t_\perp \sum_{i,\sigma} (e^{ieA\eta/c} c^\dagger_{i,1,\sigma} c_{i,2,\sigma} + H.c.) - t \sum_{i,\alpha,\sigma} (e^{ieAa/c} c^\dagger_{i,\alpha,\sigma} c_{i+1,\alpha,\sigma} + H.c.) \\ &\approx H + t_\perp \sum_{i,\sigma} ie\eta (c^\dagger_{i,1,\sigma} c_{i,2,\sigma} - c^\dagger_{i,2,\sigma} c_{i,1,\sigma}) \frac{\mathcal{A}}{c} - t \sum_{i,\alpha,\sigma} iea (c^\dagger_{i,\alpha,\sigma} c_{i+1,\alpha,\sigma} - c^\dagger_{i+1,\alpha,\sigma} c_{i,\alpha,\sigma}) \frac{\mathcal{A}}{c} \end{aligned}$$

which allows to identify the paramagnetic particle current operator after comparison to B.7

$$\hat{j} = -ie \left[\sum_{i,\sigma} t_\perp \eta (c^\dagger_{i,1,\sigma} c_{i,2,\sigma} - c^\dagger_{i,2,\sigma} c_{i,1,\sigma}) - \sum_{i,\alpha,\sigma} at (c^\dagger_{i,\alpha,\sigma} c_{i+1,\alpha,\sigma} - c^\dagger_{i+1,\alpha,\sigma} c_{i,\alpha,\sigma}) \right] \tag{B.9}$$

using the same Fourier transform for the creation operators (B.2) the current operator in momentum space reads:

$$\hat{j} = -iet_\perp \eta \sum_{k,\sigma} (e^{-ik\eta} c^\dagger_{k,1,\sigma} c_{k,2,\sigma} - H.c.) + e \sum_{k,\alpha,\sigma} \frac{\partial \epsilon_k}{\partial k} c^\dagger_{k,\alpha,\sigma} c_{k,\alpha,\sigma} \tag{B.10}$$

Using the transformation (B.5) the current operator can be transformed into:

$$\hat{j} = \sum_{k,\sigma} e \left[2at \sin(ka) \left(a^\dagger_{k,-,\sigma} a_{k,-,\sigma} + a^\dagger_{k,+,\sigma} a_{k,+,\sigma} \right) + i\eta t_\perp \left(a^\dagger_{k,-,\sigma} a_{k,+,\sigma} - a^\dagger_{k,+,\sigma} a_{k,-,\sigma} \right) \right] \tag{B.11}$$

The first term of this expression is the intraband current which gives the Drude peak. The second now more interesting is the interband current. The paramagnetic optical conductivity can be obtained from formula (8.33) from Economou [2006].

$$\sigma_p(\omega) = i \frac{e^2}{\Omega m^2 \omega} \sum_{\alpha,\beta} |\langle \alpha | p_x | \beta \rangle|^2 \frac{f_\alpha - f_\beta}{\omega - \omega_{\beta\alpha} + i\gamma} \tag{B.12}$$

where m is the electron mass, α, β are eigenstates of the Hamiltonian, Ω is the system volume in our case for this 1D system Ω=L=Na, p_x is the momentum operator, f_α is the Fermi distribution for the state α, $\omega_{\beta\alpha}$ is the Energy gap between states, and γ is a positive term corresponding to the lifetime of the states. In the zero temperature limit, only the groundstate is the relevant state of the system and the excitation given by the current operator, the Fermi functions become step functions and the Fermi surface is sharply defined.

Taking this considerations, changing $\hat{j} = \frac{ep_x}{m}$ and collecting the real part of (B.12) and we obtain:

$$\Re e\sigma_p(\omega) = \frac{\pi}{Na\omega}\sum_{\beta}|\langle GS|\hat{j}|\beta\rangle|^2(f_{GS}-f_\beta)\left[\delta(\omega-(E_\beta-E_0))-\delta(\omega+(E_\beta-E_0))\right] \quad \text{(B.13)}$$

where $|GS\rangle$ is the ground state and E_0 its energy, the delta functions are for strictly rigid band and no phonon coupling so that states are infinitely lived, to include lifetime to the states change those Dirac delta functions for Lorenzians. So inserting (B.11) and $\omega > 0$ in (B.13) one obtains for the intraband conductivity:

$$\Re e\sigma_p(\omega)_{intra} = \frac{2\pi(2eat)^2}{Na\omega}\frac{2L}{2\pi}\delta(\omega)\left(\int_0^{k_{F_1}} dk\sin^2(ka)+\int_0^{k_{F_2}} dk\sin^2(ka)\right) = \frac{\pi(2eat)^2}{a\omega}\delta(\omega) \quad \text{(B.14)}$$

Here the limit of DC conductivity is ill defined but enforcing the lorenzian instead of the Dirac delta one obtains the known Drude peak at finite frequencies.

For the interband transition the conductivity

$$\Re e\sigma_p(\omega)_{inter} = \frac{2\pi(e\eta t_\perp)^2}{Na\omega}\frac{2L}{2\pi}\int_{k_{F_2}}^{k_{F_1}} dk\delta(\omega-2t_\perp) = \frac{2(e\eta t_\perp)^2}{\omega}\delta(\omega-2t_\perp)(k_{F_1}-k_{F_2}) \quad \text{(B.15)}$$

From this expression it becomes clear that the interband transition is stronger when $\eta = a/2$, which is evident which its maximum allowed length and thus the stronger the dipole moment formed to couple to the external electric field. Also for the 1D case there is an extreme for $t_\perp > 2t$. That is strongly coupled dimers. The result of this calculus can be seen in figure B.3

B.2.2 Second alternative

One can choose not to work in a 1D model system but accept the fact we are in a dimer ladder, which is 2D and allow for the existence of the Electric field in the orthogonal direction of the ladder. For this purpose, let us restart from the dimer ladder of figure B.1 but setting η=0, so the links of between the chain are orthogonal. The for practical purposes give the distance of the links a length of $a_\perp$ as well. This change does not alter our Hamiltonian of equation (B.1) but its version in Momentum space has no phase in the off-diagonal terms in equation (B.4) nor has this phase to be included in the generating matrices of the fermion quasiparticles that diagonalize the system in equation (B.5). This happens because in the direction perpendicular to the chains there is no translation invariance, is just two levels,

so there is no crystal quasimomentum defined. Then the diagonal Hamiltonian (B.6) is the same as all our deduction procedure. Of course the current operator is now a vector which reads:

$$\hat{j} = -ie\sum_{i,\sigma}\begin{bmatrix} -at\sum_{\alpha}(c^{\dagger}_{i,\alpha,\sigma}c_{i+1,\alpha,\sigma} - c^{\dagger}_{i+1,\alpha,\sigma}c_{i,\alpha,\sigma}) \\ a_{\perp}t_{\perp}(c^{\dagger}_{i,1,\sigma}c_{i,2,\sigma} - c^{\dagger}_{i,2,\sigma}c_{i,1,\sigma}) \end{bmatrix} = e\sum_{k,\sigma}\begin{bmatrix} 2at\sin(ka)\left(a^{\dagger}_{k,-,\sigma}c_{k,-,\sigma} + a^{\dagger}_{k,+,\sigma}c_{k,+,\sigma}\right) \\ ia_{\perp}t_{\perp}\left(a^{\dagger}_{k,-,\sigma}c_{k,+,\sigma} - a^{\dagger}_{k,+,\sigma}c_{k,-,\sigma}\right) \end{bmatrix} \tag{B.16}$$

This transforms the conductivity into a tensor. Which end result is

$$\Re e\sigma(\omega > 0) = \begin{bmatrix} \frac{\pi(2eat)^2}{a\omega}\delta(\omega) & 0 \\ 0 & 2(ea_{\perp}t_{\perp})^2\delta(\omega - 2t_{\perp})(k_{F_1} - k_{F_2})/\omega \end{bmatrix} \tag{B.17}$$

Which is correspondingly the same result we obtained in the previous section. But requires a field to be applied with a component in the direction of the link.

B.2.3 Green's Functions formalism

It is possible express the optical conductivity in equation (B.12) in terms of Green functions as described in equation (8.53) from Economou [2006], which is valid at Finite temperature too.

$$\Re e\sigma(\omega)_{\mu\nu} = \int d\omega' \frac{f(\omega') - f(\omega' + \omega)}{\omega} Tr\{\hat{j}_{\mu}A(\omega')\hat{j}_{\nu}A(\omega' + \omega)\} \tag{B.18}$$

Where the Tr includes all eigenstates of the Hamiltonian in the Grand Canonical ensemble in our case (momentum k, spin σ, bands). $\hat{j}_{\mu}$ is a Cartesian component of the current operator.

The non-interacting Green's Functions can be directly constructed out of the Diagonal Hamiltonian in equation (B.6) as such

$$G(k,\omega)_{\mp} = [\omega - \epsilon_k + \mu \pm t_{\perp}]^{-1} \tag{B.19}$$

$$A(k,\omega)_{\mp} = -\frac{1}{\pi}\frac{\gamma}{(\omega - \epsilon_k + \mu \pm t_{\perp})^2 + \gamma^2} \tag{B.20}$$

Are the Green/Spectral functions for the lower$(-)$ and upper $(+)$ Peiers bands. Replacing (B.20) together with (B.10) into (B.18)

$$\Re e\sigma(\omega) = \int d\omega' \frac{f(\omega') - f(\omega'+\omega)}{\omega} \times \sum_{k,\sigma} (4a^2t^2 \sin^2(ka) \left[A_+(k,\omega)A_+(k,\omega+\omega') + A_-(k,\omega)A_-(k,\omega+\omega')\right] + \eta^2 t_\perp^2 \left[A_-(k,\omega)A_+(k,\omega+\omega') + A_+(k,\omega)A_-(k,\omega+\omega')\right]) \tag{B.21}$$

which can be evaluated directly, but it is also possible to perform an integration over energy in which case

$$\Re e\sigma(\omega) = \int d\omega' \frac{f(\omega') - f(\omega'+\omega)}{\omega} \times \int dE\rho(E)(a^2(4t^2 - E^2) \left[A_+(E,\omega)A_+(E,\omega+\omega') + A_-(E,\omega)A_-(E,\omega+\omega')\right] + \eta^2 t_\perp^2 \left[A_-(E,\omega)A_+(E,\omega+\omega') + A_+(E,\omega)A_-(E,\omega+\omega')\right]) \tag{B.22}$$

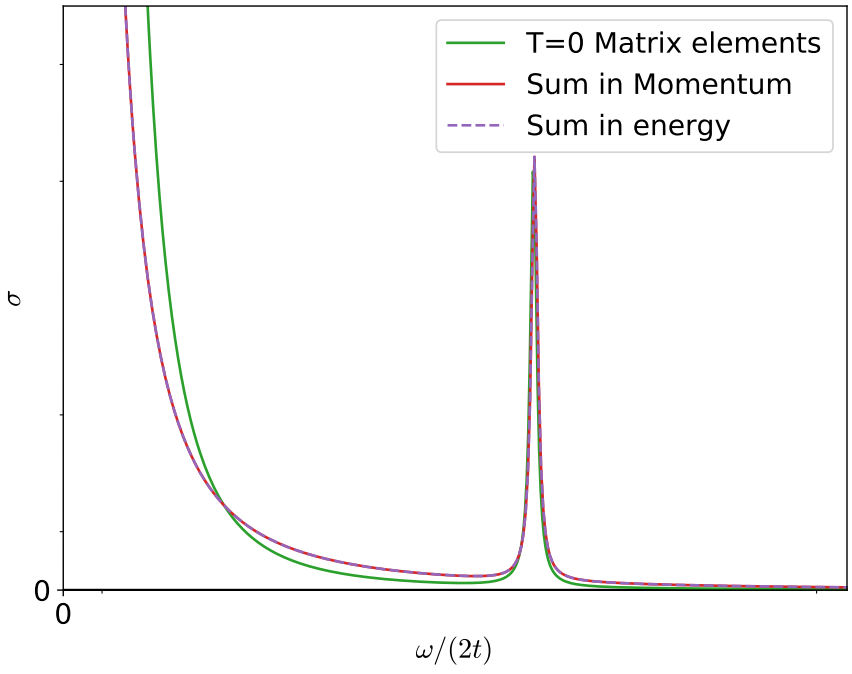

Figure B.3: Optical conductivity for the dimer ladder calculated by different approaches. T=0, $t_\perp/t = 0.6$, $\gamma = 0.01$, $\eta/a = 0.5$ using equations (B.14) (B.15). Calculated from Equation (B.21), but forgetting the factors of spin degeneracy and the $L/(2\pi)$ of the momentum space measure in the continuum limit it is very similar to the first result. Parameters are $\beta = 100$, $t_\perp/t = 0.6$, $\gamma = 0.005$ per spectral function. Using the Energy integral in equation (B.22) one obtains the last curve dotted on top. The Drude peak is narrower in the Green function calculations, the interband resonance is of equal weigth.

B.3 Infinite dimensions

With a established framework on the origin of the interband resonance one can extend the formalism to infinite dimension. The departing Hamiltonian does not change conceptually from (B.1), one will add just a tight binding extension to an hypercubic lattice with hopping among nearest neighbors. As is an standard procedure for this case, to keep the kinetic energy of the system fine one has to scale the hopping amplitude between neighboring sites transforming $t \to \frac{t}{\sqrt{2d}}$. Then we can redo the same procedure of section Peierls Ansatz to derive the current operator. We choose to maintain the isotropy of the system to position the second atom of the dimer in the center of the unit cell. This way it will be projected at the half-distance between lattice atoms in all directions and the electric dipole can be excited under the influence of the external electric field. Under this construction of isotropy the vector current operator is identical in each dimension changing only the dimension label, and it can be identified by

$$\hat{j}_l = \sum_{k_l,\sigma} e\left[2at\sin\left(k_l a\right)\left(a^{\dagger}_{k_l,-,\sigma}a_{k_l,-,\sigma} + a^{\dagger}_{k_l,+,\sigma}a_{k_l,+,\sigma}\right) + i\eta t_{\perp}\left(a^{\dagger}_{k_l,-,\sigma}a_{k_l,+,\sigma} - a^{\dagger}_{k_l,+,\sigma}a_{k_l,-,\sigma}\right)\right] \tag{B.23}$$

where definitions as identical to previous sections and l is an index that labels the dimension. From this expression we can again see that the system is isotropic and that there is no mixing of crystal quasi-momentum. This isotropy also allows to recognize that the conductivity tensor will be diagonal proportional to the unit tensor.

$$\sigma_{kl}(\omega) = \sigma_l \delta_{kl} = \bar{\sigma}(\omega)\delta_{kl} \tag{B.24}$$

More over and explaining the last equality all entries are the same. Thus one can look for the mean value of the conductivity starting from expression (B.18):

$$D\Re e\bar{\sigma}(\omega) = \sum_l \int d\omega' \frac{f(\omega') - f(\omega'+\omega)}{\omega} Tr\{\hat{j}_i A(\omega')\hat{j}_l A(\omega'+\omega)\} \tag{B.25}$$

where D is the dimension of the system. This expression can be expanded like (B.21)

$$D\Re e\bar{\sigma}(\omega) = \int d\omega' \frac{f(\omega') - f(\omega'+\omega)}{\omega} \times \sum_{l,\vec{k},\sigma} (4a^2t^2 \sin^2(k_l a) \left[A_+(\vec{k},\omega)A_+(\vec{k},\omega+\omega') + A_-(\vec{k},\omega)A_-(\vec{k},\omega+\omega')\right] + \eta^2 t_\perp^2 \left[A_-(\vec{k},\omega)A_+(\vec{k},\omega+\omega') + A_+(\vec{k},\omega)A_-(\vec{k},\omega+\omega')\right]) \tag{B.26}$$

Here it becomes necessary to sum over all states, as the Spectral functions do not have a spatial direction but hold all the information of momentum in the Brillouin zone. Following the work in Pruschke et al. [1993] in the infinite dimension limit $D \to \infty$ for a hypercube

$$\sum_{\vec{k}} \to \int dE\rho(E) \tag{B.27a}$$

$$\sum_{\vec{k},l} \sin^2(k_l) \to \frac{D}{2} \int dE\rho(E) \tag{B.27b}$$

$$\rho(E) = \frac{\exp(-E^2/(2t^2))}{\sqrt{2\pi t^2}} \tag{B.27c}$$

replacing (B.27) into (B.26) one obtains

$$\Re e\bar{\sigma}(\omega) = \int d\omega' \frac{f(\omega') - f(\omega'+\omega)}{\omega} \times \int dE\rho(E)(2a^2t^2 \left[A_+(E,\omega)A_+(E,\omega+\omega') + A_-(E,\omega)A_-(E,\omega+\omega')\right] + \eta^2 t_\perp^2 \left[A_-(E,\omega)A_+(E,\omega+\omega') + A_+(E,\omega)A_-(E,\omega+\omega')\right]) \tag{B.28}$$

A direct calculation from the last expression gives the following plot in figure B.4. Where the intraband peak is a robust feature but the Drude peak has become a lot thinner compared to the 1D case.

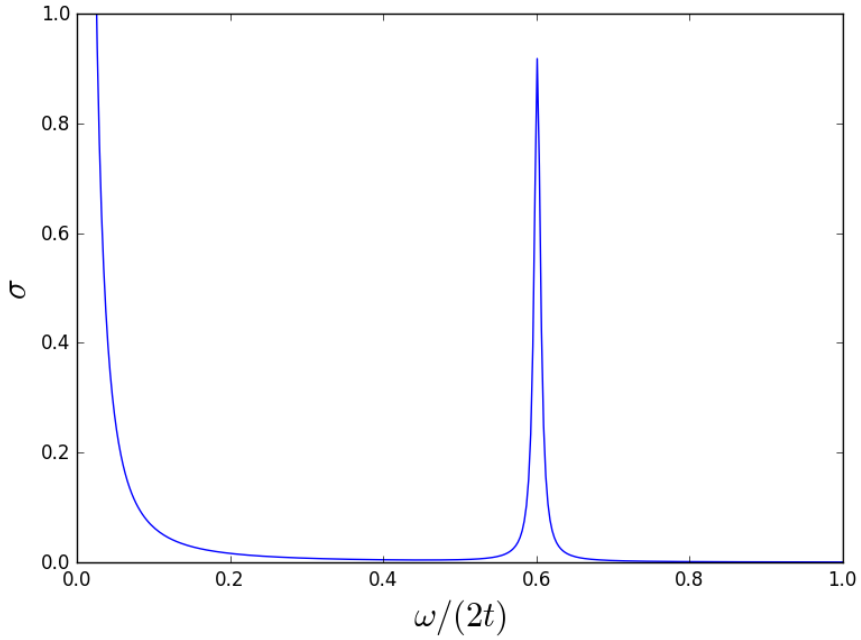

Figure B.4: Optical conductivity for an arbitrary lattice direction

Appendix C

IPT solvers

C.1 Analytical Formulation

The IPT solver is based on the use of only one of the second order skeleton diagrams of the self-energy. This diagram is the same for the single band case as for the Dimer, what is relevant to keep track is how each interaction vertex is composed so to construct the correct form of the self-energy when convoluting the Green's functions. As described in the next formula:

$$\mathbf{\Sigma}(i\omega_n) = -\frac{U^2}{\beta^2} \sum_{\omega_n', \Omega_m} \mathbf{G}^0(i\omega_n + i\Omega_m)\mathbf{G}^0(i\omega_n' + i\Omega_m)\mathbf{G}^0(i\omega_n') \tag{C.1}$$

where $\mathbf{G}^0$ is the Free propagator, in the DMFT context is the Weiss field, and $\mathbf{\Sigma}$ is the self-energy. Both functions are block matrices. In the paramagnetic case spin label is irrelevant. For the single band case this matrices reduce to scalar functions and for the dimer case they are 2×2 matrices, but they are not multiplied as matrices but **element wise**. Keeping this fact in mind the following derivation will continue ignoring the label indexes of the Greens functions as they are irrelevant for the derivation. $\omega_n^{(\prime)}$ are fermionic Matsubara frequencies and Ω_m is a bosonic Matsubara frequency, U is the contact Coulomb interaction and β the inverse temperature.

The key idea to analytically continuate from the Matsubara imaginary axis into the real frequency axis is through the following relation between the spectral function A and the Matsubara Green function:

$$\mathbf{G}(i\omega_n) = \int \frac{\mathbf{A}(\omega)d\omega}{i\omega_n - w} \tag{C.2}$$

valid for each entry of the matrix Green function. Let's start focusing on the fermionic bubble while inserting this identity.

$$\begin{aligned}
\mathbf{\Pi}(i\Omega_m) &= \frac{1}{\beta}\sum_{\omega_n}\mathbf{G}^0(i\omega_n + i\Omega_m)\mathbf{G}^0(i\omega_n) && \text{(C.3)}\\
&= \int dwdw' A(w)A(w')\frac{1}{\beta}\sum_{\omega_n}\frac{1}{i\omega_n - w}\frac{1}{i\omega_n + i\Omega_m - w'} && \text{(C.4)}\\
&= \int dwdw' A(w)A(w')\frac{f(w) - f(w')}{i\omega_n + w - w'} && \text{(C.5)}
\end{aligned}$$

where $f(w)$ is the Fermi-Dirac function. The IPT self-energy (C.1) can be written as:

$$\begin{aligned}
\mathbf{\Sigma}(i\omega_n) &= -\frac{U^2}{\beta}\sum_{\Omega_m}\mathbf{G}^0(i\omega_n + i\Omega_m)\mathbf{\Pi}(i\Omega_m) && \text{(C.6)}\\
&= -U^2\int dwdw'dw'' A(w)A(w')A(w'')\frac{[f(w) - f(w')][b(w' - w) + f(w'')]}{i\omega_n - w + w' - w''} && \text{(C.7)}\\
& && \text{(C.8)}
\end{aligned}$$

here $b(w)$ is the Bose-Einstein distribution. Numerically to calculate this function requires 4 nested loops to evaluate, and is computationally inefficient. In the search of extra improvement the following steps.

$$\mathbf{\Sigma}(i\omega_n) = -U^2\int dwdw'dw'' A(w)A(w')A(w'')\frac{f(-w)f(w')f(-w'') + f(w)f(-'w)f(w'')}{i\omega_n - w + w' - w''} \quad \text{(C.9)}$$

Introducing the new notation

$$\begin{aligned}
A^+(w) &= f(w)A(w) && \text{(C.10)}\\
A^-(w) &= f(-w)A(w) && \text{(C.11)}
\end{aligned}$$

and doing an analytical continuation $i\omega_n \to \nu + i\eta$

$$\mathbf{\Sigma}(\nu) = -U^2\int \frac{dwdw'dw''[A^-(w)A^+(w')A^-(w'') + A^+(w)A^-(w')A^+(w'')]}{\nu + i\eta - w + w' - w''} \quad \text{(C.12)}$$

Taking only the imaginary part, and integrating over w''

$$\Im m\mathbf{\Sigma}(\nu) = -\pi U^2\int dwdw'[A^-(w)A^+(w')A^-(\nu - w + w') + A^+(w)A^-(w')A^+(\nu - w + w')] \quad \text{(C.13)}$$

The terms in the integral are convolutions with the particularity that when integrating over w' this convolutions runs over the array backwards. Convolutions can be calculated at a cost of $\mathcal{O}(N \log N)$ operations using the FFT. Then to recover the real part of the self-energy through the Kramers-Kronig relation(KK), which is only valid for causal functions. In the case of the single band one applies KK directly. Nevertheless in the Dimer case one has first to rotate $\mathbf{\Sigma}$ to the diagonal basis where it is causal and negative $\forall\nu$. In the same diagonal basis one performs the Hilbert transform over the density of states to recover G_{loc} and evaluate the self-consistency condition to update G^0. Then one has to rotate back to the local basis and extract A^0.

C.1.1 Single band

Further simplifying expression C.13, using the definition of convolution for the integral in w. Because of particle-hole symmetry and a half-filled system $A^+(w) = A^-(-w)$

$$\Im m\mathbf{\Sigma}(\nu) = -\pi U^2 \int dw' \left[A^+(w')[A^- * A^-](\nu + w') + A^-(w')[A^+ * A^+](\nu + w')\right] \quad \text{(C.14)}$$

$$= -\pi U^2 \left([A^+ * [A^+ * A^+]](\nu) + [A^+ * [A^+ * A^+]](-\nu)\right) \quad \text{(C.15)}$$

In this case I'll study the Metallic solution, where the know 3 peak structure appears, also there is a lot of states in the preformed gap. As can be seen in figure C.1, where temperature is $\beta = 100$ and $U = 2.8$

C.1.2 The dimer IPT

The IPT expansion for the dimer problem conserves exactly the same diagrams as in the single band case but takes a matrix form Moeller et al. [1999].

$$\Sigma^{IPT}_{\alpha\beta}(i\omega_n) \equiv -U^2 \int_0^\beta G^0_{\alpha\beta}(\tau) G^0_{\alpha\beta}(-\tau) G^0_{\alpha\beta}(\tau) e^{i\omega_n \tau} d\tau \quad \text{(C.16)}$$

The Hartree-Fock contribution $U\langle n\rangle$ in the self-energy cancels with the chemical potential in the half-filled particle-hole symmetric problem when the self-energy is substituted into Dyson's equation. The IPT self-energy equation (C.16) can be conveniently reformulated into real frequencies by the analytical continuation of $i\omega_n \to \nu + i0^+$, and we can focus only on the imaginary part:

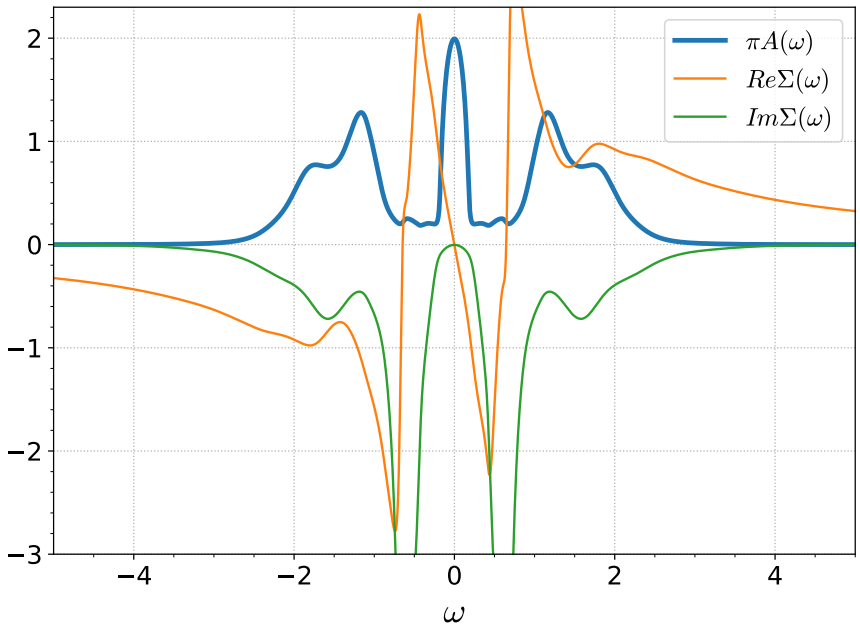

Figure C.1: Green functions for the single band DMFT real frequency IPT solution. Thick blue is $-\Im mG(\omega)$, green $\Im m\Sigma(w)$, red $\Re e\Sigma(\omega)$, cyan $-\Im m\mathcal{G}^0(\omega)$

$$\Im m\Sigma_{\alpha\beta}(\nu) = -\pi U^2 \int dwdw'[A^-_{\alpha\beta}(w)A^+_{\alpha\beta}(w')A^-_{\alpha\beta}(\nu-w+w')+A^+_{\alpha\beta}(w)A^-_{\alpha\beta}(w')A^+_{\alpha\beta}(\nu-w+w')] \tag{C.17}$$

Where

$$A^+_{\alpha\beta}(w) = \theta(w)A_{\alpha\beta}(w) = -\theta(w)\Im mG^0_{\alpha\beta}(w)/\pi \quad = \frac{1}{2}\left(\delta(w-t_\perp)+\delta(w+t_\perp)\right) \tag{C.18a}$$

$$A^-_{\alpha\beta}(w) = \theta(-w)A_{\alpha\beta}(w) = -\theta(-w)\Im mG^0_{\alpha\beta}(w)/\pi = \frac{1}{2}\left(\delta(w-t_\perp)-\delta(w+t_\perp)\right) \tag{C.18b}$$

here $\theta(w)$ is the Heaviside step function. Replacing into equation (C.17)

$$\begin{aligned}
\Im m\Sigma_{11}(\nu) &= -\pi\frac{U^2}{4}\int dwdw'[\theta(-w)\delta(w+t_\perp)\theta(w')\delta(w'-t_\perp)A^-(\nu-w+w')+ \\
&\qquad \theta(w)\delta(w-t_\perp)\theta(-w')\delta(w'+t_\perp)A^+(\nu-w+w')] \\
&= -\pi\frac{U^2}{4}\int dw'[\theta(w')\delta(w'-t_\perp)A^-(\nu+t_\perp+w')+ \\
&\qquad \theta(-w')\delta(w'+t_\perp)A^+(\nu-t_\perp+w')] \\
&= -\pi\frac{U^2}{4}[A^-(\nu+2t_\perp)+A^+(\nu-2t_\perp)] \\
&= -\pi\frac{U^2}{8}[\theta(-(\nu+2t_\perp))(\delta(\nu-t_\perp)+\delta(\nu+3t_\perp))+ \\
&\qquad \theta(\nu-2t_\perp)(\delta(\nu-3t_\perp)+\delta(\nu-3t_\perp))]
\end{aligned}$$

$$\Im m\Sigma_{11}(\nu) = -\pi\frac{U^2}{8}[\delta(\nu+3t_\perp))+(\delta(\nu-3t_\perp)] \tag{C.19}$$

And anologuous procedure is followed to calculate Σ_{12}. The real parts can be obtained by the Kramers-Kronig relation and one recovers the results presented in equation (A.16) for the zero temperature ($T=0$) isolated dimer limit ($t=0$), finally allowing us to assert the exact limits of this approximation.

Appendix D

PyDMFT

Software sources used to produce this work have led to development of this library now hosted on https://github.com/Titan-C/PyDMFT Is under GPL-v3 license

Appendix E

PyMaxent

The method of analytical continuation works with the relation between the Matsubara Green's function and the real frequency axis spectral function.

$$G(i\omega_n) = \int \frac{A(\omega)dw}{i\omega_n - \omega} \tag{E.1}$$

The numerical inversion of this equation is ill-conditioned and Quantum Monte Carlo data includes noise in the measured Matsubara Green's function. The central idea of the Maximum entropy method Jarrell and Gubernatis [1996] is to search for a spectral function that satisfies (E.1) and maximizes the information entropy $\mathcal{S}$ relative to a positive definite default model D which has the known high frequency behavior of the Green's function. Without the constraint (E.1) the maximizing entropy is the default model D.

$$\mathcal{S} = \int d\omega \left[A(w) \ln \frac{A(w)}{D(w)} - A(w) + D(w) \right] \tag{E.2}$$

The entire procedure for the Analytical continuation and various examples and benchmarks are released in the PyMaxent package, under BSD-3 clause license.

https://github.com/Titan-C/PyMaxent